

## ABSTRACT

MILY JR., EDWARD JOSEPH. Thermite at the Nano-Scale (Under the advisement of Dr. Jon-Paul Maria.)

Physical vapor deposition of thin film thermites allow for a clean avenue for probing fundamental properties of nanoenergetic materials that prove difficult for traditional powder processing. Precise control over diffusion dimensions, microstructure, and total amount of material are able to be realized with this fabrication technique and the testing of such materials provide valuable insight into how oxidation occurs.

This thesis provides several examples of how existing PVD techniques can be coupled with thermite constituents to further the energetic community's understanding of how oxidation occurs in the solid state with the variation of geometric and chemical alterations. The goal of these investigations was to elucidate which material properties and mechanisms drive exothermic activity.

The thermite thin films of Al/CuO, Zr/CuO, and Mg/Cuo with varied reducing metal constituents were tested under slow heating conditions. The trend of the metal variation demonstrated the importance of terminal oxide diffusion properties in either impeding or enhancing oxygen exchange. When the reducing metal forms a terminal oxide with limited oxygen diffusivity, exothermicity requires elevated activation energies to commence self-sustaining reaction. In addition to the effects of chemical variation, bilayer thicknesses were varied and found to decrease exothermic peak temperatures similar to the trends found in intermetallic thin film energetics and powder energetic materials.

The thin film thermites were also subjected to extreme initiation methods via laser driven flyer plate impact ignition and high heating rate heat treatment ( $10^5$  K/s). General insight into nano thermite behavior at environments characteristic of applications was sought, and similar trends discovered among slow vs rapid testing. Decreasing reaction dimensions yielded higher reactivity and diffusion barrier properties role in impacting exothermic behavior persist to into the microsecond regime.

Ultimately through this work it has been shown that the process of thermite exothermicity proceeds through more than one pathway and more than the free energy of oxidation of reducing metals should be considered when describing how oxygen exchange occurs. It has been shown that these self-sustaining reactivity can be realized in the solid and

liquid state via slow and fast initiation, and oxygen exchange depends on not just the driving force, but on extrinsic and intrinsic materials properties.

© Copyright 2015 by Edward Joseph Mily Jr.

All Rights Reserved

Thermite at the Nano-Scale

by  
Edward Joseph Mily Jr.

A dissertation submitted to the Graduate Faculty of  
North Carolina State University  
in partial fulfillment of the  
requirements for the Degree of  
Doctor of Philosophy

Materials Science and Engineering

Raleigh, North Carolina

2015

APPROVED BY:

---

Dr. Michael Dickey  
Professor of Chemical Engineering

---

Dr. Don Brenner  
Professor of Materials Science

---

Dr. Doug Irving  
Professor of Materials Science

---

Dr. Elizabeth Dickey  
Professor of Materials Science

---

Dr. Jon-Paul Maria  
Professor of Materials Science  
Committee Chair

**DEDICATION**

The entirety of this work is dedicated to my loving parents Edward and Elaine Mily. Without their love and support from childhood to adulthood none of this research would have been possible.

## **BIOGRAPHY**

Edward Mily Junior comes from the central Pennsylvanian homestead near Harrisburg Pennsylvania. He is the youngest of three and pursued an education in engineering early on. His first place science fair experiment in elementary school fostered his interest in the sciences very early in his education. In middle school he participated in the Technology Students Association (TSA) which shaped his interests greatly and pointed them towards the technological fields. This interest in the sciences shaped his high school curriculum to accentuate and further develop his mathematical and spatial reasoning skills which ultimately led him to pursue education in engineering. He enrolled at the Pennsylvania State University to study materials science and engineering with a specialty polymers processing. Upon completion of his bachelor degree materials science he decided to further study materials science engineering at North Carolina State University under the advisement of Dr. John Paul Maria to complete his doctoral degree. During his tenure as a graduate student to balance out his workload he enjoyed competitive adult league hockey and occasionally brewing his own beer.

## ACKNOWLEDGMENTS

Research is not done in a vacuum and the work described in this dissertation is no exception. First and foremost, I would like to thank my advisor Dr. Jon-Paul Maria for giving me the opportunity to become a part of a great research group. Dr. Maria's support throughout my graduate education was invaluable professionally and personally. Without his help and leadership my presentation skills would be bereft of refinement, my experimental technique not as rigorous, and ultimately none of this work would be possible. His uncanny ability to distill problems to their root cause is efficient, effective and allows for a clear path to the solution. I am grateful for the experiences from Pig Picking preparations to late night conference preparations and I thank you.

The collaborative efforts between the 3<sup>rd</sup> and 2<sup>nd</sup> floor research groups of Research Building 1 also assisted me greatly on my path through graduate school. General experimentation advice from Dr. Zlatko Sitar and Dr. Ramón Collazo was very helpful. Their allowance of my access to the UHV system and the XPS analysis is greatly appreciated. The specific rigorous training I received on XPS apparatus operation was graciously done by Christer Akoula was an great help. In addition the assistance I received from the Bryan brothers in all things from experimental procedure to car radiator replacement was highly appreciated. Pramod Reddy also shouldered my frustrations with XPS data collection and his willingness to be a sounding board did not go unnoticed. A special thanks to Dr. Brenner and Dr. Irving for their advice and perspective from a computational point of view with many valuable insights that would have most assuredly gone unnoticed without their direction. Also, credit must be given to Shijing Lu for his brilliant manipulation of thermodynamic equations to assist our understanding of activation energy calculation through his modeling.

Special thanks to Ali Moballegh and Dapo Oni for their patience in helping me chase my white whale that is the nano Kirkendall experiment. Thank you gentlemen.

Thanks must also be given to Dr. Elizabeth Dickey for her help in my undergraduate and graduate understanding of material characterization. Your classes and instruction were crucial in my development as a capable material scientist.

Dr. Michael Dickey, I appreciate your help and advisement on my final Thesis committee, thank you .

The work on thermite impact behavior would be nonexistent if not for the help of William Shaw and Dr. Dana Dlott from the University of Illinois. Will's persistent attention to detail and optimism on the testing of the thin films was exceptional. His patience when explaining shock physics to me and answering my myriad of questions was greatly appreciated.

Dr. Zachariah and Garth Egan were integral in the understanding of the thin film thermite behavior at fast heating rates. Their willingness to work with us on sample preparation and insight into the energetics community were exceptionally helpful.

Finally I must thank all past and current members of the electronic oxides thin films group: Peter Lam, Beth Paisley, Michelle Casper, Omer Gozen, David Hook, (Professor) David Harris, (Prince) Edward Sachet, Christopher Tyrel Shelton, Alex (Al) Smith, Tina Rost (Tinay Nay), Xiaoyu Kang (X-man), Kyle (the Moose) Kelley, Nicole Estrich, and William Luke. Graduate school would not have been as enjoyable without the many fun times we have had together. Our beach to mountain trips will live on in my memory for years to come. Thanks for putting up with me and most importantly for your friendship.

## TABLE OF CONTENTS

<b>LIST OF TABLES</b> .....	x
<b>LIST OF FIGURES</b> .....	xi
<b>1. Energetics History</b> .....	1
<b>1.1 Early Humans</b> .....	1
<b>1.2 Greek Fire</b> .....	4
<b>1.3 Gunpowder</b> .....	5
<b>1.4 A New Class of Materials</b> .....	6
1.4.1 Dynamite .....	6
<b>1.5 High Explosives</b> .....	9
<b>1.7 Thermite</b> .....	10
1.7.1 Metallic addition to traditional energetics .....	11
<b>1.8 Nano-sized Aluminum</b> .....	12
<b>2. Nano Energetic Materials</b> .....	14
<b>2.1 Nano Powder Mixing</b> .....	16
<b>2.2 Sol Gel Processing of Nano Energetics</b> .....	17
2.2.1 Sol-Gel Chemistry .....	17
2.2.2 Sol-Gel Fabrication of Energetic Materials .....	20
<b>2.3 Arrested Reactive Milling</b> .....	21
<b>2.4 Physical Vapor Deposition</b> .....	22
<b>3. The Role of Terminal Oxide Structure and Properties in Nanothermite reactions</b> .....	27
<b>3.1 Abstract</b> .....	27
<b>3.2 Introduction</b> .....	28
<b>3.3 Experimental Procedure</b> .....	32
3.3.1 Film Deposition .....	32
3.3.2 TEM Sample Preperation .....	32
3.3.3 Annealing Procedure .....	33
3.3.4 X-ray Analysis .....	33
3.3.4.1 Deposition Rate Determination .....	33
3.3.4.2 Phase Identification .....	33

3.3.5 Thermal Analysis .....	34
<b>3.4 Results and Discussion .....</b>	<b>34</b>
<b>3.5 Conclusion .....</b>	<b>40</b>
<b>3.6 Acknowledgements .....</b>	<b>40</b>
<b>4. Effect of Thin Film Bilayer Spacing on Thermite Exothermicity .....</b>	<b>41</b>
<b>4.1 Abstract .....</b>	<b>41</b>
<b>4.2 Introduction .....</b>	<b>41</b>
<b>4.3 Experimental .....</b>	<b>42</b>
<b>4.4 Reults and Discussion .....</b>	<b>44</b>
4.4.1 Al/CuO System .....	44
4.4.2 Zr/CuO System.....	49
<b>4.5 Conclusion .....</b>	<b>42</b>
<b>5. Interfacial Anaylsis of Multilayered Nanothermite.....</b>	<b>54</b>
<b>5.1 Interfacial Analysis Background.....</b>	<b>54</b>
<b>5.2 Experimental Procedure .....</b>	<b>56</b>
5.2.1 Substrate Preperation.....	56
5.2.2 X-ray Photoelectron Analysis .....	57
<b>5.3 Results and Discussion .....</b>	<b>57</b>
5.3.1 Copper Oxide Phase Identification .....	57
5.3.2 Aluminum Deposition on CuO .....	58
5.3.3 Zirconium Depostion on CuO.....	63
<b>5.4 Conclusion .....</b>	<b>65</b>
<b>6. Nano-Kirkendall Diffusion.....</b>	<b>66</b>
<b>6.1 Diffusion Monitoring at the Nano Scale .....</b>	<b>66</b>
<b>6.2 Diffusion Marker Deposition.....</b>	<b>70</b>
6.2.1 Nano Particle Deposition .....	70
6.2.2 Electron Beam Deposited Platinum Diffusion Markers.....	76
6.2.2.1 Sample Tracking .....	78
<b>6.3 Pt Deposition Results and Discussion .....</b>	<b>87</b>
6.3.1 Pt Deposition via Focused Ion Beam and Focused Electron Beam .....	96
<b>6.4 Concluding Remarks About Pt Feasibility.....</b>	<b>101</b>

<b>7. Shock Impact Behavior of Thin Film Thermite</b> .....	105
<b>7.1 Introduction to Impact Testing</b> .....	105
7.1.2 Shock Waves.....	106
7.1.3 Shock Wave Generation.....	107
7.1.4 Laser Driven Flyer Plates.....	107
7.1.5 Composite Energetic High Speed Testing.....	108
<b>7.2 Impact Behavior of Thin Film Thermite</b> .....	109
7.2.1 Variation of Interface Density in Thin Film Thermites.....	111
7.2.2 Variation of Reducing Metal on Thin Film Thermites.....	118
<b>7.3 Conclusion</b> .....	120
<b>8. Rapid Annealing of Thin Film Thermite and the Effects of Geometric spacing</b> .....	122
<b>8.1 Rapid Annealing Introduction</b> .....	122
<b>8.2 Thin Film Thermite Deposition on Thin Platinum Wires</b> .....	123
<b>8.3 High Speed Annealing</b> .....	127
<b>8.3 Ignition Temperature Modeling</b> .....	136
<b>8.5 Conclusion</b> .....	139
<b>9. Eutectic Melting Effect on Energy Release</b> .....	140
<b>9.1 Introduction</b> .....	140
<b>9.2 Intermetallic Phase Identificaion</b> .....	144
9.2.1 Hot Stage XRD.....	144
9.2.2 Auger Electron Spectroscopy.....	118
<b>9.3 Eutectic Thermite Testing</b> .....	149
<b>9.4 Conclusion</b> .....	154
<b>REFERENCES</b> .....	155
<b>APPENDICES</b> .....	164
<b>Appendix A- XPS</b> .....	165
<b>I. Aluminum Aging Study</b> .....	165
<b>II. CuO Surface Roughness Study</b> .....	169
<b>III. XRR Confirmation of Thin Film Thickness at the interface of Zr/CuO</b> .....	179
<b>IV. XPS Cooling System</b> .....	181

**Appendix B- TEM Sample Preperation for Kirkendall Analysis ..... 182**

## LIST OF TABLES

<b>Table 2.1-</b> Comparison of energetic materials properties .....	14
<b>Table 3.1-</b> Heat of Formation, Oxygen Diffusivity, and Pilling-Bedworth Ratio for each system studied .....	31
<b>Table 4.1-</b> Thin Film Thermite Parameters .....	43
<b>Table 6.1-</b> Input parameters for E-Beam deposited Pt.....	87
<b>Table 8.1-</b> High Speed Ignition Temperature Data.....	129
<b>Table 9.1-</b> Mg/CuO thin film thermite deposition parameters .....	150

## LIST OF FIGURES

<b>Figure 1.1-</b> Chemical structure of nitroglycerin .....	7
<b>Figure 2.1-</b> Organic Energetic vs. Inorganic order of reaction distance .....	15
<b>Figure 2.2-</b> Hydrolysis and condensation reactions that occur during sol-gel synthesis .....	18
<b>Figure 2.3-</b> Sol-Gel Synthesis solvent extraction schematic for an Aerogel and Xerogel.....	20
<b>Figure 2.4-</b> Typical microstructure obtained by ARM MIC processing.....	22
<b>Figure 2.5-</b> TEM micrograph of an Al/CuO thermite thin film, with total thickness 1080nm .....	24
<b>Figure 2.6-</b> Dual magnetron sputtering architecture used to fabricate thermite nanostructures .....	25
<b>Figure 3.1-</b> a) Idealized schematic of oxygen exchange reactions at a) the original MO   M interface and b) showing the accumulation of an intermediate barrier layer that accumulates with time .....	30
<b>Figure 3.2-</b> TEM image of Zr-CuO multilayer with 3 total bi-layers .....	35
<b>Figure 3.3-</b> X-ray diffraction patterns for (a) Al-CuO, (b) Mg-CuO, and (c) Zr-CuO reactive nanolaminates exposed to high temperature anneals. The diffraction angles for Cu metal are highlighted for clarity .....	36
<b>Figure. 3.4:</b> DSC Analysis for Al-CuO, Mg-CuO, and Zr-CuO laminate structures ramped in flowing Ar at 5 °C/min .....	38

**Figure 3.5:** Exothermic onset temperature vs terminal oxide diffusivity [ $\text{cm}^2/\text{sec}$ ] at  $500\text{ }^\circ\text{C}$ .. 39

**Figure 4.1-** XRD Spectra for the Al/CuO system stepwise anneal phase identification for the a.) 1 bilayer Al/CuO sample and the b.) 7 bilayer Al/CuO sample ..... 46

**Figure 4.2-** DSC data from the Al/CuO thin film samples testing the exothermic behavior of the samples as a function of the number of bilayers ..... 47

**Figure 4.3-** Effective activation energy Kissinger analysis plot of the Al/CuO thin film system ..... 48

**Figure 4.4-** XRD Spectra for the Zr/CuO system stepwise anneal phase identification for the a.) 1 bilayer Zr/CuO sample and the b.) 5 bilayer Zr/CuO sample..... 50

**Figure 4.5-** DSC data from the Zr/CuO thin film samples testing the exothermic behavior of the samples as a function of the number of bilayers ..... 51

**Figure 4.6-** Effective activation energy Kissinger analysis plot of the Zr/CuO thin film system ..... 52

**Figure 5.1-** Visual representation of photo-electrons from each each sample constituent ..... 56

**Figure 5.2-** Cu 2p orbital energy range, showing the affects of aluminum monolayer titration on the copper oxidation state ..... 59

**Figure 5.3-** Al 2p binding energy range showing a singular peak at  $74.7\text{eV}$  corresponding the sample that iteratively deposited 1 ML of aluminum at a time. The peak shows aluminum coordinated with oxygen..... 60

**Figure 5.4-** Al 2p binding enegy range comparing samples with 11ML of aluminum deposited via mono-layer by monolayer and deposition all at once ..... 60

**Figure 5.5-** Visual representation of metal island growth on the CuO surface, where an environment is created that promotes surface diffusion ..... 62

<b>Figure 5.6-</b> Al 2p energy range for samples with different thicknesses of Al deposited on the surface of CuO. The corresponding layer where metallic aluminum appears is at 7ML of aluminum or ~2.1 nm.....	63
<b>Figure 5.7-</b> Zr 2p energy range for samples with different thicknesses of Zr deposited on the surface of CuO. The corresponding layer where metallic aluminum appears is at 10ML of aluminum or ~3.2 nm.....	65
<b>Figure 6.1-</b> Self diffusion of metals and oxygen through common oxides.....	67
<b>Figure 6.2-</b> Original Kirkendall diffusion experiment of a brass ingot encased in a copper coating with Molybdenum wires at the surface for diffusion tracking.....	68
<b>Figure 6.3-</b> Schematic of the idealized Nano-Kirkendall Experiment. M' and MO are the original metal and metal oxide respectively. M and M'Ox are the terminal metal and terminal oxide respectively .....	69
<b>Figure 6.4-</b> Au nanoparticles deposited on CuO at the lowest concentrations .....	73
<b>Figure 6.5-</b> Au nanoparticles deposited on CuO at the medium concentration .....	73
<b>Figure 6.6-</b> Au nanoparticles deposited on CuO at the highest concentration.....	74
<b>Figure 6.7-</b> AFM micrograph of nano-gold particles that had been cast onto a copper oxide thin film from a toluene solution in an attempt to decrease particle size and maintain particle spacing .....	75
<b>Figure 6.8a-</b> Diagram of Pt deposition via e-beam deposition .....	77
<b>Figure 6.8b-</b> Diagram of Pt deposition via e-beam deposition.....	77
<b>Figure 6.9-</b> SEM Macroscopic view of asymmetric milled out location aids.....	79
<b>Figure 6.10-</b> SEM micrograph view of asymmetric milled out location aids with Pt diffusion markers located next to them .....	80
<b>Figure 6.11-</b> a.) SEM micrograph of surface damage done to CuO thin film. b.) undamaged microstructure 5 $\mu\text{m}$ away from the milled feature, c.) altered morphology due to milling 1 $\mu\text{m}$ away from milled feature .....	81

<b>Figure 6.12-</b> SEM micrograph of CuO film scribed for purposes of sample location identification .....	83
<b>Figure 6.13-</b> SEM micrograph of Pt bars deposited near the scribed location on CuO.....	84
<b>Figure 6.14-</b> SEM Micrograph of Pt Identification markers flanking diffusion markers on CuO .....	85
<b>Figure 6.15-</b> SEM micrograph of e-beam deposited Pt bars on an undamaged CuO surface .....	86
<b>Figures 6.16-</b> a.) Schematic of Pt bars on CuO surface with orientation b.) AFM image of the lateral and horizontal dimensions of deposited Pt bars c.) AFM height retrace of the Pt bars overall dimension in the Z direction .....	88
<b>Figure 6.17-</b> TEM cross-section of Zr/CuO interface with Pt diffusion markers .....	91
<b>Figure 6.18-</b> TEM cross-section of Zr/CuO interface with a bright Pt deposit 20nm in width .....	92
<b>Figure 6.19-</b> TEM cross-section of Cr/CuO interface with Pt bars between Cr and CuO layers .....	93
<b>Figure 6.20-</b> TEM cross-section of Cr/CuO interface with Pt deposit a.) after deposition b.) after a 1 year anneal at 25oC.....	94
<b>Figure 6.21-</b> TEM cross-section of annealed Zr/CuO sample devoid Pt markers and of the CuO thin film layer .....	94
<b>Figure 6.22-</b> Infographic of conductive AFM experiment to check the quality of the Pt deposition .....	97
<b>Figure 6.23-</b> a.)AFM image of E-beam deposited Pt wires at 5KeV and 13pA at the junction of sputtered Pt and silica surface b.) Conductive AFM trace over the deposited Pt bars on top of sputter coated Pt c.) Conductive AFM trace over Pt wires on the silica surface.....	98-99
<b>Figure 6.24-</b> a.) SEM Image of Ion beam deposited Pt Wires at 30KV and 0.5nA at the junction of the Sputtered Pt and Silica surfaces b.) Conductive AFM trace over the deposited Pt bars on top of sputter coated Pt c.) Conductive AFM trace over Pt wires on the silica surface .....	100-101

<b>Figure 7.1-</b> Schematic showing the principles of the Nd:YAG laser driven flyer plate apparatus with an Al flyer plate incident on a thin film thermite.....	111
<b>Figure 7.2-</b> Organic Masked thermite nanolaminate impact sample .....	112
<b>Figure 7.3-</b> Baseline emission comparison from a Zr/CuO thermite, Zr thin film, and a CuO thin film. Emission is present for the bare Zr film but at 10% of the intensity of thermite couple.....	113
<b>Figure 7.5-</b> Graphical depiction of the Zr/CuO impact samples with the exothermic peak temperature obtained for each system under slow thermal analysis via differential scanning calorimetry.....	115
<b>Figure 7.6-</b> Intensity vs time data where each trace represents the optical emission spectrum of increasing flyer plate velocities for a.) Zr/CuO 1 bilayer sample, b.) Zr/CuO 2 bilayer sample, and c.) Zr/CuO 3 bilayer sample .....	115
<b>Figure 7.7-</b> Pictograph of a visual representation of more reaction points or hot spots for laminates with increased number of bilayers.....	116
<b>Figure 7.8 -</b> Plot of threshold velocity vs. the number of bilayers in the Zr/CuO samples. ....	117
<b>Figure 7.9-</b> Exothermic peak temperature from Differential scanning calorimetric studies vs. the number of bilayers in the Zr/CuO thermite system.....	117
<b>Figure 7.10-</b> Intensity vs time data where each trace represents the optical emission spectrum of increasing flyer plate velocities for a.) Al/CuO 3 bilayer sample, b.) Mg/CuO 3 bilayer sample, and c.) Zr/CuO 3 bilayer sample .....	119
<b>Figure 7.11 -</b> Impact velocity required for thermite reaction as a function of the young's modulus of each systems respective terminal oxide.....	120
<b>Figure 8.1-</b> Schematic diagram of the dual beam magnetron system with the sample rotation axis. ....	124
<b>Figure 8.2-</b> 3-D printed Pt wires substrate holder to allow for minimal sample shadowing and rotation perpendicular about the axis normal to the deposition source. ....	125
<b>Figure 8.3-</b> Temperature Jump (T-Jump) Pt sample apparatus. This configuration allows for the controlled heating of the Pt wires at elevated heating rates up to 105K/s. ....	126

<b>Figure 8.4-</b> Cross-section SEM micrograph of a Pt wire with a conformal thermite nanolaminate coating. ....	127
<b>Figure 8.5-</b> Cross-section SEM micrograph of Pt wire with conformal Al/CuO nanolaminate coating. A columnar morphology is clearly seen in the thin film multilayers. ....	127
<b>Figure 8.6-</b> Cross-section SEM micrographs of Al/CuO nanolaminate with a.) 1 bilayer b.) 3 bilayers, and c.) 6 bilayers .....	127
<b>Figure 8.7-</b> In situ high speed temperature jump frames for the 3, 6, and 10 bilayer samples during the temperature jump. The scale is the same for each sample, where the bright wire portion of the 3 bilayer sample is 10 mm. ....	128
<b>Figure 8.8-</b> Time of flight mass spectroscopy data for a.) three and b.) six bilayer samples. The temperatures of ignition ascertained by the optical high speed video are represented by the vertical dashed line. ....	131
<b>Figure 8.9</b> – Pressure-temperature diagram for $Cu_xO_y$ .....	132
<b>Figure 8.10-</b> Differential scanning calorimetry of a 400nm CuO thin film on sapphire at 5K/min ramp rate in Argon. ....	133
<b>Figure 8.11-</b> X-ray diffraction data for 400nm CuO film at 25°C, 600°C, 850°C and 1200°C demonstrate the transition of CuO to Cu <sub>2</sub> O after 800°C. ....	134
<b>Figure 8.12-</b> Still frame from high speed photography showing the collection geometry of sample products. ....	134
<b>Figure 8.13-</b> SEM micrograph a.) & b.) of post reaction products collected after sample ejection post ignition from the 10 bilayer Al/CuO nanolaminate coated Pt wire. ....	136
<b>Figure 8.14-</b> Ignition temperatures computed vs. predicted as a function of number of bilayers. The best fit ( $R^2$ coefficient of 0.94) was found to occur with $E_a=20$ kJ/mol and $D_0=7.1 \times 10^{-13}$ m <sup>2</sup> /s. ....	138
<b>Figure 9.1-</b> Differential scanning calorimetry of Al/CuO thin film thermite samples with varying number of bilayers .....	142
<b>Figure 9.2-</b> Phase Diagram of Al-Cu displaying the aluminum rich portion where the low temperature eutectic melt occurs at 548 °C .....	143

<b>Figure 9.3-</b> XRD of Al/CuO 6 bilayer film at different temperatures indicating the presence of copper metal. No evidence of any intermetallic is seen. ....	145
<b>Figure 9.4-</b> Auger electron kinetic energy of the Cu LMM transition plotted against the binding energy of the Cu 2p 3/2 for known phases of copper and oxygen and experimentally obtained data. ....	148
<b>Figure 9.5-</b> EDS map of Zr/CuO interface showing a Cu rich region just below the overlapping layer of zirconium and oxygen. . ....	149
<b>Figure 9.6-</b> Mg-Cu Phase diagram.....	150
<b>Figure 9.7-</b> XRD of the 8 bilayer Mg/CuO thin film with evidence of intermetallic formation	152
<b>Figure 9.8 -</b> DSC of Mg/ CuO multilayered thermite displaying the eutectic influence on the exothermic behavior.....	153
<b>Figure A.1-</b> Schematic of the XPS chamber used to complete the surface analysis.....	155
<b>Figure A.2-</b> Aluminum 2p photoelectron binding energy spectra taken during the first 126 hours after deposition.....	158
<b>Figure A.3 -</b> Aluminum 2p photoelectron binding energy spectra taken incrementally up to 15 days after deposition .....	158
<b>Figures A.4 -</b> AFM map of a.) Uncleaned silicon with a 2.1 nm roughness, b.) a cleaned silicon wafer with a 100pm roughness.....	162
<b>Figure A.5 -</b> AFM of CuO 10nm on silicon with a roughness of 100pm .....	163
<b>Figure A.6 -</b> AFM of CuO 20nm on silicon with a roughness of 316pm .....	163
<b>Figure A.7-</b> AFM of CuO 30nm on silicon with a roughness of 520pm displaying the transition from layer by layer growth to island growth to coalescence. ....	164
<b>Figure A.8-</b> AFM of a.) CuO 30nm on silicon with a b.) line height retrace to display the height of the growing island. ....	165
<b>Figure A.9 –</b> AFM of CuO 50nm with a roughness of 872pm .....	166
<b>Figure A.10-</b> AFM of CuO 100nm with a roughness of 1.5nm.....	166

<b>Figure A.11-</b> AFM of CuO 200nm with a roughness of 4.5nm.....	167
<b>Figure A.12-</b> AFM of CuO 300nm with a roughness of 4.8nm .....	167
<b>Figure A.13-</b> AFM of 2um of CuO with a roughness of 11.35nm .....	168
<b>Figure A.14-</b> XRR data from the Zr/CuO interface with a modeled fit to account for a 3nm interfacial layer. ....	170
<b>Figure B.1-</b> SEM micrograph of a milled location aid next to Pt bars deposited at the interface of .....	173
<b>Figure B.2-</b> SEM snapshot of milling out a TEM sample .....	173
<b>Figure B.3-</b> SEM micrograph of the side view of a TEM sample attached to a Molybdenum grid .....	174
<b>Figure B.4-</b> SEM micrograph of the top view of the TEM sample .....	174
<b>Figure B.5-</b> SEM micrograph of the side view of the TEM sample after thinning. ....	175
<b>Figure B.6-</b> SEM micrograph of the top view of the thinned TEM sample .....	175

# 1. Energetics History

## 1.1 Early Humans

In order to understand how nano-thermite fits in with the greater picture of human interaction with energetic materials it is helpful to get a broader view of how humankind has interacted with the release of energy. History has shown our relationship with energy closely revolves around oxidation. Current prevailing wisdom among archaeologists and anthropologists suggest that humans first started using and interacting with fire around 1.8 million years ago. It is around this time that modern humans biologically first started appearing with major differences from their apelike ancestors. Much controversy and investigation has surrounded the beginnings of human history and the use of fire. The first question to be addressed is what made our ancestors leave the relative safety and comfort of a forested habitat. It has been suggested the motivating factor for the leaving trees and becoming bipedal was the search for more rich protein sources in the form of meat. This implies that the reason why human beings left the trees was because they were predatory in nature. However this theory leaves much to be desired because modern chimpanzees do in fact behave omnivorously when the opportunity presents itself and yet their main habitat is still a canopied forest[1]. Chimpanzees have been known to kill other species of smaller monkeys and mammals. So this begs the question why did our ancestors change and the chimpanzees did not? An emerging and promising theory is that our ancestors were the first to realize and utilize the control of fire for their benefit and this controlled usage of combustion is what ultimately separated us from our ape ancestors.

A casual observer of the animal kingdom will note that a large portion of animals are afraid of fire. Forest fires can be devastating to the local wildlife that once inhabited the charred environment. They spread quickly, are unpredictable, and are influenced by wind direction and the varying types of fuel in a forested area. In contrast to forest fires, brushfires that are ignited by lightning in a landscape devoid of most vegetation are relatively benign in the eyes of the animal species that commonly interact with them. These grass fires have a homogenous fuel source, can be seen from a distance, and are easily avoidable. In the

Serengeti of Africa where brushfires are commonly started by lightning, the plains animals seem relatively calm in close proximity to the burning grass [1, 2]. Our ancestors originating in the African continent would have been exposed to these two types of fire yielding a very basic understanding of what types of fire were malignant and what situations were harmless. It is then conceivable that there are certain situations where fear of a burning area would be devoid in our ancestor's mind. Lack of fear however does not motivate one to approach or attempt to corral a burning environment. A catalytic factor must have been the reason for the ultimate taming used fire. A very reasonable explanation for this comes from the perspective of a hungry apelike animal looking for food. Our earliest ancestors differed very little from chimpanzees. If one was to look at the diet of chimpanzees it would be found that they consume a large portion of fruits, nuts, vegetables, and sources high in protein. The protein that they search for is one that requires the least amount of work, namely they primarily consume insects. Our ancestors, assuming they shared a similar diet to common chimpanzees, in the search of protein rich insects as a source of food would undoubtedly learn where the best locations were to collect this food source. One area where insects are known to agglomerate is the burnt charred remains left in a fire's wake. These particular pyrophilic insects are drawn to the high nitrogen content created by the combustion of organic matter. This behavior undoubtedly would have attracted any creature that had a taste for insects and would have provided a veritable bounty for an animal in search of a protein rich meal that required very little effort to obtain. The search for insects and other food sources on the ground provided our ancestors with a dangerous task. Our earliest ancestors physically differed from modern chimpanzees only in slightly increased cranial capacity. They were very much still apelike: they slept in trees, had a mostly vegetarian diet that was supplemented by an occasional protein rich source of insects or smaller mammals. Searching for food on the ground would have been an occasional behavior because they were poorly physically equipped to defend themselves against larger predatory animals. This was why they sought out the protection of the canopy of forested areas.

Sleeping on the ground provides the hazards of being unprotected and vulnerable. As a reference, only the largest of the great apes occasionally display this ground sleeping behavior. It's likely the cultivation of fire generated the security needed to no longer rely on the safety of trees. The phasing out of forested habitats no longer requires the presence of overly developed upper body structure and muscles. Taking advantage of the heat release from the oxidation of organic material had another consequence on our ancestors: it allowed us cook our food.

Cooking is a uniquely human activity and its practice has influenced human evolution and facilitated our development into modern Homo Sapiens. The reason for this is simply nutrient absorption. Heating foods doesn't increase the overall energetic capacity of a nutrient, quite the contrary, it reduces it. However, the amount of nutrients absorbed is substantially higher while the work to access the nutrients is lower. Cooked foods are generally softer, more porous, and consequently have higher surface area than in their raw state. This lessens the burden of digestion of previously tough foods. Consuming cooked over raw foods allows for the body to use less energy to metabolize nutrients. The ingestion of cooked foods produced a number of notable changes to our physiology[2]. Biological anthropologists note that around the same time the cultivation of fire was occurring, the structure of our bodies drastically changed from our previous tree dwelling relatives. Our bodies adapted to the increased ingestion of cooked foods by losing muscle mass around the jawline and developing a less flared rib cage which is indicative of a smaller digestive system. More efficient caloric intake was made possible by the aid of adding fire to food preparation. The primitive human could get all the energy required without the same bulky digestive tract. This modification to our physiology cannot be understated because this meant that less energy was spent on nutrient absorption freeing up metabolic processing power for other functions. Namely, the excess energy previously designated for digestion was allocated for our brain cavities to grow. This difference between our ancestors and current existing primates of similar size is palpable. Apes and chimpanzees designate roughly 13% of their basal metabolic rate to their brains. Conversely, humans designate 20%

of their basal metabolic rate to cerebral function. This seemingly small difference in energy allocation resulted in drastic changes for our ancestors and helps distinguish us from other beings in the animal kingdom.

Incredibly, cultivation of energy release in its primitive forms altered human existence. We adapted and learned how to tame fire and in doing so propelled our species to what it is today. Fire created a non-solar based form of light that could extend daytime, provided heat allowing access to environments with climates that would normally be inhospitable for primates, and allowed us to cook, and externalized a portion of digestion which actively propelled us to surpass other primates intellectually and thrive as a species.

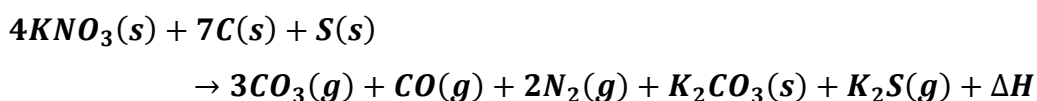
## **1.2 Greek Fire**

As the human population grew and societies began to take form, so did the usage of fire and oxidation. Most of the innovations to energy control were conflict driven. The heat released from burning naturally occurring substances like wood, grass, coal, and other carbonaceous materials was widely explored. The first noted modification and advancement in energetic materials was a formulation called Greek Fire. Discovered in around 683 A.D. Greek Fire was used by the Byzantine Empire to protect its assets. This invention allowed for the Byzantines to remain in power and defend their empire for another 800 years mainly due to its effectiveness in battle. Greek fire is particularly lethal to any flammable substance due to its stickiness and its unique nature of not being able to be doused by water. Taking advantage of this, the Greeks employed this special substance for use of its Navy to douse enemy ships with burning liquid that would burn even on the sea. The reason for this is mainly due to Greek Fire's composition. While its exact recipe is not precisely known, much can be learned just by studying its properties. The fact that this substance burned even on water points to the fact it was a composition mixed in a solvent that was immiscible in water, namely oil. That is precisely what the most successful modern formulations of re-created Greek Fire are comprised of. Using forms of rock oil or naphtha oil that was purified and then mixed with sulfur, pitch, petroleum oil, and a few other ingredients allows for a fluid

that can be ignited that will not extinguish with water. This is the ancient version of napalm that is used today in modern militaries and its composition, gelatinous gasoline, also takes advantage of its immiscibility in water to effectively burn even when it comes in contact with water. Greek Fire was paramount to the Byzantines for its ability to enhance its creator's defenses, however chemically it is essentially the oxidation of a carbonaceous material that burns relatively slow[3-5].

### 1.3 Gunpowder

Roughly 400 years later around 1100 A.D., the Chinese provided the next advancement in the history of human interaction with energetics with their discovery of gunpowder. The earliest reports of gunpowder's creation dates back 1000 years ago when Chinese alchemists, in their pursuit of an elixir of immortality, discovered a powdered formulation that had properties that ended up being quite the opposite to its intended purpose. It took another 200 years for Western society to utilize and characterize gunpowder. Roger Bacon is largely credited with deciphering gunpowder's ingredients for western societies which are saltpeter, charcoal, and sulfur. When first re-created it was noted that "the sound of thunder may artificially be produced". This is a result of gunpowder's more rapid reaction than traditional burning of plant life. At the time it was not realized that this was a new chemical reaction pathway for energetic release. The principle of combining a fuel source with an oxidant is the same but instead of using atmospheric oxygen gunpowder uses potassium nitrate as the oxidant and charcoal as the fuel source were sulfur is merely a catalyst of this reaction. As seen in the equation below.



The reaction of potassium nitrate and carbon yield significant gaseous products as well as heat. This gas production was then used to project an object at high rates of speed.

The stored energy of gunpowder allowed for projectiles to significantly increase and surpass the ranges of traditional war machines such as catapults. The new energetic material gunpowder facilitated the development of high projectile speeds and would prove to change the course of how warfare in modern life was conducted. As an example, this new invention eventually spelled the death of the Byzantine Empire because of the ability of cannons using gunpowder to project a heavy object towards its wall defenses with an order of magnitude more force than what they were designed to defend against. For an 800 year history gunpowder was the main energetic material of choice by modern societies. The fundamental nature of its chemical constituents changed little but its manufacture was refined for different purposes; as propellant in guns and cannons as well as an explosive for mining industries.

Early on in the 14<sup>th</sup> century it was noted that small grain charcoal burnt faster than large grain charcoal allowing small grain powders to be employed with rifles and shotguns for shorter burn times and large grain powders being employed for larger bore weapons requiring longer burn times to propel larger projectiles. This is the first instance when a connection was made between the size of the fuel source and it's affects on energetic behavior[3].

## **1.4 A new class of materials**

### **1.4.1 Dynamite**

The next major advancement in energetics development was initiated by researchers in a completely separate field. At the University of Turin in 1832 Asconio Sobrero, first synthesized a chemical in his medical research laboratory called glycerol tri-nitrate or by its more common name nitroglycerin (see figure 1.1).

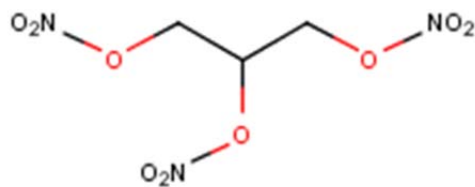


**Figure 1.1-** Chemical structure of Nitroglycerin.

Nitrate compounds at the time were known to have a depressing effect on blood pressure, so it was thought if a compound could be created with high nitrate density it would provide the same blood pressure lowering effects at a more increased effectiveness. He found that the substance once administered to the skin did indeed lower the blood pressure significantly, however he also noted that in its dry and crystallized form nitroglycerin is extremely shock sensitive and will detonate upon the mildest of disturbances. He had a notion of its potential power but declined to research it any further stating that, “science should not be made a pretext or means of dishonorable undertakings or of business speculations”. This compound would lay dormant until the early 1860s when a Swedish inventor Immanuel Nobel and his son Alfred began researching ways to safely utilize nitroglycerin’s energetic properties. During manufacture the Nobels noted its particular sensitivity to external stimuli making its energetic release quite unpredictable. Many of the formulations used by the father and son team consisted of large percentages of gunpowder with only small percentages of nitroglycerin. This approach was unsuccessful but is most likely the source of Alfred’s idea. The contribution that Alfred gave to this endeavor is as simple as it is ingenious. He noted that the energetic release of nitroglycerin could be initiated with a small amount of lesser explosives like gunpowder. This is when in 1864 he patented his nitroglycerin igniter. The igniter patent provided a way to consistently ignite nitroglycerin, however the issue of its mechanical sensitivity had yet to be addressed. It took Alfred three more years to solve this problem. He ingeniously took an inert naturally occurring abundant material called diatomite, that consists of the remains of fossilized hard

shelled algae and exposed it to nitroglycerin. He posited that if he could get an inert material to absorb the highly sensitive nitroglycerin the resulting composite would be much less sensitive to shock initiation and therefore be more safely handled. This invention for the safe handling of nitroglycerin is more commonly known as dynamite. The creation of this new explosive revolutionized the way warfare, modern construction, and mining were conducted and is the invention Alfred Nobel is best known for [3].

Dynamite was not the only energetic material advancement in the 1800s. During the same time that nitroglycerin was being synthesized another similar nitrated organic compound was created by Christian Friedrich Schönben in Germany. As is the case of many scientific discoveries it has been recorded that this invention was created by accident. Shchönben was a German chemist who was investigating the properties of nitric and sulfuric acids. Despite being forbade by his wife at the time to perform any experiments in the kitchen, Christian had several sources of each acid in his kitchen that he accidentally spilled on the floor. Not wishing to upset his spouse and in an attempt to hide the evidence that he was bringing his work home with him he attempted to clean up the acids with his wife's cotton apron. He then hung the apron up in front of the stove in order for it to dry off. Unfortunately for him and his wife, the apron violently exploded after a few minutes. The fortuitous combination of the nitric acid and sulfuric acid with cotton effectively nitrated the cellulose the apron was made out of. When it exploded, Christian temporarily ignored his justifiably cross wife and noted that it sounded like a large cannon, hence the name; guncotton. Realizing that the resultant guncotton in a very dense state produced drastic pressure changes upon ignition and detonation that would certainly rupture a gun barrel, Christian developed a technique of mixing nitrocellulose and nitroglycerin in a low density composite that gave a more gradual rise in pressure. Tailoring the composite density varied its gas release rate, which in turn allowed for a more gradual pressure rise and use in gun barrels. This new formulation of energetic material was the birth of smokeless gunpowder which was quickly adopted by militaries around the world[3, 6].

## 1.5 High Explosives

By simply exposing candidate organic molecules to nitric and sulfuric acids it was possible to insert a fuel source and an oxide source in the same molecule. The bonding of an unstable oxygen rich functional group to an organic compound with high carbon content created a new type of energetic material dubbed high explosives. In contrast with gunpowder, this creates a monomolecular energetic where the two reacting groups responsible for the energy release are in atomically close proximity. This combination yields extremely fast reaction rates. The chemical reaction that has to occur in this energetic does not have to go through any atomic transport unlike gunpowder. This eliminates the need for the combination and powder processing that gunpowder requires. Comparing the burn rates of dynamite or nitroglycerin with that of gunpowder, it is clear that the organics reacts 10 times faster. Similar organic explosives have comparable in mostly faster reaction rates the nitroglycerin. These monomolecular energetics react so fast that the rate of energy release that it exceeds the speed of sound in the material. The reaction results in a shockwave through the material with rapid gas production that has a demolishing effect on any material in close proximity. High reaction speed of gas production is what separates energetics designated as high explosives (TNT, RDX, PETN etc.) with low explosives (Gunpowder).

## 1.6 Combustion: Detonation versus deflagration

Until the mid-1800s when Italian scientists developed nitroglycerin and discovered its explosive potential, all energetic materials reacted relatively slowly. Heat was released during an oxygen exchange reaction via burning organic matter such as wood, oils, or ignition of gunpowder. This oxidative process was limited by the rate at which the oxygen could be transferred from the fuel to the reducing agent. Once those two constituents were combined in one molecule the reaction was no longer diffusion limited. The reaction proceeds solely by chemical kinetics and does not rely on mass transport which is why monomolecular explosives react much quicker than the powdered energetic alternatives. Both high and low explosives are forms of an oxygen exchange reaction however a

distinction is made by how fast the reaction occurs. Low explosives react slower and are said to deflagrate and high explosives react rapidly and are said to detonate. An oxidation reaction slower than the speed of sound in a material is called deflagration or more commonly *burning* if the oxygen source is supplied from the environment. If the reaction speed exceeds the speed of sound in the material it's called detonation. In a detonation the reaction proceeds through the initiation and continuation of a shockwave. More background on shockwave physics will be covered in chapter 7[6-8].

As is the case with many technological developments in history high explosives were mainly researched for military purposes. With the advent of nitroglycerin, guncotton, and the ease at which organic molecules can be nitrated, the late 1890s to the 1940s saw great innovation of organic energetics that were employed during both world wars.

## 1.7 Thermite

During the same time of rapid development of organic explosives another energetic formulation was discovered. In 1898 Hans Goldschmidt first reported the reducing capacity of aluminum in his paper to the Journal of the Society of Chemical Industry "Aluminum as a heating and reducing agent"[9]. Goldschmidt's motivation for investigating the reducing properties of aluminum was the search for an easier refining method to obtain pure metals from their mineral states. At the time he observed that a reaction of lead sulfide with metallic iron yielded pure lead and iron sulfate so he surmised that aluminum would produce a similar result when combined with lead sulfide and indeed it formed aluminum sulfide and pure lead. He continued on to posit that because aluminum oxide was so stable it could be used as a reducing agent to other less stable metal oxides in an attempt to refine the pure metal. Goldschmidt's experiments with metallic oxides were extensive and very exothermic. The reaction combining a reducing metal with a weaker oxide is shown in reaction below, where **M** is the reducing metal, **AO** is the oxidant, and  $\Delta H$  represents the heat released.



The oxides of chromium magnesium, iron, copper, titanium, boron, tungsten, molybdenum, nickel, cobalt, zirconium, vanadium, niobium, tantalum, cerium, thorium, barium, calcium, sodium, potassium, lead, and tin were all shown to be reduced by aluminum. Goldschmidt notes in his paper a possible source of the failure of predecessors to achieve reduction of other metal oxides. He reasoned that previous preparation of the materials was insufficient because he describes that this oxidative reduction reaction requires granulated aluminum. The granulated aluminum Goldschmidt referred to was created via an agitated slow cooling technique of the molten aluminum. This process of reduction of common metal oxides was found to accomplish his goal of obtaining and refining pure metals. The utility of the heat generated during the oxidative process of a thermite mixture was not lost on Goldschmidt either. He states, “using a cheap and pure aluminum and cheap source of oxygen such as oxide of iron, the process as a key producer possesses considerable commercial value as it can be supplied in cases where would not be convenient to use other sources of heat.” After this discovery thermitic compounds and formulations were used in welding and joining applications specifically joining to railroad ties together when means of welding were unattainable.

### **1.7.1 Metallic Addition to Traditional Energetics**

Deriving from Goldschmidt’s work the oxidation of metals and the extensive heat released from the reactions were primarily used as supplementary additions to traditional energetic materials. The bulk of the research involving metal combustion employed metal particles as additives to existing energetic formulations to enhance their thermal properties. Particular attention was paid to aluminum because of its abundance and high flame temperatures. Metal particles mostly aluminum, were added to high explosive formulations like TNT, PETN, and RDX [3] to increase their thermal signature. After World War II this particular property of dramatic energy release by metal combustion was used to aid in the design of solid rocket fuel. The Atlantic Research Corporation funded by the Navy first demonstrated, in the late 1940s, the benefits of metal particles addition to

rocket propellants [10]. Specifically they added aluminum particles of micron to millimeter size to ammonium perchlorate to increase the impulse of the solid rocket fuel. The standard metric in which rocket propellants are measured with is the specific impulse value of the fuel formulation. The impulse is computed from equation 1.3[5, 6], where  $I_{sp}$  is the specific impulse,  $N$  represents the moles per unit weight,  $T_c$  is the flame temperature, and  $k$  is a constant. Increases in flame temperature directionally influence the specific impulse value according to equation solid rocket propellants.

$$I_{sp} = k(T_c N)^{0.5} \quad 1.3$$

The rocket propellant research community from the 1940s to the 1980's employed the use of aluminum additions to its formulations for the express purpose of enhancing combustion rates and temperatures. The main parameter the Al addition amplified was combustion flame temperature. More heat can be generated in the same allotted time in which the rocket is fired when metal combustion is added. The effect of the addition was a net improvement in rocket motor characteristics.

## 1.8 Nano-sized Aluminum

In the 1980s the addition of a new kind of metal component entered the energetic scene in the form of nano aluminum. Aluminum of nano particle size was realized by a process called electro explosion of metal wires or EEW. Nano particle sized aluminum created by plasma explosion process is called Alex. This process was first discovered in 1774 by Michael Faraday and is very similar to the standard ignition method of explosives of exploding bridge wires. To fabricate this nano aluminum  $10^2$ - $10^3$ J pulse of electricity is run through a thin aluminum wire for a duration of 1 microsecond in an inert argon atmosphere. The immense current density through the wire creates a plasma that eventually interrupts the current flow and disperses violently into nano sized droplets of metal that condense and then are collected. The particles are passivated by dry air cooling or exposure to an organic coating to prevent further oxidation [6].

Reshatov et al. [11] first showed in 1984 the benefits that nano sized metal particles contribute to the energetics community. They showed that with the addition of nano aluminum particles to a high explosive called hexagon in the right proportions the detonation rate grew from 5400 m/s to 7000 m/s. With a 1600 m/s increase in velocity of detonation and a large power density increase, Alex was shown to be an exceptional explosive additive. Traditionally the aluminum powder that was added to rocket fuels was of the micron sized domain, but as with the development of gunpowder several hundred years before it was surmised that smaller particles would burn faster. Ivanov et al. and later Mench et al. showed the addition of nano aluminum to solid rocket fuels (Ammonium Perchlorate) dramatically improved the burning rates compared to the additions of traditional micron sized aluminum. Another benefit from the use of nano aluminum is its property of staying in solution longer than micron sized particles allowing for easier materials processing [12, 13].

## 2. Nano Energetic Materials

Military applications for thermite were mainly concentrated on anti-equipment munitions. Thermite grenades were developed to melt through engine blocks and armament of captured war materials to render them useless. The inability to use thermite as a propellant or anything other than a heat source was mainly due to its slow reaction rate as seen in table 2.1.

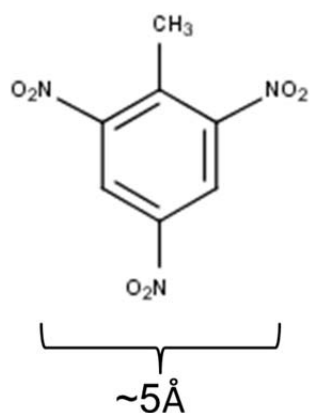
**Table 2.1-** Comparison of energetic materials properties.

<b>Energetic Material</b>	<b>Energy Density [KJ/cm<sup>3</sup>]</b>	<b>Reaction Speed [m/s]</b>	<b>Power Density [MW/cm<sup>3</sup>]</b>
Octanitrocubane ONC	10	10,000	160
Dynamite	2.4	7,000	13
Thermite-Slow	30	10	0.3
Thermite- Fast	30	900	30

The comparison of common organic explosives and inorganic energetics including thermite using the metric of solely energetic density, thermite compounds seem superior. However as was discovered during the development of organic explosives in the late 1800s, the organics possess vastly superior power densities due to their extreme rates of energy release. As was mentioned previously this is due to the fact that organic explosives contain the fuel and the oxidant in one molecule allowing for extreme rapid reactions to take place. These reactions are kinetically controlled where the two reactant functional groups only have to traverse several angstroms to reach its complementing reactant. The velocity in which this happens is on the order of the frequency of molecular vibrations. Conversely inorganic energetics are governed by mass transport which historically meant atomic motion occurring

over several microns in distance which yields considerably slower reaction velocities. Comparison of the length scales is seen in figure 2.1.

### Trinitrotoluene (TNT)



**Vs.**

### Thermite Interface

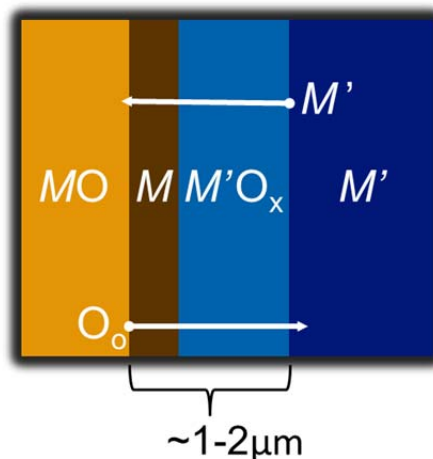


**Figure 2.1-** Organic Energetic vs. Inorganic order of reaction distance.

Organic energetic synthesis takes advantage of the fast kinetics of modern molecular chemicals to obtain very high power densities. However the total energetic density of an organic molecule is limited by the formation energies of the common bonds found between carbon, hydrogen, oxygen, and nitrogen. The formation energies of most inorganic energetic materials such the formation of borides, carbides, silicides, intermetallic compounds and thermite's equal and surpass that of the organic formation energies. The main goal of the nano-energetics research community has been and continues to be to increase the power densities of inorganic energetics in order to more efficiently utilize the high formation energies they possess. Namely, the community aims to foster reaction parameters that accelerate the energy release rate of the inorganic energetic chemistries by aiding diffusion. Atomistic transport is a function of the material that is in motion and the barrier properties of the material being traversed. Generally speaking variation of processing parameters will not have an effect on the activation energy required for diffusion to occur nor will it enhance the diffusion coefficient that is an intrinsic property of the material. The goal then is to design

energetic systems that promote the fastest avenues of diffusion and decrease the net reaction distance between both reactants.

Until recently, traditional processing technologies have been unable to intimately mix the oxidant and the fuel source below micron sized domains significantly hampering the energy release. However at the advent and utilization of nano aluminum as additives to standard energetics[6], it was then introduced by Aumann et al. the idea of combining two nano sized energetics to form stand-alone explosives[14]. These materials were dubbed metastable intermolecular composites (MICs). MICs represent a subclass of energetic materials that are comprised of traditional energetic components combined at the nanoscale. The motivating reasons are straightforward. If the features of the reactants can be decreased more material will readily participate in rapid reaction. To obtain energetic materials that intimately mix on the order of nanometers several recently developed processing techniques must be utilized. The four main methods of MIC creation are nano powder mixing, sol-gel synthesis, arrested reactive milling (ARM), and thin-film deposition.

## **2.1 Nano Powder Mixing**

The first and most straightforward manner of combining energetic materials at the nano scale is simply the physical mixing of nano particulate sized reactants or nanopowders [15-32]. The theory behind nano powder mixing is trivial; however the creation of nano-sized constituents that are uniformly distributed in size is more involved. As was discussed previously in chapter 1, nano particles of metals can be realized via an exploding bridge wire design where current is passed through a thin wire of metal, which then creates a plasma that will explode into metal nanoparticle droplets once the circuit is broken. These droplets condense from the vapor phase on prepared sample collection surfaces [14, 33]. Other ways of nanoparticle fabrication include electrospraying, and induction plasma technology. Each method is a different path to the same result; creation of nanoparticulate material [34-37]

Commercially available powders with nanometer diameters (10-100nm) are obtained via one of the aforementioned methods. Each reactant is weighed out in varying desired

stoichiometry and placed in an organic solvent, normally hexane, and sonicated to homogenize the mixing. The resulting solution is then dried in air, sometimes with the assistance of a warm hot plate (40°C), and filtered through screen mesh to ensure a free flowing powder. The powder mixtures obtained via nanopowders mixing react considerably faster than micron sized formulations of the same chemical constituents. High propagation velocities can be achieved (1000m/s) with this methodology. Another consequence of MIC fabrication in this manner is the extreme sensitivity to impact, spark, and friction related insults. In addition to the relatively high price of prepared nanopowders, these properties can provide significant challenges to scale up methods for bulk applications outside the laboratory but are an excellent way to easily obtain an experimental system to test the influence of varying reaction parameters.

Notable discoveries from the investigation of nanopowders energetics reveal in thermite MICs a slightly fuel rich stoichiometry provides the fastest reaction rates and powder reaction velocity scales with the diameter of the confined burning space[16, 17].

## **2.2 Sol gel processing of nano energetics**

### **2.2.1 Sol-gel chemistry**

In solution chemistry, the sol-gel process itself has been investigated for over 150 years[6, 38] and has been employed to create varying sizes and morphologies of interconnected nano-particles. The structures from this processing technique develop unique porous macrostructures of metals and ceramics that have extremely high surface areas up to  $1000 \frac{m^2}{gram}$  and low bulk densities. The elevated porosity and low densities of these materials lead to the addition of sol-gel prepared materials into commercial applications of filtration, insulation, sensing devices, and optical guides. It is a relatively low cost procedure that requires only several types of solvents and a beaker. The reactant materials are either inorganic salts or more commonly organic alkoxides which are added to aqueous/alcoholic solutions. These starting materials consist of an elemental metallic component that is chemically bound to different types of ligands which are predominantly alkyl or alkoxy

functional groups. As depicted in figure 2.2, when exposed to water, metal alkoxides readily undergo hydrolysis which cleaves the alkoxy-metal bond and replaces it with an alcohol functional group.

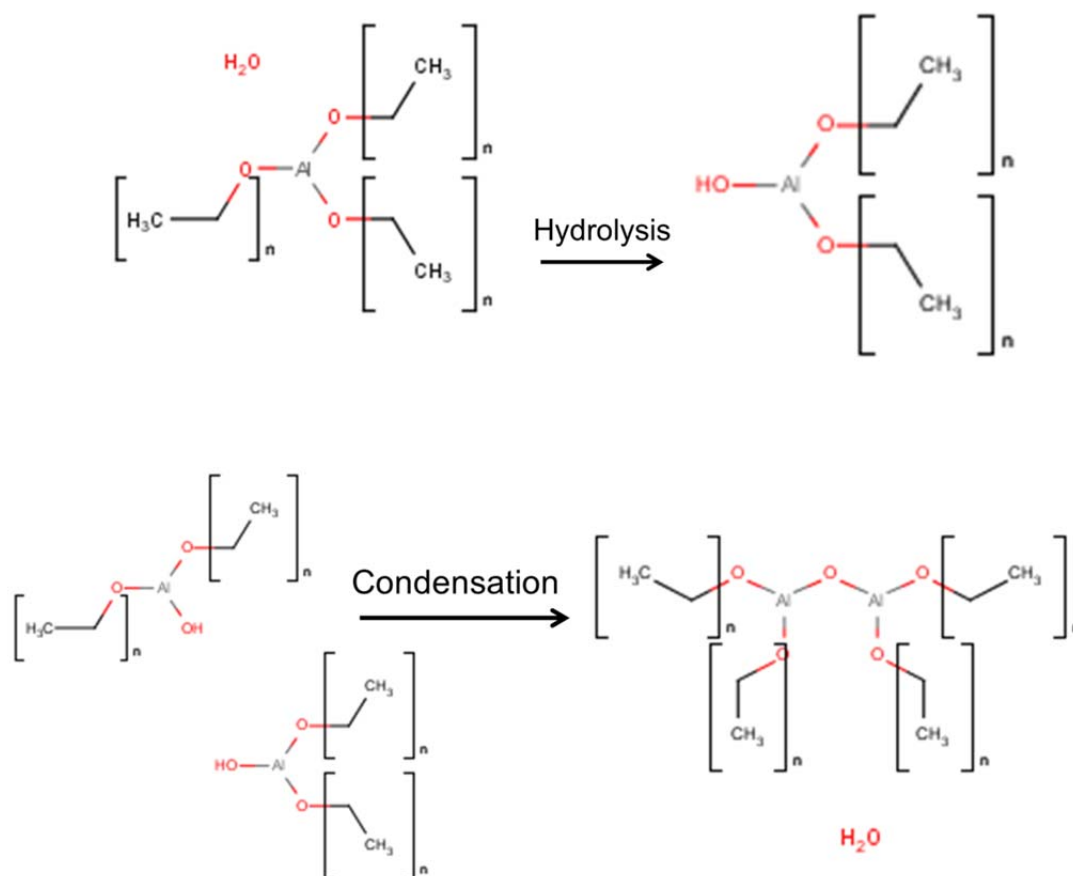


**Figure 2.2-** Hydrolysis and condensation reactions that occur during sol-gel synthesis.

The extent of hydrolysis of the metal is a function of water and catalyst concentration and will completely replace the organic ligands with hydroxyl groups (-OH) if the corresponding reaction parameters are met. For a networked monolith or gelled structure to be formed, the metal is only partially hydrolyzed to create a chemical environment where two partially hydrolyzed molecules can undergo further reaction to link together via a condensation reaction that binds the metals together with oxygen. For a three dimensional network to be formed the starting material must have the capability to form at least three

bonds, or have a functionality of three or more. A colloidal suspension of metal oxide particles begins to form in solution as the condensation is continued which is called a 'sol'. As the reaction progresses the suspended particles begin to accumulate and start to impinge on one another. When these particles begin to bond to each other the viscosity of the solution rapidly increases where the resistance to motion is corresponding to the 'gel-point'. After the particles are linked a 'gel' is created consisting of a connected porous network throughout the solution that is enveloped by solvent. Particles with nano sized spherical features that are linked together in the gel are created in uniform size, morphology, and composition through the manipulation of solvent type, temperature, pH of the solution, and the concentration of the reactants [6, 39]. Particle sizes can range from 1 nm to 1000 nm in diameter.

The gel can be extracted from the solution via two different pathways resulting in two different types of networked nanoparticles. If the solvent is left to evaporate in ambient conditions the resulting structure of the sol-gel yields a monolithic structure called a xerogel. This type of extraction causes compressive stresses that facilitate the pseudo collapse of the 3D network because of the capillary forces that are exerted on the structure by the retreating evaporating liquid. The second method of extraction evacuates the solvent super critically via an autoclave which removes the liquid from the porous network without the stress of the surface tension of the solvent. This preserves a more open and porous agglomeration of nano particles called an aerogel. Xerogel densities range from 30- 80% of bulk values where the more porous aerogels yield 1- 20% bulk densities. See figure 2.3 for a schematic of the extraction process.

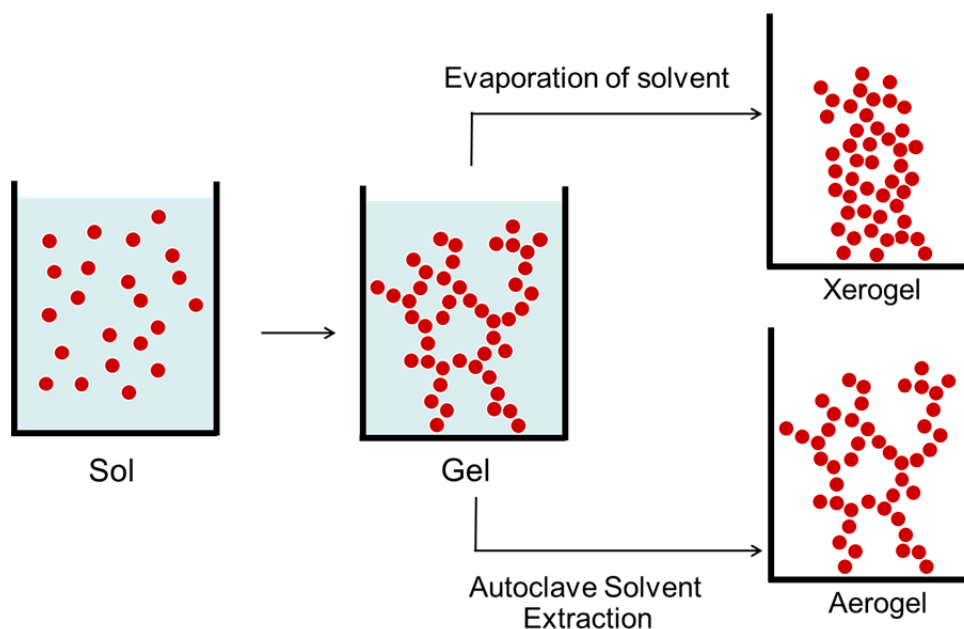


**Figure 2.3-** Sol-Gel Synthesis solvent extraction schematic for an Aerogel and Xerogel.

## 2.2.2 Sol-Gel Fabrication of Energetic Materials

This synthesis technique has been applied to create intimate mixtures of energetic materials [15, 39-45]. Several sol-gel methods can be employed to incorporate the reactants together however the most common technique used is the creation of a networked oxidizer such as iron oxide which is infiltrated with metal fuel particles most commonly aluminum. This can be easily realized by the addition of metal particulates at the onset of a viscosity increase right before the gel forms. This simple yet crucial step allows for the addition of nano particulate metals to be suspended in the porous oxide matrix. The metal nanoparticles are not allowed to self-segregate due to gravity because the porous network structure locks the particles in suspension before they can precipitate out of solution. The sol-gel process is not limited to only making oxide networks as evidenced by researchers at Lawrence Livermore National Laboratory (LLNL)[39, 44]. Gash et al. specifically pioneered the

feasibility of sol-gel created energetics and explored their physical and reactive properties. Under the right conditions sol-gel [38] prepared thermites have demonstrated reaction velocities up to 900 m/s which is a drastic increase from a traditional thermite reaction of 1 m/s. While this speed is still not eclipsing that of organic energetics it certainly proves that sol-gel nano composites and MIC's in general are capable of at least supplementing energetic formulations.

Sol-gel chemistry also has the added benefit over nanoparticle mixing of using relatively environmentally benign solvents such as alcohol and water instead of hexanes as is the case for nanopowder physical mixtures. When compared in relation to burn properties nano particle mixing and sol-gel techniques both generate materials that can react rapidly above 500m/s [43, 46]. In current reports some sol-gel prepared nanocomposites burn faster even when both have comparable surface area per volume values[47]. In this case Al and Fe<sub>2</sub>O<sub>3</sub> were combined via nanopowders mixing and sol-gel synthesis with both having similar particle sizes and surface areas but the phase of the commercially obtained Fe<sub>2</sub>O<sub>3</sub> nanopowder was of an amorphous metastable phase whereas the sol-gel prepared oxide was  $\alpha$ -Fe<sub>2</sub>O<sub>3</sub> allowing for better transport characteristics.

### **2.3 Arrested Reactive Milling**

A complementary method to that of physical mixing of reactive precursors that are already nanopowders is arrested reactive milling (ARM). This technique starts with micron sized reactants that then through processing creates alternating geometry of the reactants where the reaction distances are on the order of nanometers (50-100nm) inside micron sized powder compacts[37, 48, 49] schematically shown in figure 2.4. Lamellar compacts are made by adding micron sized powders to a vessel with milling media and ball milled to the point right before ignition. The ignition time and temperature is empirically derived by adding a small amount of reactants to a vial with a thermocouple and the temperature is monitored over time. The ignition of the powder is proportional to the amount of mechanical energy transferred to the powder by the milling media and the mechanical energy transferred is a

function of the milling media diameter and the time allowed to mill. Once the parameters for the specific chemical formulation are known, a larger batch is milled and then the mixing is arrested before spontaneous reaction can occur in order to not damage any of the milling equipment [35, 36, 48-53].

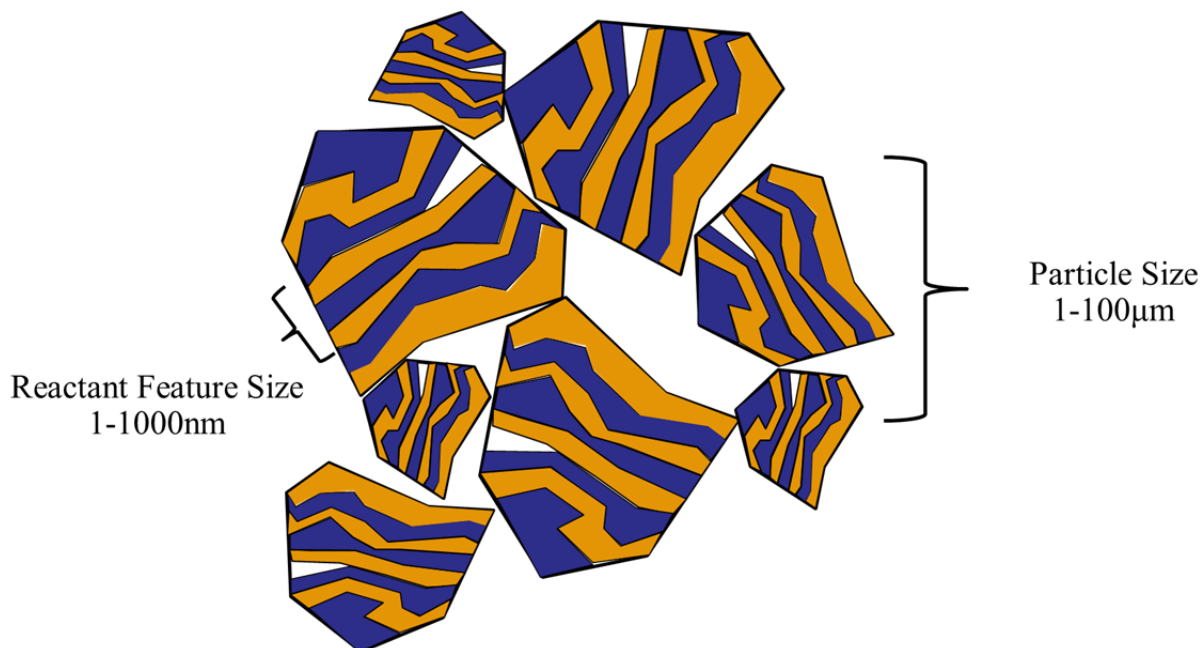


**Figure 2.4-** Typical microstructure obtained by ARM MIC processing.

The starting powder reactant materials are considerably more affordable than obtaining nanoparticulate starting powders. This method also involves low cost and easy experimental fabrication only requiring a standard milling apparatus. The most notable advantage of this technique however is the ability to create large macroscopic quantities of energetic material that contain nano-sized domains that can be readily implemented in industry.

## 2.4 Physical Vapor Deposition of Nanoenergetics

Another method to create nanoenergetic materials is by physical vapor deposition (PVD). This can include pulsed laser ablation deposition (PLD), electron beam deposition, molecular beam epitaxy (MBE), or sputter deposition. These techniques are borrowed from

the semiconductor industry and are predominantly used for the purpose of assembling varying electronic component architectures that form the basis of transistor fabrication. Each method differs in how experimental execution is undertaken, however the end results are similar: precise deposition of thin layers of material. The most common PVD method in which energetics are created is sputter deposition and is the technique the author has employed to investigate thermite reactions.

Sputtering is a process by which a source material to be deposited is inserted into a reaction chamber that is placed under vacuum. An inert carrier gas, typically argon, is introduced to the chamber at a specified pressure and a negative bias is applied to the source material. This potential repels free electrons in the gas which collide with and subsequently ionize the argon atoms. The positively charged ions are then attracted to the negatively charged source material called the target and impact the surface with energies proportional to the bias applied and the mean free path of the gas molecules which is a function of pressure[54].

After impacting the surface several processes can and do take place in response to the incident kinetic energy.

- The ions can be reflected which is the fundamental basis of Ion Scattering Spectroscopy techniques such as Rutherford Back Scattering (RBS), medium energy ion scattering (MEIS), or low energy ion scattering (LEIS). Each technique differs by the amount of incident ion energy, however each measure the energy loss of the reflected ions to determine specific information about the surface. As probing depth increases with the incident energy (0.1eV-10MeV) compositional and topographical information can be collected.

- The ions can also implant themselves in the matrix of the target which is the phenomena utilized for surface treatments in electronics for specific doping concentrations of beneficial impurities (i.e. P in Si).

- Incoming ions may structurally distort the target materials lattice by creating vacancies or other defects in the crystal structure.

-The incident ions can cause a cascade of collisions with the atoms of the target which leads to target atoms being ejected. This ejection is called **sputtering**[54].

The ejection of the atoms from the target source is a function of the energies used to accelerate the ions into the target, the target atomic mass to the ionic mass ratio, and the pressure of the sputtering gas. When the appropriate conditions are met the ejected atoms can be collected on a substrate surface and thin films of material can be achieved.

When sputtering is used to create energetic materials the prevailing geometry used is a multilayered alternating geometry that creates a laminate microstructure [55-78] seen in figure 2.5.

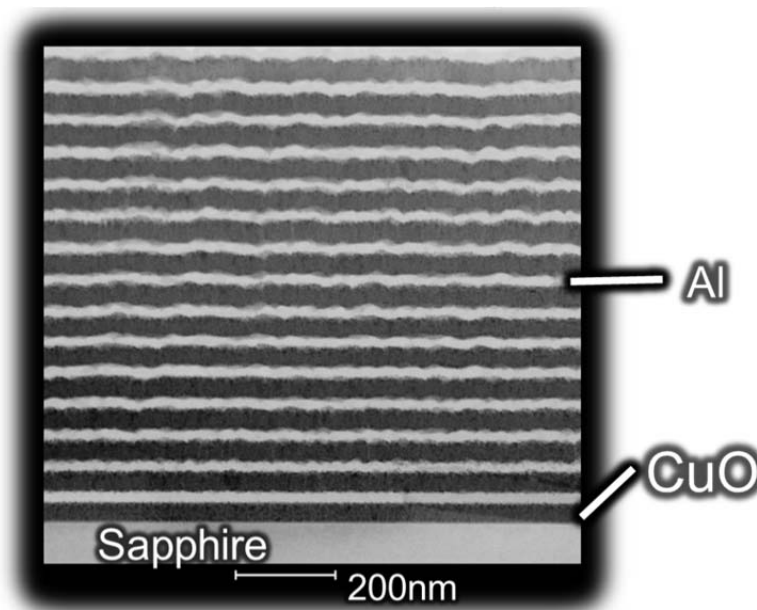


**Figure 2.5-** TEM micrograph of an Al/CuO thermite thin film, with total thickness 1080nm.

This layered hierarchy is created by exposing a sample surface to two different source materials with either a rotating substrate carousel while both sources are depositing simultaneously or an alternating deposition sequence where only one source is on at a time. The simultaneous deposition method with a rotating sample stage allows for less experimental oversight and ease of operation. The purpose sequential deposition is to reduce intermixing and decrease cross contamination of the target sources where a shutter shields

the non-depositing target. It is in this sequential deposition method that the thin thermite films in this manuscript were created. A schematic of a deposition chamber used to create these thin films is shown in figure 2.6.

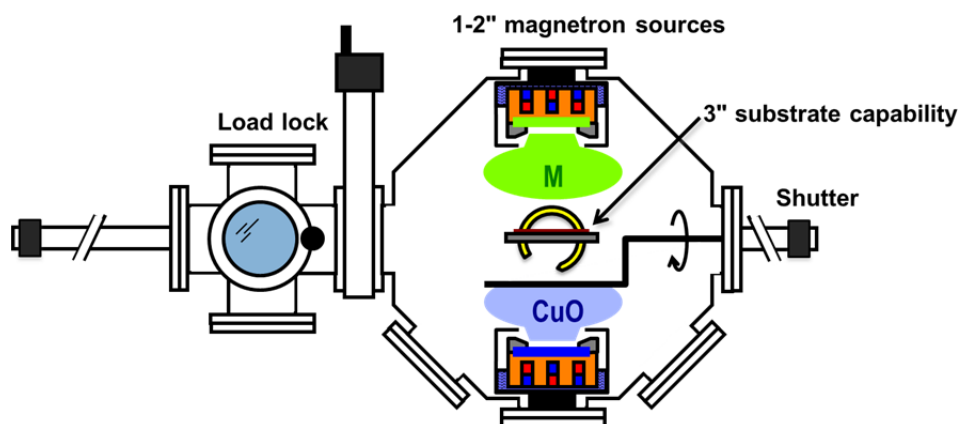


**Figure 2.6-** Dual magnetron sputtering architecture used to fabricate thermite nanostructures

These laminate structures are used to combine thermite compounds [55-60, 79-84] like in figure 2.4, other reactive intermetallic species that possess a negative heat of mixing, or exothermic formation reactions [64-67, 71-74, 76, 77, 85-94]. Nanolaminate films can either be left on the starting substrate or can be subsequently delaminated to create free standing foils. The delamination process involves thin film deposition on top of a photo-resist layer that is later dissolved in solvents after deposition. A consequence of delamination requires that the total thickness of the energetic foil be thicker than  $5\mu\text{m}$  for the samples to have enough supportive mechanical strength for handling. The PVD technique of fabrication has several advantages over the other powder centric methods of nanoenergetic assembly. While all of the previously described methods of MIC processing are effective, they lack the ability to create a clean avenue to learn about the fundamentals of reactions. Powder processing affords the experimenter ease of creation and the ability to scale up production but has poor control over absolute sizes of reactant constituents. Conversely, thin film deposition allows for precise control over reactant thicknesses, diffusion distances, interface quality, and total amount of material involved.

Previous investigations into nanolaminate behavior have shown as the thickness of the reactant layers, also known as bilayer thickness, decreases an increase in reaction velocity is observed [75, 76]. A tradeoff for this increased velocity is how bilayer thickness affects the energetic output [76, 95]. In the laminate geometry it was shown at the interface of the two reactant materials that a small but finite amount of product phase is present. The authors increased the number of bilayers and kept the material volume constant and found the overall energy available for reaction decreased as reactant interfacial area increased. The power of experimentation with laminate geometry is the ease of which its behavior can be transposed to other MIC fabrication methods and provides for valuable insight into how future energetics should be designed.

### 3. The role of terminal oxide structure and properties in nanothermite reactions

Authors: <sup>1</sup>E. J. Mily, A. <sup>1</sup>Oni, J. M. LeBeau, <sup>1</sup>Y. Liu, \*H. J. Brown-Shaklee, \*J. F. Ihlefeld, and <sup>1</sup>J-P. Maria

<sup>1</sup>North Carolina State University, Department of Materials Science and Engineering, Raleigh NC, 27606 USA \* Sandia National Laboratories, Electronic, Optical, and Nanomaterials Department, Albuquerque, NM 87185 USA

doi: 10.1016/j.tsf.2014.05.005

Published in journal “Thin Solid Films”

#### 3.1 Abstract

In this report, thin films of copper oxide, a common thermite oxidant, and varying metallic species (Al, Zr, and Mg) were deposited in an alternating layered geometry on sapphire by magnetron sputtering. Keeping stoichiometric equivalence, effects of varying metallic constituents were studied with respect to their onset reaction temperature and energy output. Reaction progression was characterized by a systematic step wise vacuum anneal followed by subsequent *ex situ* x-ray diffraction, and differential thermal analysis. It was found that reaction temperature depends heavily on the terminal oxide's diffusion properties, showing a correlation of lower reaction temperatures with higher values of anion diffusivity.

*Keywords: energetic material, barrier layer, film*

## 3.2 INTRODUCTION

Thermite reactions have been studied since 1893, and are utilized in applications and fields where high heating rates and temperatures are desired due to their extreme exothermic output upon reaction [60]. The thermite geometry pairs an oxygen source with an adjacent oxygen scavenger in a metastable configuration that can be triggered into action by a supply of energy arriving via a thermal, optical, electrical, or acoustic form. When sufficient energy is added to promote the initial interfacial reaction, oxygen and metal are exchanged between source and sink, and heat is released according to reaction below.



where  $M$  and  $AO$  are the parent metal and oxide respectively, and  $\Delta H$  represents the heat released. These exchange reactions are some of the most exothermic known, commonly exceeding 300 kJ/mol and, when they occur under adiabatic conditions, *i.e.*, heat accumulates much faster than it can be dissipated to its surroundings, they can produce temperatures in excess of 3000 K [96].

A common goal of research in energetic materials is to generate the capability for controllable or tunable energy release from a single material. Regulating either the fraction of material that reacts, or the time during which that reaction occurs enables one to tailor the energy and power outputs respectively. Furthermore, it is also desired that energetic systems exhibit the desired sensitivity to external stimuli to ensure the appropriate predictability and reproducibility for safe and reliable use. In order to understand how energetic materials will behave macroscopically, fundamental explorations of microscale and nanoscale interfacial reaction mechanisms are essential and motivate this study.

In many examples of energetic materials research, the reactant phases are combined at small length scales on the order of nanometers to microns for the purpose of controlling transport/diffusion distance and thus reaction times. This class of materials is commonly referred to metastable intermolecular composites [25, 95, 97-99]. The architectures of the

majority of nano-energetics consist of powdered systems [15, 23, 24, 27, 30, 41, 96, 100-105] or multi-layered laminate structures [48, 55-60, 65, 74, 76, 83, 84, 89, 90, 106-111].

The multi-layered structures, or reactive nano-laminates (RNLs), are created most commonly by physical vapor deposition of the constituent materials in alternating fashion to obtain the desired stoichiometry. For example, this architecture for energetic materials used by Coffey *et al.* shows that reaction progression is influenced by local chemical structure/mixing at the parent interfaces and the extent to which this interfacial region penetrates into the total stack. [89, 90, 108-110]. Other studies using this geometry show exothermic dependencies on bilayer spacing [76], and effects of intermixing on reaction velocities [65, 66].

Reactive thermite nanolaminates, which are the focus of the present work have been explored by a small group of researchers, with investigations of layer thickness and the limits of interfacial perfection, but the overwhelming majority of experiments focus on the CuO-Al system [56, 57, 59, 60, 83, 84, 96, 100, 102]. While reports exploring the influence of oxidizers, fuel mixtures, geometry on energy output, ignition, and reaction propagation speed can be found [27, 65, 74, 76, 88] there is a comparative paucity of research addressing the barrier properties of the terminal oxides in these thermite systems and how they affect energy release. Investigations by Zachariah *et al.* illuminate the importance of the terminal oxide in regulating reaction progression. They show that the oxidation of aluminum nanoparticles is regulated by oxygen diffusion through the terminal oxide shell [21, 24, 30]. Furthermore the initial oxide skin thickness can be used to regulate exothermic behavior [23]. The laminate geometry demands that these reactions are to a finite extent regulated by the accumulation of the terminal oxides phase, that by default, form at the precursor interfaces. As such, the physical, thermal, and chemical properties of this oxide must play a role in the progression of the oxygen exchange. The schematic in Fig. 3.1 illustrates this situation.

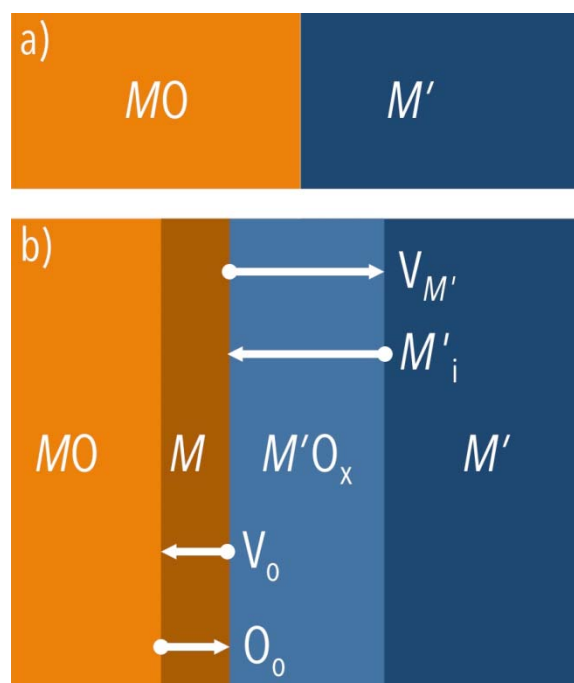


**Figure 3.1-** a) Idealized schematic of oxygen exchange reactions at a) the original MO | M interface and b) showing the accumulation of an intermediate barrier layer that accumulates with time.

While the structure and properties of the terminal oxide are only one aspect that regulate laminates reactions, their intimate role in transport provides them with a particularly important role, this argument underpins the central hypothesis of the present investigation, that by understanding transport across the thermite terminal oxide, one can rationally select and engineer the precursor scavenger metal such that energy release is tuned for the correct energy/power ratio, and that the sensitivities are practically useful.

To do so, a set of experimental results are presented which compare the behavior of thermite laminates that use Al, Zr, and Mg as the oxygen sink with a constant CuO oxygen source. The selection of these metals is predicated on the facts that all have similar free energy of oxide formation per mole oxygen and their terminal metal oxides span a wide spectrum of oxygen diffusivity values; alumina is one of the best oxygen passivators,

zirconia is a fast oxygen anion conductor at elevated temperatures, while MgO has intermediate properties [112-118]. CuO was chosen as the constant oxidizer due to its relative stability in ambient conditions, its ease of fabrication by physical vapor deposition, and its known use as a reducing agent/ oxygen source for thermite reactions. Table 3.1 lists the formation energies, the diffusivity values, and the molar volumes of oxidation for each metal/metal oxide combination [15, 112, 114, 118].

While thermite-based energetic materials are of most interest in a powdered form factor, studying such reactions in a nanolaminate geometry provides a unique opportunity to control initial interface density, contact area, and the extremes of surface to volume ratios. Furthermore, preparing such materials via thin film routes enables one to create pristine and flat interfaces that offer insight into the fundamental structure-property relationships that regulate energy release.

**Table 3.1.** Heat of Formation, Oxygen Diffusivity, and Pilling-Bedworth Ratio for each system studied.

Thermite System	Heat of Formation	Heat of Formation	Oxygen	Pilling-Bedworth Ratio
	[kJ/mol]	/mole oxygen [kJ/mol]	Diffusivity in Terminal Oxide at 600 °C [cm <sup>2</sup> /sec]	
Al-CuO	-1676	-527	$2.33 \times 10^{-28}$	1.29
Mg-CuO	-601	-601	$1.31 \times 10^{-26}$	0.81
Zr-CuO	-1097	-548	$2.41 \times 10^{-11}$	1.55

### **3.3 EXPERIMENTAL PROCEDURE**

#### **3.3.1 FILM DEPOSITION**

Reactive nano-laminates were created using a load-locked dual magnetron sputtering system with shuttered confocal sources oriented at 180 °. Substrates were mounted with double-sided tape on a rotatable substrate puck at the chamber center. For all experiments the substrate material was *c*-oriented sapphire that was precision diced into 4 mm x 4 mm squares. The precision sizes were used to facilitate quantitative thermal analysis. Multilayer stacks were prepared by alternating depositions of CuO and the component metals with a 15 minute rest between each deposition to allow the heat from sputtering to dissipate. The thickness values of the individual layers in each case were chosen to maintain global stoichiometry, i.e., enough oxygen to oxidize the entire metal layer. All samples contain three bi-layers and bilayer thicknesses were 356 nm, 363 nm, and 491 nm for Al/CuO, Zr/CuO, and Mg/CuO respectively. Both magnetron sputtering guns were 2 ” in diameter, and the sputtering metal targets (Al, Mg, and Zr) were purchased from Kurt Lesker. Metals were deposited using a DC power supply with 20 Watts of power under pressure of 0.4 Pa Argon (purity > 99.9999%) with a pre-sputter period of 10 minutes before deposition. CuO was deposited using a CuO sputtering target with an indium bonded copper backing plate also acquired from Kurt Lesker. CuO was layered using an RF power supply in the presence of 0.27 Pa Argon with 100 Watts of power with a pre-sputter period of 1 minute. The Al, Zr, and Mg films were deposited at 13, 10, and 15 nm/min respectively. The CuO films for each system were layered at a deposition rate of 15 nm/min.

#### **3.3.2 TEM SAMPLE PREPARATION**

Transmission electron microscopy (TEM) samples are prepared and thinned to electron transparency via lift-out technique [119] using a dual-beam focused ion beam (Quanta 3D FEG, FEI). Platinum protective layer was first deposited over the surface of the sample, to

prevent ion beam damage. A probe-corrected FEI Titan G2 60-300 kV S/TEM equipped with a high-brightness Schottky field emission gun operated at 200 kV was used for high-angle annular dark-field- scanning transmission electron microscopy (HAADF-STEM) imaging.

### **3.3.3 ANNEALING PROCEDURE**

To assess reactivity, RNL samples were exposed to vacuum anneals in a turbopumped quartz tube furnace at pressures below  $1.3 \times 10^{-4}$  Pa to minimize the influence atmospheric oxygen on reaction progression. All samples were heat treated by direct insertion into a preheated hot zone while under vacuum, ramped at 10K/min, and held at temperature for thirty minutes.

### **3.3.4 X-RAY ANALYSIS**

The phase assemblage and film thickness was measured by x-ray diffraction using a PANalytical Empyrean diffractometer that uses a Cu  $K\alpha$  source with Bragg-Brentano and parallel beam optics, respectively.

#### **3.3.4.1 Deposition Rate Determination**

Deposited materials CuO, Al, Mg, and Zr were first coated onto polished silicon substrates for a set amount of time. Samples were then placed in the diffractometer with parallel beam optics. Scanning at low glancing angles ( $0-2^\circ$ ) yields the critical angle of total internal reflection  $\Theta_{\text{crit}}$  and subsequent constructive interference fringes  $\Theta_1, \Theta_2, \Theta_3$  etc. at higher angles. From these values the total film thicknesses were computed using the Fresnel equations. Using the computed thicknesses and known exposure times, deposition rates were then computed.

#### **3.3.4.2 Phase Identification**

X-ray diffraction patterns were collected using Bragg-Brentano optics. The presence of the Cu [111] and Cu [200] metal peaks were used to track reaction progression (discussed further below).

### 3.3.5 THERMAL ANALYSIS

Thermal analysis was conducted using a differential thermal calorimeter (Netzsch Proteus Jupiter F3). The calorimeter was calibrated for sensitivity and temperature using pure standards with known melting points and heats of fusion provided by Netzsch (Al, Zn, In, Bi, and Au). During analysis a protective gas (Ar 99.999% -AirGas) flow (20 ml/min) was used. Due to mechanical instability when delaminated, the thin film samples were left on sapphire substrates and set in covered alumina crucibles on a power compensated platinum sample stage. The overall thickness of the thin films did not exceed 1.5  $\mu\text{m}$  and the mass of the thin films which were estimated using bulk density values were on the order of 100  $\mu\text{g}$ . A baseline program used for these samples ramped two empty alumina Netzsch crucibles with three dynamic sections. First the program ramped to 1200  $^{\circ}\text{C}$  at 5  $\text{Cmin}^{-1}$ , followed by a 30  $\text{Cmin}^{-1}$  cooling period to 30  $^{\circ}\text{C}$ , then a final ramp to 1200  $^{\circ}\text{C}$  at 5  $\text{Cmin}^{-1}$ . The thermal signal from the oxygen exchange is irreversible and only occurs during the first temperature ramp. To achieve a flat baseline the second ramp was subtracted from the first to clarify the exothermic activity.

## 3.4 RESULTS AND DISCUSSION

The initial experiment evaluates the relative reactivities of the candidate laminates by determining the temperature at which the oxygen exchange reaction becomes active. Since oxygen exchange is thermodynamically favorable at all conditions, the reaction is occurring at all temperatures, but is sufficiently kinetically hindered to be considered negligible. Fig. 3.2 shows a representative TEM image of a Zr-CuO multilayer acquired in HAADF-STEM mode. HAADF imaging is an incoherent mode of imaging whereby the image contrast is approximately proportional to the atomic number ( $\sim Z^2$ ) of constituent atoms due to Rutherford-like scattering[120]. Therefore, the heavier Zr layers have higher intensity compared to CuO layers in the image. It can be seen that while the two dominant materials are that of the deposited reactants, there is a layer of terminal phase at the interface. Taylor

and Martin [82] examined the evolution of aluminum oxide formed at the interface of at CuO surface via a stepwise deposition of Al. They detected that the first 7-8 mono layers of Al deposited were corresponding to 2-3 nm of  $\text{Al}_2\text{O}_3$ , further Al deposition led to metal accumulation. This indicates that while finite reaction occurs at a thin film thermite interface, further oxygen exchange is hindered by the presence of this barrier at room temperature.

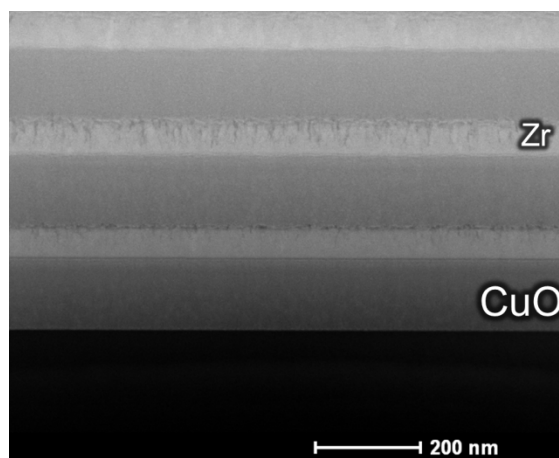


**Figure 3.2-** TEM image of Zr-CuO multilayer with 3 total bi-layers.

Considering this metastable initial state, the temperature at which the reaction becomes rapid is arbitrary to an extent because of its dependency on kinetic factors, the ramp-rate of heating, and the finite time needed to determine signatures of reactions. In light of this, we define the onset of reaction as the lowest annealing temperature after which we identify the presence of metallic copper by x-ray diffraction. We use metallic copper as the indicator of reaction given its strong x-ray scattering and its relative ease of crystallization. For this experiment annealing refers to direct insertion of samples into a tube furnace in vacuum, ramped to desired temperature and then held for thirty minutes. The heating rates are on the order of 10 K/minute in the temperature range of interest.

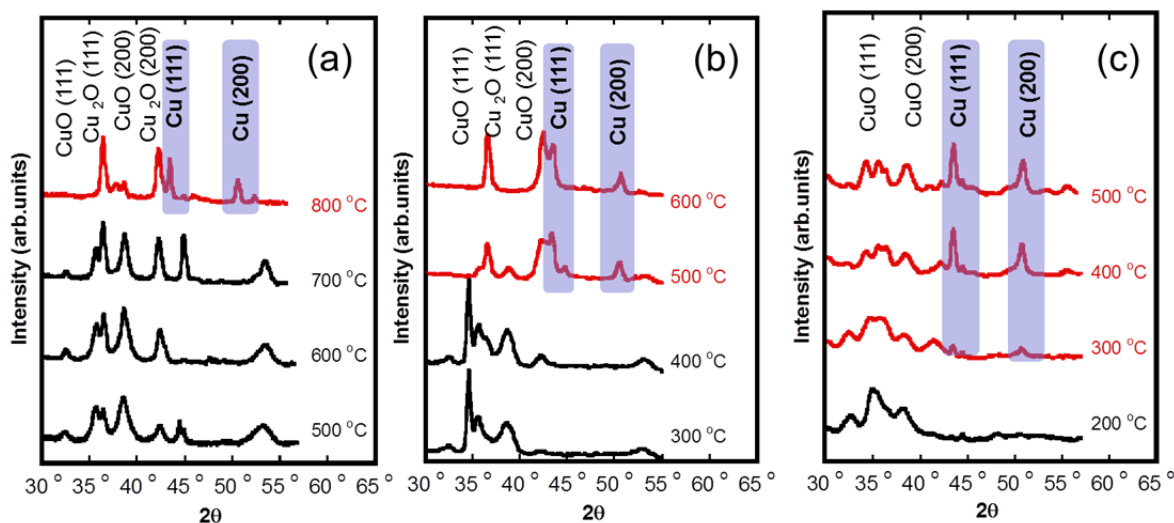


**Figure 3.3-** X-ray diffraction patterns for (a) Al-CuO, (b) Mg-CuO, and (c) Zr-CuO reactive nanolaminates exposed to high temperature anneals. The diffraction angles for Cu metal are highlighted for clarity.

Fig. 3.3 illustrates a strong relationship between the temperature onset of the self-propagating reaction and chemistry of the initial metal layers, despite the fact that the thermodynamic driving forces for the respective oxygen exchange reactions are similar. The diffraction patterns reveal that the onsets of reaction occur at 800 °C, 500 °C, and 300 °C for the Al, Mg, and Zr samples respectively. These temperatures are in no way fundamental to the specific systems as they depend on thermal boundary conditions and heating rate, however, they are meaningful for relative comparison.

A corroborating data set providing additional reaction information was collected using differential scanning calorimetry (DSC). Fig. 3.4 shows the DSC data for the three materials systems collected at a heating rate of 5 °C/min. It is important to note that the total theoretical energy released by these samples is comparable to the margin of sensitivity error for the instrument. While the exothermicity can be detected reliably at defined temperatures and relative peak sizes can be compared, an absolute and unambiguous value of heat released

cannot be reported with accuracy. While the DSC data gives no information regarding specific reactions, the data clearly shows that Zr-CuO system has an exothermic response from the initial ramp and an initial exothermic peak centered at roughly 350 °C, the Mg-CuO system exhibits a less pronounced exothermic increase with a broad initial peak at about 530 °C, and the Al-CuO system shows no exothermic behavior until around 500 °C with a peak centered near 800 °C. It is interesting to note that temperatures at which the first exothermic peaks occur are comparable to the temperatures at which Cu metal is first visible to x-ray diffraction.

In thermite analysis the presence and nature of exothermic activity is dependent on many experimental parameters including heating rate, sample substrate, and the melting point of the metal fuel. Similar investigations into Al-based nano-thermites detect reactivity below the melting point of the parent metal [21, 45, 50, 59, 105, 121-123]. Above a certain threshold dimension for some energetics, generating a liquid phase is a requirement for full energy release to occur. This behavior is expected in bulk diffusion-controlled energetics, specifically thermites, where complete reactions would be challenged if only solid-state transport mechanisms were available. If however, sufficient heat is generated to initiate fusion, liquid phase transport will assist solid-state diffusion. The extra contribution from the mobility of the liquid plays a key role in why exothermic activity occurs either before or right around the melting point of the metal. It is interesting to note that in the present work, two of the systems contain a low melting point metal: Mg and Al. However, the aluminum system shows peak exothermic activity well beyond the melting point of Al. This observations is in contrast with several other reports comparable Al-CuO experiments where full reaction of nano Al-CuO is seen below the melting point, particularly in slow heating rate regimes [24]. The dimensions of these nano multilayer films, which are ~2X thicker than the particulate work, and the reduced interface area can be used to understand this difference. Full energy release occurs after Al melting, in which case the initially formed alumina skin slows the exchange reaction until approximately 100 °C after melting, when presumably, the mass transport becomes more rapid, cracks form in the encapsulating oxide layer, or both. In

comparison, particulate studies contain much more interfacial area, thus the volumetric heat generation in the early stages is substantially greater.

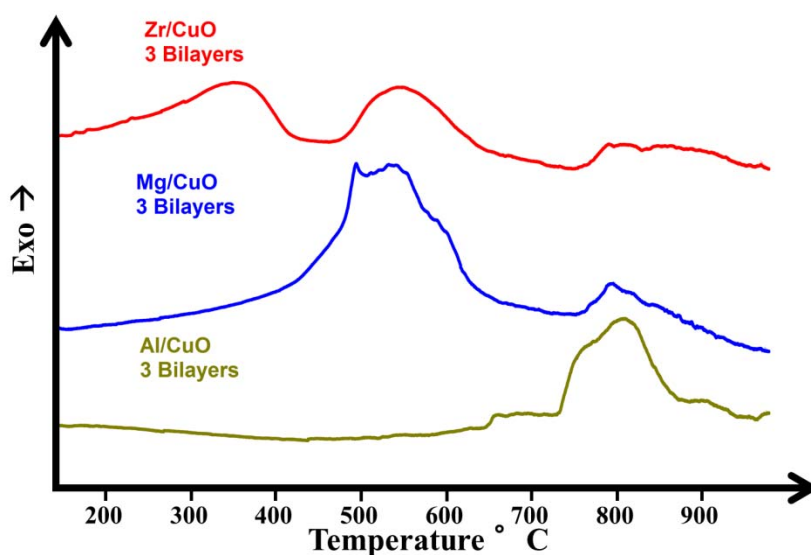


**Figure. 3.4:** DSC Analysis for Al-CuO, Mg-CuO, and Zr-CuO laminate structures ramped in flowing Ar at 5 °C/min.

The present study probes how mass transport of the terminal oxide impacts the release of energy in a reactive oxygen exchange system. This is accomplished by fixing the physical geometry and substrate – thus identical thermal boundary conditions – while varying the initial scavenger metal base on the structure of its oxide. We do so under the assumption that oxygen transport across the newly forming oxide regulates the rate of reaction.

Consequently, we expect that oxides that are most passivating, in the corrosion context, will yield the least reactive multi-layered system, despite having comparable enthalpies of formation driving the exchange. Passive oxides are characterized by chemical stability, low ionic conductivity, and modest volume change upon oxidation [118]. This connection is established in Fig. 3.5, where oxygen diffusivity for the terminal oxides are plotted with respect to the observed exothermic onset temperature. [114, 115, 124, 125]

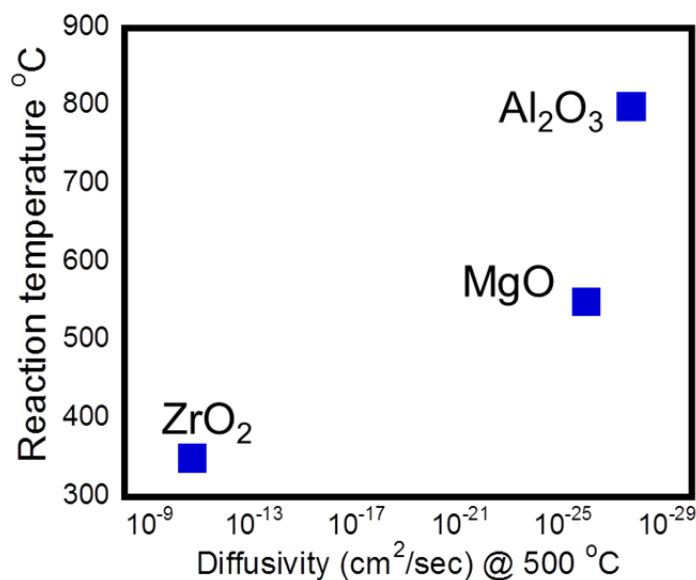


**Figure. 3.5:** Exothermic onset temperature vs terminal oxide diffusivity [cm<sup>2</sup>/sec] at 500 °C.

give insight into the spectrum of properties and the origin of the observed behaviors. Oxygen self-diffusion through zirconia is several orders of magnitude larger than that of magnesia and alumina at comparable temperatures which explains why Zr-based multilayers react most readily. At a similar initiation temperature, the Zr-based sample will support more oxygen transport, thus a greater volume of reaction and a greater amount of heat per unit volume. This in turn drives the system into the self-sustaining reaction mode where sufficient kinetics are present to drive mass-transport across the continuously forming terminal oxide until the reaction is complete.

The intermediate behavior of Mg-CuO is less obvious. The oxygen exchange reaction initiates at lower temperatures than Al-CuO, but its diffusivity values and free energies of oxidation are comparable. Again, the corrosion context can be used to explain, specifically via molar volume changes. It is customary to use the Pilling-Bedworth parameter (R), which is the ratio of the volume of the oxide to the metal [118, 126]. This parameter indicates the stress present between the metal in the oxide that arises from a change in volume which is in

turn, a gauge to assess the likelihood of mechanical failure. The Mg|MgO combination has an R factor of 0.88. When R is less than unity a poorly passivating layer is expected since the brittle oxide is under tensile strain thus prone to cracking and creating physical pathways to a fresh supply of unreacted metal. Zr and Al show R values in between 1 and 2 which puts their native oxides in compression which is a more stable state.

Considering the aforementioned arguments, one expects that the Al-CuO system is the least reactive. Its oxide forms with modest compressive stresses and its oxygen diffusivity values are amongst the lowest of all oxides.

### **3.5 CONCLUSION**

Thermite multilayered stacks were created by magnetron sputtering with a constant oxygen source, tenorite (CuO), with varying metal constituents (Al, Mg, and Zr). The product oxide forms between the two reactants creating a barrier to diffusion. The level of reaction inhibition as a function of the diffusivity of the terminal oxide was probed. It was confirmed that the reactivity of a thermite system scales with its terminal oxides transport properties using DSC and annealing XRD techniques. Higher diffusivity values of the product oxide correspond to higher temperatures required to observe the oxygen exchange reaction. Therefore the temperature where reaction occurs is lowest for the Zr-CuO system, intermediate for the Mg-CuO system, and highest for the Al-CuO multilayers.

### **3.6 ACKNOWLEDGEMENTS**

The authors would like to thank Ralph Athenian and the U.S. Army Research Office for continued financial support. Sandia National Laboratories is a multi-program laboratory managed and operated by Sandia Corporation, a wholly owned subsidiary of Lockheed Martin Corporation, for the U.S. Department of Energy's National Nuclear Security Administration under contract DE-AC04-94AL85000.

## **4. Effect of Thin Film Bilayer Spacing on Thermite Exothermicity**

**Authors: <sup>1</sup>E.J.Mily, <sup>8</sup>J. Ihlfeld, <sup>1</sup> D. Irving, <sup>1</sup>D. Brenner, <sup>1</sup>J.P. Maria**

<sup>1</sup>North Carolina State University, Department of Materials Science and Engineering, Raleigh NC, 27606 \* Sandia National Laboratories, Electronic, Optical, and Nanomaterials Department, Albuquerque, NM 87185

### **4.1 Abstract**

Multi-layer thin films thermite samples were fabricated via magnetron sputtering with each sample having a constant total thickness of roughly 1  $\mu\text{m}$  and an individual thickness of each constituent layer was varied from 700 nm down to 50 nm. The effect of layer thickness variation on the exothermic activity was studied on two common thermite systems: Al/CuO and Zr/CuO. Al/CuO and Zr/CuO samples were each tested with a varying number of bilayers and interfacial areas and it was found that as the reaction distance decreases and the amount of material in close proximity increases heat release occurs at lower temperatures. It was found that the activation energy for Al/CuO ranges from 1.5 eV down to 0.57 eV as layer thickness decreases and exothermic activity peaks transition from above to below the Al melting temperature at bilayer thicknesses below  $\sim 250\text{nm}$ . Zr/CuO thin films samples show an average reaction activation energy of 0.23eV.

### **4.2 Introduction**

Initially small particles of reactive reducing metals were added to rocket fuel during the 1960s race to the moon to increase rockets fuel temperature [4, 5]. Through this work it was realized that upon decreasing the size of the reactants of energetics to nano sized dimensions an increase in reaction speed is observed.

Since the birth of “metastable intermolecular composites” reactive Nanolaminates that include thermite reactants and intermetallic constituents have shown promise in a multitude of applications both in civilian and military avenues. Researchers have shown with these systems that as the layer thickness of the reactive nanolaminates decreases an over-all decrease in exothermic onset temperature occurs and have reported activation energy data [45, 59, 64, 70, 77, 89, 121]. This can be attributed to the decreased diffusion distance and increase in interfacial interaction area [21, 24].

This effect implies that the total energy required to initiate the thin film multilayer reaction decreases as individual layer thickness decreases. The thrust of this work is to characterize how the variation in diffusion distance and interfacial area in the Al/CuO and Zr/CuO thermite systems affect the exothermic oxygen exchange reaction while total thickness is held constant. The following work utilizes stepwise vacuum anneals followed by ex situ x-ray analysis for phase identification and differential scanning calorimetry (DSC) was used to perform classic Kissinger analysis.

### **4.3 Experimental**

Multilayers of thermite reactants were layered in an alternating geometry on C plane sapphire by physical vapor deposition using dual beam magnetron sputtering sources positioned 180° from each other. Each substrate of sapphire was laser cut to 3.5 x 3.5 mm to ensure comparison of equal amounts of reactants. Deposition rates were determined via X-Ray reflectivity measurements described elsewhere [127]. The bilayer spacing, number of bilayers, and total thickness of the samples can be found in table 4.1.

**Table 4.1-** Thin Film Thermite Parameters

<b>Thin Film Thermite Parameters</b>					
<b>Number of Bilayers</b>	<b>Total Thickness</b>	<b>Bilayer Thickness</b>	<b>CuO thickness</b>	<b>Al thickness</b>	<b>Activation Energy [eV]</b>
1	1070	1070	700	370	1.46
2	1070	535	350	185	1.58
3	1070	356	233	123	1.42
4	1070	268	175	93	1.04
5	1070	213	140	73	0.59
6	1070	179	117	62	0.58
7	1070	153	100	53	0.57
<b>Number of Bilayers</b>	<b>Total Thickness</b>	<b>Bilayer Thickness</b>	<b>CuO thickness</b>	<b>Zr Thickness</b>	<b>Activation Energy [eV]</b>
1	1090	1090	700	390	0.4
2	1090	545	350	195	0.17
3	1090	363	233	130	0.21
4	1090	273	175	98	0.3
5	1090	218	140	78	0.11

All samples were annealed in a stepwise manner in a vacuum furnace with a base pressure of  $1 \times 10^{-4}$  torr and held at the dwell temperature for half an hour. Samples were then removed from the furnace and analyzed via x-ray diffraction analysis (XRD) with Bragg Brentano geometry scanning in two theta. As reported previously [127] this method used the evolution of the copper metal peak as a means to track the reaction progression. The lack of mechanical stability of freestanding  $\sim 1 \mu\text{m}$  films dictated delamination unfeasible, therefore all thin films were left adhered to the sapphire substrates during analysis.

A Netasch Proteus F3 Juptier differential scanning calorimeter (DSC) was used to characterize the effect of bilayer thickness variation on exothermic behavior. Samples were ramped in the DSC at 5K/min under an inert argon atmosphere with a temperature program that ramped the samples to 1200°C cooled them back down to 100°C and a final ramp to 1200°C. The desired exothermic phenomena is irreversible under these conditions, therefore

the second ramp was subtracted from the first ramp for baseline refinement. Thermal Kissinger analysis utilized the DSC at five different ramping rates 5, 10,15,20, and 25 K/min.

## 4.4 Results and Discussion

The characterization and research into Al-based thermites is extensive [16, 37, 46, 50, 56, 57, 60, 81, 83, 96, 100, 102, 103, 105, 121, 122, 128-134]. Our work is meant to supplement existing knowledge in the aluminum thermite arena and to better understand thermite reaction mechanisms under slow heating rate regimes. As reported elsewhere, nano thermite reactions undergo oxygen exchange at varying temperatures depending on the heating rate they are exposed to, the geometric constraints in the physical system, and their overall surroundings. Generally under fast heating rates around  $10^5$  Celsius a minute, exothermic activity occurs right at the melting temperature of the metal fuel or above it.[28, 135]. Under slow heating rates it is widely reported that nano thermite powders and laminates exhibit exothermic activity below the metal fuels melting point. In this slow heating regime micron sized thermites exhibit exothermic activity at or above the melting temperature of the metal. This behavior is seen for several metal and metal oxide systems [57, 136]. In this work we have prepared an exhaustive array of samples ranging in bilayer spacing with overall thickness constant keeping stoichiometric equivalence ratio equal to unity seen in table 4.1. The thickness parameters were chosen as characteristic diameters of thermites commonly ball milled that would be considered on the higher end of the roughly defined nano-scale in which the nano-energetics operate.

### 4.4.1 Al/CuO System

In figure 4.1 we compare the limiting cases of the study in the stepwise anneal and x-ray phase identification analysis. The copper metallic peak was used as an indicator to when the oxygen exchange starts to go to completion. Comparing the Al/CuO samples with 1 bilayer to 13 bilayers the presence of copper metallic peaks arises at lower temperatures when the number of interfaces increases. Copper peaks are present after the 800°C anneal for the one bilayer sample and after the 600°C anneal in the 13 bilayer sample. The presence of

other intermediate phases are acknowledged such as  $\text{Cu}_2\text{O}$ , the less oxygen dense oxide of copper, at lower temperatures which indicates oxygen exchange occurs below the temperature which copper is seen however the presence of copper metallic peaks indicate the reaction is approaching completion by the presence of final product. Complementary DSC data seen in figure 4.2 showcase an array of Al/CuO samples with varying layer thicknesses and bilayers. Each of these samples is represented by a separate thermal trace at  $5^\circ\text{C}$  per minute. The data show three important exothermic regions in this graph: low, medium and high interfacial density systems as labeled in figure 4.2.

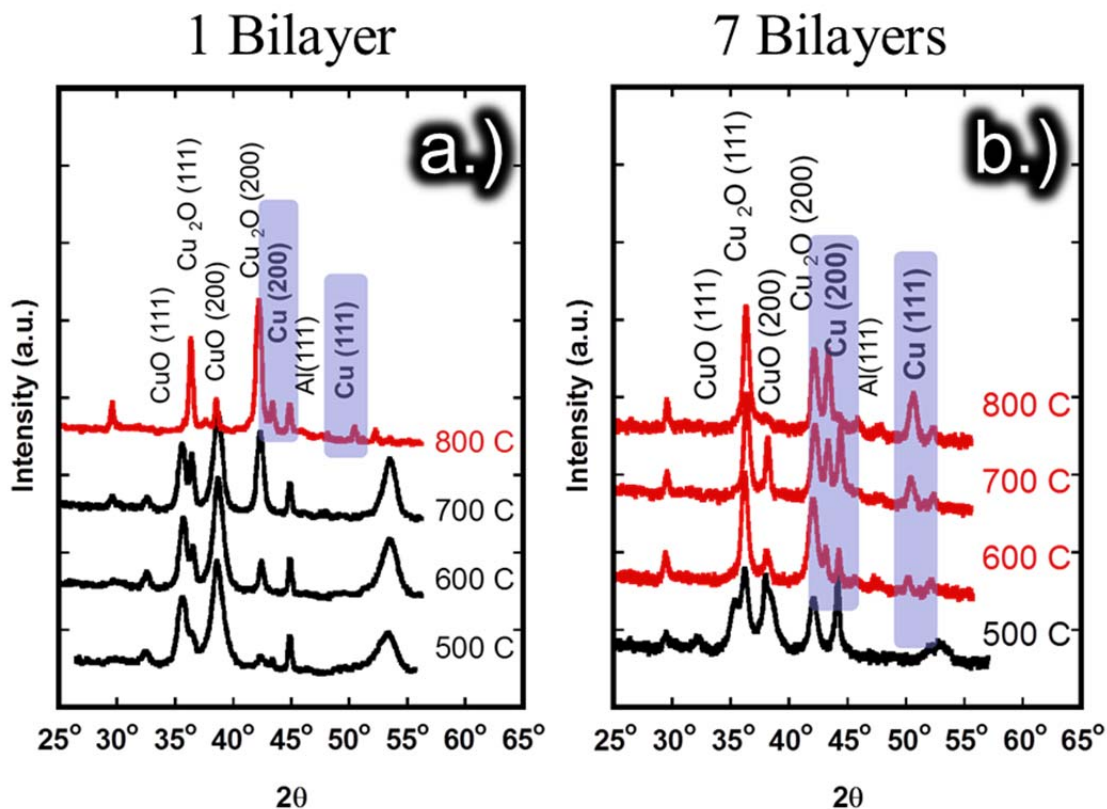


**Figure 4.1-** XRD Spectra for the Al/CuO system stepwise anneal phase identification for the a.) 1 bilayer Al/CuO sample and the b.) 7 bilayer Al/CuO sample

This thermal analysis yields two important features. The first feature of note is the exothermic peak temperature decreases as the interfacial area to volume ratio increase. The depression of this temperature can be explained by an increase in simultaneous reaction sites and a decrease in diffusion distance. All samples have the same thermal boundary conditions; therefore the heat loss for each sample is equal. When the interfacial density is increased, the heat flux generated is increased to allow for more oxygen exchange to occur. Another consequence of a total bilayer thickness decrease in the multilayered geometry is a reduction in the distance reactive atoms need to transverse in order to complete the thermite reaction. A smaller dimension for atoms to diffuse through requires less total energy than transport

across a thicker barrier. The decrease in diffusion length and the elevated exothermic reaction density are the reasons for the decrease in exothermic peak temperature.

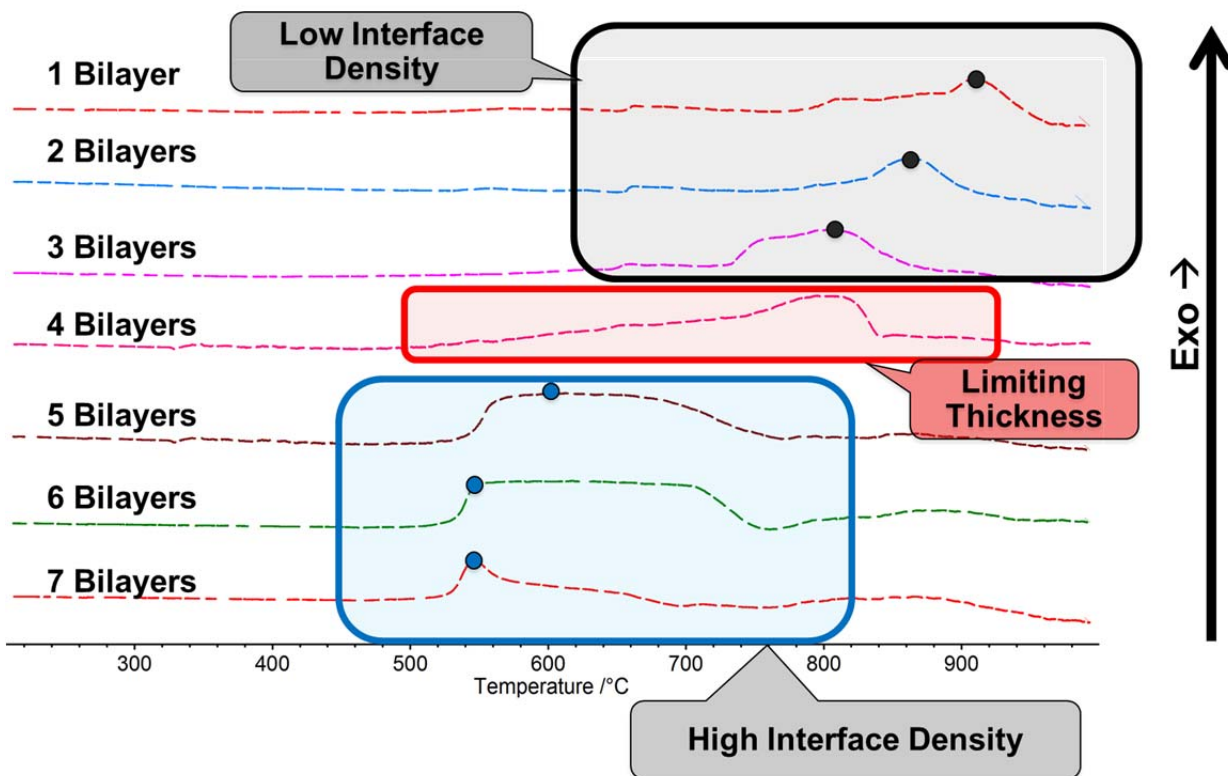


**Figure 4.2-** DSC data from the Al/CuO thin film samples testing the exothermic behavior of the samples as a function of the number of bilayers

The second feature of interest in the DSC's plot of the Al/CuO samples is the temperature at which exothermicity is seen for samples having more than four bilayers. The onset temperatures of these samples are very close to the eutectic melting temperature of aluminum and copper oxide in the aluminum copper oxide system at 548°C [137, 138]. The presence of this eutectic in this thermite system has been seen [50] in the cryo-milling of Al/CuO powders. A possible explanation for the depression of the exothermic peak temperature is that during transport across a product layer at the interface a finite amount of intermetallic aluminum copper is formed. As interfacial densities increase this phase supplies an added heat of formation energy term that increases the heat flux increasing the samples

temperature. Or this product is present upon deposition during the multilayer film fabrication and during its melting, which accelerates the oxygen exchange reaction due to increased ion mobility in the melt. This transition starts to become present when bilayer thickness is at or below 278 nm. More experimentation is needed to confirm this artifact and will be investigated further in chapter 9.

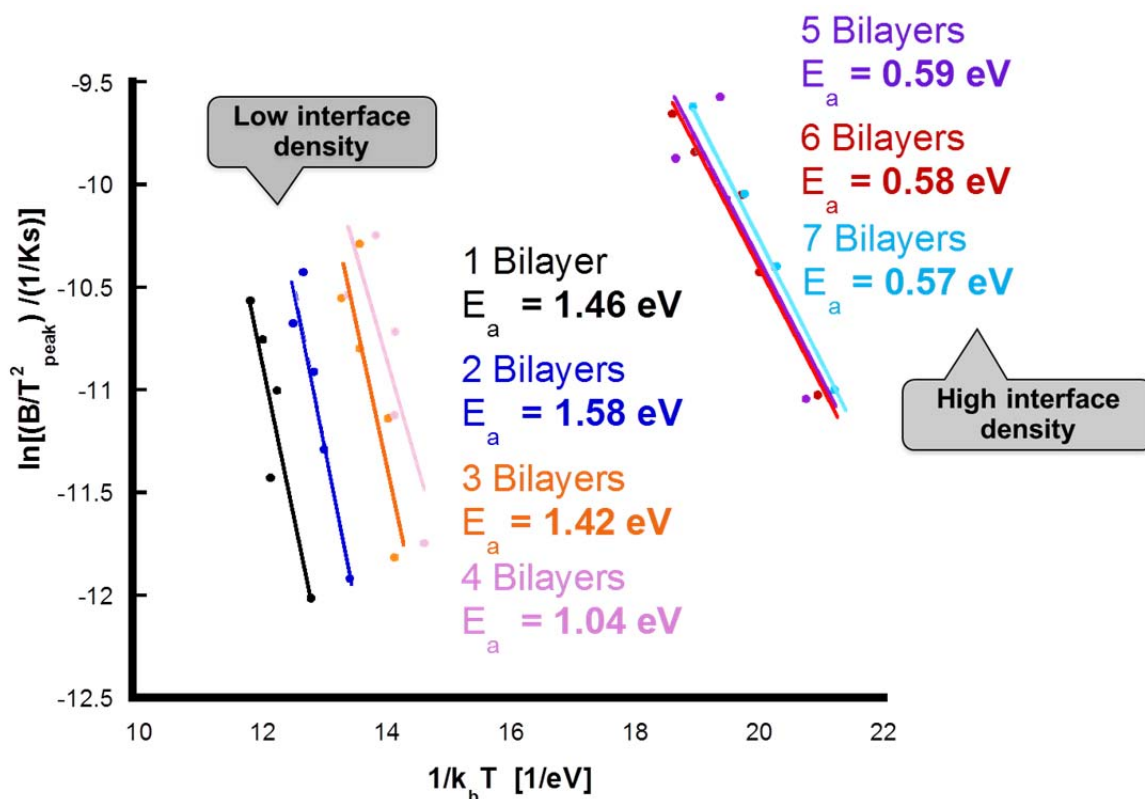


**Figure 4.3-** Effective activation energy Kissinger analysis plot of the Al/CuO thin film system

The effect of the increased interfacial density on the exothermic peak temperature was calculated using methods developed by Kissinger [139, 140]. As shown in figure 4.3 the effective activation energy for exothermic behavior was compared for each of the aluminum samples. It was found that the activation energy values for low interfacial density decreased as number of interfaces increased as indicated previously from 1.5 eV to 0.5 eV. The

transition is marked by a drop in 0.5 eV for the samples of four bilayers to five bilayers. This lowering and activation energy corresponds to the heat release occurring at and around the aluminum copper eutectic temperature. This result along with the supporting evidence from the figure 4.2 indicate the oxygen exchange occurs more readily when more interfacial area is present also it stands to reason that heat release follows the diffusion model set by other works [21, 29, 31, 32] whereas mobility is heightened when the liquid phase present which is critical to reaction progression.

#### **4.4.2 Zr/CuO System**

Identical analysis of the Zr/CuO system was performed and the layer thicknesses are reported in table 1. Fabrication attempts were made to decrease bilayer thickness comparable to that of the aluminum system however bilayer spacing's below ~215nm proved unstable at ambient conditions. Despite this practical experimental limitation interesting information is gained from this study. The x-ray stepwise anneal analysis as performed similarly to the aluminum system indicate the presence of copper metal at a lower exothermic peak temperature for samples with increased interfacial area as seen in figure 4.4.

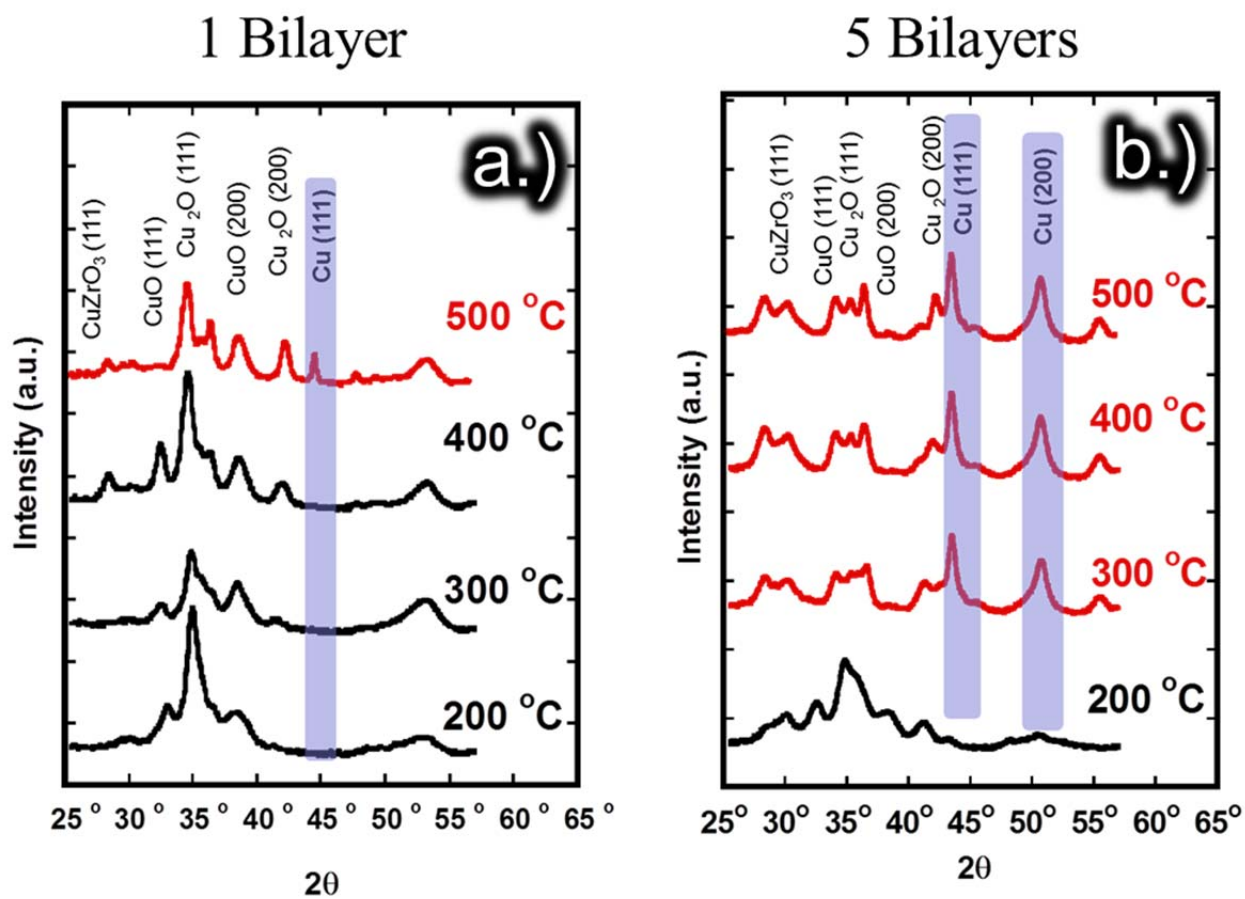


**Figure 4.4-** XRD Spectra for the Zr/CuO system stepwise anneal phase identification for the a.) 1 bilayer Zr/CuO sample and the b.) 5 bilayer Zr/CuO sample

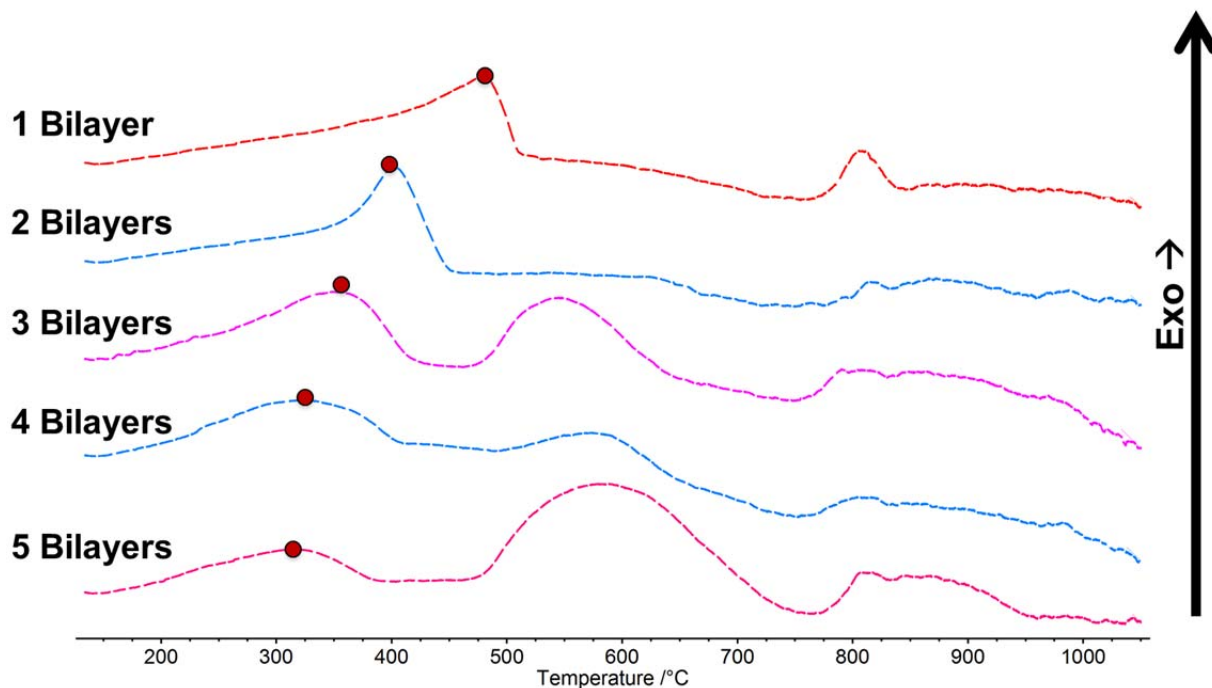


**Figure 4.5-** DSC data from the Zr/CuO thin film samples testing the exothermic behavior of the samples as a function of the number of bilayers

The Zr/CuO system forms terminal products at lower temperatures than seen in Al/CuO and in other work[127]. This system then follows the trend seen for the aluminum copper oxide system as product phase copper is seen at lower temperatures as the number of interfaces increases. Analysis of the DSC data from the system seen in figure 4.5 show the depression of the exothermic peak temperature as a function of bilayers. With this thermite couple it is important to note exothermic activity occurs below the melting point of zirconium at 1850°C, therefore all oxygen exchange occurs in the solid phase. No large depression is seen like that of the aluminum system however a modest decrease in exothermic peak temperature is still noted. Performing the same Kissinger activation energy analysis as was done in the aluminum system we find in figure 4.6 that the overall values are smaller than the aluminum systems lowest values.

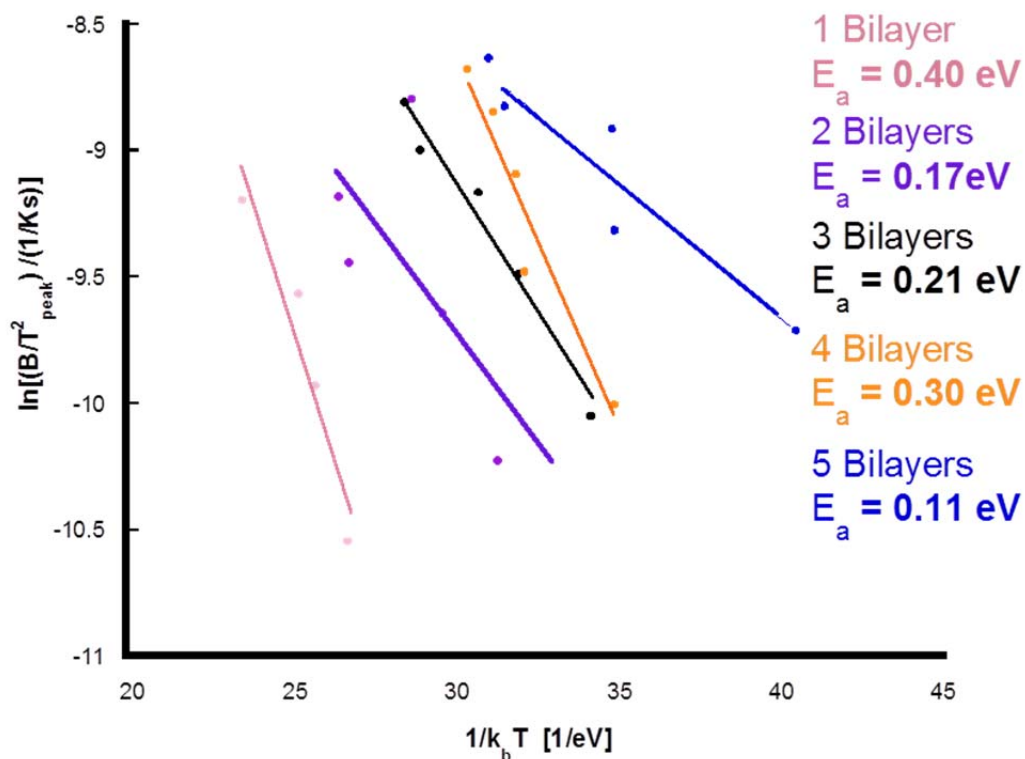


**Figure 4.6-** Effective activation energy Kissinger analysis plot of the Zr/CuO thin film system

## 4.5 Conclusion

Multilayer thin-film thermites of Al and Zr were coupled with an oxygen sink CuO, were deposited in a series of experiments that kept the overall thickness and amount of material constant but varied the number of bilayers present in each sample. This was done to test how exothermic activity is affected by increase in surface area and decrease in diffusion distance. It was found for both systems the decrease in layer thickness which resulted in a decreased diffusion distance lowered the temperature at which exothermicity occurred. Activation energies for Al/CuO and Zr/CuO systems were computed via Kissinger thermal analysis. The

Al/CuO system displayed two values of activation energies for thinner and thicker bilayers suggesting another possible mechanism involved when thinner dimensions are realized. The overall values of activation energy for the Al system were greater than that of the Zr system and this was described previously by the consideration of the terminal oxides diffusion properties. Al/CuO also exhibit an interesting behavior where exothermic activity occurs above the melting temperature of aluminum at a larger layer thicknesses, then exhibits exothermic activity below this temperature when bilayer thicknesses are decreased below 250 nm.

## 5. Interfacial Analysis of Multilayered Nanothermite

**Authors: <sup>1</sup>E. J. Mily, <sup>1</sup>C. Akoula, <sup>1</sup>R. Collazo, <sup>1</sup>Z. Sitar, <sup>1</sup>J.P. Maria**

<sup>1</sup>North Carolina State University, Department of Materials Science and Engineering, Raleigh NC, 27606

In this study, the authors report a series of experiments designed to probe the interface between bulk thermite constituents. CuO acted as the oxygen source while Al and Zr were the reactive metals. The sputter deposited oxide thin film was introduced into high vacuum where the metal thin films were e-beam evaporated with monolayer precision. In vacuo x-ray photoelectron spectroscopy spectra were collected after each metal deposition had been completed. The pre-reacted thicknesses of the Al<sub>2</sub>O<sub>3</sub> and ZrO<sub>2</sub> that formed during deposition were found to be 2nm and 3nm respectively. The oxide formation was also found to be deposition rate dependent, where thicker oxide layers form under slower deposition rates. In addition, the sputtered phase of copper oxide corresponds to the desirable oxygen dense phase of tenorite (CuO). These results confirm the presence of the thermite terminal oxide at room temperature and suggest metal species with different reactive tendencies exhibit similar formation trends.

### 5.1 Interfacial Analysis Background

Energetic materials research into metastable intermolecular composites (MICs) provides new avenues to supplement organic energetic materials with inorganics. They have been shown to increase burning rates of rocket fuel, raise adiabatic flame temperatures, and even create lead free matches[104, 141]. The lynchpin of MIC fabrication to achieve these extraordinary properties is by pairing reactive precursors at the nano-scale. The driving factor for this is the increased reactivity of the reactive materials due to the increase in interaction

area, which in turn decreases reaction diffusion distances in multi-layered thermites and accelerates heat generation per time.

When reactive materials are combined at any scale, a finite amount of product components are present at the interface before intentional energy release takes place. For any energetic material composition that is augmented by nano-scale fabrication to increase reaction rate, usually thermites[15, 27, 55-60, 81, 83, 84, 96, 100-104] or intermetallics[65, 66, 74, 76, 88, 89], there is a trade-off of increased pre-reacted material volume at the interface due to higher interaction areas as shown by Knepper et al. [76]. This region of reacted material at the interface decreases the overall energetic output of the system and is a result of mixing these materials in intimate proximity[96].

It is theoretically predicted that energetic material reaction rates should increase as particle size decreases. Thorough investigations have shown this empirically to be the case [65, 66, 69, 72, 73, 75, 76, 78, 142] where the initial increase in reaction velocity is seen as particle size is decreased. However in contrast with theory, below a certain critical particle size or thickness the reaction velocity decreases rapidly until no reaction is observed. The cause of this drop-off in reaction speed and deviation from theoretical predictions is due to the high volume percent of already reacted material at the interface. Understanding and characterizing the pre-reacted volume of nano energetics is therefore crucial to the design and fabrication of such materials. Consequently it is prudent that we investigate more thoroughly when these layers form, under what conditions they form, and how we can remove or enhance them. To do this we initiated an x-ray photoelectron spectroscopy (XPS) experiment, to do in-situ deposition and spectroscopy. The ability to use physical vapor deposition of thin films with monolayer precision provides an ideal system for a clean avenue to quantifiably characterize the pre-reacted material that forms at the interface.

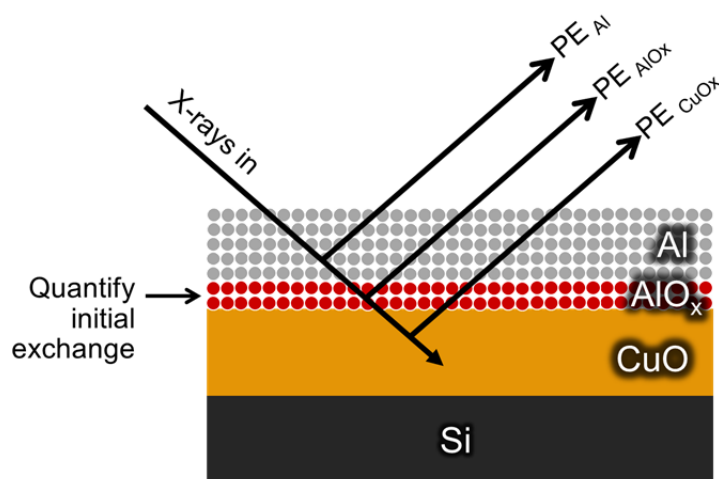


**Figure 5.8-** Visual representation of photo-electrons from each each sample constituent.

A schematic of the following experiment is shown in figure 5.1. X-rays incident upon the sample excite photoelectron's from the surface of the copper oxide and the subsequent metal monolayers allowing for accurate measurement of the copper oxides reduction from the titration of metal layers.

## 5.2 Experimental Procedure

### 5.2.1 Substrate Preparation

It was desired to observe how vapor deposited metal scavenged oxygen from copper oxide and test the limits and thickness of metal oxidation at room temperature. To do so, a sufficiently thick copper oxide film (relative to the aluminum thickness) was required to provide an oxygen sink. The majority of literature [104, 134, 143, 144] that explore aluminum oxidation report a scale thickness usually no larger than 10 nm. To provide a sufficient source of oxygen for the aluminum to scavenge a 20 nm thin-film of CuO was deposited on silicon substrates using an RF power supply in the presence of 2mT Argon (purity > 99.9999%). The samples were transferred into an ultrahigh vacuum analysis

chamber with a base pressure of ( $1 \times 10^{-9}$  torr) that allowed for samples to be deposited on and analyze without exposure to the environment.

The aluminum and zirconium (Sigma Aldrich 99.9999%) for all samples analyzed in this work were deposited using an electron beam deposition chamber with a deposition rate of  $.2 \text{ \AA/s}$ . The metal fluence and deposition rate were calculated using a quartz crystal microbalance (QCM).

## **5.2.2 X-ray Photoelectron Analysis**

Photoelectron analysis was performed using a hemispherical detector using an aluminum x-ray source with a pass energy of 20 eV. Igor peak fitting spectra analysis software was utilized. In order to track metal oxidation and copper reduction the energy ranges of interest were the Al 2p, Zr 3d, Cu 2p and the O 1s peaks. Survey scans were conducted with 50 eV pass energy and the orbital specific scans were done with 20 eV pass energy.

## **5.3 Results and discussion**

### **5.3.1 Copper Oxide Phase Identification**

Copper oxide can exist in three different oxide phases with two stable phases  $\text{Cu}_2\text{O}$  (cuprite, or cuprous oxide) and  $\text{CuO}$  (tenorite, or cupric oxide), and one semi-stable phase  $\text{Cu}_4\text{O}_3$  (paramelaconite). Each have considerably different oxygen content with 33.3, 50, and 43.9 percent oxygen respectively[145]. Due to  $\text{CuO}$  having the highest oxygen content, it is the oxidized form of copper that is most ideal for the integration into thermite structures and is the reason why it was chosen for the following experiments.

The most oxygen dense phase of copper  $\text{CuO}$ , or tenorite, has been previously reported by other authors[146] to be difficult to deposit using the physical vapor deposition technique of magnetron sputtering without the other less oxygen rich phases present of

paramelaconite or  $\text{Cu}_2\text{O}$ . Before metal analysis was performed a preliminary survey of the copper oxide phase was executed. The spectra from the Cu 2p energy range shows the Cu  $2p_{3/2}$  and  $2p_{1/2}$  are at 933 eV and 953 eV respectively. This corresponds to an oxidation state of  $\text{Cu}^{+2}$ . In addition to the presence of a higher binding energy peak for copper the characteristic shakeups satellite peaks that are seen only for the CuO phase are present which indicates the predominant phase of copper in this substrate is tenorite. It is important to note the phase of the beginning oxygen source to monitor any changes once metal deposition is completed.

### **5.3.2 Aluminum Deposition on CuO**

The CuO coated Silicon wafer sample was inserted in the metallization chamber with a base pressure of  $1 \times 10^{-7}$  Torr where 1 ML of aluminum was deposited on the copper oxide surface. The sample was then transferred to the X-ray photoelectron spectroscopy (XPS) analysis chamber with a base pressure of  $1 \times 10^{-10}$  torr and analyzed. Then this process was repeated until 11 monolayers were deposited on the same copper oxide sample.

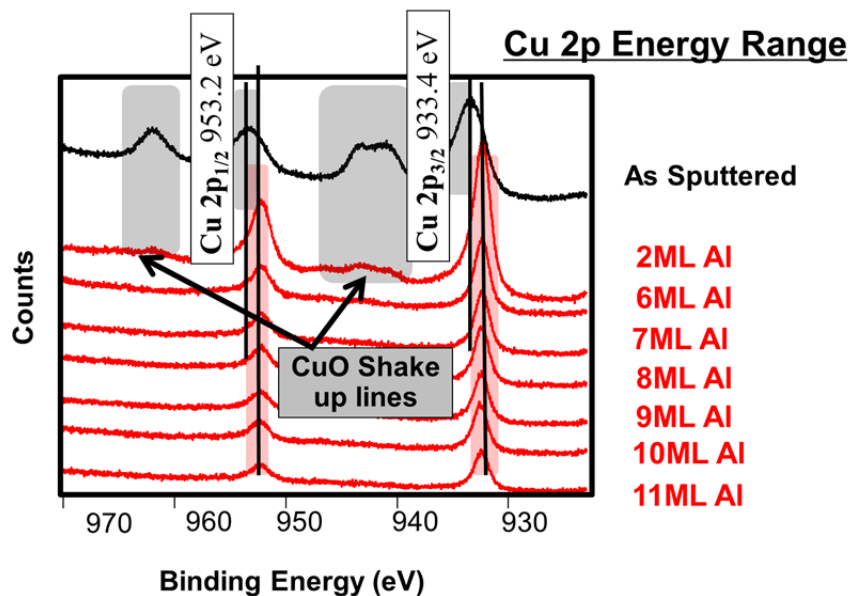


**Figure 5.9-** Cu 2p orbital energy range, showing the affects of aluminum monolayer titration on the copper oxidation state.

Figure 5.2 shows a plot of the copper 2p binding energy range where each trace represents a different layer thickness of aluminum deposited upon copper oxide. From this data it can be seen that after just two monolayers of aluminum deposited upon the copper oxide surface the shakeup satellites that are indicative of the CuO phase depreciate in intensity by 97 %. This corresponds to the aluminum scavenging oxygen from the underlying copper oxide. Further determination of the copper oxidation state was not possible because the  $\text{Cu}^{+1}$  and  $\text{Cu}^{+0}$  states have a difference in binding energy lower than the resolution of the detection limits of the XPS. The 2p binding energy range of aluminum shown in figure 5.3 is the result of this iterative deposition and analysis. No peak associated with metallic aluminum develops even after 11 monolayers of aluminum are deposited on the surface which corresponds to a 3.15 nm thick alumina layer.

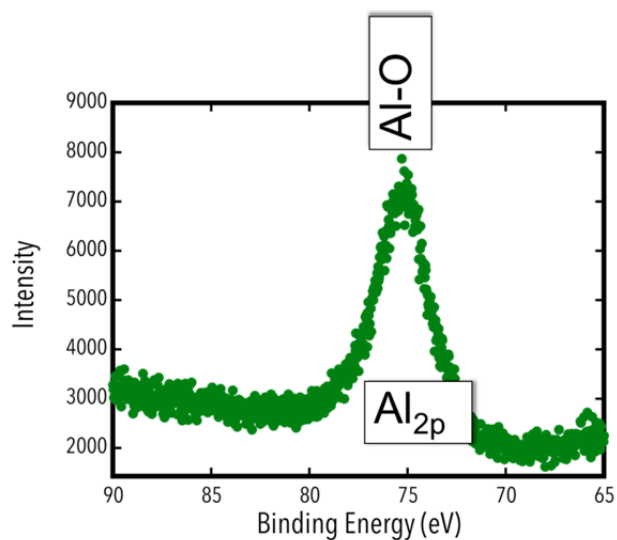


**Figure 5.10-** Al 2p binding energy range showing a singular peak at 74.7eV corresponding the sample that iteratively deposited 1 ML of aluminum at a time. The peak shows aluminum coordinated with oxygen.

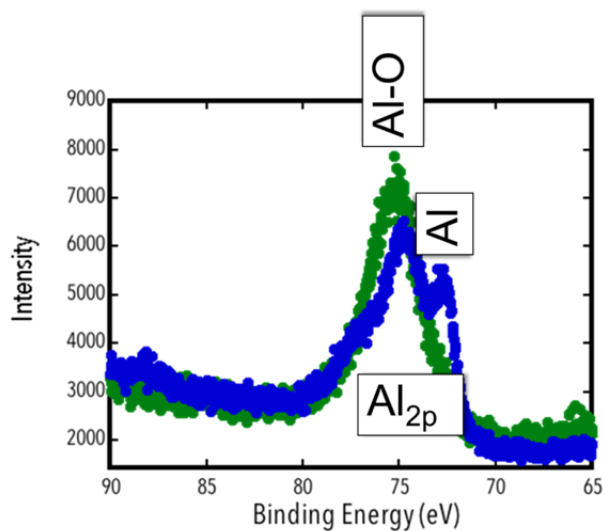


**Figure 5.11-** Al 2p binding energy range comparing samples with 11ML of aluminum deposited via mono-layer by monolayer and deposition all at once.

This thickness is considerably larger than previous vacuum studies of alumina scale on weaker oxide surfaces specifically the work of Taylor and Martin[82], which show the development of a Al metallic peak at 73.3 eV after around seven and eight monolayers of aluminum. This previous investigation used relatively short time intervals between measurements. The one monolayer deposition then analysis method in the present study allowed for significant analysis time between each deposition. The discrepancy between these two results is due to the difference in time allowed between each deposition segment. This extra time between each monolayer deposition allows for increased surface diffusion to occur in addition to the always present oxygen exchange pathway via bulk diffusion in thin films. To measure and confirm the affect deposition rate has on the extent of oxidation, a separate sample of CuO layered on a Si wafer was created and 11 ML of Al was deposited in one deposition cycle and then analyzed. Comparing the two methods of deposition in figure 5.4, both photoelectron traces show the presence of Al bound with oxygen at 74.7 eV. The binding energy peak associated with Al bound with Al at 73.3 eV is only seen for the 11ML deposited all at once and not present for the sample created by the repeated 1 monolayer deposition then analysis procedure. Depicted in figure 5.5 the metal deposits on the surface via island growth to coalescence mechanism[147, 148], and before coalescence and complete surface coverage is achieved, sections of the oxide surface that are not covered can participate in surface oxygen transfer. The atomic transport between the bulk oxide under-layer and the metal coalesced droplet is throttled by the growth of a product layer that acts as a diffusion barrier. The oxygen exchange mechanism associated with surface diffusion is not hindered by this, therefore while the diffusion from the bulk is limited the surface movement is not and continues to oxidize the metal during the analysis procedure. This implies that more time between layers results in a thicker oxidation layer. As a result of this, the method of 1 ML of Al deposition per measurement cycle creates a sample with a thicker terminal oxide layer.

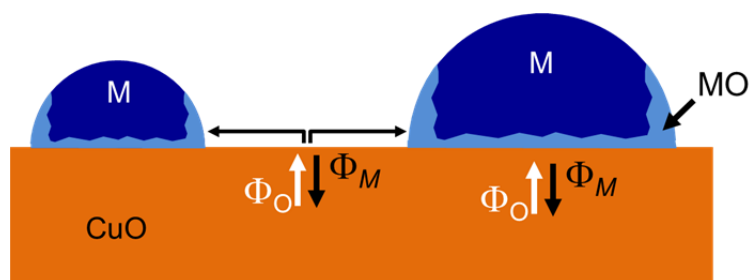


**Figure 12.5-** Visual representation of metal island growth on the CuO surface, where an environment is created that promotes surface diffusion.

In order to circumvent this deposition rate phenomenon, a series of copper oxide samples were prepared separately. Aluminum was deposited on each copper oxide sample with differing thicknesses in separate deposition sequences. With this approach, the global deposition rate is increased minimizing the effects of surface diffusion to occur. In this manner tracking the evolution of the metallic aluminum peak in the aluminum 2p energy range for an assay of different aluminum thicknesses should better represent the oxide formation at the boundary of two reactive materials. Figure 5.6 illustrates the XPS spectra collected from samples with different aluminum metal thicknesses deposit. This approach generates a metallic un-oxidized aluminum peak at 73.3 eV that appears at seven monolayers of aluminum deposited corresponding to 2 nm thick oxide as was reported by Taylor and Martin.

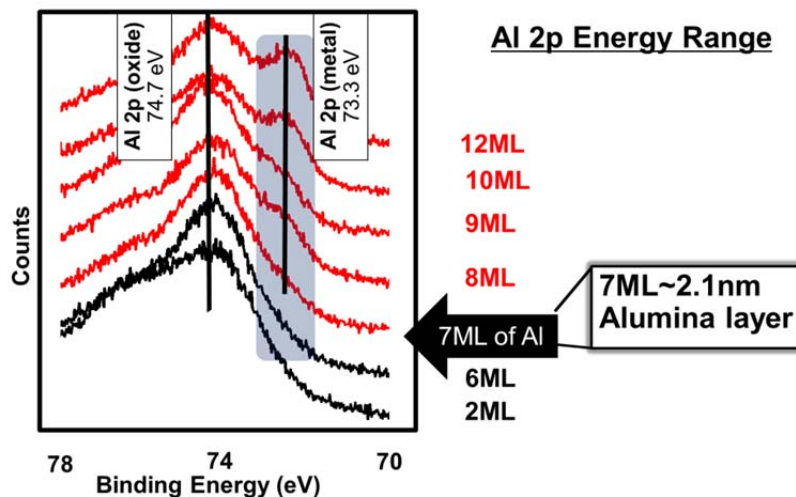


**Figure 5.13-** Al 2p energy range for samples with different thicknesses of Al deposited on the surface of CuO. The corresponding layer where metallic aluminum appears is at 7ML of aluminum or  $\sim 2.1$  nm.

It is important to note that combining nano thermite constituents in a laminate architecture usually employs magnetron sputtering where the energy of incoming depositing atoms is  $\sim 2$ - $3$  eV and the energy of the depositing metal in this study via electron beam deposition is  $\sim 0.5$  eV. It is acknowledged that the incoming energy of the depositing metal in this study is lower than what is normally characteristic of the thin-film thermite samples, and the oxide thickness detected may be artificially lower than what would be found in a typical thermite system, however it is the only technique able to deposit metal with such precision for this surface analysis study.

### 5.3.3 Zirconium Deposition on CuO

Our previous work on thermite couples of zirconium aluminum and magnesium paired with copper oxide have illuminated the importance of the terminal metals oxides diffusion properties[127]. In this study it was found that the metals that transform into an oxide with the highest diffusion coefficient requires more thermal activation than a system

with the terminal oxide with a lower or smaller diffusion coefficient. This is the case for aluminum versus zirconium, where the aluminum transforms into a passive oxide that acts as a robust diffusion barrier and zirconium transforms into an oxide that is an ion conductor. With this knowledge it is important to understand and analyze the interfaces of these two systems. The same stepwise deposition and analysis was done for the Zr/CuO system as was done for the aforementioned Al/CuO system. The zirconium metal binding energy peak evolution was tracked as increasing amounts of zirconium was deposited on copper oxide. Figure 5.7 contains the binding energy data of the zirconium  $3d_{5/2}$  energy range. Each curve represents a different sample with a different thickness of zirconium deposited upon a 20 nm copper oxide coated silicon substrate. As is seen in the aluminum copper oxide system, after only two monolayers of zirconium deposited on the CuO surface the only zirconium metal peak at 181 eV corresponds to zirconium only bound to oxygen. The metallic peak at a lower binding energy of 179.3 eV appears after 10 monolayers zirconium is deposited. This result signifies that the oxide thickness is no larger than roughly 3.2 nm. It was initially expected that the zirconium copper oxide system would yield a substantially thicker oxide layer because of zirconia's ion conducting nature. In contrast to this expectation, this experiment points to a reality where both systems display similar dimensional characteristics. From this it can be further deduced that the combination of a weak oxide and two reactive metals with dissimilar terminal oxide properties produces interfaces that vary only slightly at room temperature. This means that the manner in which two reactive materials are combined together at the nanoscale is an equally important parameter to consider in addition to the chemistry involved. Consequently extrinsic factors such as deposition method, substrate integrity, deposition temperature etc. add another metric for the experimenter to control to tune the energetic release of nano-thermites.

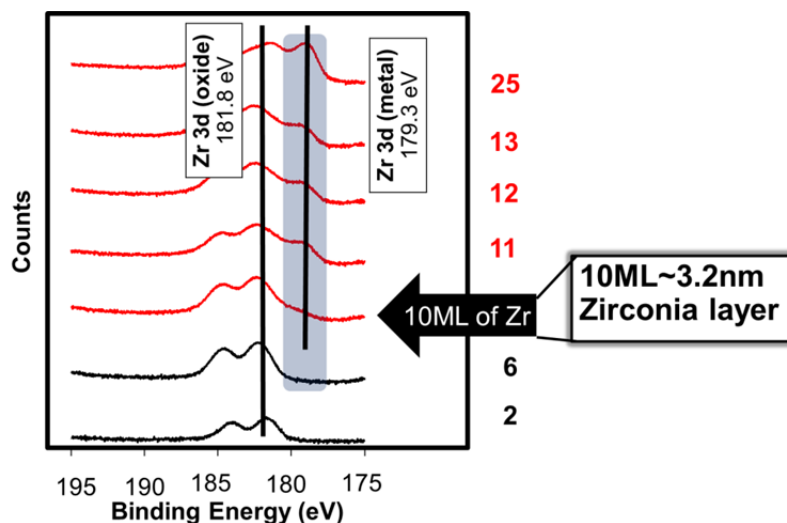


**Figure 5.14-** Zr 2p energy range for samples with different thicknesses of Zr deposited on the surface of CuO. The corresponding layer where metallic aluminum appears is at 10ML of aluminum or ~3.2 nm.

## 5.4 Conclusion

Interfacial surface analysis was performed on Al/CuO and Zr/CuO material systems. Iterative deposition of the reactive metal on the copper oxide films was achieved by electron beam deposition and followed by XPS analysis under ultrahigh vacuum conditions. The copper oxide phase was determined to be CuO as indicated by characteristic phase identifying CuO shakeups satellite peaks. It was discovered that oxide formation is deposition rate dependent, where if the metal is deposited slowly, enough time is allowed for sufficient surface transport to occur yielding a thicker oxide layer. The thickness of the terminal oxide formed upon deposition was characterized by the evolution of the metallic species binding energy peak. The two systems with different terminal oxide diffusion rates exhibited similar formation behavior indicating interface formation in nano energetics is also dependent on extrinsic deposition parameters.

## 6. Nano-Kirkendall Diffusion

### 6.1 Diffusion Monitoring at the Nano Scale

A survey of current literature in the nano energetics field illuminates a particular deficiency in the current understanding of how oxygen exchange reactions proceed. It is understood that for condensed phase reactions of oxygen exchange, diffusion across a barrier layer is required for reaction progression. The rates in which movement occurs across this barrier depend on the chemical composition of the barrier, the temperatures the energetics are exposed to, the length scales the reactants are combined in, and particular geometries involved. Most investigations have articulated the importance of understanding diffusion yet neglected specifically characterize what species is the primary diffusant. Some evidence suggests that the oxygen is the mobile species and responsible for the reaction to occur [149-152] and other reports blame the metal species[121]. It is not prudent to solely look upon the diffusion of oxygen as the prime mover especially if one considers the self-diffusion of metals in their respective oxides compared to oxygen movement. The comparison of the atomic diffusivities of the metals and the oxygen in common oxides is shown in figure 6.1. It is not readily apparent why oxygen is labeled the prime diffusing species when the metals in these common oxides diffuse faster than the oxygen at low temperatures. Solely based on this observation more research is required to ascertain more clarity of the oxygen exchange reaction.

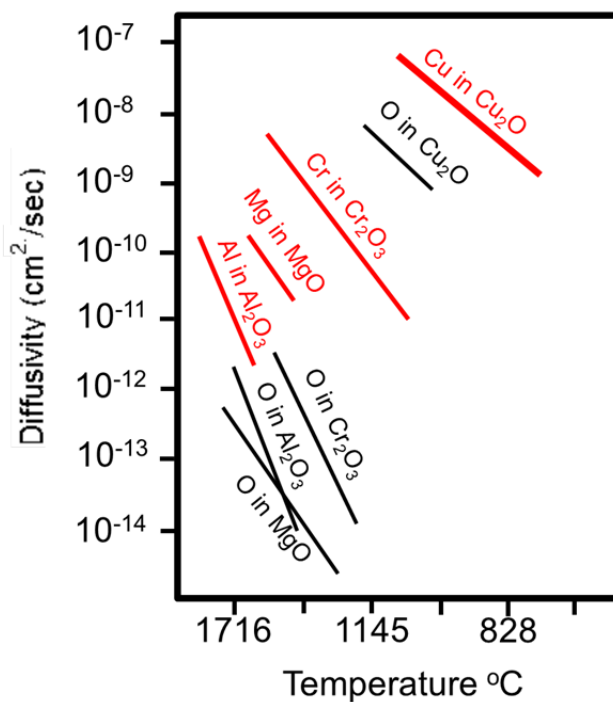


**Figure 6.1-** Self diffusion of metals and oxygen through common oxides[153].

Traditional means of monitoring diffusion involve radioactive particle fluxes, isotope doping of different materials, ion implantation and backscattering techniques [154-157]. These methods provide extremely accurate and sensitive information regarding the atomistic diffusion. Unfortunately these experiments employ costly instruments and radioactive material not readily available for a large percentage of the scientific community.

A complementary macroscopic technique for diffusion tracking was first developed by Ernest Kirkendall [158]. Kirkendall was the first researcher to investigate diffusion flux inequalities in materials. He discovered that a boundary layer between two soluble metals undergoes a displacement due to different diffusion rates across a boundary with respect to an inert marker. In his original experiment Kirkendall placed molybdenum wires evenly across a brass ingot which he then encased in copper. The entire ensemble was annealed and

cross sectioned at different stages of its thermal history to monitor the movement of the interface if a diffusion inequality existed between zinc and copper. In this set up the concentration gradients are the driving forces for zinc diffusion out of the brass and copper diffusion into it. It was found that during the anneal the molybdenum wires migrated towards the center of the metal composite. This was the first time experimental evidence had shown that when the driving forces are held constant for diffusion there still can exist an inequality in movement. It was found that zinc diffuses out of the brass faster than the copper diffusing into the brass center by the observation of the molybdenum wire migration towards the center of the metal ingot described pictorially in figure 6.2[158].

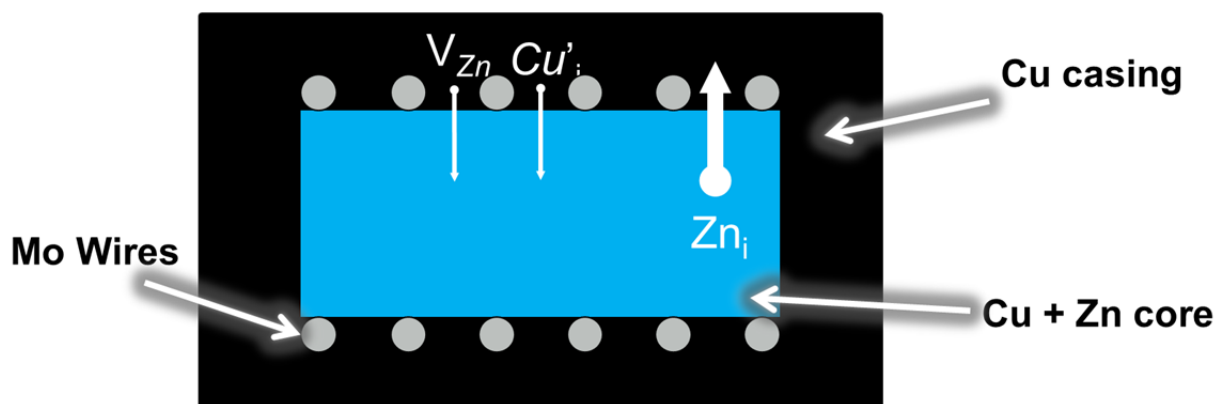


**Figure 6.2-** Original Kirkendall diffusion experiment of a brass ingot encased in a copper coating with Molybdenum wires at the surface for diffusion tracking.

It is believed that there is an inequality in diffusion across a boundary layer in nano energetics. Therefore an investigation was conducted to implement the Kirkendall experiment at the nanoscale. Figure 6.3 describes an idealized experimental design where an oxide and a reactive metal are placed in intimate contact with one another while an inert marker is placed at the interface. The expected experimental outcomes are straightforward. If the metal diffuses faster through the terminal oxide than oxygen transverses through the terminal metal, the marker position would be expected to be at the boundary between the original metal and terminal oxide. Conversely if the oxygen undergoes atomic movement

faster than the metal the marker should reside at the terminal metal and terminal metal oxide interface.

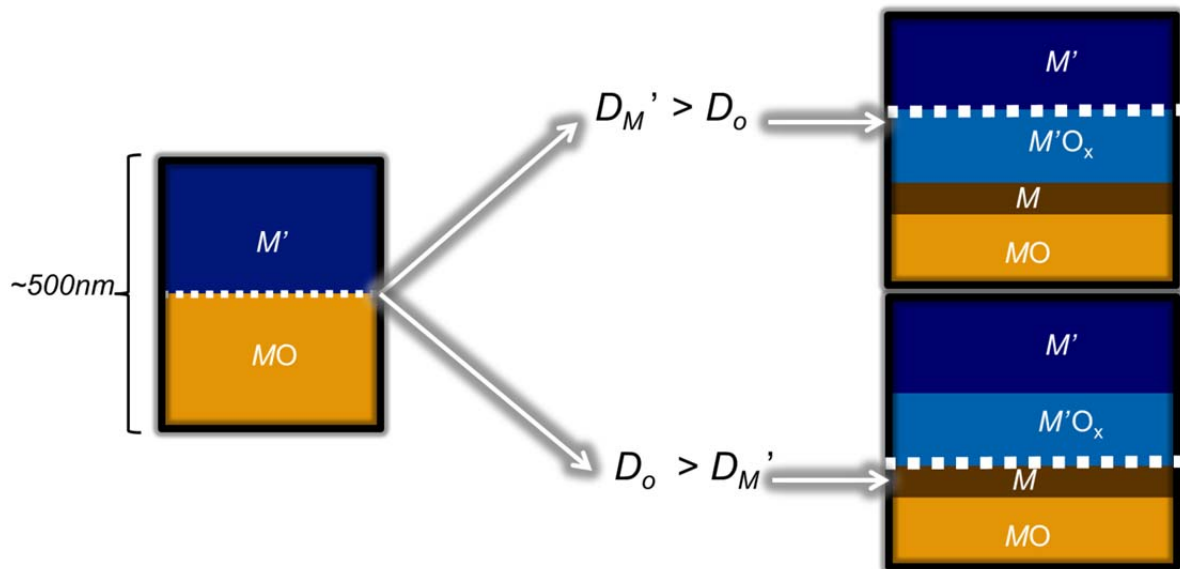


**Figure 6.3-** Schematic of the idealized Nano-Kirkendall Experiment.  $M'$  and  $MO$  are the original metal and metal oxide respectively.  $M$  and  $M'O_x$  are the terminal metal and terminal oxide respectively.

## 6.2 Diffusion Marker Deposition

The Kirkendall experiment was a macroscopic observation of a behavior originating from nano sized origins. Transposing these same ideas at the nanoscale provides its own unique challenges that must be overcome before any diffusion can be observed. Before the diffusion marker is laid at the interface the proper material for diffusion tracking must be selected and several criteria must be met. The diffusion marker must:

- be dimensionally smaller than the length scale in which diffusion is to occur
- not chemically react with any of the constituents
- not participate in diffusion itself
- not degrade under the thermal conditions diffusion is to be observed at

A literature review was conducted to determine the compatibility of potential marker materials with Al, Zr, Cu and their respective oxides. The list of candidate marker materials is sparsely populated from these constraints and under the current material systems utilized by the nano energetic community.

### 6.2.1 Nano Particle Deposition

The preliminary attempt at the nano Kirkendall experiment employed the use of two nano particle dispersions: nano diamond and nano gold. Both gold and diamond do not react with any of the products or reactants, they are thermally stable in the temperature regimes oxidation is to occur, and they can be prepared with dimensions smaller than that of which diffusion is to be observed.

The material system chosen was the copper oxide zirconium thermite mixture. The methods of interface observation involved copper oxide sputter deposited on silicon substrates at a thickness of 100 nm followed by the deposition of the inert markers then the coating of a layer of reactive metal on top of this ensemble. A cross-section of the reacting interface

would be prepared by focused ion beam milling (FIB) followed by subsequent thinning in preparation for transmission electron microscope (TEM) observation. In order for this procedure to be successful an idealized marker surface density is required for adequate diffusion marking capabilities to be realized. Specifically, the nanoparticles must be deposited on the surface with a uniform spacing that is neither too close as in the case of agglomeration or spaced too far apart. This spacing constraint is crucial in guaranteeing that any location on the sample that is formed into a TEM sample will contain a marker to track diffusion. Typical TEM samples prepared by focused ion beam milling have rectangular dimensions of roughly 15  $\mu\text{m}$  in length, 10  $\mu\text{m}$  in height, and a desired thickness of no more than 100 nm to ensure optimal electron transmission for imaging. This experimental constraint therefore dictates the separation of nano particles to be 100 nm or less.

Another parameter that must be considered in the design of the nano Kirkendall experiment is the relative roughness of the interface between the two reactants. Due to the nature of thin film deposition the roughness scales with the thickness where thicker films are rougher. See appendix A for a more in depth analysis of different thickness copper oxide films.

The bilayer thickness of the metal/metal oxide diffusion couple should be on the order of a typical bilayer spacing that was used in chapters 3 and 4 which are between 150nm to 1  $\mu\text{m}$  to accurately probe atomic motion in thermite nanolaminates. Deposition of thin films via sputtering yields rougher films as thickness increases (see appendix A) therefore thinner bilayer thicknesses are preferred to preserve the integrity of a smoother interface. The thinner bilayers reported were around 200nm. If diffusion on this length scale should be observed in this experimental design, nanoparticles 50 nm in diameter or smaller and spaced 200nm apart would be the optimal scenario for observing diffusion at the interface of copper oxide and reactive metal.

Deposition techniques for both nanoparticles involve properly dispersing the nanoparticles in a solvent. For the gold nanoparticles, a commercially obtained solution of 15 nm diameter particles was diluted with deionized water and filtered with a cellulose-based filter paper

with a pore size of 0.45  $\mu\text{m}$ . Three concentrations were employed to observe how the particles deposited upon copper oxide surface. It is noted that as concentration increased the transparency of the solution decreased significantly. No light transmission experiments were done. The three different concentrations of nano gold were solution cast onto a polymer spin coating machine at 3000 RPM for 60 seconds. The samples were left to dry over night in a vacuum hood. The dried samples were then imaged using atomic force microscopy (AFM) to ascertain average particle size and particle separation distance. The results from this experiment are visually seen in figures 6.4, 6.5, and 6.6 where particle sizes are 30 nm, 125 nm, and 600 nm for the low, medium, and high concentrations respectively. It is also noted that the separation distances decrease as concentration is increased from 3  $\mu\text{m}$  down to 500 nm. This particle size and separation trade-off is counterproductive to the end goal of having an optimal density and small particle size for the Kirkendall experiment.

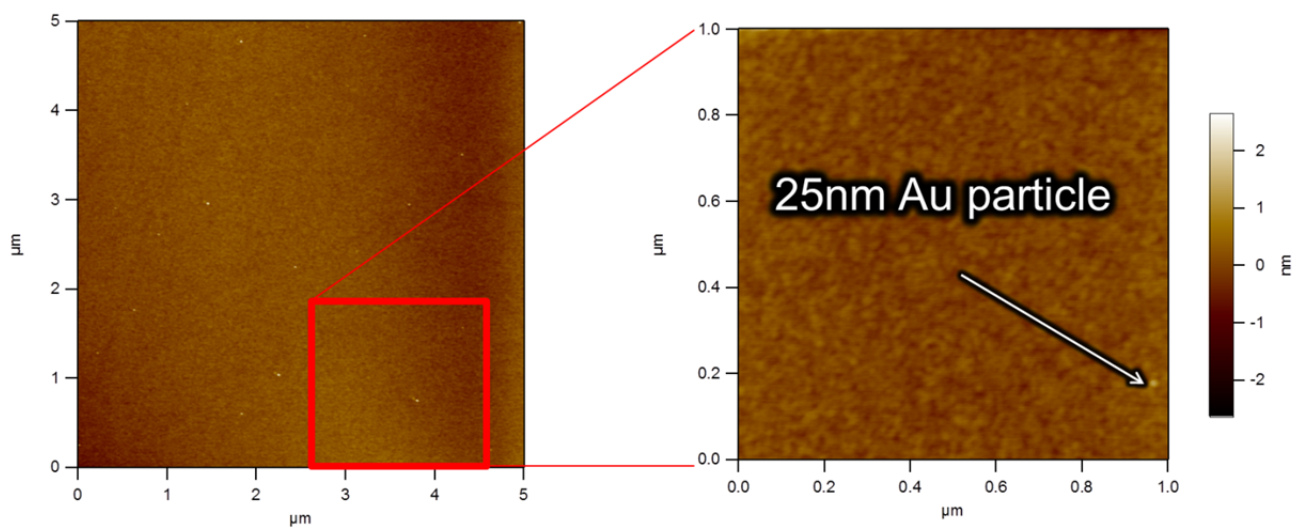


**Figure 6.4-** Au nanoparticles deposited on CuO at the lowest concentrations

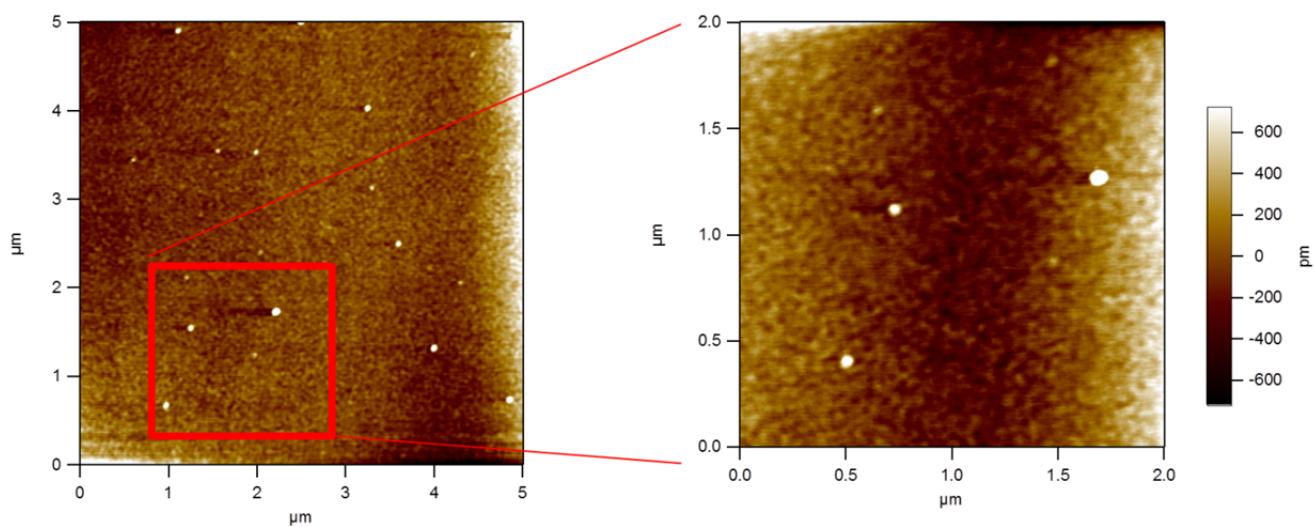


**Figure 6.5-** Au nanoparticles deposited on CuO at the medium concentration

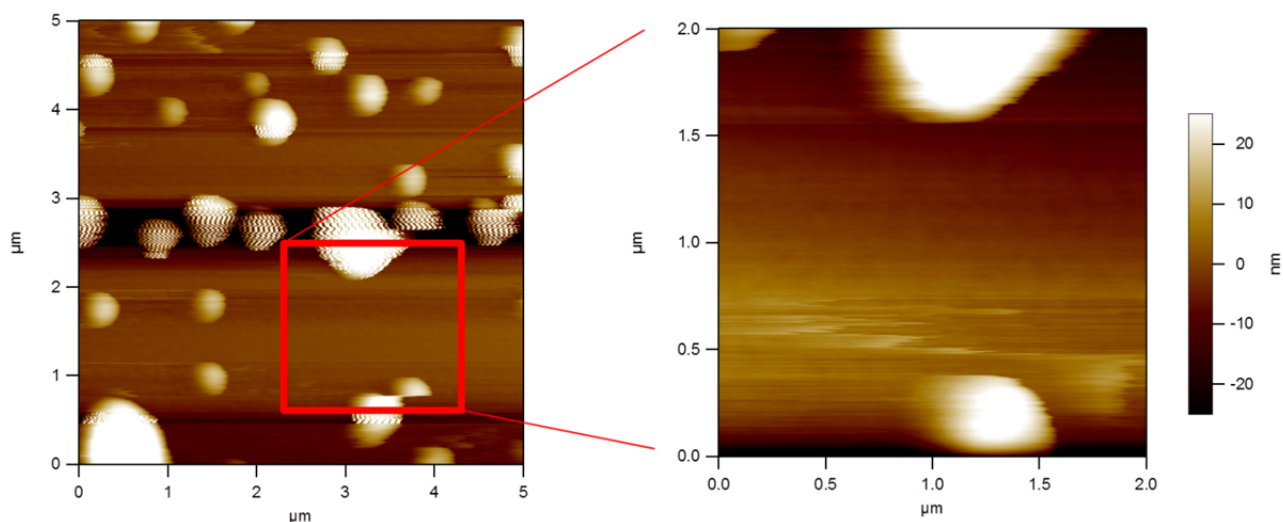


**Figure 6.6-** Au nanoparticles deposited on CuO at the highest concentration

Toluene was then added to the higher concentration solution of nano diamond in an attempt to decrease the agglomerated particles sizes while maintaining optimal separation distance. As can be observed in figure 6.7, the average particle separation distance stays more or less the same as a high concentration of nano gold without toluene but the size decreases substantially but are much too large to be employed in a thin-film diffusion experiment with an average particle size of around 350 nm.

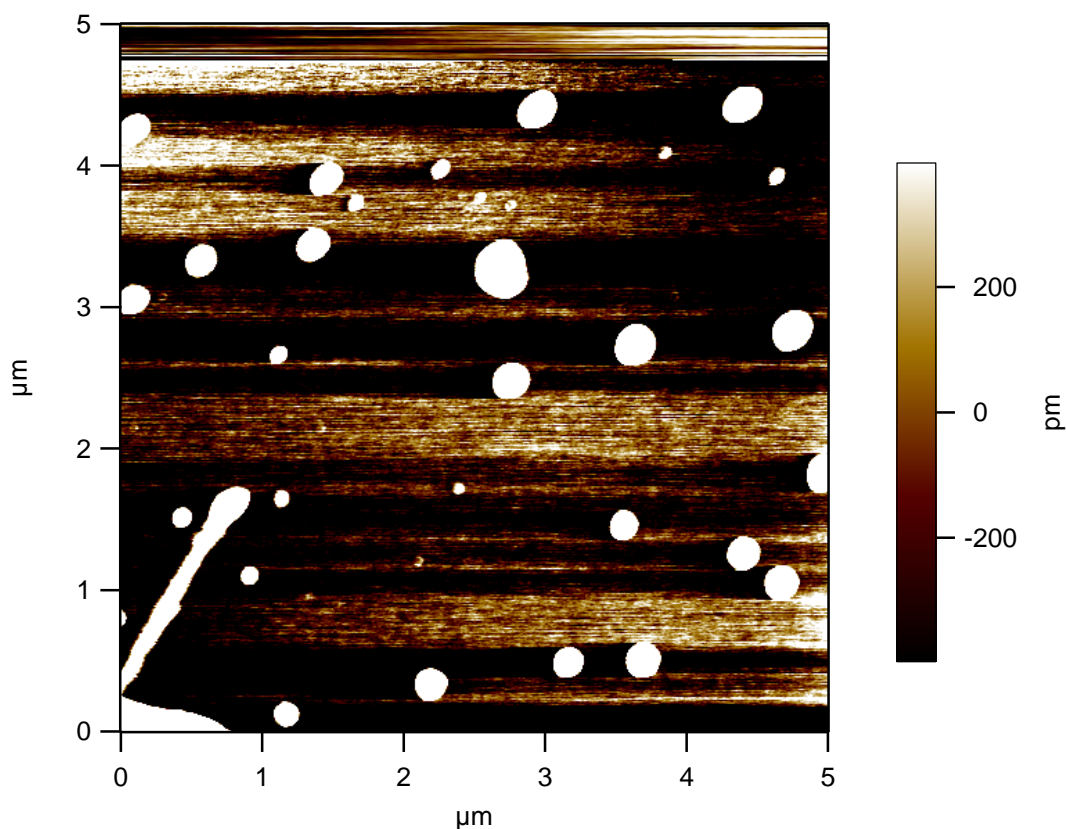


**Figure 6.7-** AFM micrograph of nano-gold particles that had been cast onto a copper oxide thin film from a toluene solution in an attempt to decrease particle size and maintain particle spacing.

Nano diamond particles were used in the same experimental procedure with similar results. Another avenue of particle dispersion was then sought after by way of polymer dispersants. Three polymers that were chosen readily dissolve in water: Polyvinyl acrylic acid (PAA), polyethylene oxide (PEO), and polyvinyl pyrrolidone (PVP). Each polymer was placed into beaker with a stir bar filled with water to obtain one weight percent polymer. PEO and PVP readily dissolved overnight however the PAA created a gel at one weight percent and was discarded from this study. In each polymer dispersion one volume percent of nano diamond solution was added and solution cast onto copper oxide films in the same manner nano gold was. It was found through AFM that both polymer solutions increase the agglomeration of the nanoparticles and had a deleterious effect on surface roughness. At this

point in the study it was deemed more fruitful to investigate other methods of inert marker deposition.

## **6.2.2 Electron Beam Deposited Platinum Diffusion Markers**

In the semiconductor industry focused ion beam and electron beam deposition techniques are used routinely to create contacts between semiconductor components with tight control over deposited geometries with nanometer resolution. It was then decided to borrow this technique of deposition and employ it for usage of diffusion tracking. The equipment used for the remainder of the study was a dual beam secondary electron microscope (SEM) coupled with a focused ion beam (FIB) from FEI. The methodology to deposit metallic species on a surface via electron or ion beams is schematically represented in figures 6.8a and 6.8b. In this methodology the operator illuminates a specific area to be deposited upon with either the electron beam or ion beam. Methylcyclopentadienyl trimethyl platinum, a metal organic gas, is a gaseous platinum source in this case is introduced close to the sample surface with a gas injection needle. The metallic gaseous precursor is comprised of a metal atom that is dispersed in a gaseous phase with volatile functional groups attached to it similar to sol-gel precursors. When the metallic source molecules interact with the illuminated region of the sample the energy of the beam breaks off a carbonaceous material from the metal which then deposits on the surface of the sample.

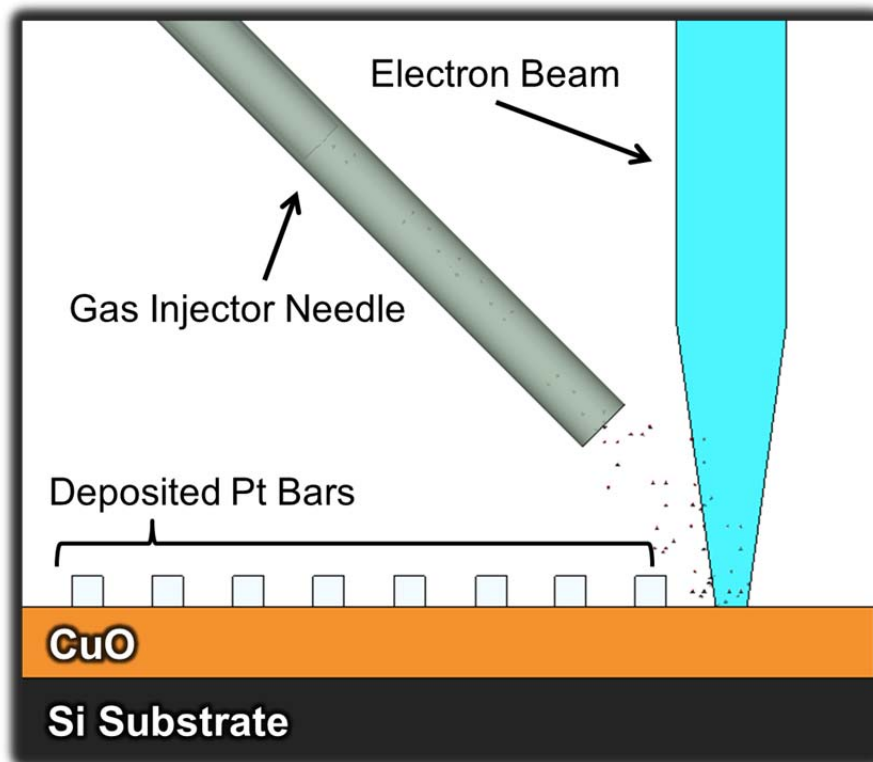


**Figure 6.8a-** Diagram of Pt deposition via e-beam deposition

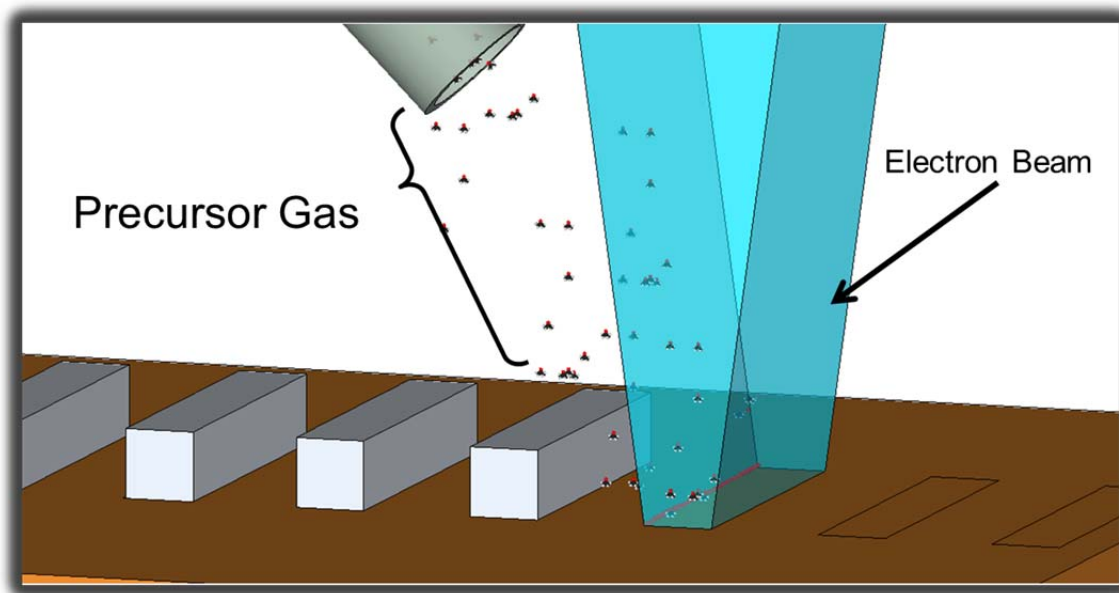


**Figure 6.8b-** Diagram of Pt deposition via e-beam deposition

For this study it is desired to have a series of platinum bars spaced evenly across a copper oxide thin film surface roughly 100-200 nm apart in order to be observed after preparation for transmission electron microscopy which dictates the majority of the constraints for this experiment.

### **6.2.2.1 Sample Tracking**

In order to prepare a TEM nano Kirkendall sample via vapor deposition of inert markers the experimenter must be vigilant in the tracking of the sample position, orientation, and integrity throughout the preparation process. The deposited platinum bars are only feasibly created with a maximum of micron sized features that are difficult to locate even in an electron microscope on a macroscopic (millimeters) sample without a hierarchy of identification features increasing in size. The first approach used created an asymmetric pattern of shapes that were subtractively milled out (figures 6.9,6.10) of the sample surface with the gallium ion beam at elevated currents (30nA). The asymmetry of the design allowed for the manipulation of the sample without the orientation of the deposited platinum being skewed. It is desired during the implementation of the Kirkendall experiment to leave the interface between the two diffusing species as unmolested as possible from the inert marker placement. It was then unfortunately discovered that while the milling out of asymmetric features from the sample surface successfully identified the position and orientation of the deposited platinum it also significantly changed the surface morphology of the copper oxide thin film as seen in the successive SEM micrographs in figure 6.11a, 6.11b, and 6.11c.

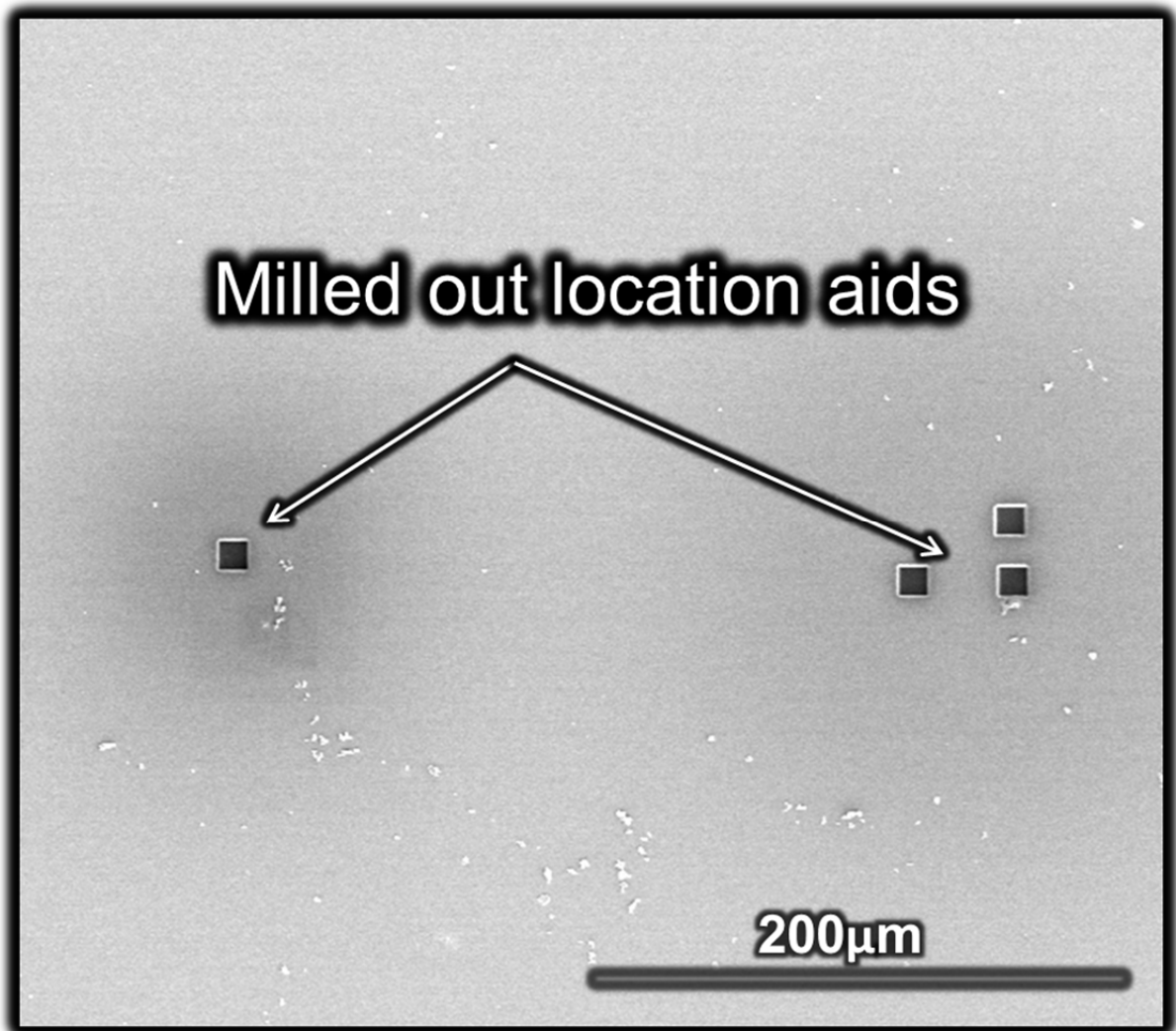


**Figure 6.9-** SEM Macroscopic view of asymmetric milled out location aids.

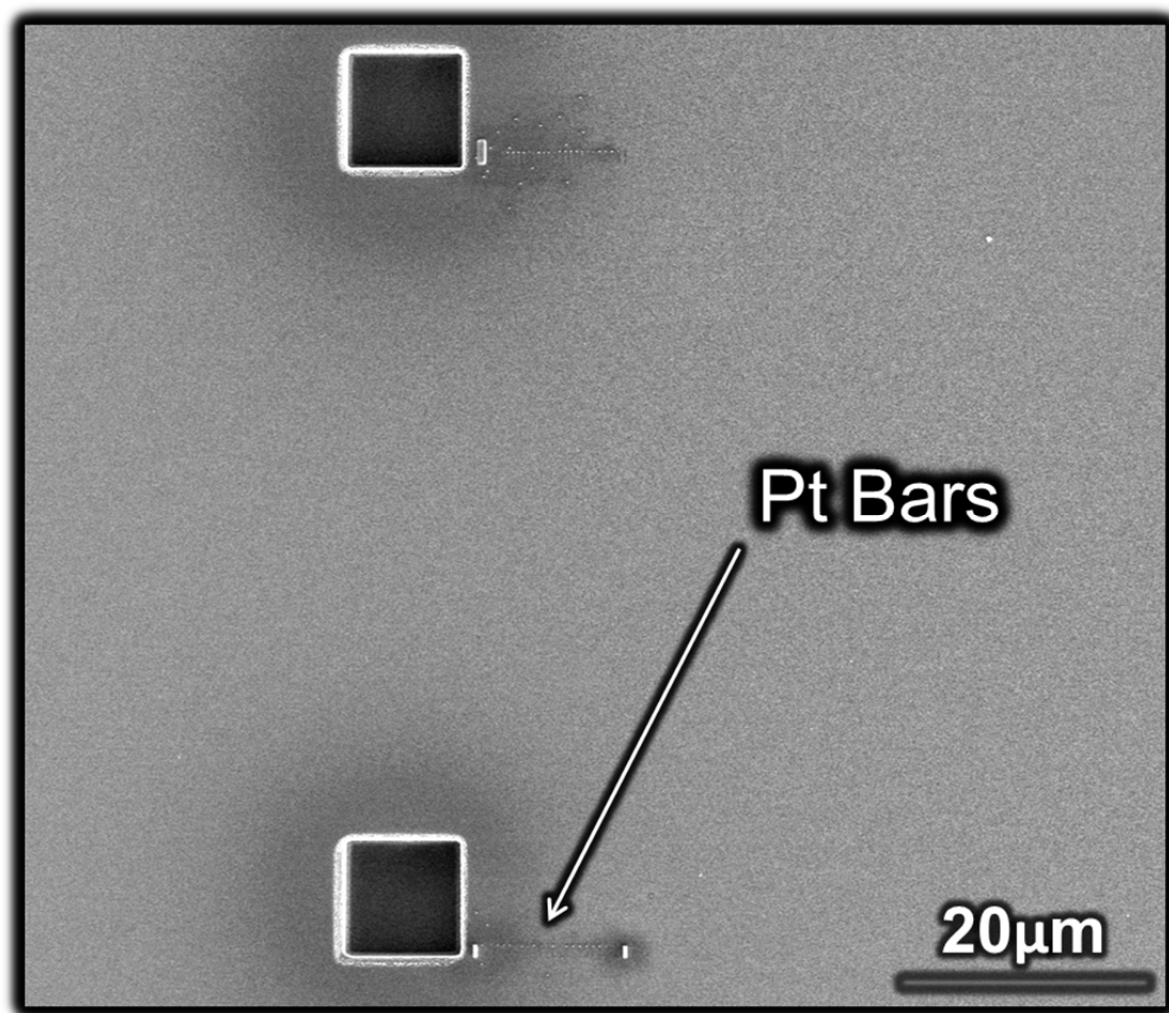


**Figure 6.10-** SEM micrograph view of asymmetric milled out location aids with Pt diffusion markers located next to them.

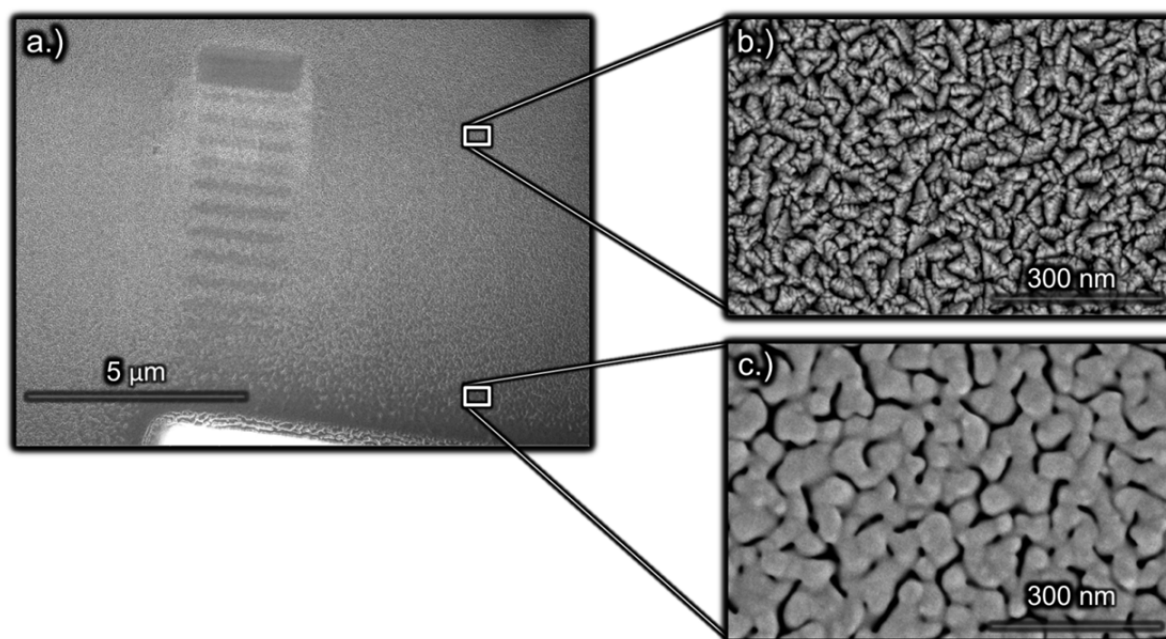


**Figure 6.11-** a.) SEM micrograph of surface damage done to CuO thin film. b.) undamaged microstructure 5  $\mu\text{m}$  away from the milled feature, c.) altered morphology due to milling 1  $\mu\text{m}$  away from milled feature.

Copper oxide thin films when unperturbed by the ion beam have a morphology of a faceted structure in 6.11b, however the copper oxide surface closer to the ion milled feature shows considerable ion damage to the surface with a morphology that has an extremely distorted crystal structure. This damage is counterproductive if diffusion properties are to be observed because diffusion can depend on crystal structure. If the starting material to be used in a diffusion experiment differs from what the original material diffusion occurs in whatever result is obtained wouldn't be characteristic of what actually occurs. In order to circumvent the surface damage that the ion milling created a micro scratching technique was used by scribing the copper oxide surface with a diamond scribe typically used for cleaving semiconductor substrates. This scribing method of sample identification minimally damaged the sample surface in the surrounding area of the scribe and allowed for ease of sample

relocation as seen in figures 6.12 and 6.13. This scribing method proved successful in locating the general area where platinum bars deposited and exact sample location was then denoted by the deposition of two thick platinum markers on either side of the diffusion markers in the center that can be seen in figure 6.14. The purpose of these flanking thick platinum bars is not for diffusion but for sample preparation. These larger platinum bars mark the beginning and end of where diffusion is to be observed and assists in TEM sample preparation, namely these flanking platinum bars indicate where the protective coating of sputtered platinum should be laid out in order to not damage the interface of interest during the thinning process.

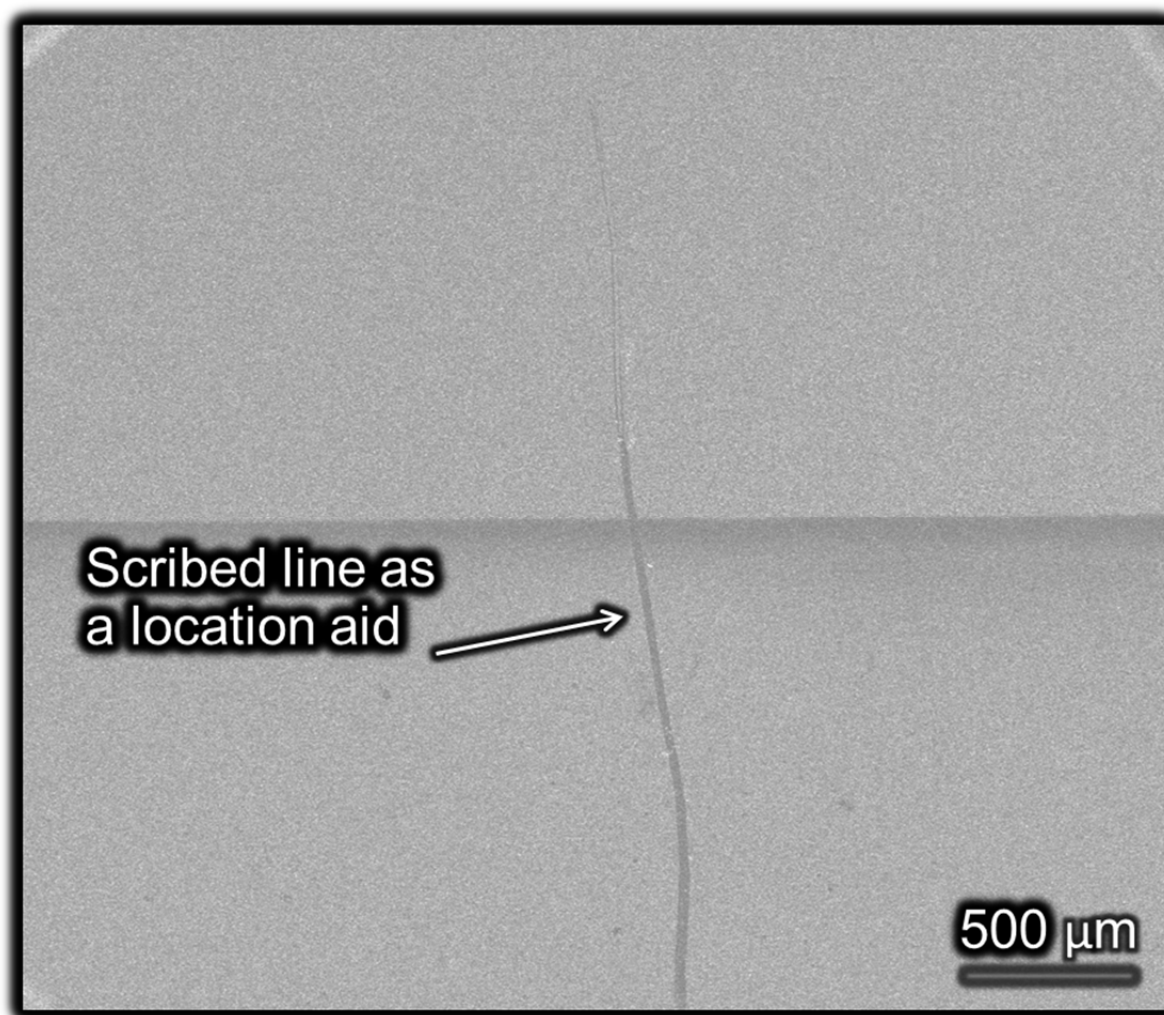


**Figure 6.12-** SEM micrograph of CuO film scribed for purposes of sample location identification.

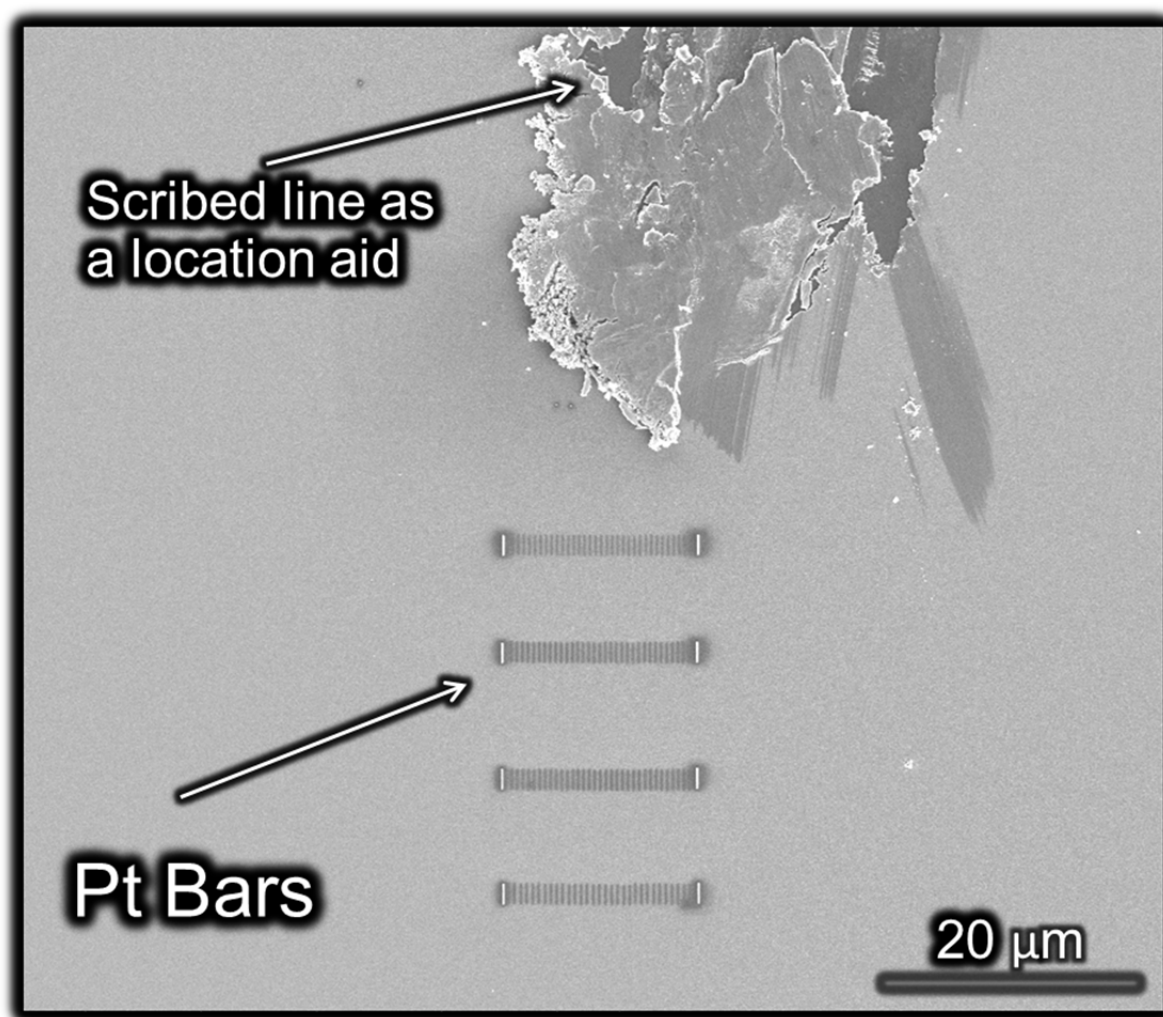


**Figure 6.13-** SEM micrograph of Pt bars deposited near the scribed location on CuO.

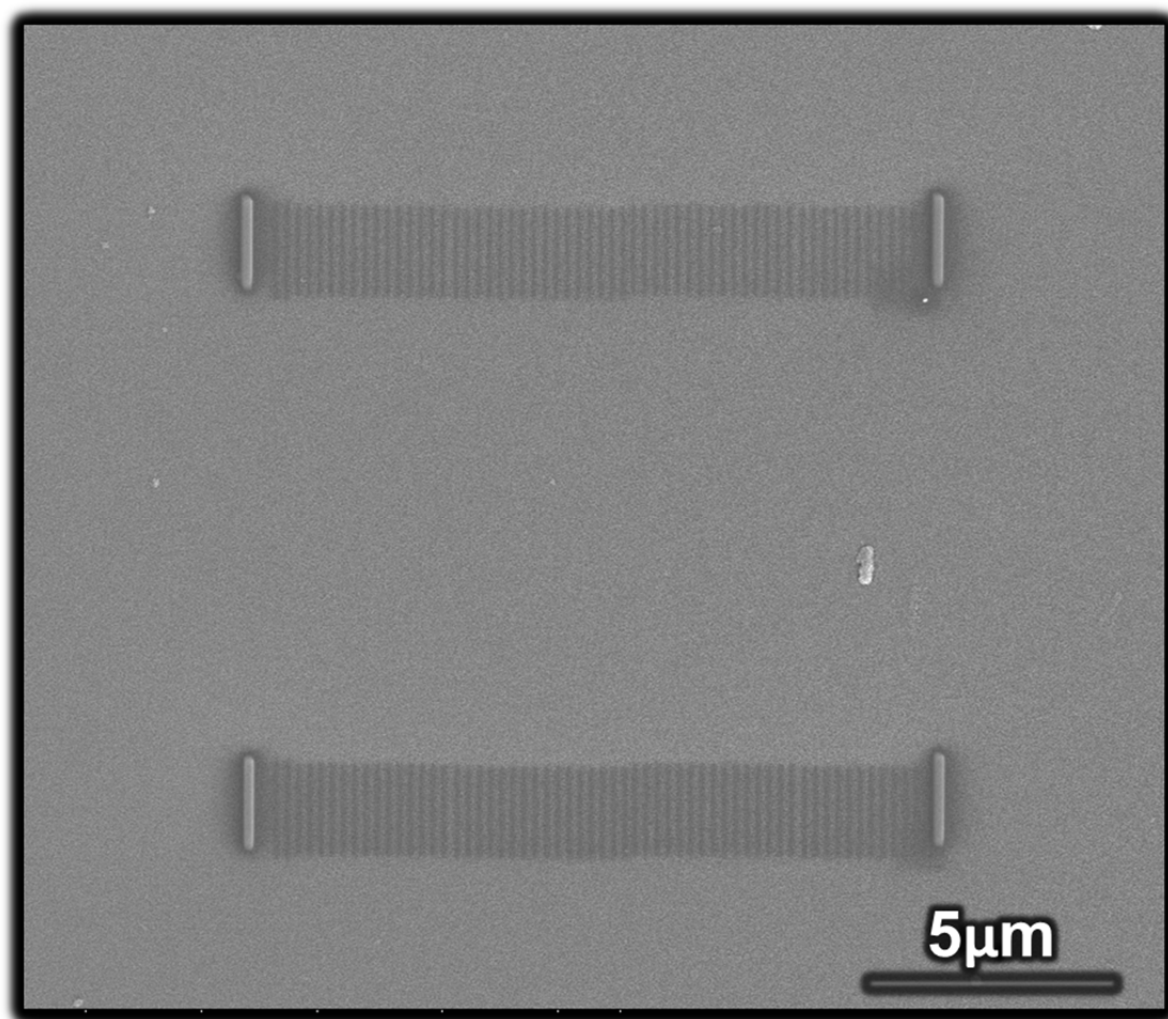


**Figure 6.14-** SEM Micrograph of Pt Identification markers flanking diffusion markers on CuO.

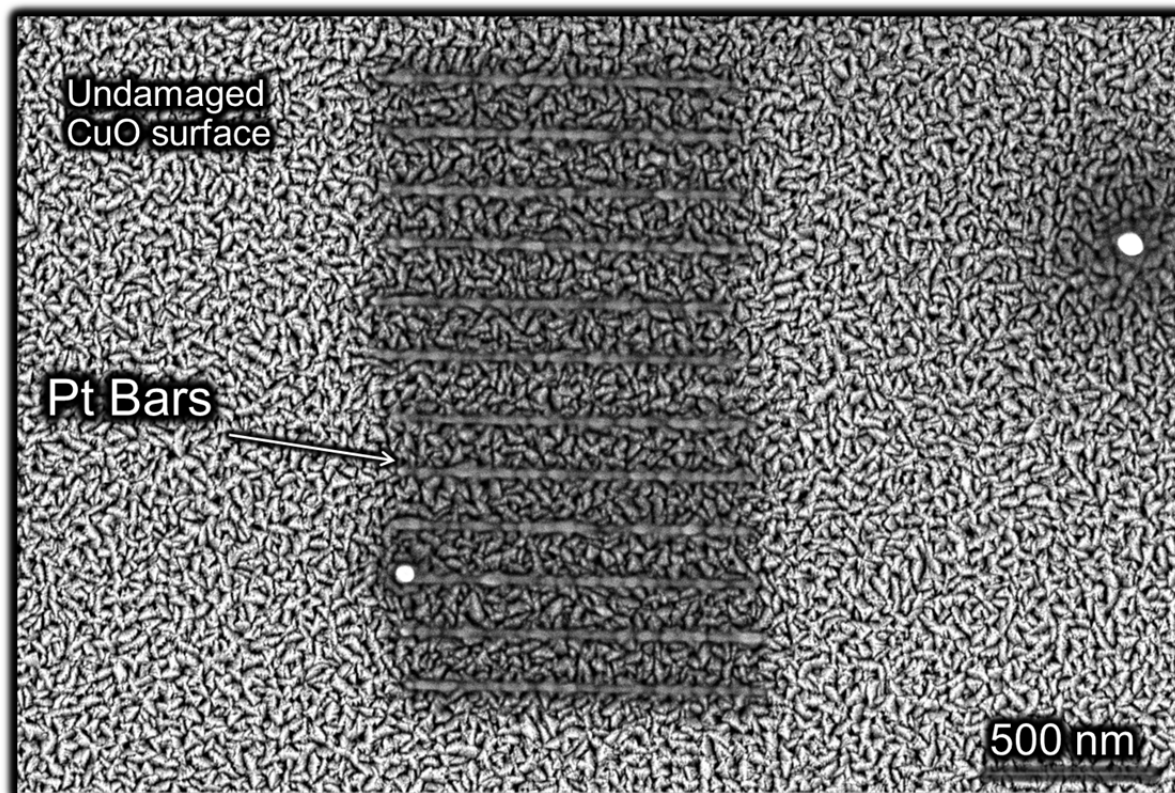


**Figure 6.15-** SEM micrograph of e-beam deposited Pt bars on an undamaged CuO surface.

### 6.2.2.2 Platinum Deposition Technique

The parameters to deposit platinum with nano sized dimensions are more or less well understood however to the author's knowledge it has not been implemented extensively for the use of diffusion tracking. Therefore a short platinum deposition assay experiment was conducted to determine the optimal conditions that platinum can be deposited on the copper oxide surface in a timely manner that does not readily damage the surface. Table 6.1 shows the methodology and parameters implemented in the machine with corresponding input values and actually measured values by a secondary technique via SEM and AFM. The nature of this experiment requires as smooth of an interface as possible which then subsequently necessitates a thinner film geometry. The architectures that were desired to observe diffusion employ thin films with a limiting thickness of 300 nm. As was previously discussed in this chapter the marker must be small in the order of diffusion that is

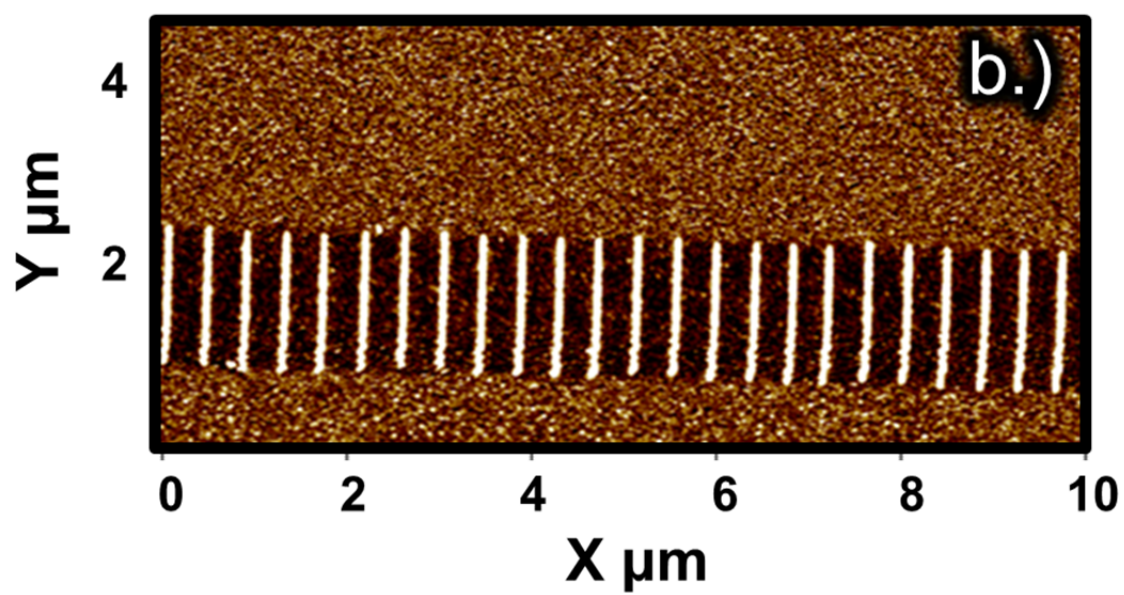
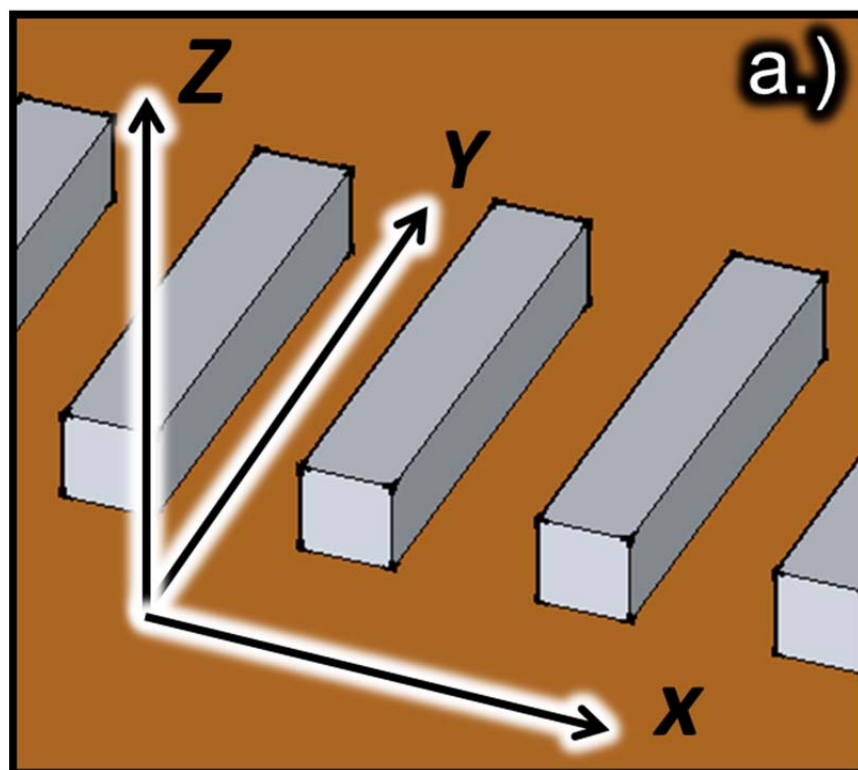
going to be observed therefore the marker size should be no larger than 50 nm and would be desirable if it's dimensions could be pushed smaller than that. The results in the deposition assay experiment point to the optimal deposition conditions of 5 kV 13 pA under the line deposition geometry. With an average thickness of 24 nm and height of 20nm which can be visualized from figures 6.14 and 6.15 this is the deposition recipe chosen for optimal marker deposition. More details about the nuances of platinum deposition and TEM sample preparation can be found in appendix B.

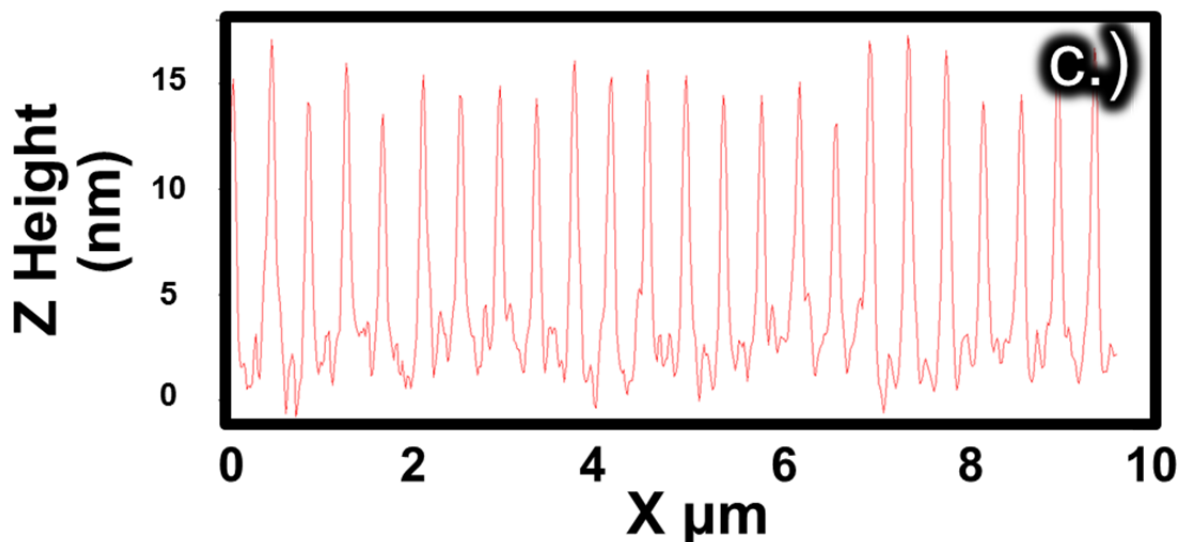
**Table 6.1-** Input parameters for E-beam deposited Pt

Deposition Function	Type	Input Height[nm]	Input Width [nm]	Measured Width	L[um]	Notes
Pt dep Surf	Rectangle	10	10	39	1	Left to Right
Pt dep Surf	Rectangle	10	10	34	1	Right to Left
Pt dep Surf	Line	n/a	10	25	1	100nm spacing
Pt dep Surf	Line	n/a	10	23	1	200nm Spacing
Pt dep Surf	Rectangle	10	10	47	1	Bottom to top
Pt dep Surf	Rectangle	10	10	41	1	Top to Bottom
Pt dep Surf	Rectangle	10	10	51	1	Right to Left

### 6.3 Pt deposition Results and Discussion

The results from the optimization of the inert marker deposition allowed for precise deposition of platinum wires on copper oxide thin film as seen in figure 6.16a,6.16b,and 6.16c with a spacing of 200 nano meters in separation with a height and width of 15 nm and 25 nm respectively as confirmed by AFM.





**Figures 6.16-** a.) Schematic of Pt bars on CuO surface with orientation b.) AFM image of the lateral and horizontal dimensions of deposited Pt bars c.) AFM height retrace of the Pt bars overall dimension in the Z direction

Following the deposition of platinum bars the reactive metal was then deposited upon the ensemble. A TEM cross-section of this geometry was realized by focused ion beam milling followed by thinning lift out and attachments to a molybdenum TEM grid (details in appendix B). In order to compare diffusion across an interface in this manner pre-and post anneal micrographs are required in order to ascertain any scientifically relevant data. Figures 6.17, 6.18, 6.19, and 6.20 are the results of platinum bars at the surface interface of the CuO/Zr and the Cr/CuO systems. These two material systems were chosen to allow solid-state reaction to occur. Sample reaction temperatures macroscopically can be ascertained by previously gathered DSC data where zirconium and copper oxide thermite displays exothermic activity well below any of the constituents melting points, but the aluminum copper oxide system reacts above and below the low melting point of aluminum.

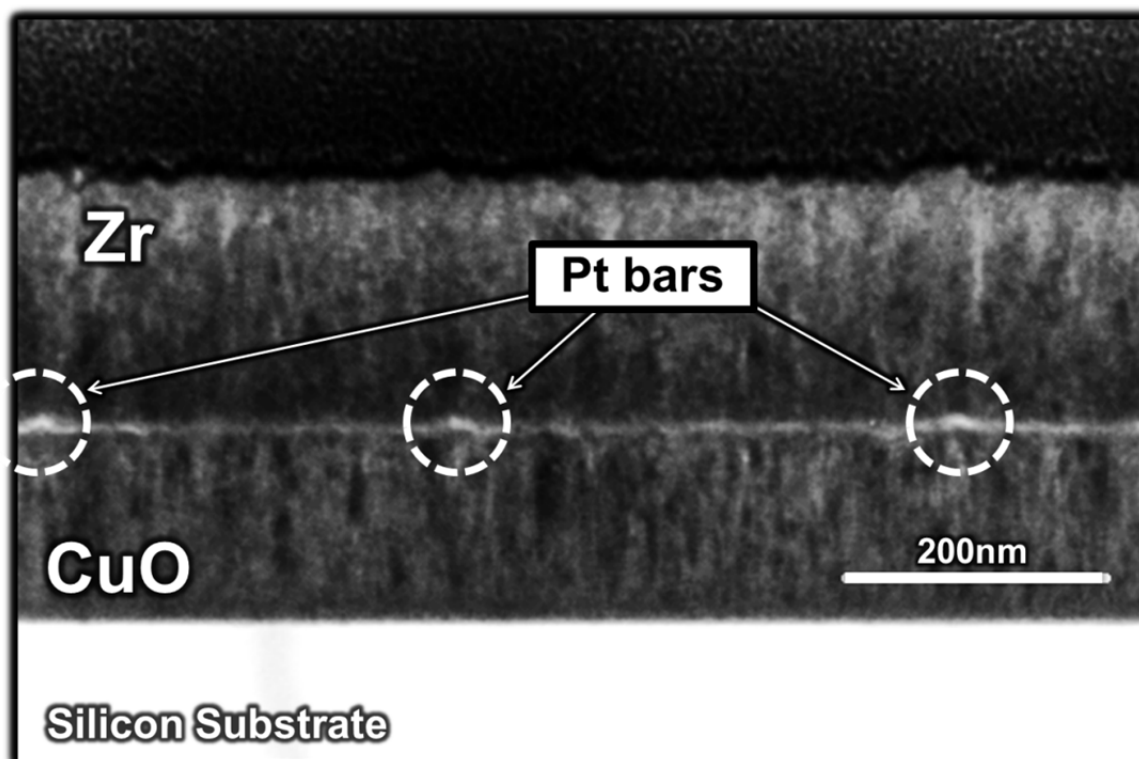


**Figure 6.17-** TEM cross-section of Zr/CuO interface with Pt diffusion markers

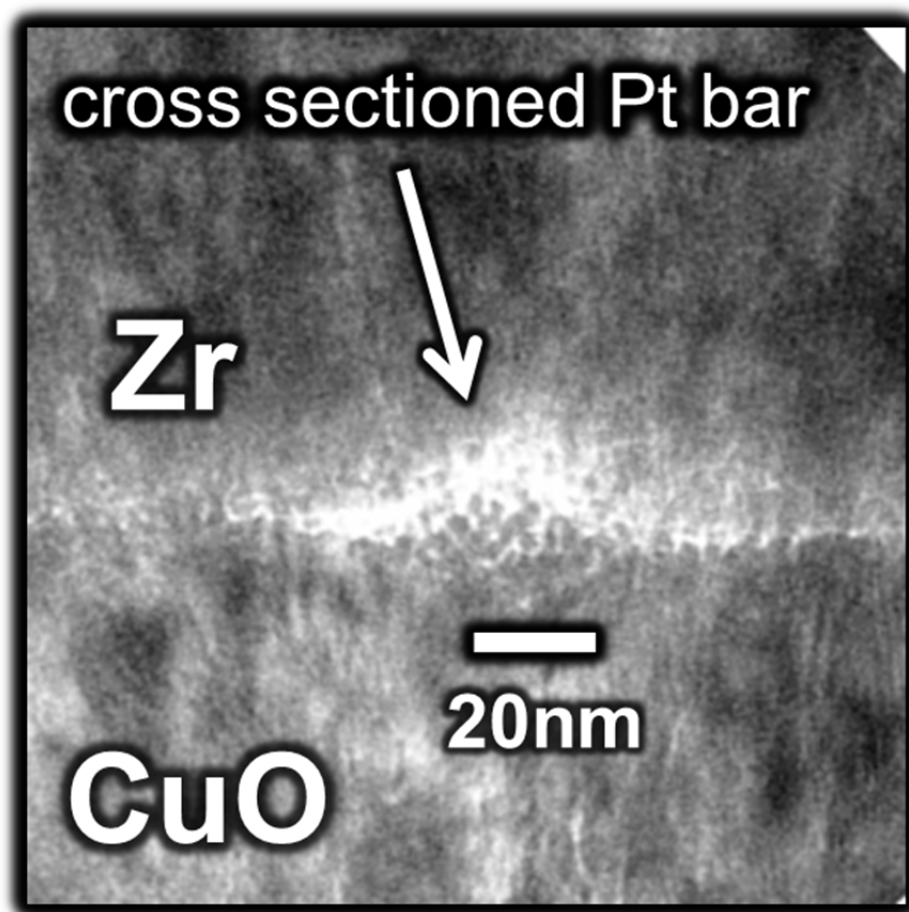


**Figure 6.18**-TEM cross-section of Zr/CuO interface with a bright Pt deposit 20nm in width

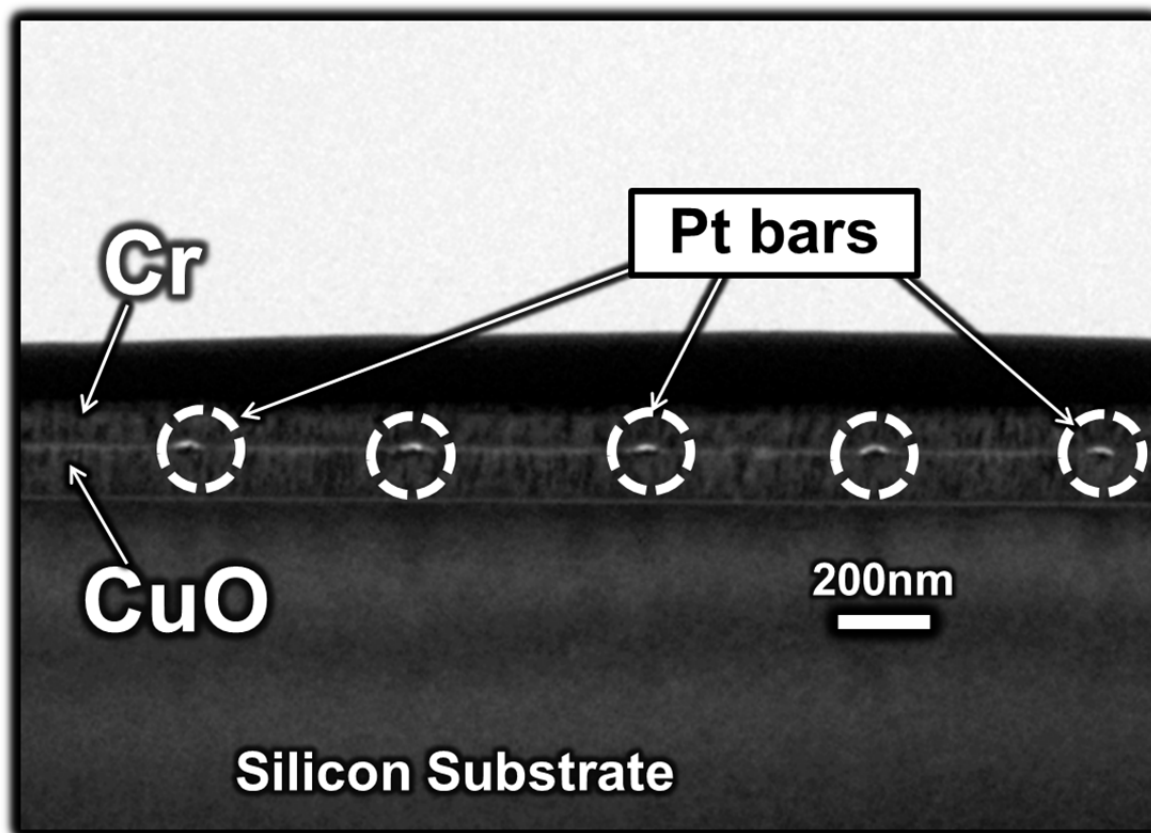


**Figure 6.19-** TEM cross-section of Cr/CuO interface with Pt bars between Cr and CuO layers

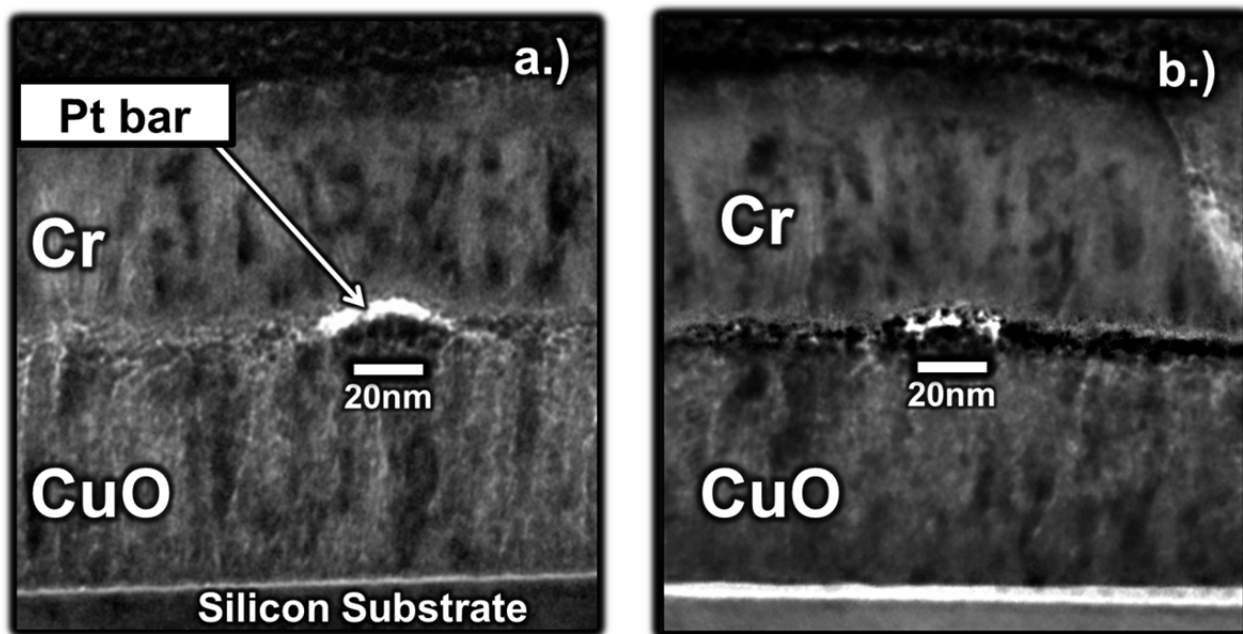


**Figure 6.20-** TEM cross-section of Cr/CuO interface with Pt deposit a.) after deposition b.) after a 1 year anneal at 25°C.

These two results show that platinum deposition is feasible potential diffusion marker. To track the progression of atomic transport a final thermal step is required to initiate a portion of the reaction at the interface. The difficulty in this experimental step presents itself in the uncertainty of how the microstructure changes as a function of temperature before complete reaction has taken place. The TEM sample on the molybdenum grid was then subjected to a controlled anneal in a differential scanning calorimeter for one hour at 500°C. Further inspection of interface post anneal for the zirconium copper oxide sample in figure 6.21 yields an interface that is devoid of the copper oxide thin film.

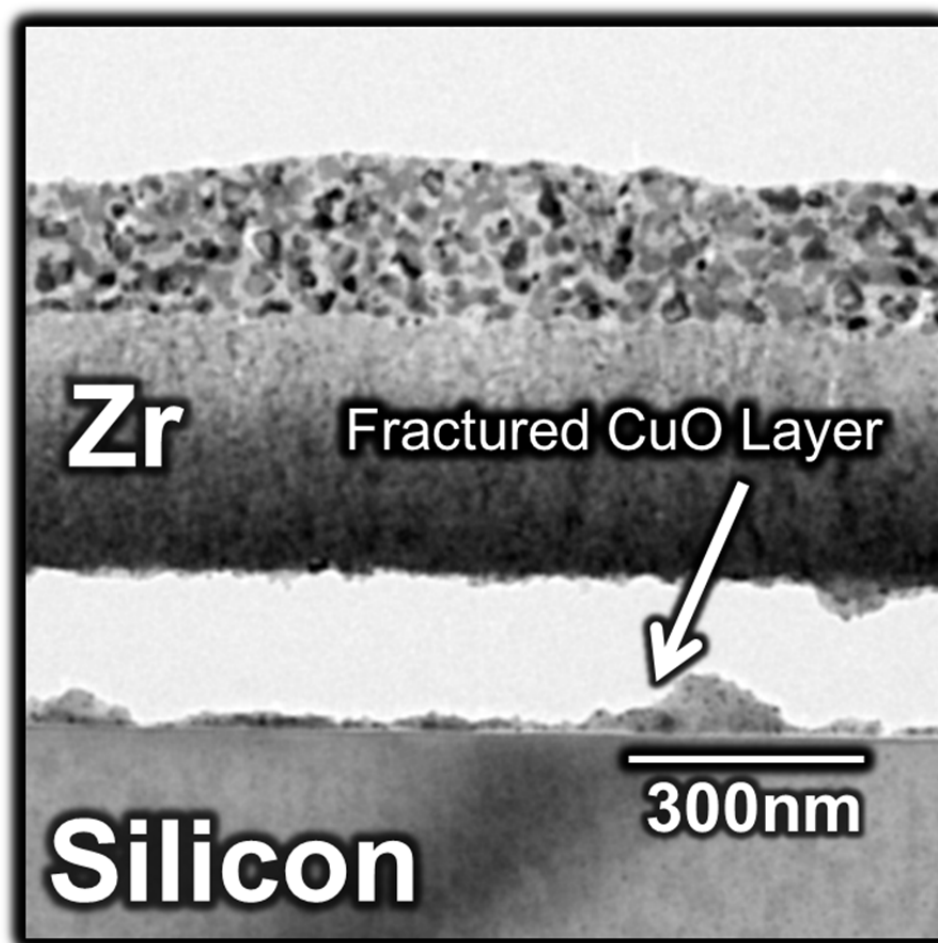


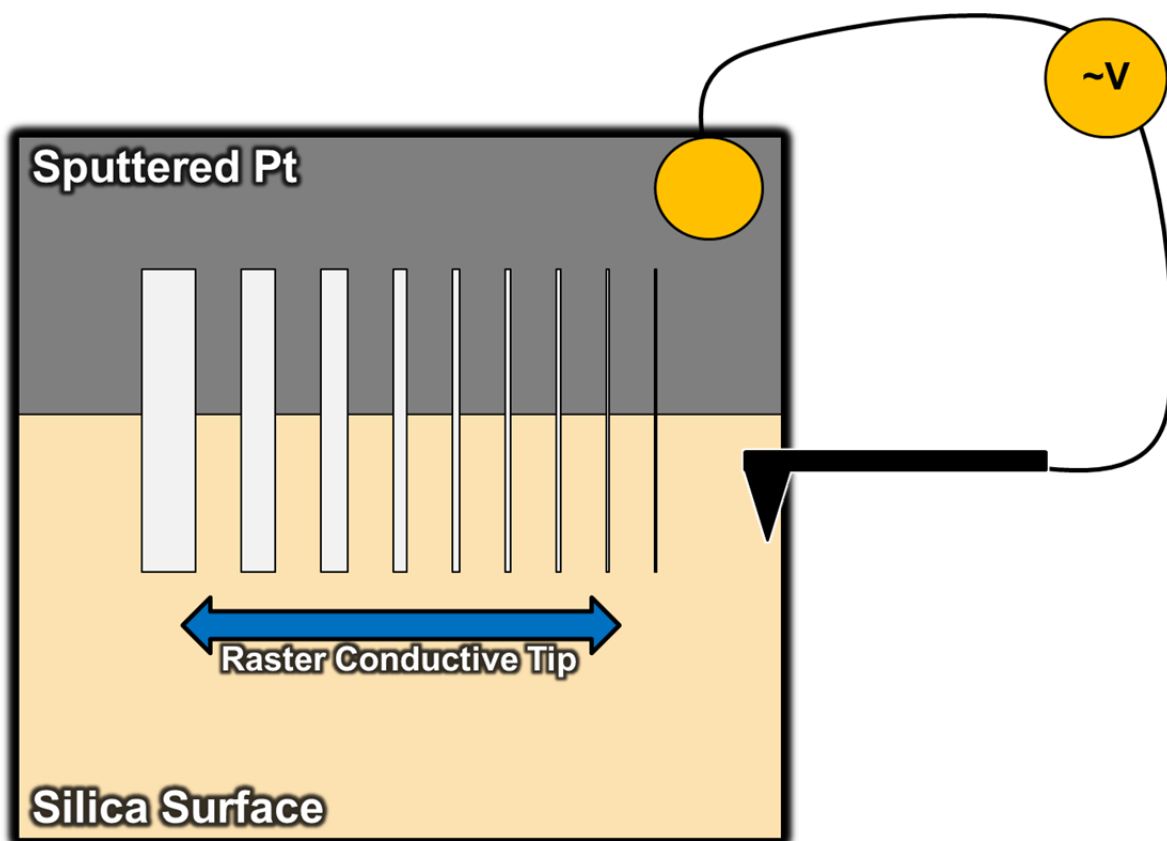
**Figure 6.21-** TEM cross-section of annealed Zr/CuO sample devoid Pt markers and of the CuO thin film layer

### **6.3.1 Pt Deposition via Focused Ion Beam and Focused Electron Beam**

Several reasons are possible for the lack of copper oxide film post the thermal treatment. The thermal stresses present in the thin 100 nm thick film may have caused enough stress to break apart the continuous copper oxide layer. Bulk copper oxide is stable at atmospheric conditions until it undergoes a phase change around 800°C to Cu<sub>2</sub>O, therefore no phase change should be observed in this heating regime. Upon further analysis of the TEM micrographs with the Zr/CuO and the Cr/CuO interfaces it is noted that these are taken in a bright field imaging setting. Brightfield TEM micrographs display contrast associated with atomic weight. This means that the heavier the element the darker it appears and the lighter the element the brighter it appears because more electrons can pass through. It then stands to reason that platinum would be darker than both copper zirconium and chromium because it is heavier. This however is not observed in the micrographs and the “platinum” markers are significantly brighter than any other portion of the sample. This then suggests the platinum being deposited via electron beam deposition at 5 kV 13 pA is not depositing a pure platinum marker but a carbonaceous platinum deposit. Conductive atomic force microscopy was then undertaken to measure the conductivity of the platinum bars. The reasoning behind this is that if the platinum deposits do not conduct and are insulating the carbon content of the platinum is high. If this is the case the carbonaceous contaminant portion of the tracer is likely to vaporize into gaseous products upon thermal treatment and have a destructive effect on the interface to be monitored. It was taken for granted up to this point in the experimental procedure of the nano Kirkendall investigation that the platinum originating from electron beam source was 100% platinum. The subsequent TEM micrographs suggest otherwise and a further deposition study was undertaken to measure the conductivity of the platinum bars deposited.

If the platinum bars are conductive then it stands to reason that there is minimal amounts of contaminant carbon compounds. In order to explore the conductivity of the platinum bars deposited a silicon substrate was annealed in air at 1200°C in order to create an insulating

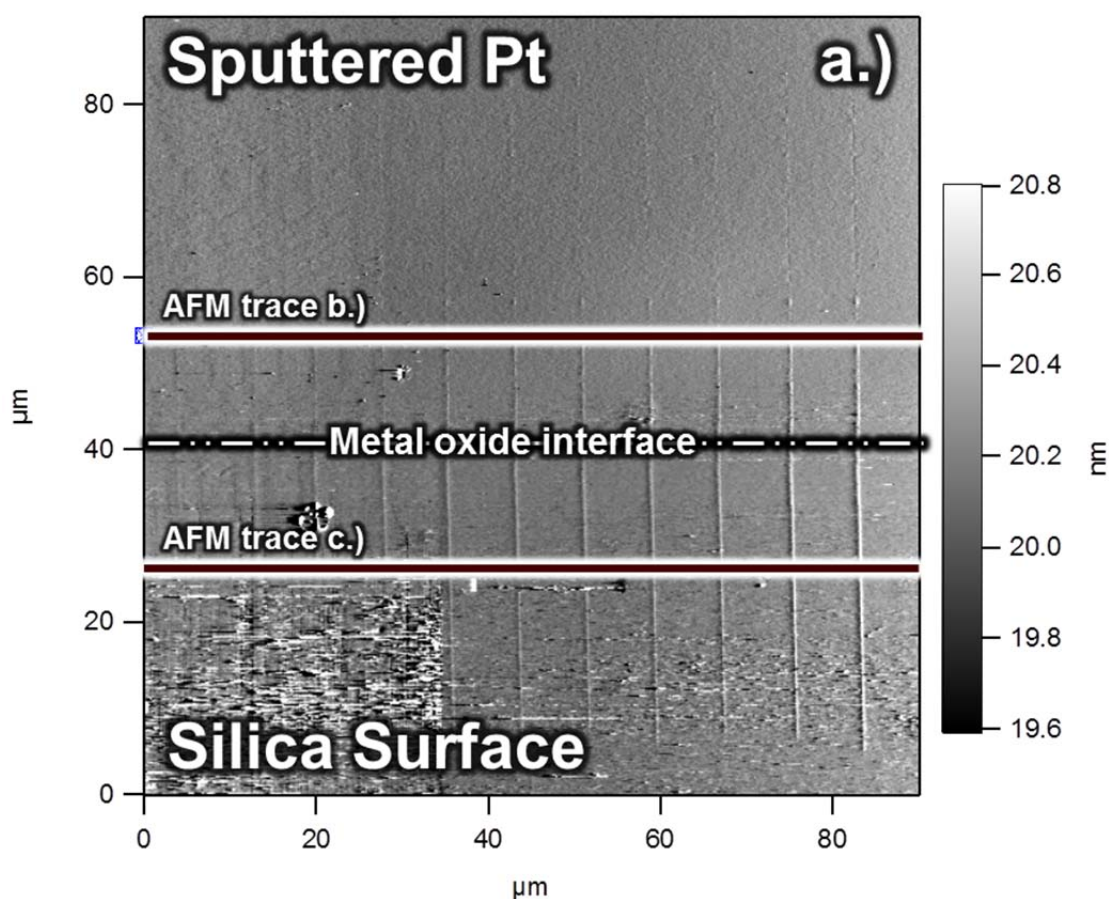
oxidized surface. Sputter deposited platinum was then placed on a third of the sample substrate and platinum bars were e-beam and ion beam deposited straddling the platinum-silica junction as depicted in the schematic in figure 6.22 .

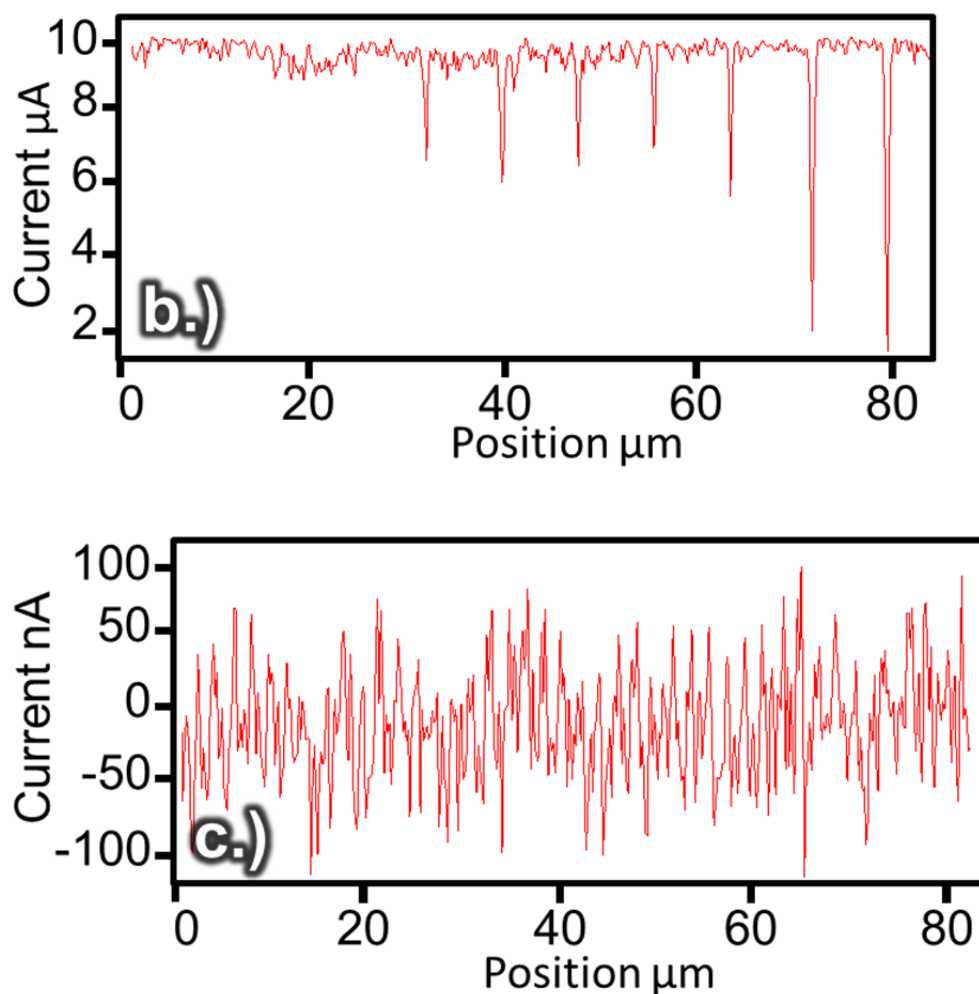


**Figure 6.22-** Infographic of conductive AFM experiment to check the quality of the Pt deposition

The sample was then biased with 10  $\mu$ -volts on the sputter deposited platinum surface with the conductive AFM tip tracing over the platinum bar features. From this technique a plot of current versus position can be obtained. If no current runs through the platinum marker the composition is most certainly heavily contaminated with a carbonaceous functional groups characteristic of that gaseous precursor used. A height retrace over the surface of e-beam

deposited Pt bars at the 5 kV 13 pA setting show the presence of the platinum bars in figure 6.23a. Line traces with the conductive AFM tip were done then to obtain information on the current through the Pt bars on the Sputtered Pt side and on the silica surface. Figure 6.23b corresponds to the trace done over the sputtered Pt surface. The trace reveals 10 $\mu$ A run through the majority of the scan until the tip tracked over the e-beam deposited locations where the current dips. Figure 6.23c corresponding to an AFM trace over Pt bars on the silica surface shows that this Pt is not ideally conductive and yielding a Pt deposit that contains considerable amount of carbon contaminants.

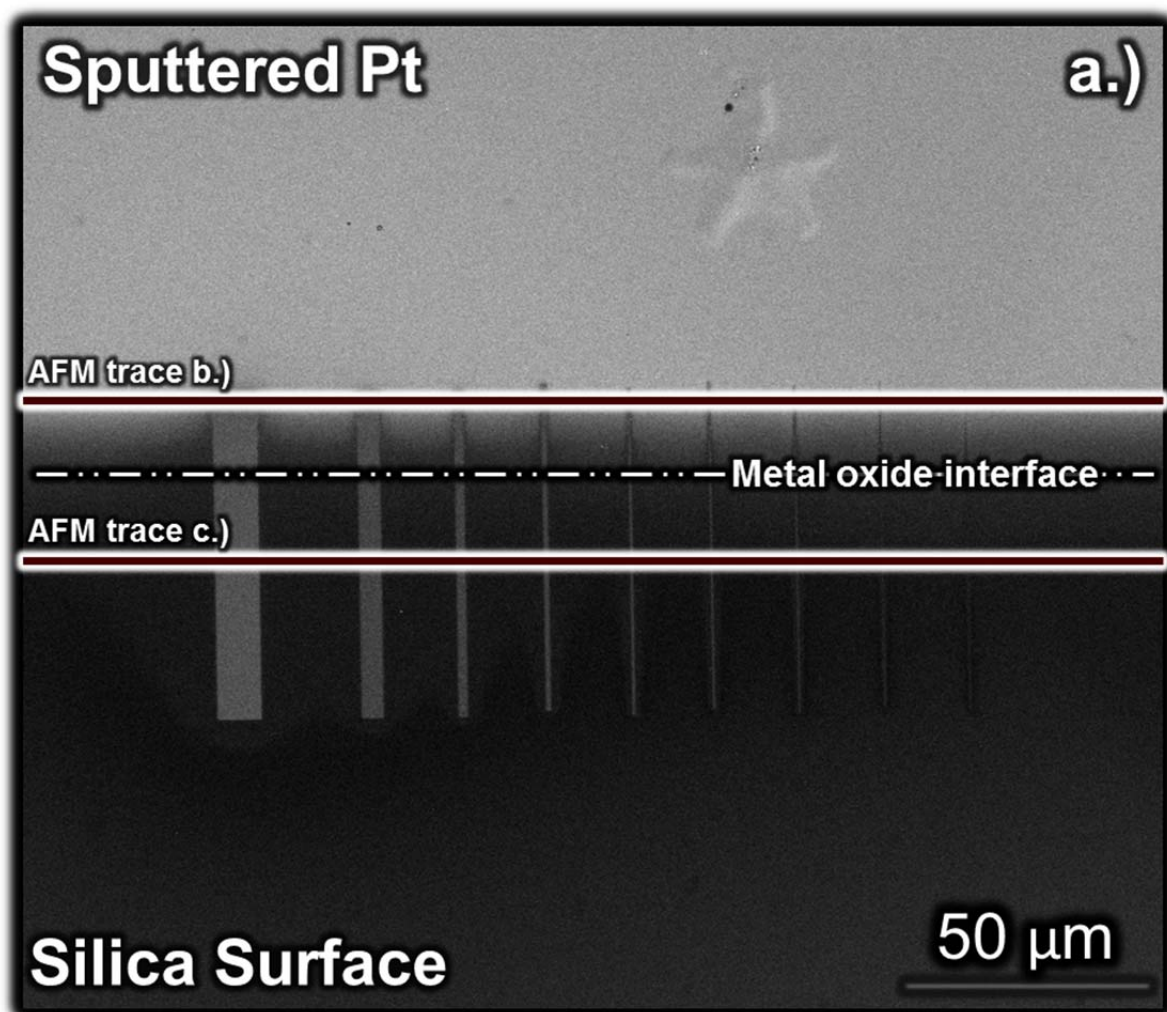




**Figure 6.23-** a.) AFM image of E-beam deposited Pt wires at 5KeV and 13pA at the junction of sputtered Pt and silica surface b.) Conductive AFM trace over the deposited Pt bars on top of sputter coated Pt c.) Conductive AFM trace over Pt wires on the silica surface

The other method of depositing Pt bars via vacuum vapor deposition is Ion beam assisted deposition. Figure 6.24a shows an SEM micrographs of platinum bars deposited at the junction of sputtered platinum and silica surfaces. These platinum bars were deposited via ion beam deposition at an accelerating voltage of 30 KV and current have 0.5 nA. The respective conductive AFM traces shown in figures 6.24b over the sputtered platinum surface

and 6.24c on top of the silica surface yield platinum deposits that are conductive. A caveat to this deposition method is seen in figure 6.24c where the AFM trace over the conductive platinum bars shows current passing through the platinum however as the dimensions of the platinum bars decreases so too does the current, which may indicate carbon contamination as well.



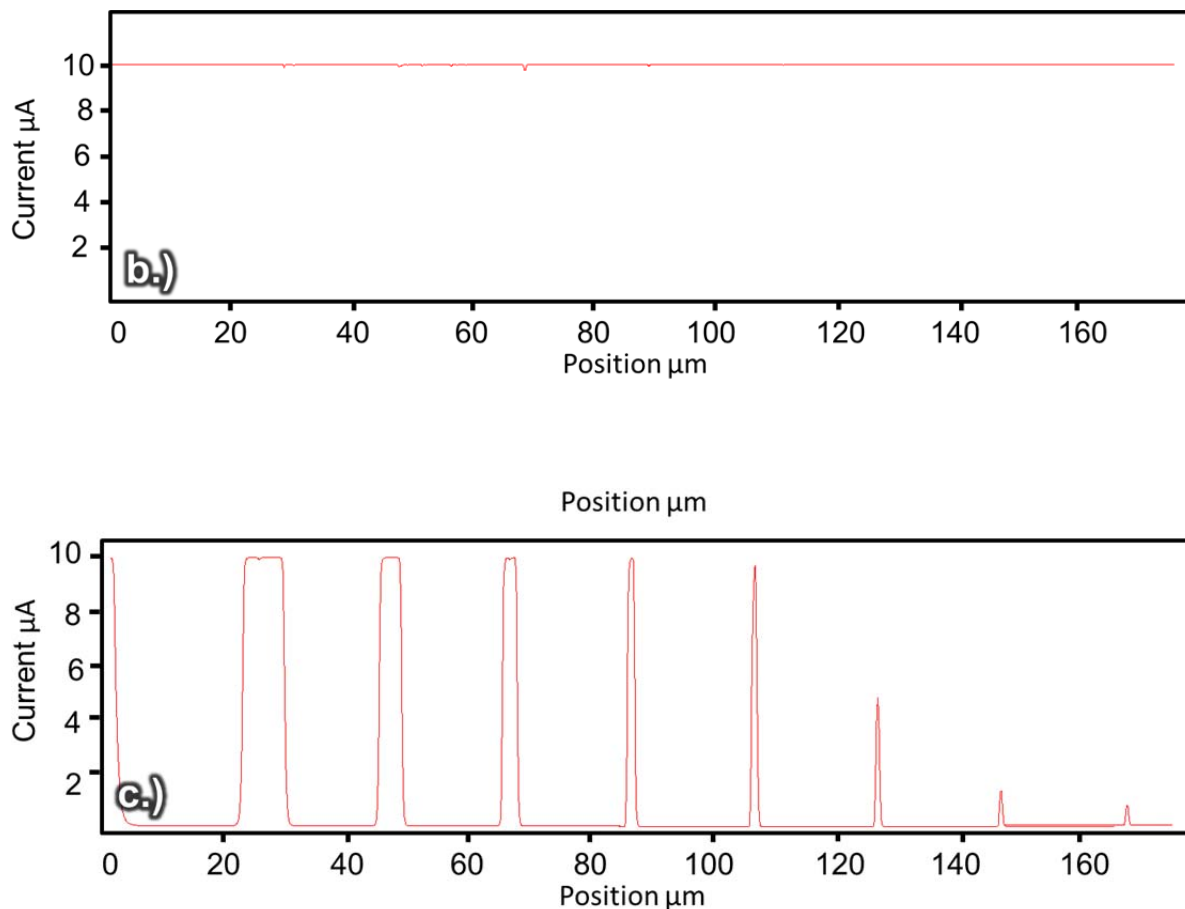


**Figure 6.24** a.) SEM Image of Ion beam deposited Pt Wires at 30KV and 0.5nA at the junction of the Sputtered Pt and Silica surfaces b.) Conductive AFM trace over the deposited Pt bars on top of sputter coated Pt c.) Conductive AFM trace over Pt wires on the silica surface

## 6.4 Concluding remarks about Pt feasibility

It is acknowledged at this time that the authors have had little experience with focused ion beam and focused electron beam deposition of metals. The discrepancy in quality of platinum deposition was first believed to be due to the higher energy values of the platinum deposition.

The true reason behind this is more complicated. Several previously conducted deposition optimization experiments [159-162] point to several hurdles that need to be overcome if energy beam assisted platinum deposition via metal organic precursors is to be used for diffusion tracking.

Focused ion beam and focused electron beam deposits on semiconductor films have been used to repair contacts however the the issue of relatively elevated resistivity's of these deposited materials yields less than desirable results. Methods to first characterize why the resistivity is so high and then improve it have been undertaken. The main cause of the high resistivity values of these two techniques is the presence of carbon contamination [162]. Langford et. al deposited comparable platinum bars via ion and electron beam assisted deposition and found that both contain large percentages of carbon at 45 and 70 atomic percent for ion and electron methods respectively. It is noted in this study that the resistivity of the electron beam deposited platinum is three orders of magnitude higher than that of ion beam assisted deposition which is blamed on the higher carbon content. In an effort to reduce resistivity the platinum deposited bars originating from electron beam source were annealed at 500° C for an hour which saw the carbon content reduced to 50 weight percent and the resistivity reduced by one order of magnitude. The other mechanism of decreasing resistivity was the doping of e-beam deposited platinum with gallium ions to mimic the gallium content found in the ion deposited platinum. This reduced the resistivity but did nothing to change the carbon content. From this study and others it is then considered that any metallic diffusion marker placed at the interface of diffusion couples via energy beam assisted deposition with metal organic precursors will have deleterious carbon content. This carbon content will be detrimental to the observation of diffusion due to its volatilization upon annealing.

The reasons for why the metal does not deposit solely in its pure form are not entirely elucidated in the deposition literature. This is most likely due to the fact that the deposition mechanism of how a focused ion beam and focused electron beam actually interact with the metal organic precursor is not straightforward.

The deposition of a metal on the surface of a substrate via electron beam techniques yield an environment where the metal organic bond is broken and the metals dissociated from the carbon chains where the non-volatile metal deposits on the surface while the volatile product is pumped away. Conflicting reports speculate on how exactly the focused electron beam assisted deposition (FEB) deposits. Both primary and secondary electron interaction with precursor molecules are shown to play a role in the deposition dissociation mechanism. It is understood that while gas phase interactions can occur with electrons the dominating pathway is governed by electron interaction with surface adsorbed precursor molecules. In this manner electrons originating from the microscope called primary electrons (PEs) with variable energies on the order of 5 to 30 keV impacts the substrate atoms and penetrate the surface. Primary electrons can be backscattered elastically from the surface with energies on the order of their initial incoming kinetic energy. Primary electrons can also generate less energetic secondary electrons, with energies less than 50 eV, from inelastic collisions with the atomic species that they collide with. The secondary electrons have less energy and therefore have a smaller escape depth than primary electrons that is on the order of nanometers. These secondary electrons are what some researchers theorize generate the majority of the metal deposition on the surface by dissociating the metal organic bond of the surface adsorbed precursor molecules because their energies are closer to the resonant frequencies of the metal organic bond than the backscattered electrons.

Ion beam deposition results from the interaction of ions and the substrate materials cascade of collisions and resultant secondary interactions. As ions are accelerated toward the surface ions collide with the substrate atoms and elastically an inelastically transfer their energy. There are two main pathways energetic ions can interact with the surface material. Ions can inelastically scatter with material and generate secondary electrons which then contribute to surface deposition when there is an adsorbed precursor material available. The other route ions interact involve a collision cascade that results from an elastic collision between the incoming ion and the surface atom. This collision transfers energy to surface atoms yielding a distribution of energies that can exceed that of the surface binding energy in a phenomenon

known as sputtering. The surface atoms that receive less energy than the surface binding energy are titled 'excited surface atoms' that then have the potential to interact with surface adsorbed precursor molecules and dissociate a metal organic bond from a precursor material. Generally both methods are viable for metal deposition on surfaces. The advantages of ion beam deposition are faster deposition rates due to higher deposition yields per incoming species and less carbon content. Electron beam advantages lie within its smaller radius of excited secondary events that cause deposition yielding higher deposition resolution. From this exhaustive study of diffusion, it is concluded that Pt diffusion markers can be reliably placed with precision at the interface of question. The limitation encountered with this approach to obtain the ability to measure a diffusive flux in this manner with vapor deposited Pt assisted with focused ion or electron beams is the large atomic percent of carbon mixed with the deposited Pt. This high impurity level will ultimately prove annealing to be destructive to the interface and therefore yield broken surfaces instead of an interface that diffusion can be observed at.

A possible use for this technique of monitoring diffusion is when placed at the interface of two materials that will undergo mass transport at lower temperatures than seen with thermite couples. However, for the current intended purpose of measuring diffusion inequalities at the interface of thermite reactants, Pt markers derived from this technique are inappropriate.

A closer look at the Cr/CuO sample interface after a year long anneal at room temperature reveals in figure 6.20b that there is indeed a copper metal layer underneath the carbonaceous marker and a chromium oxide layer above it. The geometry of this morphology points to the fact that oxygen is then the primary diffusing species. This is an important result which needs further refinement of marker placement to get a more segmented view of what occurs during a thermal annealing process, but it is sufficient in concluding the process is dominated by oxygen motion.

## **7. Shock Impact Behavior of Thin Film Thermite**

**Authors: <sup>1</sup>Edward Mily, <sup>2</sup>William Shaw, <sup>2</sup>Dana Dlott, and <sup>1</sup>Jon-Paul Maria**

<sup>1</sup>North Carolina State University, Department of Materials Science and Engineering, Raleigh NC, 27606 USA

<sup>2</sup>University of Illinois, Department of Chemistry, Urbana IL, 61801 USA

### **7.1 Introduction to Impact Testing**

Chapters 3 through 6 attempt to answer fundamental questions and illuminate discrepancies in the scientific community's knowledge of thermite couples. The experimental techniques and trends observed are crucial in the understanding of how oxygen exchange occurs, however all of this testing has been done at relatively slow time scales. In this manuscript the fastest these systems have been heated through DSC analysis is 25 Kelvin a minute. This heating rate is sufficient to test exothermicity and diffusion trends. Ultimately nanolaminate thermite will most likely be implemented in applications that initiate exothermic activity rapidly and are several orders of magnitude higher than conventional furnace heating rates or mechanical drop strain rates. In an effort to explore nano thermite behavior in these extreme environments the authors have subjected the thin-film thermite samples to high strain rate initiation testing via laser driven flyer plate shock studies. The following investigation is represents a collaboration between the electronic thin-film oxides research group at North Carolina State and the shock physics experimental group at the University of Illinois at Urbana.

In the previous chapters, these samples under have been tested slow heating rates, it is wished to Impact testing in this light refers to testing methods which produce strain rates in

materials that are on the order of  $\dot{\epsilon} = 10^8/s$  that generate shockwaves in materials. Not to be used with slower strain rate testing experimental techniques such as Charpy or Izod impact testing and which only reached strain rates of around  $\dot{\epsilon} = 10^{2-4}/s$ .

### **7.1.2 Shock Waves**

A shockwave is a discontinuity in density and velocity that traverses a medium abruptly faster than the sound speed of a material. The energetics community is interested in the shockwave phenomenon because shock waves can initiate explosive behavior in energetic formulations, or they can initiate detonation [7, 8, 163]. A detonation is a shock wave that is sustained by a chemical reaction. In order for detonation to occur the reaction conditions must initiate energy release at a rate faster than the speed of sound in the material that propagates a shock front through the material that then reacts the entire sample or substance instantaneously.

As was alluded to in chapter 1, shock waves were first artificially manufactured at the advent of organic explosives research. Prior to the birth of organic energetics the scientific community had little motivation or opportunity to investigate the effects of an energy wave through matter faster than the speed of sound in that material. The detonation of organic explosives significantly changed that. Organic energetics can deflagrate and release energy slowly or can detonate rapidly depending on the particular initiation conditions. The burning of organic explosives can lead to the detonation and propagation of a shock front called the deflagration to detonation transition. The inherent mechanism of the shock induced initiation is different. In order for burning to initiate detonation the burn rate must approach the sound speed in the material being consumed to further the reaction front faster than the speed of sound. Shock initiation supplies the initial supersonic impulse that is then propagated by the chemistry of the explosive. Since then, a myriad of work has been compiled describing how matter responds to extremely high velocity impacts [7, 8, 34, 52, 163-181].

Detonation can be realized through several pathways however it is usually brought upon by a shockwave. Any energetic material that is predominantly insensitive to mechanical insult and is initiated by high-speed impact or shockwaves is termed a secondary explosive and

materials that detonate from slight mechanical agitation are primary explosives used primarily to initiate secondary explosives.

### **7.1.3 Shock Wave Generation**

The applications for high strain rate and extreme environment testing is of obvious interest to the energetics community, however it should be noted that astrological and geological scientific communities benefit from extreme environment testing [182]. Within the context of this manuscript the focus will solely be on energetic materials testing. In order to produce munitions that only initiate under extreme circumstances, namely shockwave initiated detonation, experimental methods are employed to create high strain rate shocking environments. Traditionally the creation of a man-made shockwave is done by using either gas propelled impactors or explosively driven impact plates. Explosively driven experiments require explosive material with known detonation characteristics that are then used to impact a sample. These two methods provide experimentally valuable data on the shock behavior of materials. Main drawbacks of these testing methods are the laboratory size and the safety precautions needed to employ them. Explosively driven shock testing specifically, extreme caution and experimental safety procedures must be adhered to because the high pressure impacting originates from explosives. The unfortunate reality of these testing methods is that the constraints on the availability and authorization to legally obtain such testing materials prohibit a large number of institutions from developing the capability to empirically test materials responses to shockwaves.

### **7.1.4 Laser Driven Flyer Plates**

A complementarity shock experiment technique called laser driven flyer plate testing is able to probe energetic materials under high strain rates ( $\dot{\epsilon} = 10^8/s$ ) and impact samples with velocities the order of  $1 \times 10^3$  meters per second characteristic of the velocities of detonation of explosives without the use of hazardous organic explosives. This technique also allows for rapid testing of multiple samples and provide little hazard due to small amounts of material being used

### 7.1.5 Composite Energetic High Speed Testing

Non-organic powdered energetics are generally initiated by a thermal source. Despite being overwhelmingly used for organic explosives characterization shock studies, have been conducted on thermitic and formation reaction mixtures to better understand their response to high strain rates [52, 182, 183]. Previous work on powder by Thadhani et al. have examined the effects of shock on several energetic powder formulations. The majority of this work concentrates on characterizing two main facets of energetics response to shock. The first behavior described is a parameter called the “crush strength” of the composite powder energetic. This parameter is a measure of the amount of energy required decrease void volume and to increase the density of the powder to that of a fully dense material. It was found that this crush strength is a function of packing density, particle size, and particle microstructure in the powders [34, 167, 171, 174, 178, 179]. Through this work it was also shown that energetic particles of powder formulations undergo two types of reaction when exposed to shock compression. One mechanism is titled *shock induced* where the reactions are very fast and occur while the material is still in a highly dense compressed state and the other is a slow reaction that is called *shock assisted* where at later times after the shock incident on the sample reaction occurs only after thermal equilibrium is reached. Shock induced reactions commonly seen in organic energetics occur in detonation and on the order of microseconds. Shock assisted reactions are initiated by the incident shock after thermal equilibrium is reached in the sample which is a slower process than shock induced reactions and is typically on the order of milliseconds. Granular energetic materials that are exposed to shock were found to initiate and release energy in both micro and millisecond timescales, however the main energetic release events only occurred after a few milliseconds. Therefore the reaction is mostly shock assisted. This work was mainly done on micron sized particles. It is of the hope and motivation of the community to generate materials that could possibly achieve solid-state detonation under the shock induced reaction regimes. Few reports probe the affects nano sized particles have on shock properties [52, 172, 173, 175, 183]. In these reports the shock behavior on composite powdered energetics created mainly by arrested

reactive milling was studied. They find that a small amount of material reacts very quickly in the regime of microseconds but then the majority of energetic release occurs at longer timescales from 1 to 100 milliseconds after the corresponding shock. They attribute the initiation to the initial shock induced hot spot generation in the first few microseconds. These hot spots then grow and create burning fronts that consume the majority of the material on longer timescales indicative of shock assisted reactions. They assert that the mechanical shock initiation of powdered energetics is attributed to the hot spot generation at regions of the sample that exhibit a density gradient which produces elevated temperatures. It is also noted these studies that the nano material energetics exhibit more energetic output earlier than the micron sized counterparts.

Nano-sized energetics provide a possible way to achieve solid-state detonation depending on the impact initiation properties [53, 173, 175, 184, 185] but more work is required to fully realize a solid state detonation of nano energetics. The energetics research literature is bereft of examples that explore the shock behavior of fully dense nano composite thin films and the remainder of this section will explore the shock initiation and exothermicity of nanothermite thin films at short timescales by way of laser driven flyer plates.

## **7.2 Impact Behavior of Thin Film Thermite**

Multilayered geometry that a thin-film thermite provides is a perfect experimental system to study the effects of increased areas of density discontinuity. Since this trait of energetics has been previously attributed to microsecond mechanical initiation corresponding to the shock induced regime, it is highly desired to explore multilayered energetics further.

Few reports describe the impact behavior and initiation of thermite [52, 173, 182, 183] however the literature points to the fact that the majority of thermite requires rather large incident energies to be initiated via mechanical means. To the authors knowledge there has been no impact initiation of thin film thermite to date. Therefore when this work was initiated between NC state and the University of Illinois the initial parameters of impact initiation were completely unknown.

Before any experimental data from the impact behavior could be collected thin-film thermite samples first were deposited on transparent substrates of borosilicate glass. The alternating geometry of the thin-film thermite was produced in the same manner as the samples analyzed in chapters 3, 4, and 5. The deposited nanothermite multilayered samples on glass were then inserted into the laser driven flyer plate testing apparatus and impacted with aluminum flyer plates with variable incident velocities. The laser testing apparatus was a Nd:YAG laser capable of producing 100 J pulses for 10 nano seconds. The laser driven flyer plate apparatus is capable of shooting flyer plates with velocities from 500 m/s to 4000 m/s. The way the flyer plate is launched is by the laser ablation of an aluminum layer on a glass substrate. As depicted in figure 7.1 laser radiation is incident at the glass aluminum interface with a spot size of 1 mm. The incident laser energies can be varied which directly relate to speeds of the resultant ablated aluminum flyer plate. The laser energy is absorbed by the metal layer and rapidly heated which causes a plasma to form that rapidly expands and propels the flyer plate. For laser driven flyer plates the pressures and shock durations are lower than the capabilities of macroscopic flyer plate testing facilities, however tabletop laser driven flyer plate shock testing yields better time resolved data. This shock testing method also provides the advantage of multiple tests shots in a short duration of time by simply moving the location of the irradiated aluminum flyer material to an un-ablated area[163]. The data collected from the impact event corresponds to visual light intensity versus time with the capability of nanosecond resolution over a timescale of several microseconds.

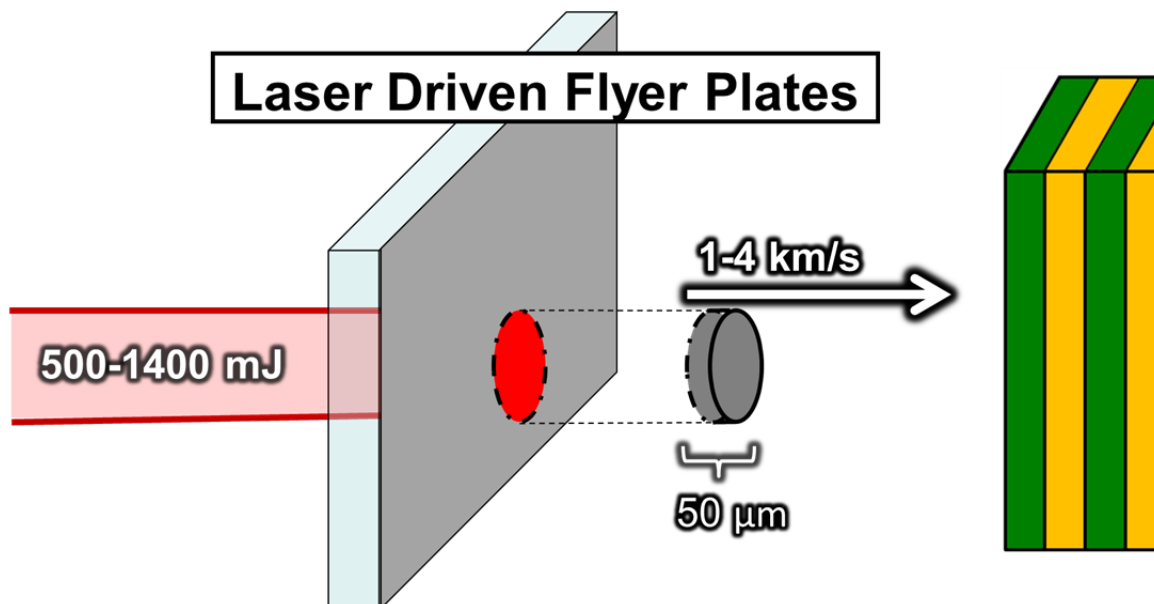


**Figure 7.1-** Schematic showing the principles of the Nd:YAG laser driven flyer plate apparatus with an Al flyer plate incident on a thin film thermite sample.

### 7.2.1- Variation of Interface Density in Thin Film Thermites

The first and most straightforward thin-film thermite behavior tested under impact conditions was the exothermic release behavior as a function of interface density. In chapter 4 the behavior seen at slow heating rates and long time scales correlate peak exothermic temperatures with the number of interfaces and the diffusion distance. It was found that as interface density increased and diffusion distance decreased the peak exothermic temperature also decreased. In an effort to characterize the effects of bilayer spacing and interface density under shock conditions, the thermite system chosen was the zirconium and copper oxide system because it demonstrated the lowest exothermic peak temperatures during slow thermal analysis out of the systems studied.

As a result of very limited complementary research on thin film thermite shock induced or shock assisted initiation, the shock parameters in which initiation would occur were unknown. Therefore the first few sample sets sent for impact testing coated the entirety of the

glass sample substrate and were tested at a myriad of flyer plate velocities to ascertain if this testing method was appropriate for this thermitic system. An example of a coated impact test sample is shown in figure 7.2. It was discovered that the zirconium copper oxide thin film thermite system could indeed be ignited by incident aluminum flyer plates. In these early tests it was also found that the samples were not only initiated but the entire thermite film was consumed entirely after initiation. Sample exothermic propagation dictated the need for sample substrate masking during thermite deposition to allow for multiple test shots on one glass substrate to not interfere and react the rest of the material.



**Figure 7.2-** Masked thermite nanolaminate impact sample

Several masks were used with varying diameter holes for testing sites. It was found that the optimal area of the deposited thermite coating was three times in the diameter of the incoming flyer plate to allow for uniformity of the thin-film tested and the spacing between each coated area was equal to that to the diameter of coated test area. This allowed for 16 individual tests shots for one thermitic system.

In this testing method initiation of exothermic activity is characterized by the emission of light after impact. To confirm optical emission from the sample's initiation originates from

the thermite reaction, baseline testing of pure copper oxide and zirconium were run and emissions from the thermite samples and bare reactants were compared in figure 7.3. From this preliminary experiment it is shown that the Zr/CuO thermite thin film emits significantly more light than the impacted reactants by themselves. The Zr thin film sample does emit some light but only at 20% intensity of the thermite

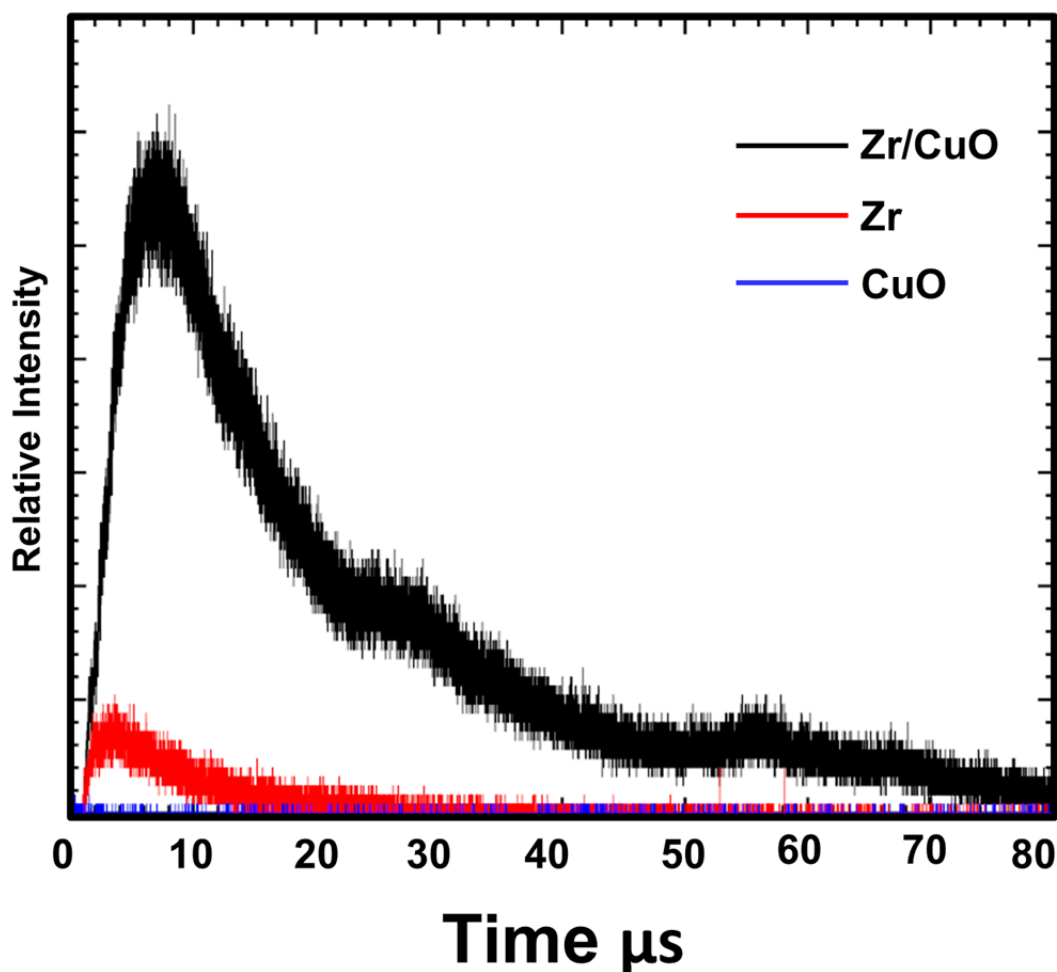


**Figure 7.3-** Baseline emission comparison from a Zr/CuO thermite, Zr thin film, and a CuO thin film. Emission is present for the bare Zr film but at 10% of the intensity of thermite couple.

The Zr/CuO thin film samples were then deposited on the masked glass with varying bilayer thicknesses from 1  $\mu\text{m}$  down to 400 nm overall sample volume and thickness was kept constant at 1  $\mu\text{m}$  shown in figure 7.5. The samples correspond exactly to the samples tested at slow heating rates in chapter 4. The samples were then tested by the University of Illinois at varying flyer plate velocities and optical emission versus time data was collected from the back side of the thin-film thermite samples. Figure 7.6 a 7.6 B and 7.6 C contain the results of the bilayer thickness variation experiment where each trace represents a different flyer plate velocity incident on the sample. As expected as the interfacial density increased and the diffusion distance decreased the required flyer plate velocity to initiate exothermic oxygen exchange decreased from 1120 meters per second for the one bilayer system 940 m/s for the two bilayer system and 750 m/s for the three bilayer system.

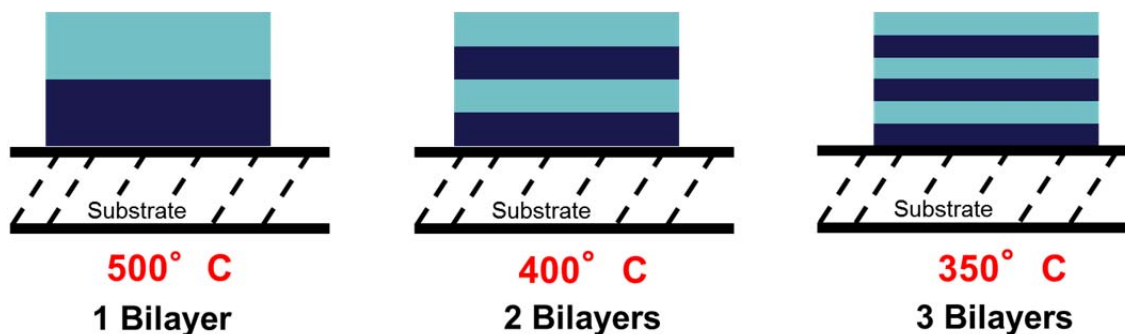


**Figure 7.5-** Graphical depiction of the Zr/CuO impact samples with the exothermic peak temperature obtained for each system under slow thermal analysis via differential scanning calorimetry.

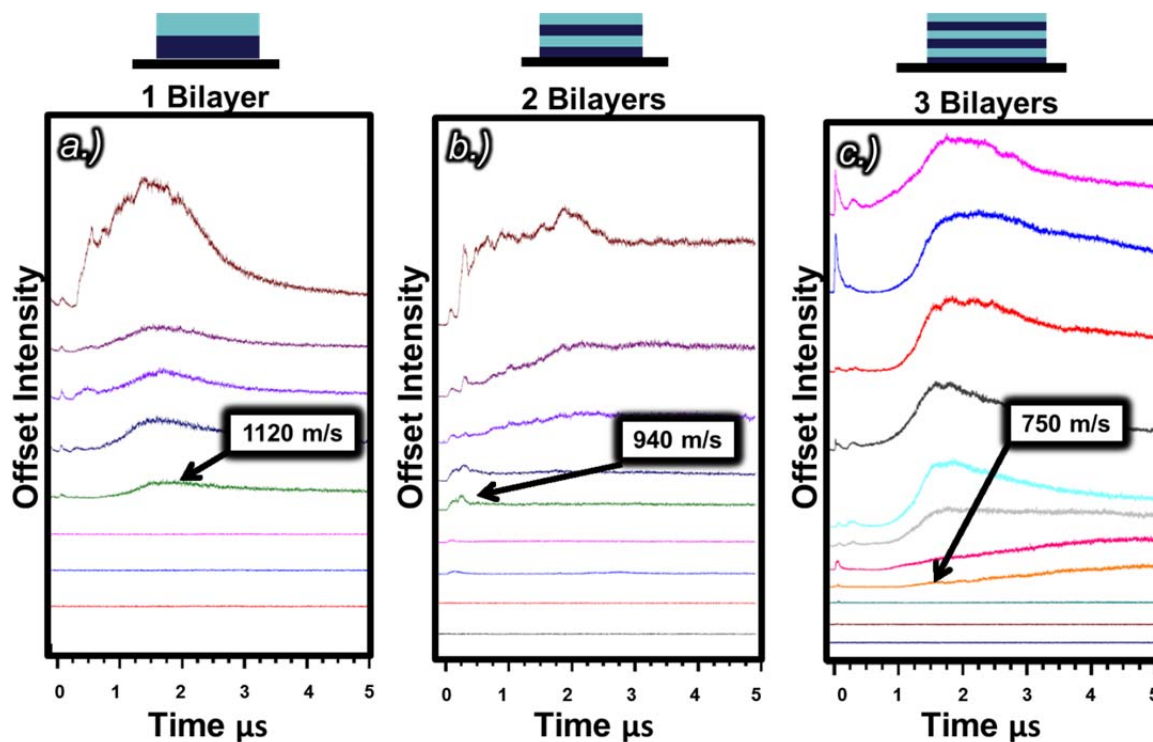


**Figure 7.6-** Intensity vs time data where each trace represents the optical emission spectrum of increasing flyer plate velocities for a.) Zr/CuO 1 bilayer sample, b.) Zr/CuO 2 bilayer sample, and c.) Zr/CuO 3 bilayer sample

As a result of the inherent thin-film thermite architecture, higher interface density predicated a higher volume fraction of density discontinuities. Current literature on powdered energetic reactions under impact testing blame density gradients for hot spot generation and contribute to the shock induced portion of the energy release as depicted in figure 7.7 [183]. It then stands to reason that the thin-film thermite samples with the higher number of bilayers will require less impact energy for initiation.

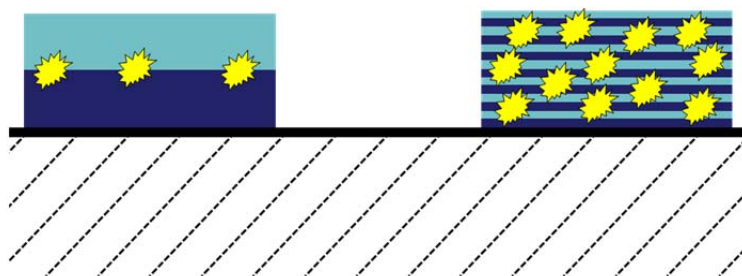


**Figure 7.7** - Pictograph of a visual representation of more reaction points or hot spots for laminates with increased number of bilayers

It is interesting to note that at short timescales and long time scales similar exothermic release behaviors are observed. In the plots in figure 7.8 in figure 7.9 the number of bilayers in the zirconium copper oxide samples are plotted versus the incident velocity of the flyer plate required for initiation and peak exothermic temperature respectively. One must be careful in drawing absolute initiation energy values from these experiments however the overall sensitivity trend of increasing number of bilayers still holds at fast timescales.

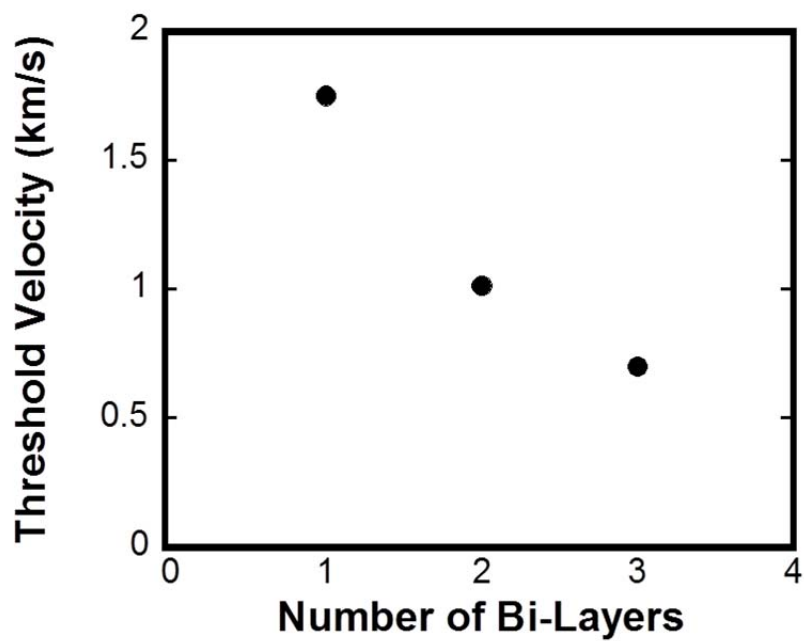


Figure 7.8 - Plot of threshold velocity vs. the number of bilayers in the Zr/CuO samples.

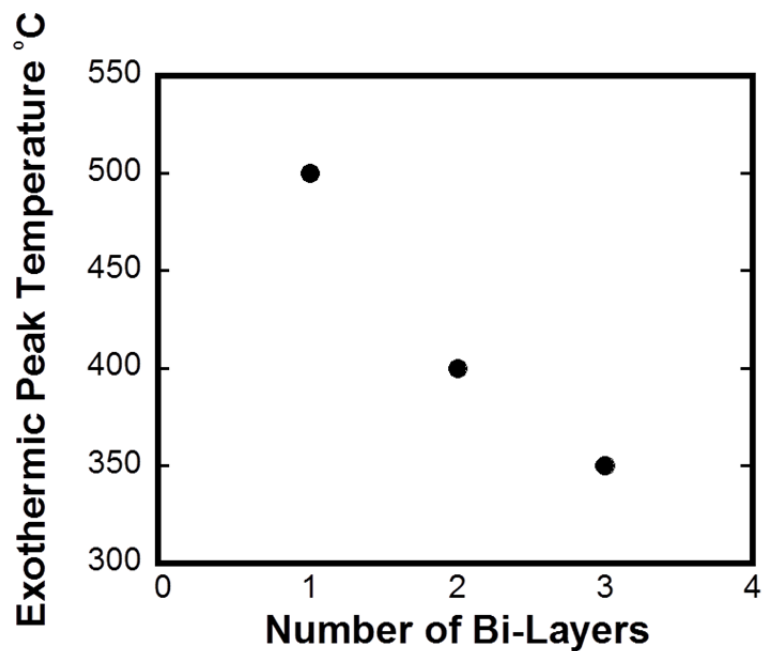
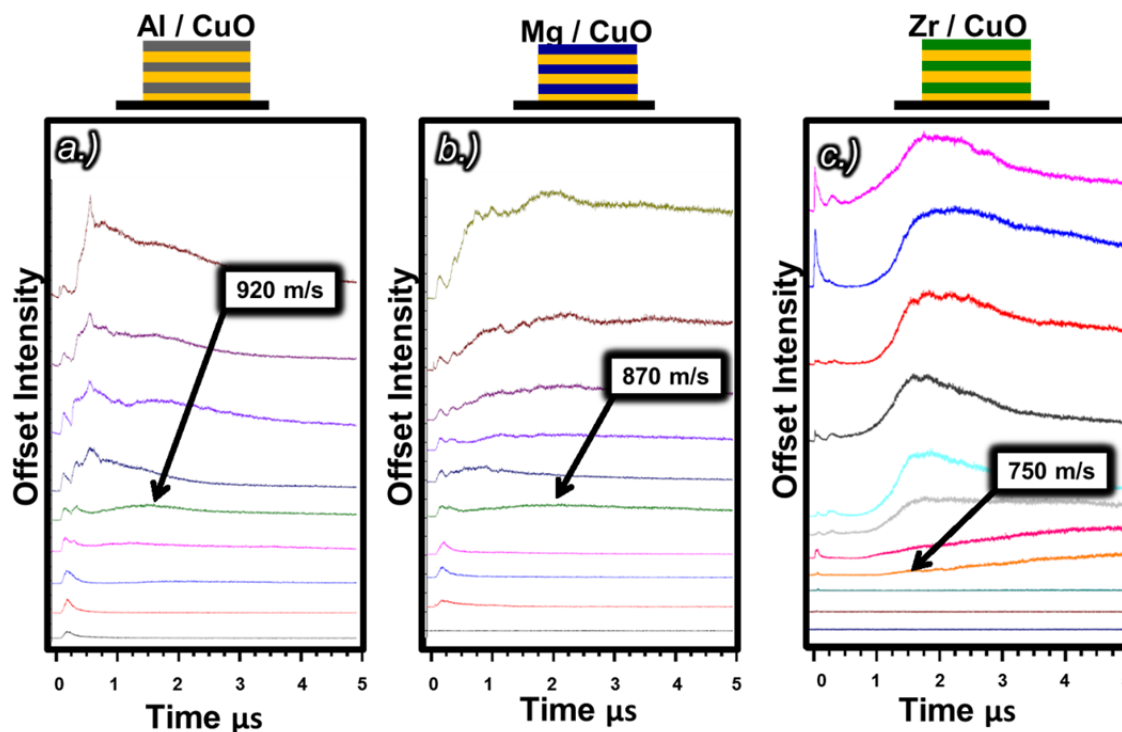


Figure 7.9- Exothermic peak temperature from Differential scanning calorimetric studies vs. the number of bilayers in the Zr/CuO thermite system

### **7.2.2- Variation of Reducing Metal on Thin Film Thermites**

The other characteristic behavior of the thin-film thermite samples elucidated in chapter 3 was the effect of metal fuel variation on exothermic activity as the oxygen source was held constant. At slow heating rates and long time scales it was posited and confirmed that the terminal oxide diffusion properties play a significant role in regulating oxidative energy release. The role in which the terminal oxide plays in the energy release during impact initiation is less clear. In order to probe the terminal oxides affects, three bilayer thermite films were deposited on masked glass substrates like the aforementioned impact experiment with a constant oxide source of copper oxide and a varying reactive metal. The metals used were the same as in chapter 3: aluminum magnesium and zirconium. The results from this experiment shown in figure 7.10 indicate a similar trend found in chapter 3, where the aluminum thermite requires the highest flyer plate velocity to initiate reaction at 920 m/s magnesium with an intermediate value of 870 m/s and zirconium copper oxide at the lowest value of 750 m/s.



**Figure 7.10-** Intensity vs time data where each trace represents the optical emission spectrum of increasing flyer plate velocities for a.) Al/CuO 3 bilayer sample, b.) Mg/CuO 3 bilayer sample, and c.) Zr/CuO 3 bilayer sample

In chapter 3 the reason for this behavior was connected to the terminal oxide's diffusion properties. Where alumina, magnesium, and zirconia have increasing values of oxygen diffusion respectively. It is not straightforward nor prudent to extrapolate this behavior to high strain rate testing especially if reaction is seen before thermal equilibrium on the order of microseconds can be obtained. While this diffusive barrier atomic transport mechanism almost certainly plays a role in short timescales it is probable that the mechanical properties of the terminal oxides are equally important because mechanical effects occur in the time regime before thermal equilibrium is reached [174, 178, 179, 183]. Plotting the values of the respective oxides Young's modulus versus the flyer plate impact velocity required to initiate reaction in figure 7.11 reveals that the stronger oxide containing thermite samples require

higher values. More impact testing is certainly called for to solidify this position however it most certainly is not a coincidence.

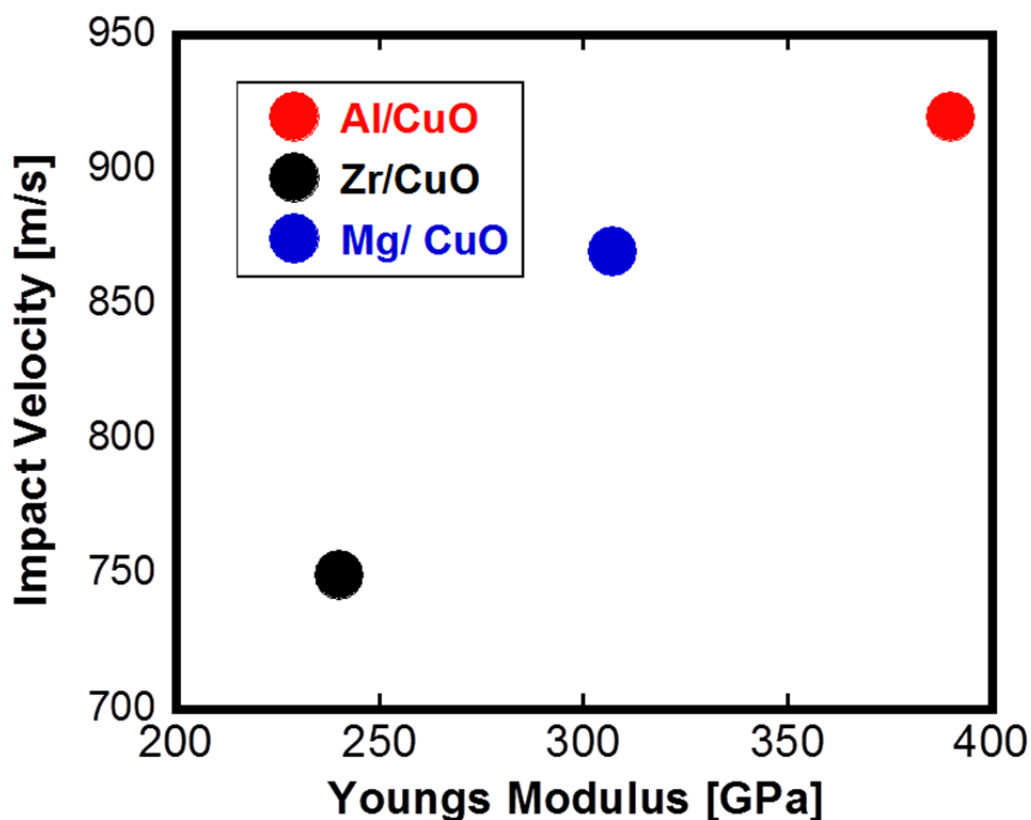


**Figure 7.11** - Impact velocity required for thermite reaction as a function of the youngs modulus of each systems respective terminal oxide

### 7.3 Conclusion

Thin film thermite samples consisting of Al/CuO, Mg/CuO, and Zr/CuO were deposited upon masked glass substrates. The coated regions of the glass were subjected to a laser driven flyer plate impact at velocities approaching 1500 m/s. The optical spectral signal from the impact effects were recorded with nanosecond precision and correlated to thermite reaction initiation. The thin film thermite samples showed increased sensitivity to shock impact as bilayer thickness decreased and interfacial density increased similar to

characteristic behavior seen at longer reaction time scales. When layer thicknesses are held constant and the reacting metals are varied the thin films showed an increase in sensitivity going from the Al/CuO, Mg/CuO, and to the Zr/CuO.

## **8. Rapid Annealing of Thin film thermite and the Effects of Geometric Spacing**

**Authors: <sup>1</sup>Edward Mily Jr, <sup>2</sup>Garth Egan, <sup>2</sup>Michael Zachariah, and <sup>1</sup>Jon-Paul Maria**

<sup>1</sup>North Carolina State University, Department of Materials Science and Engineering, Raleigh NC, 27606 USA

<sup>2</sup>University of Maryland, Department of Chemistry and Biochemistry, College Park MD, 20742 USA

### **8.1- Rapid annealing Introduction**

Following the theme from chapter 7 the thermite thin-film geometries were desired to be tested at faster timescales. In a collaborative effort with University of Maryland with Garth Egan and Dr. Michael Zachariah we have demonstrated the ability to test thin-film thermite with heating rates on the order of  $10^5$  Kelvin a second. The following thermal characterization technique in this chapter is called temperature jump heating coupled with time of flight mass spectroscopy[128, 186, 187]. This testing technique is able to reach elevated heating rates by applying variable amounts of current through a thin platinum wire to resistively heat the platinum with precision. During annealing, the high-speed mass spectroscope also allows for the chemical characterization of material ejected from the rapidly heated platinum wire. Typical methods of testing energetic materials in this manner involve the coating of the platinum wire with nanoparticles by immersing the platinum wire in a solvent that contains the nanoparticles. The samples are then tested at variable heating rates and ignition temperatures are collected which are characterized by the optical emission observed in high speed photography. During the ignition mass spectroscopy is performed to obtain the ejected species chemical makeup. This method is extremely useful for characterizing energetic materials high heating rate behavior. Applying this testing mechanism to thin-film thermites provides the advantage of fully dense reacting materials

with known quantities over the testing surface of the platinum whereas the total amount of reacting material is unknown for nano particle testing with this method. The deposition of the thermite samples was carried out at NC State while the temperature jump coupled with time of flight mass spectroscopy (T-Jump/ToF MS) was performed by Garth Egan at the University of Maryland.

## **8.2- Thin-film Thermite Deposition on Thin Platinum Wires**

The thin platinum wires that are used in the fast thermal characterization process are 75  $\mu\text{m}$  in diameter. It is desired to obtain a conformal thin-film thermite coating around these wires such that the material is uniform over the entire length the thermite is to be deposited. The experimental apparatus as seen in figure 8.1 required the addition of a stepper motor to incorporate sample rotation to ensure the entire platinum wire was coated. The stepper motor was mounted onto the vacuum deposition chamber with a in-house 3-D printed faceplate that allowed for sample rotation about an axis perpendicular to the plane of deposition. In order to suspend the platinum wire for deposition around its circumference a 3-D printed sample substrate holder was designed as depicted in figure 8.2 to provide minimal amounts of sample substrate shadowing during the deposition rotation and maximized the exposure to the depositing species during rotation. The top sample metal scaffolding support was required because 75  $\mu\text{m}$  diameter platinum wires are not mechanically strong enough to support their own weight on the longitudinal axis.

The platinum wires were cleaned via 15 minutes of sonication in acetone and were then rinsed with deionized water, isopropyl alcohol, and methanol. They were mounted vertically suspended from the metal scaffolding on the sample substrate holder and the center 10 mm of the wires were exposed to the deposition with 5 mm of each end of the platinum wires masked from deposition to allow for platinum electrical contact to the rapid annealing apparatus as shown in figure 8.3. Contrary to the previous deposition rate characterization of XRR used in all of the previous chapters a separate SEM cross-section technique was used. X-ray reflectivity requires a flat surface for x-rays to interfere with and form an interference

pattern that ultimately is characteristic of the thickness. Obtaining any interference data in a reflective geometry x-ray experiment not only would be tedious because of the small diameter of the platinum wires but the data would be ill-suited due to the substrate's cylindrical geometry. Aluminum and copper oxide were deposited on a rotating platinum wire with known deposition duration. The platinum wire was then cross sectioned and the individual layer thicknesses were analyzed to determine deposition rate on a cylindrical substrate pictorially represented in figure 8.4 and figure 8.5. It was found that the deposition rates for aluminum and copper oxide on platinum wires were 60% of the planar deposition rates at 3.75 nm/min and 3.3 nm/min respectively. The aluminum layer was deposited first followed by the oxide. During the thin-film thermite deposition each sample had a total thickness of 1800 nm and the number of bilayers was varied from 1 to 12. Morphological visualization of the 1,3, and 6 bilayers demonstrated in figure 8.6a, 8.6b, and 8.6c.

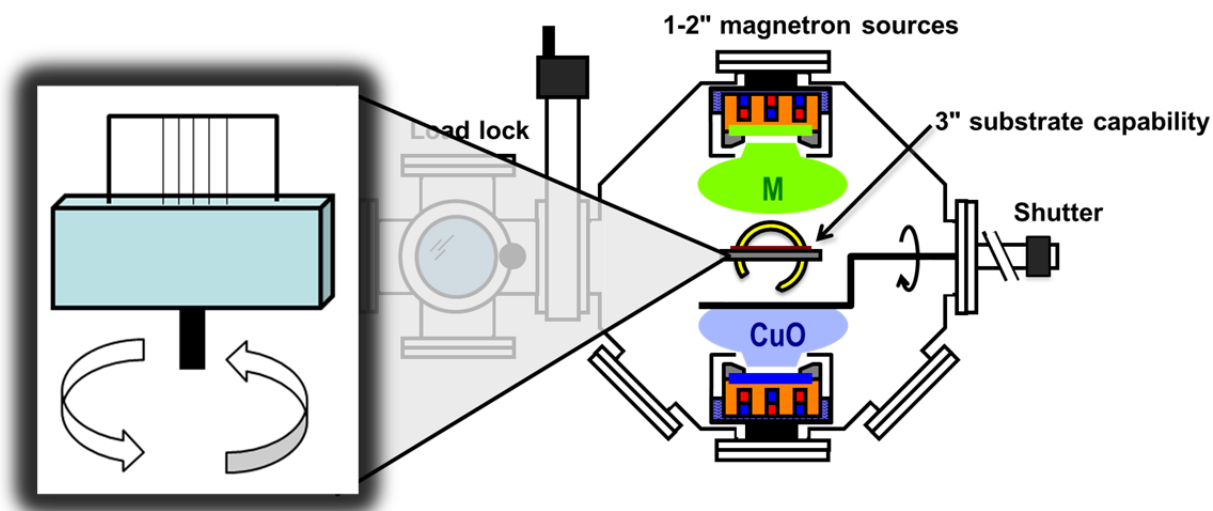


**Figure 8.1-** Schematic diagram of the dual beam magnetron system with the sample rotation axis.

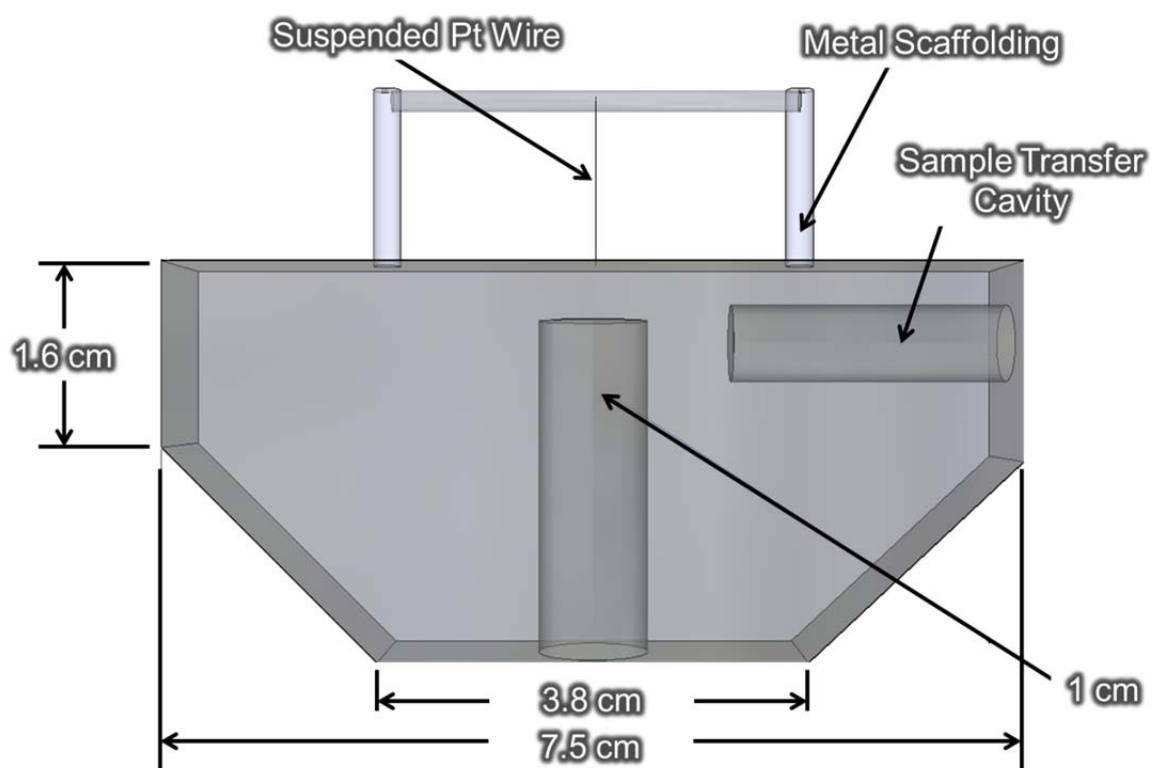


**Figure 8.2-** 3-D printed Pt wires substrate holder to allow for minimal sample shadowing and rotation perpendicular about the axis normal to the deposition source.

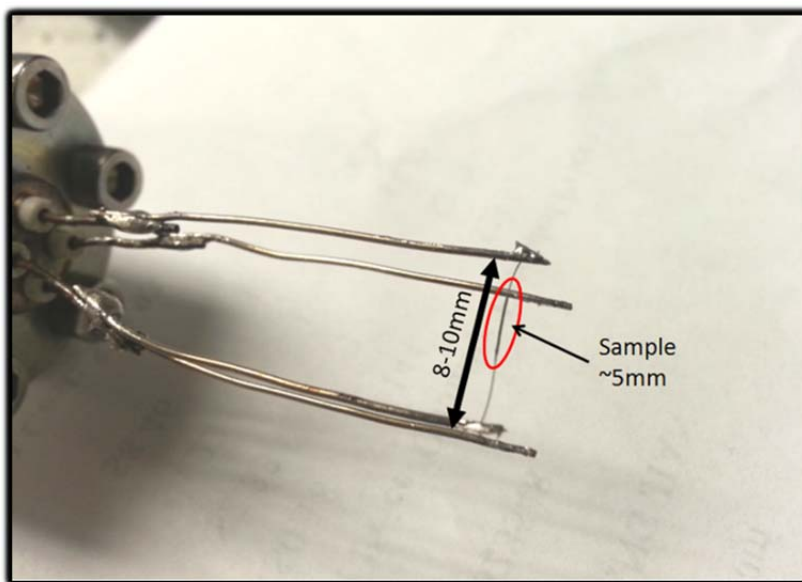


**Figure 8.3-** Temperature Jump (T-Jump) Pt sample apparatus. This configuration allows for the controlled heating of the Pt wires at elevated heating rates up to  $10^5$  K/s.

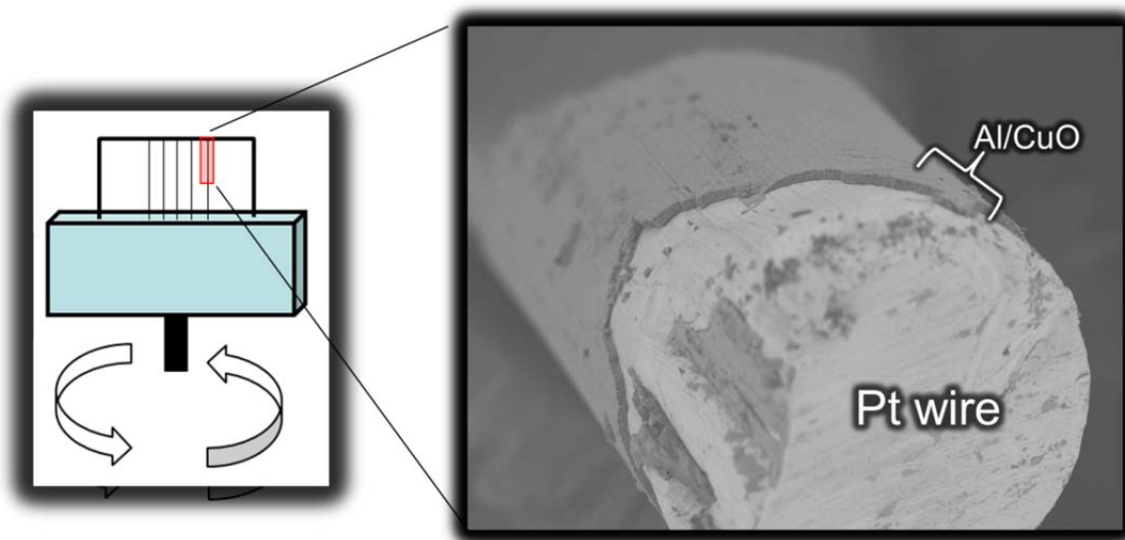


**Figure 8.4-** Cross-section SEM micrograph of a Pt wire with a conformal thermite nanolaminate coating.

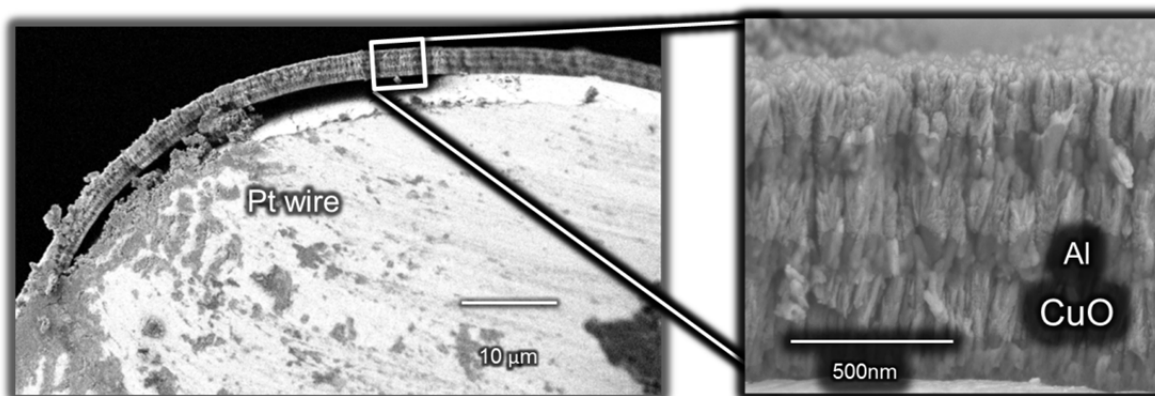


**Figure 8.5-** Cross-section SEM micrograph of Pt wire with conformal Al/CuO nanolaminate coating. A columnar morphology is clearly seen in the thin film multilayers.

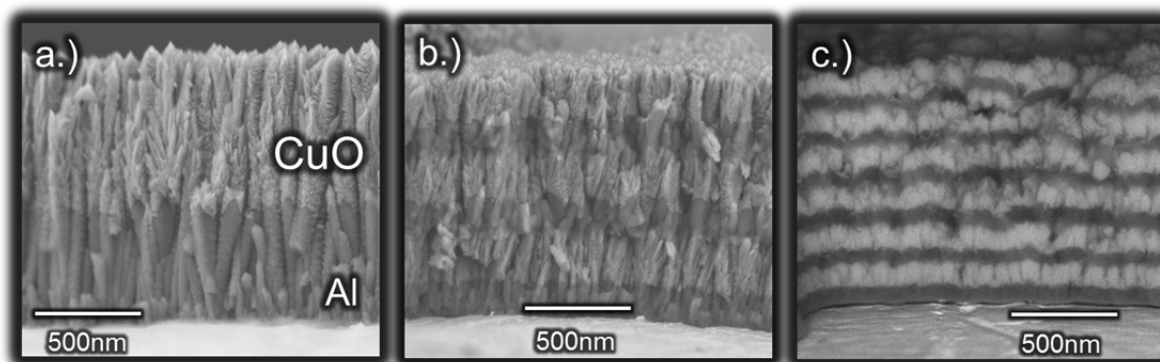


**Figure 8.6-** Cross-section SEM micrographs of Al/CuO nanolaminate with a.) 1 bilayer b.) 3 bilayers, and c.) 6 bilayers

### 8.3 High Speed Annealing

The platinum wires coated with thermite nanolaminates were subjected to temperature jump experiments coupled with time of flight mass spectroscopy (T-Jump/Tof-MS). This method for testing energetic formulations was previously developed by Zachariah et al. at the University of Maryland [21, 29, 188][citation]. This testing approach resistively heats platinum wires with 3 ms pulses that can reach temperatures of 1600 Kelvin. The specific heating rate obtained to for these experiments with roughly  $4 \times 10^5 \text{K/s}$ . The temperature of the wire was determined by the established relationship of the resistivity of platinum with

temperature. During the rapid anneal high-speed camera images taken 67,000 times a second from a Phantom v12.0. Visual identification of ignition time (the temperature in which the reaction is self sustaining) is confirmed as shown in figure 8.7. These images are then matched to the corresponding temperature obtained in the platinum wire's resistivity time and temperature dependence. From this analysis, accurate ignition temperatures can be ascertained within 50K. During the high-speed anneal the chemical identification of the reaction products is analyzed every 100  $\mu$ s via time of flight mass spectroscopy. Collectively this experimental procedure allows for the determination of ignition temperature and the characterization of the chemical products ejected from the platinum wire for nano laminate thermite samples.

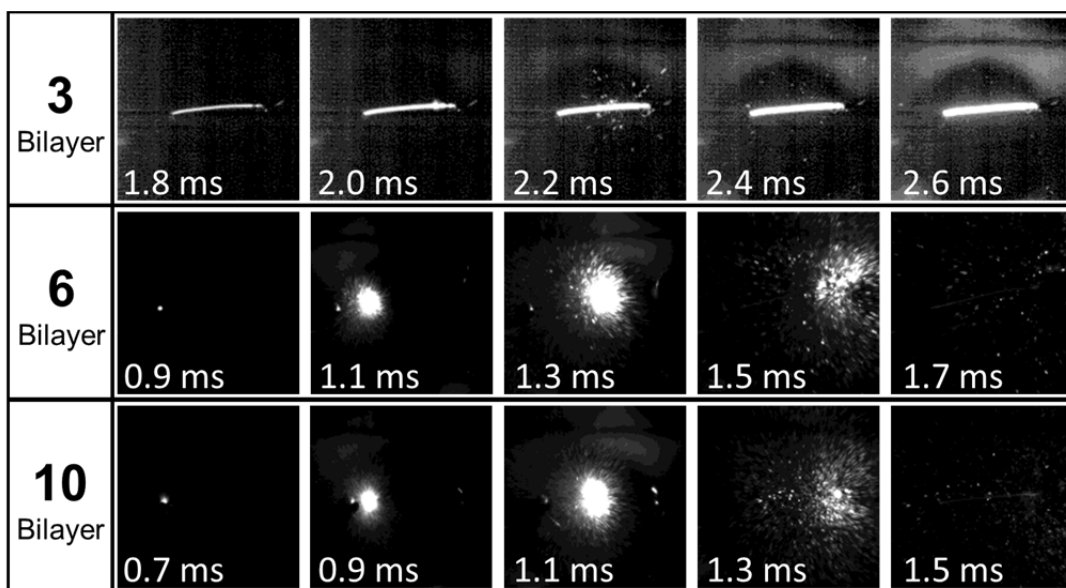


**Figure 8.7-** In situ high speed temperature jump frames for the 3, 6, and 10 bilayer samples during the temperature jump. The scale is the same for each sample, where the bright wire portion of the 3 bilayer sample is 10 mm.

With this technique, the point of ignition is determined for all of the samples where the ignition temperature and relative geometric characteristics are displayed in table 8.1. The

data show a clear trend of decreasing ignition temperature with the increase in interfacial density.

**Table 8.1** High Speed Ignition Temperature Data.

<b>Multi-layered Thermite on Pt wires (Fast Anneal <math>\sim 10^5</math> K/s)</b>					
Number of Bilayers	Total Thickness [nm]	Bilayer thickness [nm]	CuO thickness [nm]	Al thickness [nm]	Ignition Temp [°C]
1	1800	1800	1020	780	n/a
2	1800	900	510	390	977
3	1800	600	340	260	857
6	1800	300	170	130	407
8	1800	225	127	98	377
10	1800	180	102	78	397
12	1800	150	85	65	347

Further analysis of the emission from these thermite thin films on platinum wires via integrated intensity from the high-speed video frames show that in addition to lower ignition temperature the samples with the higher number of bilayers also displayed an increase in reactivity. Namely the integrated intensity from these reactions, which can be correlated to a hotter reaction, grew as a number of interfaces increased. A closer look at this increased reactivity, originating from a brighter emission from the thermite sample, show that the samples with 6 to 12 bilayers generate significantly brighter emission than the 1 to 3 bilayer samples by a factor of 10. Closer inspection of figure 8.7 shows a distinct difference in the reaction profiles comparing the 3 bilayer to the 6 and 10 bilayer samples. The 3 bilayer sample seems to gradually increase in temperature while the 6 and 10 bilayer samples violently explode reacted material off of the platinum wire. This increased reactivity is also observed in the time of flight mass spectroscopy displayed in figure 8.8a and 8.8b. Samples containing one, two, and three bilayers displayed very little product particulate signal during

the temperature ramp. Each display ignition behavior after an oxygen species is detected leaving the sample at roughly 800°C shown in figure 8.8a. Oxygen release by CuO has been described before in other publications [187] under similar thermal environments which has been attributed to the reduction of cupric oxide to cuprous oxide ( $2\text{CuO} \rightarrow \text{Cu}_2\text{O} + \frac{1}{2} \text{O}_2$ ). Further evidence of this is apparent after the consultation of the unary phase diagram of copper oxide under different partial pressures of oxygen in figure 8.9. Previous scanning calorimetry on CuO films has shown this release and phase change at similar temperatures in figure 8.10 at 820°C which is confirmed by corresponding x-ray diffraction data in figure 8.11. It is around this temperature that  $\text{Cu}_2\text{O}$  becomes the more thermodynamically stable phase. This suggests that for the samples that react post oxygen release the thermite reaction may be either oxygen-poor when it initiates in the solid state or initiated in the vapor phase which then continues to propagate through the solid-state. At this point in the analysis it is not certain the role the oxygen release plays in the energetic release. Figure 8.8b displays a significantly different behavior of energetic release. Prior to the characteristic reduction of cupric oxide the release of reaction products show significant signal and the mass spectroscopy data where you after the ignition temperature of the six bilayer aluminum copper oxide thermite. The species detected are Cu, Al,  $\text{Al}_2\text{O}_3$ , and a much weaker  $\text{O}_2$  signal which correspond to an oxidization event to the materials expected to be in the wake of a Al/Cu thermite reaction.

**Figure 8.8-** Time of flight mass spectroscopy data for a.) three and b.) six bilayer samples. The temperatures of ignition ascertained by the optical high speed video are represented by the vertical dashed line.

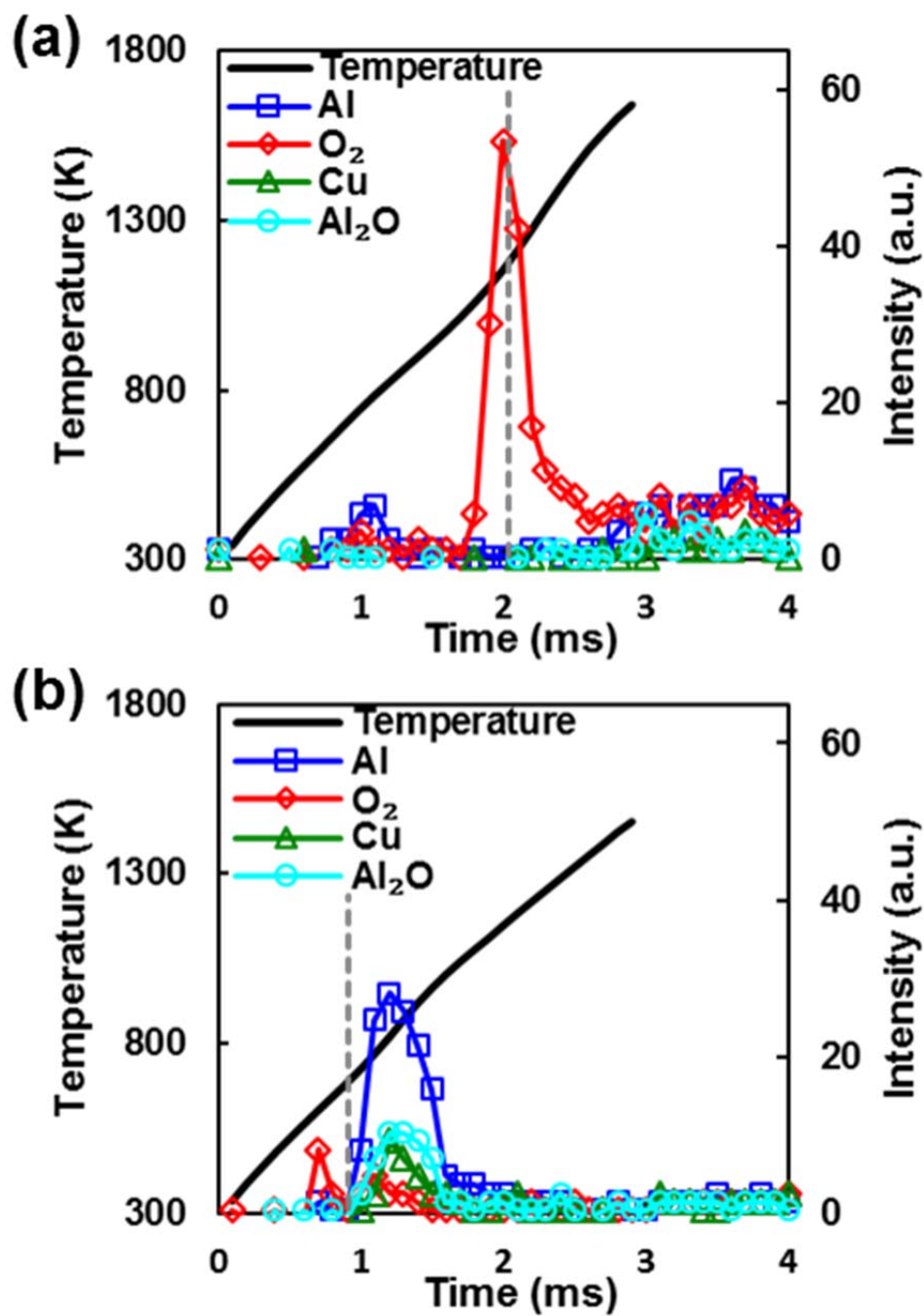


**Figure 8.8-** Time of flight mass spectroscopy data for a.) three and b.) six bilayer samples. The temperatures of ignition ascertained by the optical high speed video are represented by the vertical dashed line.

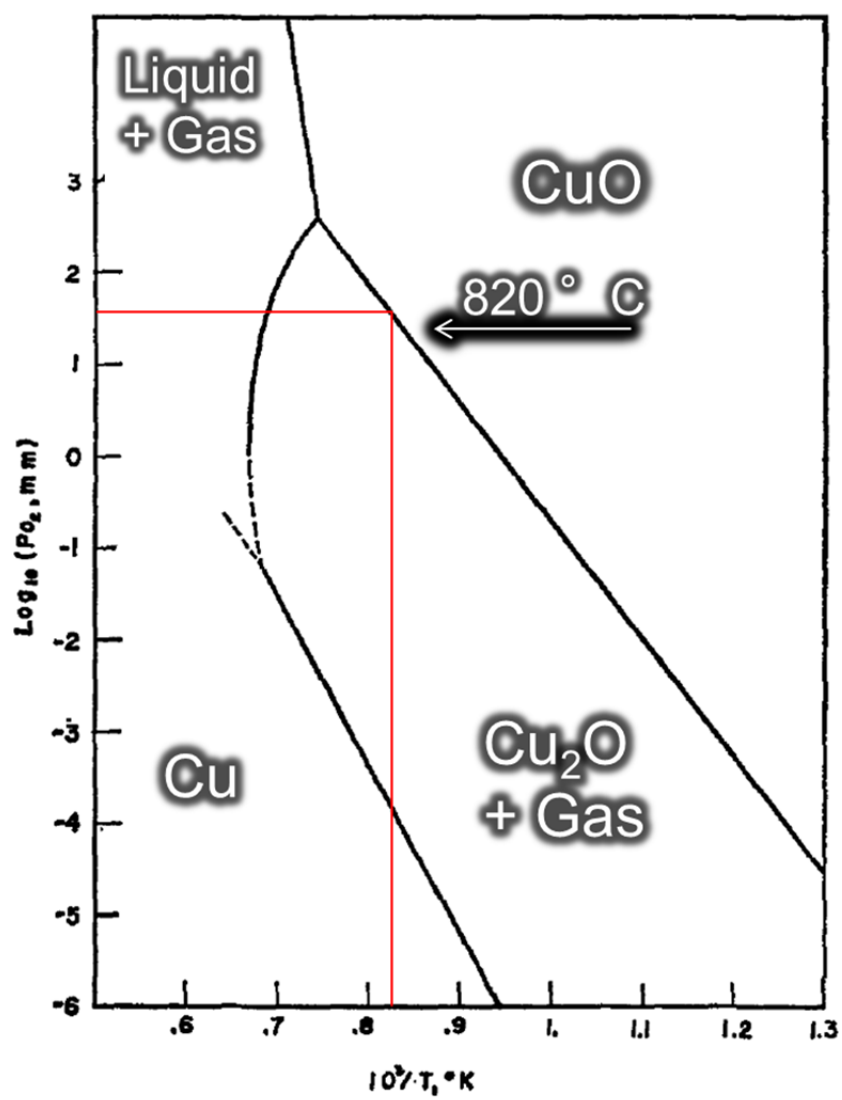
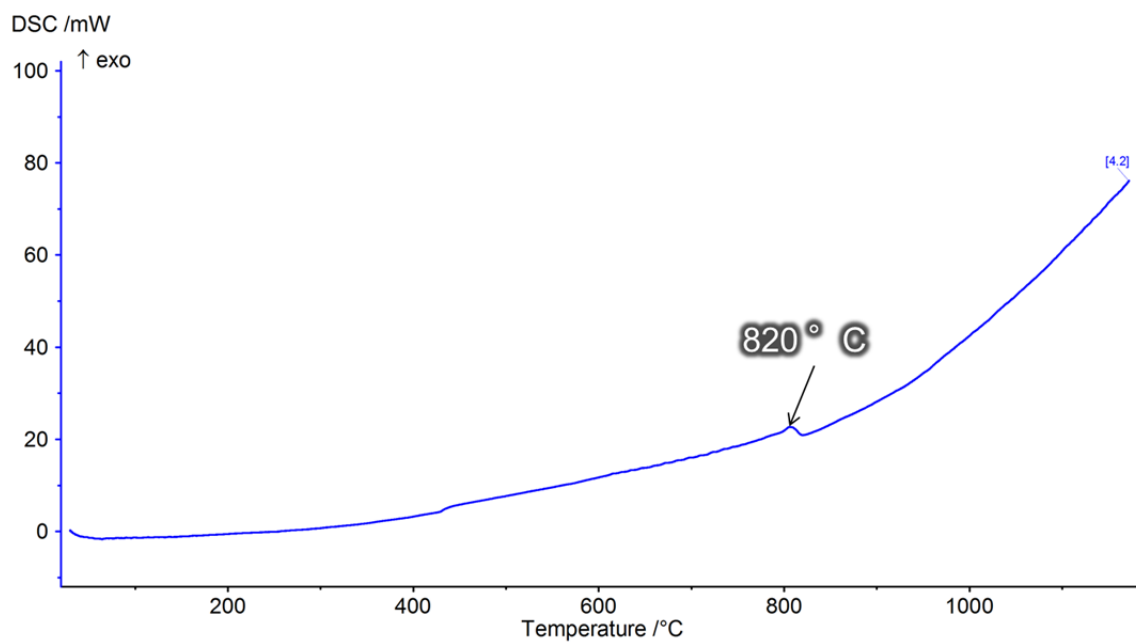
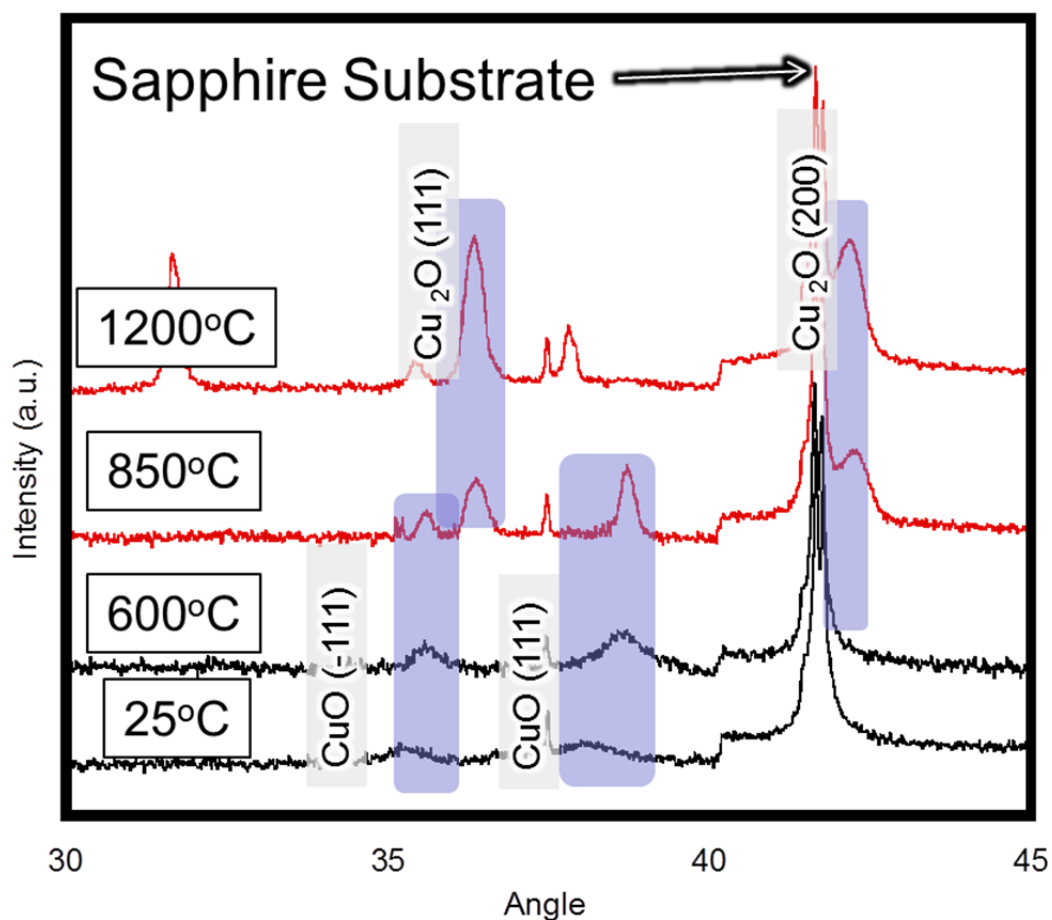


Figure 8.9 – Pressure-temperature diagram for  $\text{Cu}_x\text{O}_y$  [189]



**Figure 8.10-** Differential scanning calorimetry of a 400nm CuO thin film on sapphire at 5K/min ramp rate in Argon.



**Figure 8.11-** X-ray diffraction data for 400nm CuO film at 25°C, 600°C, 850°C and 1200°C demonstrate the transition of CuO to Cu<sub>2</sub>O after 800°C.

While the nature of this explosive reactive mechanism is not entirely understood and more testing is required, the behavior of product ejection during reaction can be taken advantage of. A particular note of interest is that while CuO layer is the outermost constituent both aluminum and copper species are detected by the mass spectroscopy. As previously reported by Zachariah et al.[Citation], in addition to time of flight spectroscopy during rapid anneal platinum wire testing sample reactants can be collected and analyzed post reaction if explosively ejected from the platinum wire. Figure 8.12 contains the location of the collection substrate and its proximity to the exploding platinum wire. Figures 8.13 a and

8.13b are the SEM and energy dispersive x-ray spectroscopy (EDS) results of this post anneal event which reveal a spherical particle morphology. This microstructure is indicative of materials that solidified from the molten state. The EDS spectra of an individual particle reveals also that the particulate is made up of two main domains namely the red area being populated mostly by copper at 77 atomic percent copper, 20 atomic percent oxygen, and 3 atomic percent aluminum. The area shaded blue corresponds to alumina with 35 atomic percent Al, 64 atomic percent oxygen and 1 atomic percent copper. The results of this analysis show that a thermite reaction did indeed occur from the resulting distribution of the chemical composition in the particles.

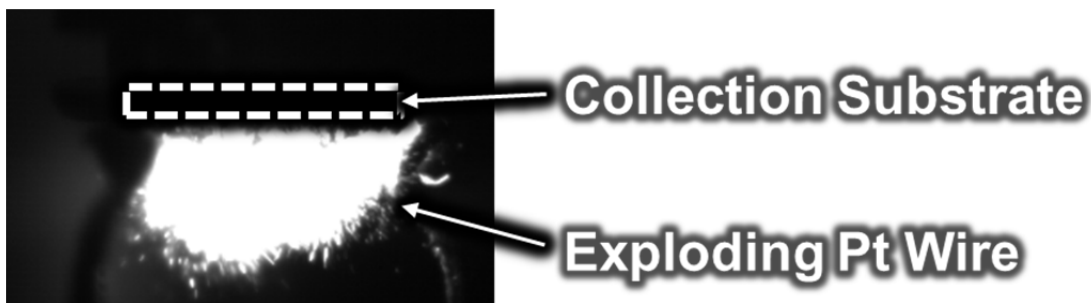


**Figure 8.12-** Still frame from high speed photography showing the collection geometry of sample products.

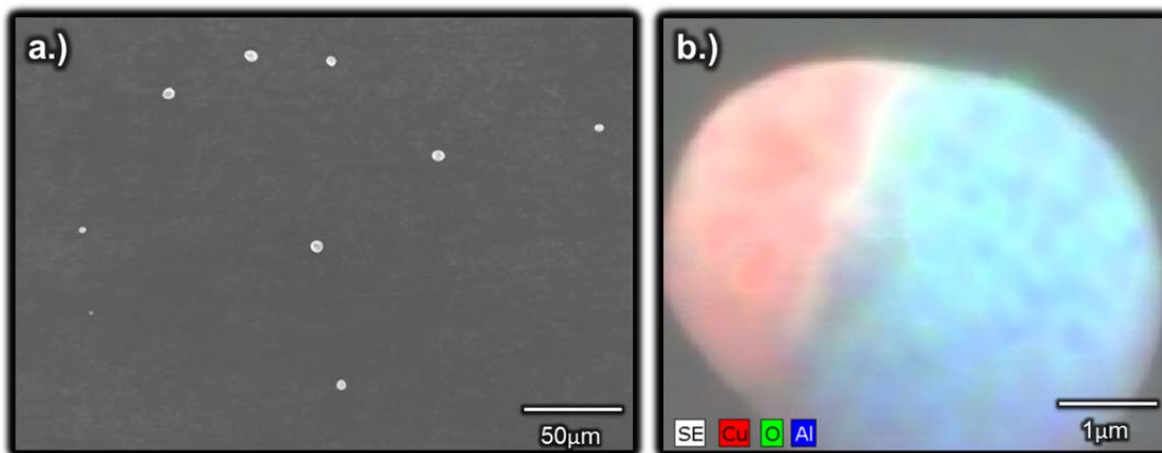


**Figure 8.13-** SEM micrograph a.) & b.) of post reaction products collected after sample ejection post ignition from the 10 bilayer Al/CuO nanolaminate coated Pt wire.

## 8.4- Ignition Temperature Modeling

In an effort to acquire further insights into the behavior of the thin-film thermite samples analysis of the data was undertaken in an attempt to ascertain activation energy and diffusion data characteristic of this reaction. Due to the nature of these thin film reaction can only occur in one direction and as has been demonstrated very capable of auction exchange in the solid-state. Therefore mass transport can be studied in this light. The rate of change of temperature over time or the heating rate is equal to one over the heat capacity times the heat generated during the reaction as seen in the first equation below. The heat generated by the reaction is proportional to the number of interfaces in a thin-film thermite, the interfacial area of an interface the heat of the reaction and the overall flux the material at the interface as demonstrated in second equation below. The mass transport across one interface is explained by the Arrhenius behavior given by Fick in third equation below. Combining these equations and solving for temperature yields fourth equation below, where the ignition temperature is defined as the point where the material self-heats faster than the energy supplied by the wire.

$$\frac{dT}{dt} = \frac{1}{C_p} \dot{Q}_{rxn}$$

$$\dot{Q}_{rxn} = nA \Delta H_{rxn} J$$

$$J = \nabla c D_o e^{\left(\frac{-E_a}{RT}\right)}$$

$$T_{ign} = -\frac{E_a}{R} \left( \ln \left( \frac{(5 \times 10^5 \text{ K/s}) C_p}{n \Delta H_{rxn} \nabla c A D_o} \right) \right)^{-1}$$

The two unknowns in this equation are the activation energy and the diffusion constant. Varying reports on both parameters make using any literature data suspect. Therefore they are left as variables for multivariable analysis. Experimental versus measured ignition temperatures are shown in figure 8.14. The best fit found for this experimental data yields an activation energy of 0.2 eV and the diffusion coefficient of  $7.1 \times 10^{-13} \text{ m}^2/\text{s}^2$ . Both of these values are significantly different than previously reported for aluminum and copper oxide [37, 60, 190, 191]. The activation energy for this reaction is much lower than that found in other reports in the literature and in chapter 4. The mechanism responsible for depression of the activation energy demands more characterization and analysis however due to the columnar morphology of the multilayers deposited on platinum wire it's possible that the jagged interfaces and the rough morphology yield diffusion pathways that support elevated mass transport than previously seen [191]. Despite the uncertainty of the reaction mechanism the results from this rapid annealing experiment point to a diffusion controlled reaction that rapidly reacts below the melting point of all constituents. The results from this experiment also show a possible transition from micro-sized domains to nano sized domains where the behavior of the fewer bilayer samples mimics that of micron sized energetic particulates and once a relative sized domain is decreased namely the bilayer thickness, reaction becomes more characteristic of the nano regime behavior [57, 105, 132].

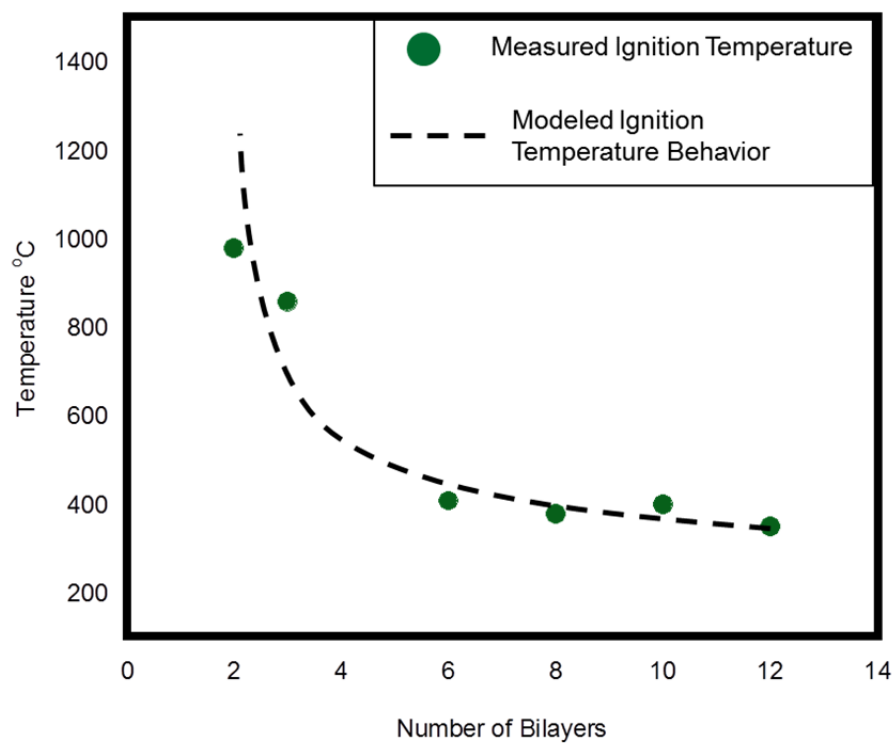


**Figure 8.14-** Ignition temperatures computed vs. predicted as a function of number of bilayers. The best fit ( $R^2$  coefficient of 0.94) was found to occur with  $E_a=20$  kJ/mol and  $D_o=7.1 \times 10^{-13}$  m<sup>2</sup>/s.

## 8.5 Conclusion

Thin Pt wires were coated with thin film thermite reactants pairing aluminum with cupric oxide. Temperature jump coupled with mass spectroscopy experiments were done on the thin laminate films with a variation of interfacial density and reaction distance while the total volume of reactants held constant. The temperatures of ignition were determined to decrease as a function of decreasing bilayer thickness. Ignition temperatures ranged from above the melting temperature of aluminum for samples with 3 or fewer bilayers, and below the melting temperatures of Al and the Al-Cu eutectic melt to 400°C. A simple ignition model was devised to estimate the activation energy of the reaction process that was found to be lower than any reported values for the activation energy of diffusion through alumina. The results yield the lowest experimental value for Al/CuO thermite ignition temperature and corresponding activation energy and supports the case for solid state diffusion especially within this sample geometry.

## 9. Eutectic Melting Effect on Energy Release

### 9.1 Introduction

The activation energies of the Al/CuO and Zr/CuO exothermic oxygen exchange reactions in chapter 4 were computed via Kissinger analysis. In the Zr/CuO system the reaction that takes place via a solid state diffusion reaction where exothermic activity is released before any constituent melted. It was found that the aluminum copper oxide system exhibited two regimes dependent upon the number of bilayers deposited. Fewer bilayers and thicker spacing yielded a higher activation energy of 1.4 eV and as bilayer thickness decreased and the number of bilayers increased a lower characteristic activation energy of 0.5 eV was determined. This bimodal affect in the Al/CuO system was not seen in the Zr/CuO system despite similar length scales. The activation energy measured via the Kissinger analysis that is used as a standard measurable in the community is a complicated term that encompasses all reaction phenomena into one value. This “effective activation energy” is a measure of the energetic barrier required to be overcome before self-sustained exothermic reaction can take place. The true activation energy should not change as reactant spacing is varied unless the dominating reaction mechanism has changed. It is believed that the difference in activation energy regimes seen in the Al/CuO thermite system is evidence of one such mechanistic change. It was reasoned that the higher activation energy regime in the Al/CuO that occurred after the Al melting point corresponded to melt dependent mechanism, where the higher transport values of the molten phase increased the reaction rate to the point of self-sustaining energy release. The main mechanism in lower activation energy regime was considered to be solid state ion transport because exothermicity is seen below the aluminum melting point of 660°C. With this reaction pathway more interfacial density increases the number of reaction sites which generate enough heat to become self-sustaining once a critical interface density is reached. This transition is observed for samples with four or more bilayers with the thickness of 400 nm and below, and the exothermic behavior peaks around 550°C.

One aspect left out of the analysis chapter 4 is the more nuanced interpretation of why the aluminum copper oxide system exhibits to activation energies. The decreasing size of reacting distances that occur in nano energetics speed up energetic release compared to their macroscopic counterparts because of the decreased time needed for the reactants to diffuse towards one another.

As has been discussed throughout this manuscript thermite oxidation is influenced by many factors including heating rate at which the reaction is initiated at. The literature on oxygen exchange reactions regarding thermite constituents underlines the importance of increased species mobility at slow heating rates once one of the constituents, namely the metal, barrier [22, 24, 28, 29, 32, 102, 104, 135, 186, 188, 192-195]. The melting of the metal is said to also affect the high-speed initiation behavior of thermite nanoparticles as well. Exactly what mechanism is at play at high heating rates is still contested. One theory called the melt dispersion mechanism (MDM) claims that in nano particle spherical geometries at high heating rates molten metal creates a critical stress in the surrounding solid oxide shell that ruptures the diffusion barrier explosively, which disperses the molten metal in small clusters that proceed to oxidize uninhibited by a diffusion barrier [28, 102, 132, 135, 186, 192, 196]. This understanding however does not illuminate why nanoparticles energetics react considerably below the bulk metal constituents melting temperature. The other predominant theory for exothermic oxygen exchange reactions is that at small length scales diffusion in the solid-state can lead to self-sustaining reaction and at high heating rates the mechanism of oxidation is a complicated relationship between the melting of the metal the gas release of the oxide and the size of the constituents [24, 29, 32, 186, 188].

The liquidus phase therefore is clearly an important factor in how thermite reactions proceed. As was just mentioned it is widely accepted that once a liquid phase is present the transport of any species will be accelerated. A consultation of the differential scanning calorimetry experiments done on the Al/CuO system in chapter 4 in figure 9.1 reveal an interesting trait, specifically the reaction proceeds at a much earlier temperature of around 550° which

corresponds almost exactly with the melting eutectic temperature of an aluminum copper intermetallic seen in figure 9.2.

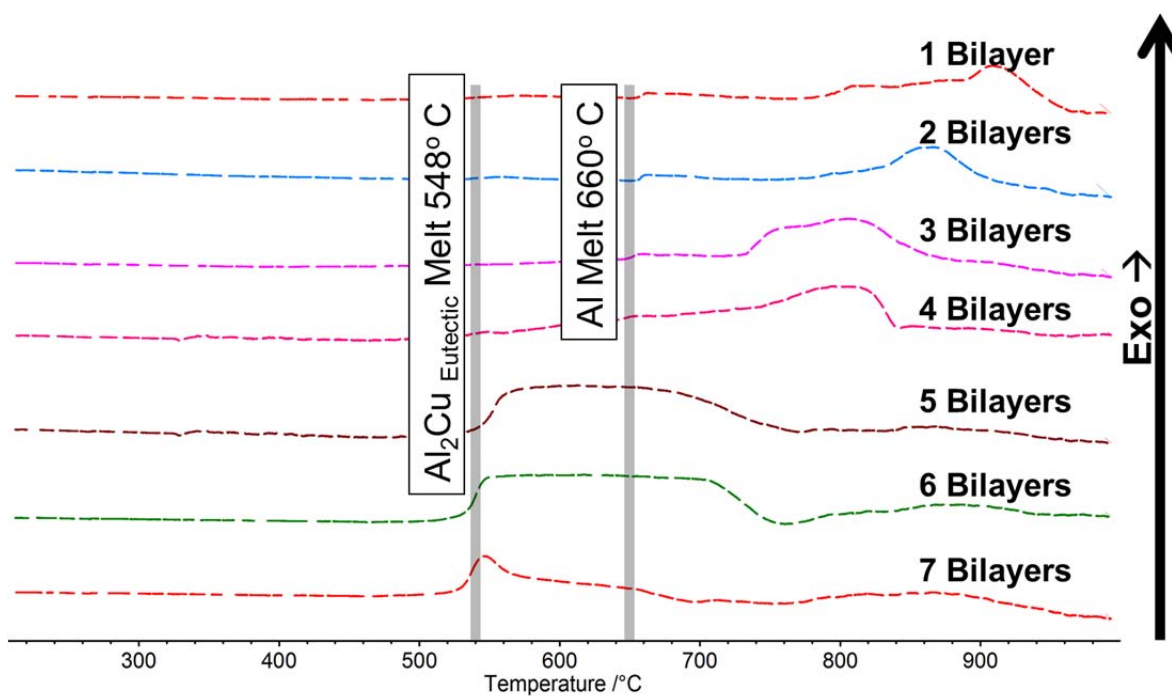


**Figure 9.1-** Differential scanning calorimetry of Al/CuO thin film thermite samples with varying number of bilayers[193].

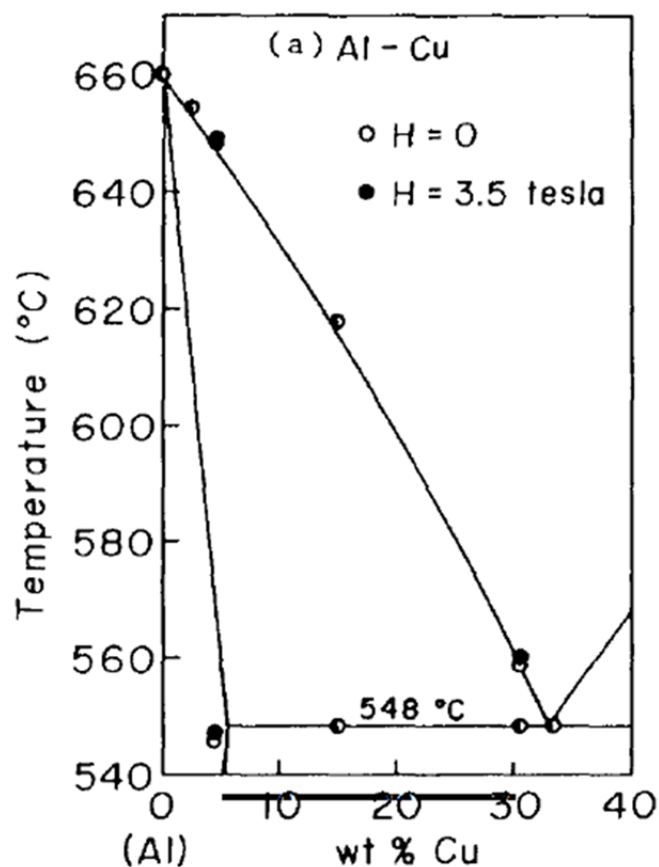


**Figure 9.2-** Phase Diagram of Al-Cu displaying the aluminum rich portion where the low temperature eutectic melt occurs at 548 °C[193].

This phase is aluminum rich and suggests that perhaps the Al/CuO thermite thin-film system at slow heating rates only undergoes exothermic reaction once a constituent has melted not does not react in the solid state as previously presumed. Previous studies by Dreizin et.al and others report the presence of a eutectic melt in arrested reactive milled nano energetics [22, 104, 194]. They postulate that in order for this to accelerate exothermic activity the intermetallic must be present in the powder before any heat treatment has commenced. The intermetallic was shown to be formed during the milling process of the two thermite materials.

## 9.2 Intermetallic Phase Identification

### 9.2.1 Hot Stage XRD

Hot stage XRD phase identification was implemented with the intent of testing phase evolution of the Al/CuO thermite and probing the intermediate interface phase characteristics. A thin film Al/CuO 6 bilayer nanolaminate was sputter deposited on silicon (as described in previous chapters) and placed in an X-ray hot stage sample holder under an argon environment. The sample was annealed at 5K/min and diffraction spectra was collected from 32-52° 2 $\theta$  in a bragg-brentano geometry in 1 degree increments. Several temperature traces from this experiment at varying stages of the annealing process are plotted in figure 9.3. The phases that evolve from this study show the evolution of the starting CuO phase to the less oxygen dense Cu<sub>2</sub>O and finally metallic Cu. No trace of intermetallic Al<sub>2</sub>Cu is detected. It is possible that the interface cannot be analyzed using x-ray diffraction techniques because the intermediate intermetallic that is thought to have formed at the interface will most likely be amorphous or nano-crystalline rendering the phase undetectable for diffraction techniques.

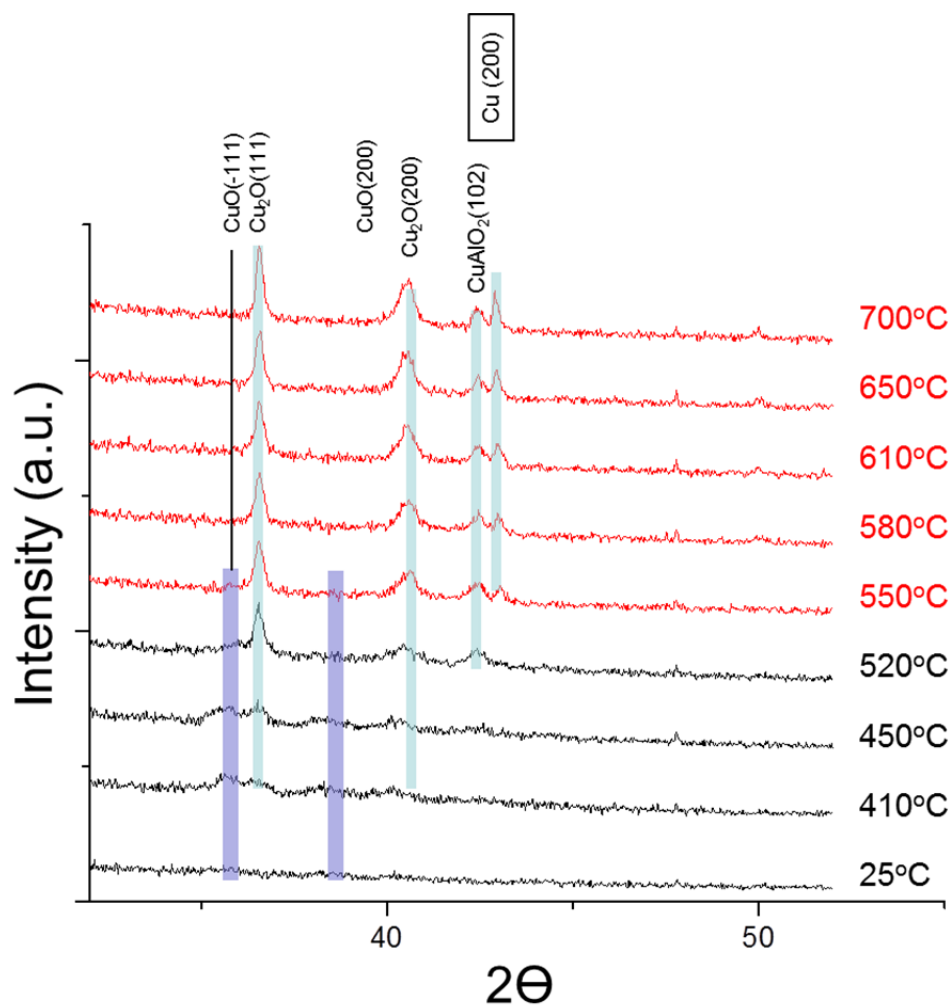


**Figure 9.3-** XRD of Al/CuO 6 bilayer film at different temperatures indicating the presence of copper metal. No evidence of any intermetallic is seen.

### 9.2.2 Auger Electron Spectroscopy

Employment of x-ray photoelectron and Auger electron spectroscopy was implemented as another means to determine the presence of intermetallic phase between copper oxide and aluminum. The surface analysis chamber previously described in chapter 5 was used to probe the surface for any possible intermediate phases. Copper oxide 10 nm thin films were deposited on silicon substrates introduced into the ultrahigh vacuum system and sequential

amounts of aluminum were deposited on the surface. After the deposition of Al on the CuO, the Cu 2p 3/2 peak shifts to a lower binding energy from 933.3 eV to 932.5 eV which is indicative of the reduction of copper oxide as seen in chapter 5, however a more rigorous analysis of the data collected compares the auger electron peaks from the Cu 2p 3/2 to the auger peaks from other copper compounds. It is common practice to plot the Auger electron kinetic energy versus the photo electron binding energy of the corresponding orbital and compare measured values to known standards [197].

The auger peaks of interest have kinetic energies centered around 918 eV. Knowing this, the scanning range on the photoelectron detection device must be therefore adjusted to a lower binding energy to account for the correction the machine makes for assuming only photoelectrons are being collected. Namely, the kinetic energy of a photoelectron is the primary event that XPS detectors scan for and take into account the incident energy of the x-ray radiation to display the results in binding energy. This relation between the kinetic energy (KE), incoming radiation ( $h\nu$ ), and the binding energy (BE) is shown in the equation below, where  $\phi$  is the energy correction of the machine that accounts for a few eV lost to the machine by the electron as its being absorbed.

$$KE = h\nu - BE - \phi$$

The kinetic energy of the electrons is then adjusted to display the binding energy of the electrons. This correction is applied to all incoming electrons including auger electrons as well, and artificially reports the auger peaks at lower energies. Therefore an auger electron with an energy of 918 eV when collected with a corresponding Al anode source of 1486.6 eV incoming radiation, the auger scanning range was centered at 568 eV. Auger electron data was gathered and the results of which are displayed in figure 9.4. In this figure the black markers represent standard literature values with their corresponding phases next to them. The measured values represented by the red markers indicate the auger electron to binding energy values do not correspond to a pre-existing intermetallic. The lack of direct evidence to support the notion that pre-existing aluminum copper intermetallic is vexing and suggests then that in order to explain the eutectic melt behavior the intermetallic must be formed at

some intermediate reaction point before the bulk exothermic activity takes place. This implies that at the oxide metal junction, at some intermediate reaction time, aluminum atoms diffusing through the terminal thermite product phase of alumina may arrive at the interface of the alumina and copper matrix before oxygen traversing from the copper oxide does. In this scenario as the reaction progresses the copper phase is leached of oxygen such that the unreacted diffusing oxygen is required to move across an growing oxygen poor environment of copper. This then generates a diffusion inequality where the aluminum and copper would be able to interact and form an intermetallic before more diffusing oxygen could reach the interface.

There is a slight trend present in the oxidation state of the copper as more Al is deposited on the surface. The electronic environment of copper atoms shifts from a cuprous oxide influence to that of a more metallic copper phase. This trend is indicative of a layer of oxygen deficient copper oxide, or an oxygen depletion region. This depletion is noted in figure 9.4 as the character of the copper becomes more metallic has more oxygen reacts with the deposited aluminum.

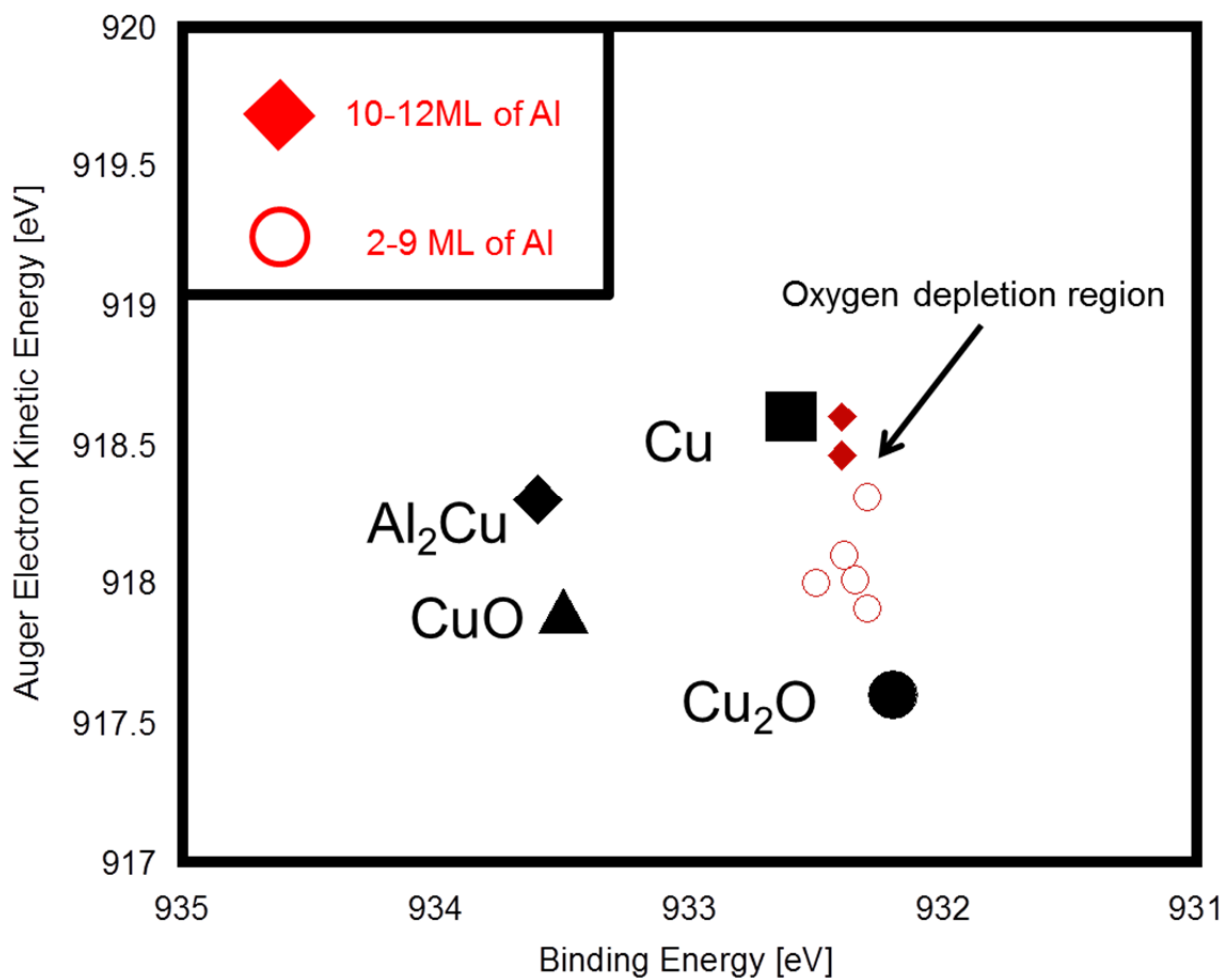


**Figure 9.4-** Auger electron kinetic energy of the Cu LMM transition plotted against the binding energy of the Cu 2p 3/2 for known phases of copper and oxygen and experimentally obtained data.

This behavior can be qualitatively seen in another thermite couple at the interface of copper oxide and zirconium with an cross section energy x-ray dispersive spectroscopy EDS map in figure 9.5. In this example it can be seen that there is an overlap of zirconium and oxygen which corresponds to the product phase zirconia and in the copper film there is a gradient of oxygen at the interface that decreases in concentration with proximity to the reactive metal

which supports the assertion that the reducing metal could come in contact with the product metal during the reaction.

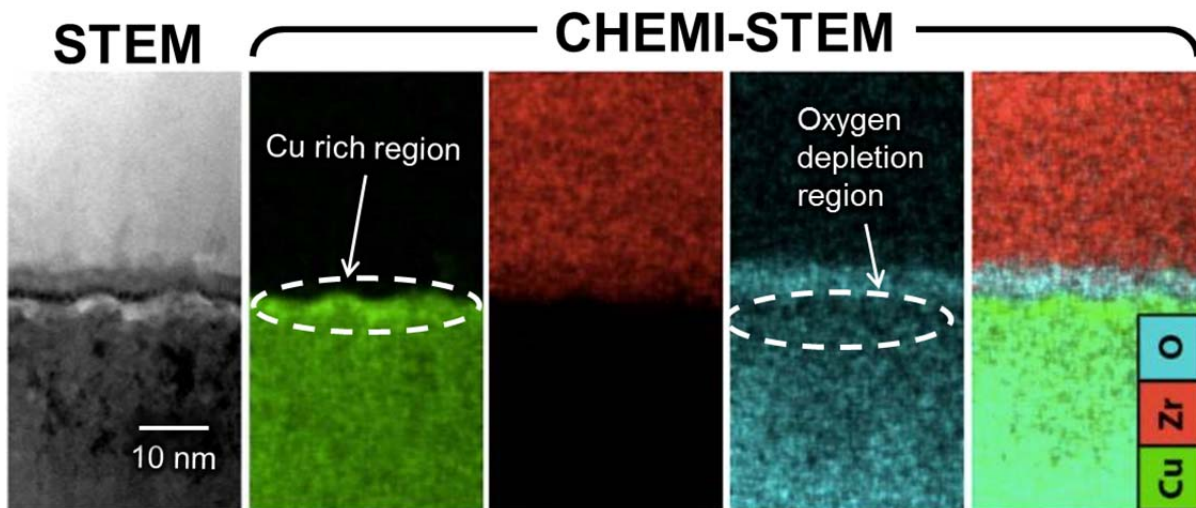


**Figure 9.5-** EDS map of Zr/CuO interface showing a Cu rich region just below the overlapping layer of zirconium and oxygen.

### 9.3 Eutectic Thermite Testing

To further test this hypothesis of a eutectic melting mechanism affecting a thermite reaction another thermite system consisting of magnesium and copper oxide was chosen. As demonstrated in chapter 3 magnesium has a relatively similar thermodynamic driving force for oxidation per mole oxygen as aluminum. Magnesium also forms two low melting temperature intermetallics with copper seen in the Mg-Cu phase diagram in figure 9.6. Thin-film thermite samples of magnesium and copper were then fabricated and tested in the same manner as the aluminum and copper oxide thin film samples with varying bilayer thicknesses. The parameters of deposition thicknesses and bilayers are presented in table 9.1.

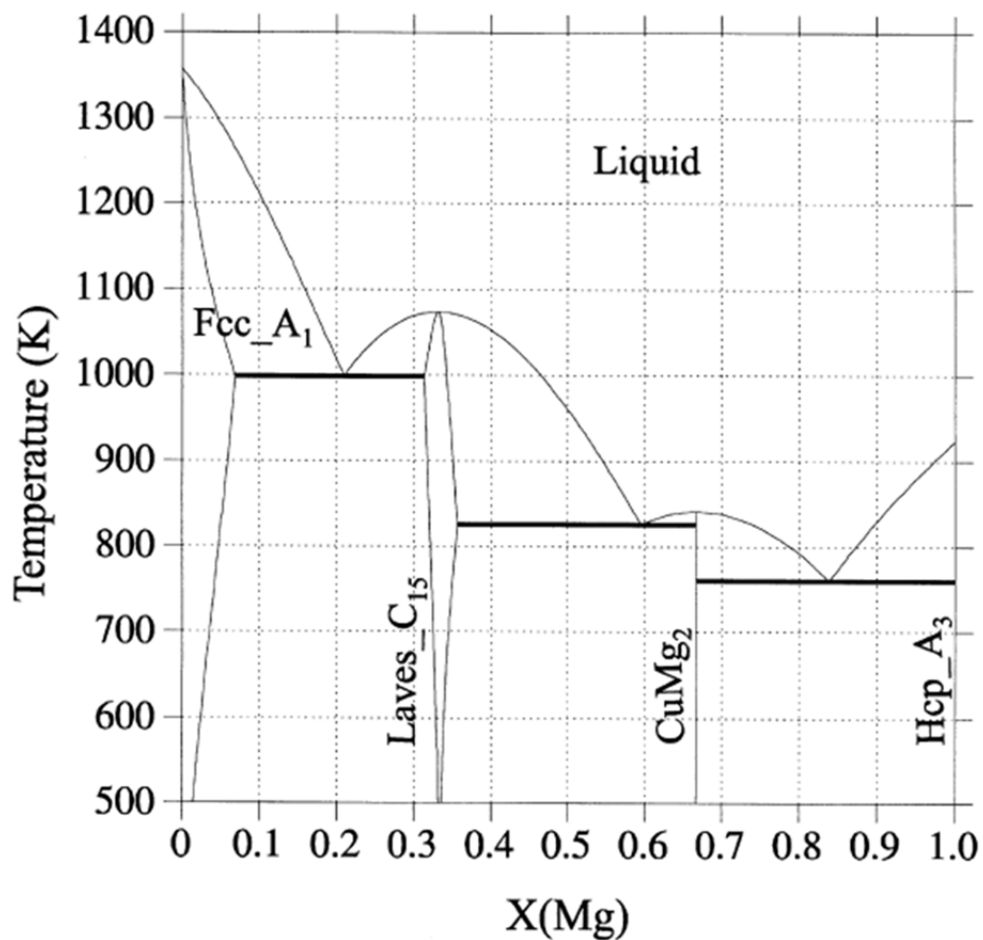
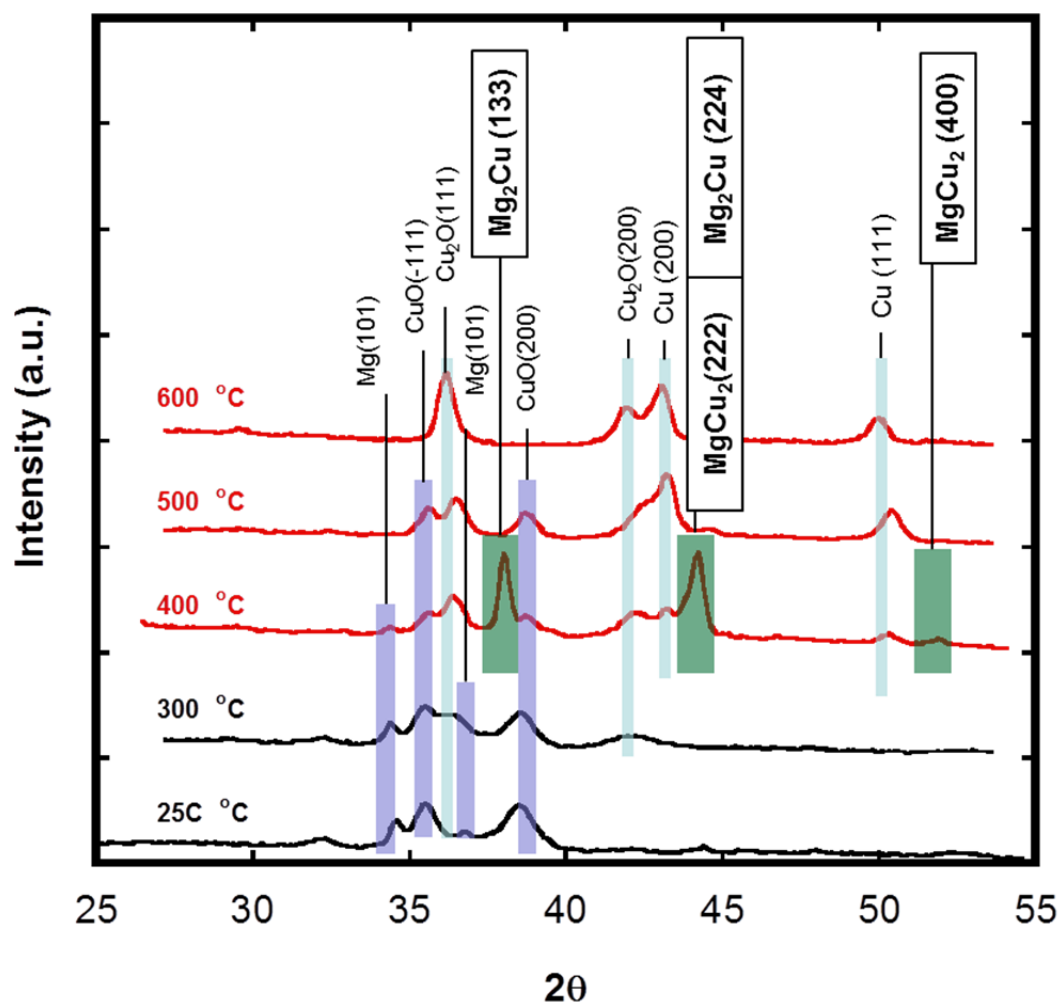


Figure 9.6- Mg-Cu Phase diagram [195]

Table 9.1- Mg/CuO thin film thermite deposition parameters.

Multilayered Mg/CuO Thermite				
Number of Bilayers	Total Thickness [nm]	Bilayer thickness [nm]	CuO thickness [nm]	Mg thickness [nm]
1	1475	1475	700	775
2	1474	737	350	387
3	1473	491	233	258
4	1476	369	175	194
5	1475	295	140	155
6	1482	247	117	130
7	1477	211	100	111
8	1476	184.5	87.5	97

The thicknesses were kept close to the thicknesses in the Al/CuO system while maintaining stoichiometric equivalence. The Mg/CuO thermite samples were annealed in varying incremental temperatures and XRD was performed ex situ. The final copper metal phase was used to track the onset of reaction going to completion figure 9.7. In addition to the presence of copper metal, two intermetallic phases can be distinguished at 400 °C that extinguish after the 500°C trace. The appearance and then the subsequent elimination of the intermetallic  $Mg_2Cu$  and  $MgCu_2$  diffraction peaks support the theory that the two metals involved in the thermite reaction will reside next to one another for enough time during slow heating rates to form intermetallics before the terminal phases can form. This points to an even more intricate interaction between the reactants than was taken into account at the beginning of this study. It was initially thought that the intermetallics were formed as a result of deposition that had been previously seen by in other works[104]. Differential scanning calorimetry was also performed in an identical manner to that described in chapters 3 and 4. Figure 9.8 results from this thermal analysis. Each trace on this graph represents a different Mg/CuO thin film sample with a different number of bilayers and individual layer thicknesses. As the bilayers were decreased in size and increased in number a similar shift to lower reaction temperatures was seen. Highlighted on this graph are the two eutectic points of magnesium copper intermetallics with one appearing at 540°C and another at 480°C. The onset of exothermic activity appears to shift from the higher eutectic melting temperature to the lower eutectic melting temperature which points to two critical interface densities of intermetallic composition. The higher melting temperature eutectic appears to initiate the dominant exothermic event seen for the thickest bilayered samples. As the thickness is decreased and the interfacial density is increased the lower temperature eutectic melt begins to dominate the exothermic behavior.



**Figure 9.7-** XRD of the 8 bilayer Mg/CuO thin film with evidence of intermetallic formation

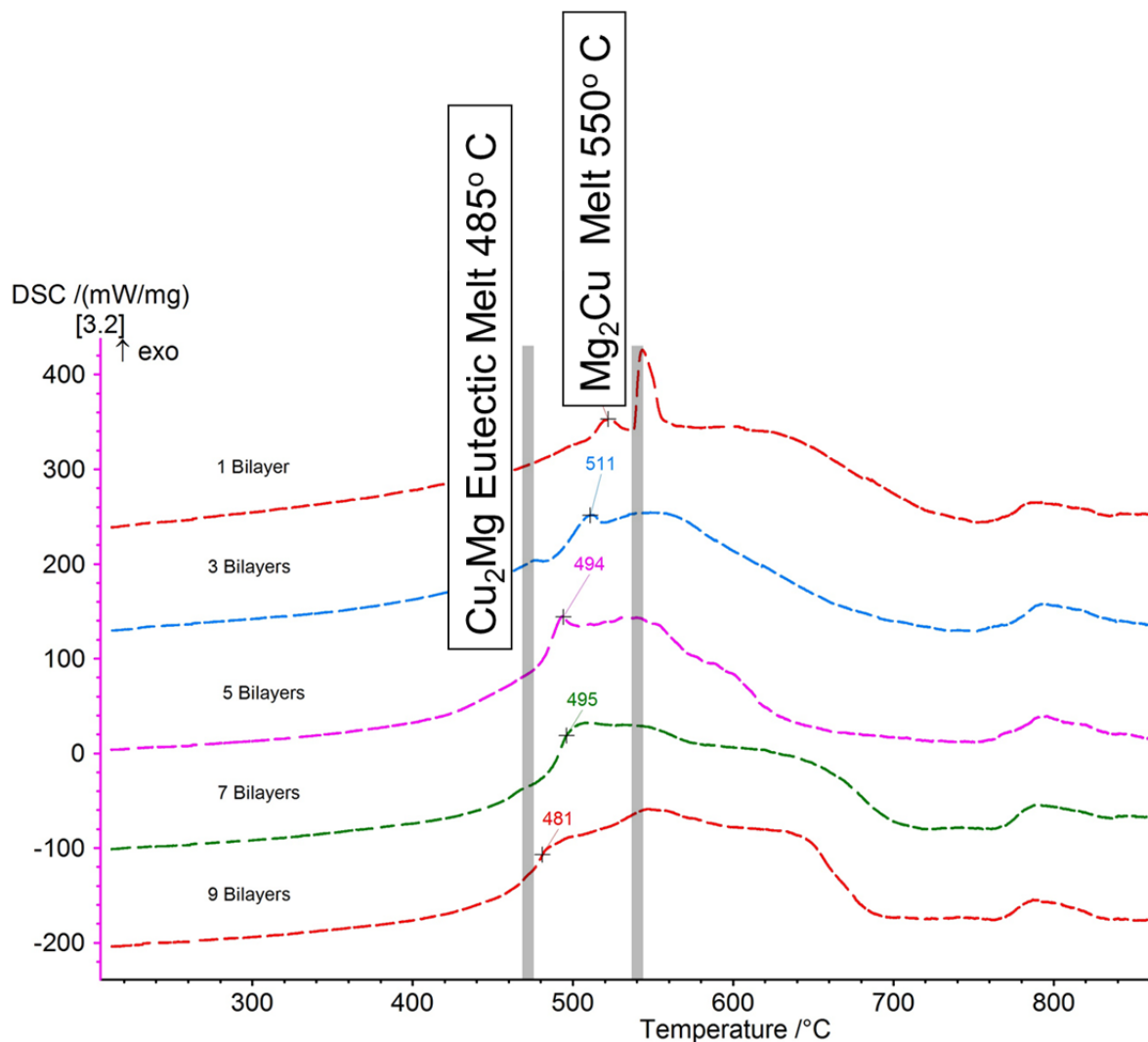


**Figure 9.8** - DSC of Mg/ CuO multilayered thermite displaying the eutectic influence on the exothermic behavior

## 9.4 Conclusion

The Mg/CuO thermite testing coupled with the Al/CuO data support the idea that low melting intermetallic eutectics that form as intermediate products between the terminal metal and the initial reducing reactive metal play a role in oxygen exchange reactions at slow time scales. This behavior then adds another dynamic into how nano energetic composites react

and ultimately as another design metric for scientists to employ and consider while fabricating energetic chemistries. The rapid testing done in chapter 8 with temperature and temporal resolution however show ignition temperatures below that of even the eutectic melting aluminum copper oxide. It is of the authors believe that the high heating rate of the platinum wire experiment is at such an elevated rate the eutectic phase does not form because the reaction happens too quickly and the intermetallic is not given enough time to materialize. It then stands to reason that within the Al/CuO system exothermicity is a function of heating rate where if the heating rate is fast enough it will display predominately a solid state diffusion mechanism whereas upon slow annealing self-sustaining reaction is not reached until a liquidus phases are present. Future work into the mechanism of magnesium and copper oxide at high heating rates would test this theory with another chemical system. It is believed that as the heating rate is increased and the size constraints are decreased to such a point many thermite couples will behave in the same way in the solid state.

## REFERENCES

- [1] F. Burton, Fire: The Spark that Ignited Human Evolution, University of New Mexico Press, Albuquerque NM, USA, 2009.
- [2] R. Wranham, Catching Fire, Basic Books, New York, 2009.
- [3] G.I. Brown, The Big Bang: A History of Explosives, Sutton Publishing, 1998.
- [4] P. Macinnis, Rockets: Sulfer, Sputnik and Scramjets, Allen & Unwin, Australia, 2003.
- [5] T.S. Taylor, Introduction to Rocket Science and Engineering, CRC Press, Boca Raton FL, 2009.
- [6] U. Teipel, Energetic Materials: Particle Processing and Characterization, 2005.
- [7] J.W. Forbes, Shock Wave compression of Condense Matter: Shock Wave and High Pressure Phenomena, Springer-Verlag, Berlin, Heidelberg, 2012.
- [8] Y.B. Zel'dovich, Physics of Shock Waves and High-Temperature Hydrodynamic Phenomena Vol. 1, Academic Press, New York and London, 1966.
- [9] H. Goldschmidt, C. Vautin, J. Soc. Chem. Ind, 19 (1898) 543-515.
- [10] J.D. Hunley, The Development of propulsion technology for U.S. Space-Launch Vehicles, 1926-1991, Texas A&M University Press, 2007.
- [11] A. Reshetov, V. Shneider, N. Yavorovsky, Mendeleev All-Union Society Abstracts, 1 (1984).
- [12] F. Tepper, G. Ivanov, M. Lerner, V. Davidovich, R.I. Iit, Energetic formulations from nanosize metal powders, I I T Research Inst, Chicago, 1998.
- [13] M.M. Mench, K.K. Kuo, C.L. Yeh, Y.C. Lu, Combust. Sci. Technol., 135 (1998) 269-292.
- [14] C.E. Aumann, G.L. Skofronick, J.A. Martin, J. Vac. Sci. Technol. B, 13 (1995) 1178-1183.
- [15] R.A. Yetter, G.A. Risha, S.F. Son, Proc. Combust. Inst., 32 (2009) 1819-1838.
- [16] S.F. Son, B.W. Asay, T.J. Foley, R.A. Yetter, M.H. Wu, G.A. Risha, Journal of Propulsion and Power, 23 (2007) 715-721.

- [17] G.M. Dutro, R.A. Yetter, G.A. Risha, S.F. Son, *Proc. Combust. Inst.*, 32 (2009) 1921-1928.
- [18] S.M. Begley, M.Q. Brewster, *Journal of Heat Transfer-Transactions of the Asme*, 129 (2007) 624-633.
- [19] D.E.G. Jones, R. Turcotte, R.C. Fouchard, Q.S.M. Kwok, A.M. Turcotte, Z. Abdel-Qader, *Propellants Explosives Pyrotechnics*, 28 (2003) 120-131.
- [20] J.T. Mang, R.P. Hjelm, S.F. Son, P.D. Peterson, B.S. Jorgensen, *Journal of Materials Research*, 22 (2007) 1907-1920.
- [21] K. Park, D. Lee, A. Rai, D. Mukherjee, M.R. Zachariah, *J. Phys. Chem. B*, 109 (2005) 7290-7299.
- [22] B. Rufino, F. Boule'h, M.V. Coulet, G. Lacroix, R. Denoyel, *Acta Materialia*, 55 (2007) 2815-2827.
- [23] A. Prakash, A.V. McCormick, M.R. Zachariah, *Nano Lett.*, 5 (2005) 1357-1360.
- [24] A. Rai, K. Park, L. Zhou, M.R. Zachariah, *Combustion Theory and Modelling*, 10 (2006) 843-859.
- [25] K. Sullivan, G. Young, M.R. Zachariah, *Combust. Flame*, 156 (2009) 302-309.
- [26] K. Sullivan, M.R. Zachariah, *Journal of Propulsion and Power*, 26 (2010) 467-472.
- [27] K.T. Sullivan, N.W. Piekiet, C. Wu, S. Chowdhury, S.T. Kelly, T.C. Hufnagel, K. Fezzaa, M.R. Zachariah, *Combust. Flame*, 159 (2012) 2-15.
- [28] V.I. Levitas, *Combust. Flame*, 156 (2009) 543-546.
- [29] D. Lee, R. Mahadevan, H. Sakurai, M.R. Zachariah, *Characterization of Nanoparticle Composition and Reactivity by Single Particle Mass Spectrometry*, in: *Defense Applications of Nanomaterials*, American Chemical Society, 2005, pp. 211-226.
- [30] B.J. Henz, T. Hawa, M.R. Zachariah, *Journal of Applied Physics*, 107 (2010) 024901-024909.
- [31] D.A. Firmansyah, K. Sullivan, K.S. Lee, Y.H. Kim, R. Zahaf, M.R. Zachariah, D. Lee, *J. Phys. Chem. C*, 116 (2012) 404-411.
- [32] S. Chowdhury, K. Sullivan, N. Piekiet, L. Zhou, M.R. Zachariah, *J. Phys. Chem. C*, 114 (2010) 9191-9195.

- [33] R. Schefflan, S. Kovenklioglu, D. Kalyon, M. Mezger, M. Leng, *Journal of Energetic Materials*, 24 (2006) 141-156.
- [34] D.E. Eakins, N.N. Thadhani, *Acta Materialia*, 56 (2008) 1496-1510.
- [35] M. Schoenitz, T. Ward, E.L. Dreizin, Preparation of energetic metastable nano-composite materials by arrested reactive milling, in: R. Armstrong, N. Thadhani, W. Wilson, J. Gilman, R. Simpson (Eds.) *Synthesis, Characterization and Properties of Energetic/Reactive Nanomaterials*, 2004, pp. 85-90.
- [36] M. Schoenitz, T.S. Ward, E.L. Dreizin, *Proc. Combust. Inst.*, 30 (2005) 2071-2078.
- [37] S.M. Umbrajkar, M. Schoenitz, E.L. Dreizin, *Thermochimica Acta*, 451 (2006) 34-43.
- [38] S. Brinker, *Sol-Gel Science: The Physics and Chemistry of Sol-Gel Processing*, Harcourt Brace Jovanovich Publishers, New York, 1990.
- [39] E. Gash Alexander, L. Simpson Randall, H. Satcher Joe, Direct Preparation of Nanostructured Energetic Materials Using Sol-Gel Methods, in: *Defense Applications of Nanomaterials*, American Chemical Society, 2005, pp. 198-210.
- [40] R.L. Simpson, T.M. Tillotson, L.W. Hrubesh, A.E. Gash, *Current*, (2000).
- [41] A.E. Gash, T.M. Tillotson, J.H. Satcher, J.F. Poco, L.W. Hrubesh, R.L. Simpson, *Chem. Mat.*, 13 (2001) 999-1007.
- [42] G. Li, X.B. Zhu, H.C. Lei, H.F. Jiang, W.H. Song, Z.R. Yang, J.M. Dai, Y.P. Sun, X. Pan, S.Y. Dai, *J. Sol-Gel Sci. Technol.*, 53 (2010) 641-646.
- [43] O.G. Cervantes, J.D. Kuntz, A.E. Gash, Z.A. Munir, *Combust. Flame*, 157 (2010) 2326-2332.
- [44] A.E. Gash, R.L. Simpson, T.M. Tillotson, J.H. Satcher, L.W. Hrubesh, in: *International Pyrotechnics Seminars*, 2000, pp. 1-15.
- [45] O.G. Cervantes, J.D. Kuntz, A.E. Gash, Z.A. Munir, *Combust. Flame*, 158 (2011) 117-122.
- [46] K.B. Plantier, M.L. Pantoya, A.E. Gash, *Combust. Flame*, 140 (2005) 299-309.
- [47] D. Prentice, M.L. Pantoya, B.J. Clapsaddle, *The Journal of Physical Chemistry B*, 109 (2005) 20180-20185.
- [48] M.A. Wall, *Microsc. Res. Tech.*, 27 (1994) 262-267.

- [49] S.M. Umbrajkar, S. Seshadri, M. Schoenitz, V.K. Hoffmann, E.L. Dreizin, *Journal of Propulsion and Power*, 24 (2008) 192-198.
- [50] C. Badiola, M. Schoenitz, X. Zhu, E.L. Dreizin, *Journal of Alloys and Compounds*, 488 (2009) 386-391.
- [51] D. Stamatias, X.Y. Zhu, M. Schoenitz, E.L. Dreizin, P. Redner, *Powder Technology*, 208 (2011) 637-642.
- [52] F.X. Jette, S. Goroshin, D.L. Frost, A.J. Higgins, J.J. Lee, *Propellants Explosives Pyrotechnics*, 37 (2012) 345-358.
- [53] R.V. Reeves, A.S. Mukasyan, S.F. Son, *Propellants Explosives Pyrotechnics*, 38 (2013) 611-621.
- [54] B. Chapman, *Glow Discharge Process*, New York, 1980.
- [55] J. Kwon, J.M. Ducéré, P. Alphonse, M. Bahrami, M. Petrantoni, J.-F. Veyan, C. Tenailleau, A. Estève, C. Rossi, Y.J. Chabal, *ACS Applied Materials & Interfaces*, 5 (2013) 605-613.
- [56] X. Zhou, R. Shen, Y. Ye, P. Zhu, Y. Hu, L. Wu, *Journal of Applied Physics*, 110 (2011) 094505-094506.
- [57] M. Petrantoni, C. Rossi, L. Salvagnac, V. Conedera, A. Esteve, C. Tenailleau, P. Alphonse, Y.J. Chabal, *Journal of Applied Physics*, 108 (2010) 084323-084325.
- [58] N.A. Manesh, K.R. Coffey, R. Kumar, Asme, in: *Proceedings of the Asme International Mechanical Engineering Congress and Exposition 2007*, Vol 8, Pts a and B: Heat Transfer, Fluid Flows, and Thermal Systems, ASME International Mechanical Engineering Congress and Exposition, Seattle Washington, USA, 2008, pp. 1189-1197.
- [59] K.J. Blobaum, a.J. Wagner, J.M. Plitzko, D. Van Heerden, D.H. Fairbrother, T.P. Weihs, *Journal of Applied Physics*, 94 (2003) 2923-2923.
- [60] K.J. Blobaum, M.E. Reiss, J.M. Plitzko, T.P. Weihs, *Journal of Applied Physics*, 94 (2003) 2915-2915.
- [61] A.S. Edelstein, R.K. Everett, G.Y. Richardson, S.B. Qadri, E.I. Altman, J.C. Foley, J.H. Perepezko, *Journal of Applied Physics*, 76 (1994) 7850-7859.
- [62] A.S. Edelstein, R.K. Everett, G.R. Richardson, S.B. Qadri, J.C. Foley, J.H. Perepezko, *Materials Science and Engineering a-Structural Materials Properties Microstructure and Processing*, 195 (1995) 13-19.

- [63] T.P. Weihs, T.W. Barbee, M.A. Wall, *Journal of Materials Research*, 11 (1996) 1403-1409.
- [64] K. Barmak, C. Michaelsen, G. Lucadamo, *Journal of Materials Research*, 12 (1997) 133-146.
- [65] M.E. Reiss, C.M. Esber, D.V. Heerden, A.J. Gavens, M.E. Williams, *Materials Science and Engineering A*, 261 (1999) 217-222.
- [66] A.J. Gavens, D.V. Heerden, A.B. Mann, M.E. Reiss, T.P. Weihs, I. Introduction, *Journal of Applied Physics*, 87 (2000) 1255-1263.
- [67] E. Besnoin, S. Cerutti, O.M. Knio, T.P. Weihs, *Journal of Applied Physics*, 92 (2002) 5474-5481.
- [68] J. Wang, E. Besnoin, A. Duckham, S.J. Spey, M.E. Reiss, O.M. Knio, M. Powers, M. Whitener, T.P. Weihs, *Appl. Phys. Lett.*, 83 (2003) 3987-3989.
- [69] A.S. Rogachev, A.E. Grigoryan, E.V. Illarionova, I.G. Kanel, A.G. Merzhanov, A.N. Nosyrev, N.V. Sachkova, V.I. Khvesyuk, P.A. Tsygankov, *Combustion Explosion and Shock Waves*, 40 (2004) 166-171.
- [70] M.J. Starink, *Int. Mater. Rev.*, 49 (2004) 191-226.
- [71] J. Wang, E. Besnoin, O.M. Knio, T.P. Weihs, *Acta Materialia*, 52 (2004) 5265-5274.
- [72] D.P. Adams, M.A. Rodriguez, C.P. Tigges, P.G. Kotula, *Journal of Materials Research*, 21 (2006) 3168-3179.
- [73] D.P. Adams, V.C. Hodges, M.M. Bai, E. Jones, M.A. Rodriguez, T. Buchheit, J.J. Moore, *Journal of Applied Physics*, 104 (2008).
- [74] a.S. Rogachev, *Russian Chemical Reviews*, 77 (2008) 21-37.
- [75] D.P. Adams, M.A. Rodriguez, J.P. McDonald, M.M. Bai, E. Jones, L. Brewer, J.J. Moore, *Journal of Applied Physics*, 106 (2009).
- [76] R. Knepper, M.R. Snyder, G. Fritz, K. Fisher, O.M. Knio, T.P. Weihs, *Journal of Applied Physics*, 105 (2009) 083504-083504.
- [77] M.A. Rodriguez, D.P. Adams, R.G. Tissot, *Powder Diffraction*, 24 (2009) 82-84.
- [78] S.C. Barron, R. Knepper, N. Walker, T.P. Weihs, *Journal of Applied Physics*, 109 (2011).

- [79] D. Spitzer, M. Comet, C. Baras, V. Pichot, N. Piazzon, *Journal of Physics and Chemistry of Solids*, 71 (2010) 100-108.
- [80] K.T. Sullivan, S. Bastea, J.D. Kuntz, A.E. Gash, *Journal of Applied Physics*, 114 (2013) -.
- [81] H.M. Xu, R. Li, J.P. Shen, G.C. Yang, C.H. Pei, *Micro & Nano Letters*, 7 (2012) 1251-1255.
- [82] T.N. Taylor, J.A. Martin, *J. Vac. Sci. Technol. A-Vac. Surf. Films*, 9 (1991) 1840-1846.
- [83] M. Petrantoni, C. Rossi, V. Conédéra, D. Bourrier, P. Alphonse, C. Tenailleau, *Journal of Physics and Chemistry of Solids*, 71 (2010) 80-83.
- [84] K. Zhang, C. Rossi, M. Petrantoni, N. Mauran, *Combustion*, 17 (2008) 832-836.
- [85] L.A. Clevenger, C.V. Thompson, R.C. Cammarata, K.N. Tu, *Appl. Phys. Lett.*, 52 (1988) 795-797.
- [86] R.J. Highmore, R.E. Somekh, J.E. Evetts, A.L. Greer, *Journal of the Less Common Metals*, 140 (1988) 353-360.
- [87] R.J. Highmore, R.E. Somekh, A.L. Greer, J.E. Evetts, *Materials Science and Engineering*, 97 (1988) 83-86.
- [88] U. Anselmitamburini, Z.A. Munir, *Journal of Applied Physics*, 66 (1989) 5039-5045.
- [89] K.R. Coffey, L.A. Clevenger, K. Barmak, D.A. Rudman, C.V. Thompson, *Appl. Phys. Lett.*, 55 (1989) 852-854.
- [90] K. Barmak, K.R. Coffey, D.A. Rudman, S. Foner, EFFECT OF MICROSTRUCTURE ON PHASE FORMATION IN THE REACTION OF NB/AL MULTILAYER THIN-FILMS, *Materials Research Soc, Pittsburgh*, 1992.
- [91] D.P. Adams, M. Vill, J. Tao, J.C. Bilello, S.M. Yalisove, *Journal of Applied Physics*, 74 (1993) 1015-1021.
- [92] K.J. Blobaum, D. Van Heerden, A.J. Gavens, T.P. Weihs, *Acta Materialia*, 51 (2003) 3871-3884.
- [93] J. Wang, E. Besnoin, A. Duckham, S.J. Spey, M.E. Reiss, O.M. Knio, T.P. Weihs, *J. Appl. Phys.*, 95 (2004) 248-256.
- [94] H. Nathani, J. Wang, T.P. Weihs, *Journal of Applied Physics*, 101 (2007).

- [95] A. Duckham, S.J. Spey, J. Wang, M.E. Reiss, T.P. Weihs, E. Besnoin, O.M. Knio, J. Appl. Phys., 96 (2004) 2336-2342.
- [96] M. Aeronautical, M. Engineering, Journal of Materials, 28 (1993) 3693-3708.
- [97] W.L. Perry, B.L. Smith, C.J. Bulian, J.R. Busse, C.S. Macomber, R.C. Dye, S.F. Son, Propellants, Explos., Pyrotech., 29 (2004) 99-105.
- [98] L. Pantoya Michelle, F. Son Steven, C. Danen Wayne, S. Jorgensen Betty, W. Asay Blaine, R. Busse James, T. Mang Joseph, Characterization of Metastable Intermolecular Composites, in: Defense Applications of Nanomaterials, American Chemical Society, 2005, pp. 227-240.
- [99] A.E. Stiegman, C.-D. Park, M. Mileham, L.J. van de Burgt, M.P. Kramer, Propellants Explosives Pyrotechnics, 34 (2009) 293-296.
- [100] J. Wang, A. Hu, J. Persic, J.Z. Wen, Y. Norman Zhou, Journal of Physics and Chemistry of Solids, 72 (2011) 620-625.
- [101] W. Li, H. Cheng, Solid State Sciences, 9 (2007) 750-755.
- [102] V.E. Sanders, B.W. Asay, T.J. Foley, B.C. Tappan, A.N. Pacheco, S.F. Son, Journal of Propulsion and Power, 23 (2007) 707-714.
- [103] Y. Wang, W. Jiang, Z. Cheng, W. Chen, C. An, X. Song, F. Li, Thermochemica Acta, 463 (2007) 69-76.
- [104] E.L. Dreizin, Prog. Energy Combust. Sci., 35 (2009) 141-167.
- [105] M.L. Pantoya, J.J. Granier, Propellants, Explosives, Pyrotechnics, 30 (2005) 53-62.
- [106] F. Spaepen, C.V. Thompson, Applied Surface Science, 38 (1989) 1-12.
- [107] C. Michaelsen, K. Barmak, T.P. Weihs, Journal of Physics D-Applied Physics, 30 (1997) 3167-3186.
- [108] K.R. Coffey, K. Barmak, D.A. Rudman, C.L.H. Thieme, S. Foner, IEEE Trans. Magn., 25 (1989) 2093-2096.
- [109] K. Barmak, K.R. Coffey, D.A. Rudman, S. Foner, Journal of Applied Physics, 67 (1990) 7313-7322.
- [110] K. Barmak, K.R. Coffey, D.A. Rudman, S. Foner, Journal of Applied Physics, 67 (1990) 3780-3784.

- [111] K.R. Coffey, K. Barmak, D.A. Rudman, S. Foner, *Journal of Applied Physics*, 72 (1992) 1341-1349.
- [112] Y. Oishi, W.D. Kingery, *Journal of Chemical Physics*, 33 (1960) 480-486.
- [113] U. Aschauer, P. Bowen, S.C. Parker, *Acta Materialia*, 57 (2009) 4765-4772.
- [114] P.J. Harrop, *Journal of Materials Science*, 3 (1968) 206-222.
- [115] Y. Oishi, K. Ando, H. Kurokawa, Y. Hiro, *J. Am. Ceram. Soc.*, 66 (1983) C60-C62.
- [116] R.H. Doremus, *Journal of Applied Physics*, 100 (2006) 2-15.
- [117] S. Chevalier, Diffusion of oxygen in thermally grown oxide scales, in: A. Aguero, J.M. Albella, M.P. Hierro, J. Phillibert, F.J.P. Trujillo (Eds.) *Diffusion in Materials - Dimat2008*, Trans Tech Publications Ltd, Stafa-Zurich, 2009, pp. 405-412.
- [118] E. McCafferty, Passivity, in: *Introduction to Corrosion Science*, Springer New York, 2010, pp. 209-262.
- [119] K.B. LA Giannuzzi, Schwarz SM, Lomness JK, Prenitzer BI, Stevie FA, *Introduction to Focused Ion Beams*, Springer, United States, 2005.
- [120] S.J.P. P.D. Nellist, *The principles and interpretation of annular dark-field z-contrast imaging.*, Elsevier, 2000.
- [121] R.H. Fan, H.L. Lu, K.N. Sun, W.X. Wang, X.B. Yi, *Thermochimica Acta*, 440 (2006) 129-131.
- [122] Y. Yang, D.G. Xu, K.L. Zhang, *Journal of Materials Science*, 47 (2012) 1296-1305.
- [123] M.L. Pantoya, J.J. Granier, *Journal of Thermal Analysis and Calorimetry*, 85 (2006) 37-43.
- [124] F.J. Keneshea, D.L. Douglass, *Oxidation of Metals*, 3 (1971) 1-14.
- [125] Y. Oishi, K. Ando, N. Suga, W.D. Kingery, *J. Am. Ceram. Soc.*, 66 (1983) C130-C131.
- [126] M. Schütze, *Materials and Corrosion*, 54 (2003) 346-347.
- [127] E.J. Mily, A. Oni, J.M. LeBeau, Y. Liu, H.J. Brown-Shaklee, J.F. Ihlefeld, J.P. Maria, *Thin Solid Films*.
- [128] G. Jian, N.W. Piekiel, M.R. Zachariah, *J. Phys. Chem. C*, 116 (2012) 26881-26887.

- [129] M. Schoenitz, S. Umbrajkar, E.L. Dreizin, *Journal of Propulsion and Power*, 23 (2007) 683-687.
- [130] A. Ermoline, M. Schoenitz, E.L. Dreizin, *Combust. Flame*, 158 (2011) 1076-1083.
- [131] J.J. Granier, M.L. Pantoya, *Combust. Flame*, 138 (2004) 373-383.
- [132] K.W. Watson, M.L. Pantoya, V.I. Levitas, *Combust. Flame*, 155 (2008) 619-634.
- [133] A. Prakash, A.V. McCormick, M.R. Zachariah, *Adv. Mater. (Weinheim, Ger.)*, 17 (2005) 900-903.
- [134] P.S. Wang, L.D. Haws, W.E. Moddeman, A. Rengan, *Journal of Hazardous Materials*, 5 (1982) 297-308.
- [135] V.I. Levitas, B.W. Asay, S.F. Son, M. Pantoya, *Appl. Phys. Lett.*, 89 (2006).
- [136] C. Rossi, K. Zhang, D. Esteve, P. Alphonse, P. Tailhades, C. Vahlas, *Journal of Microelectromechanical Systems*, 16 (2007) 919-931.
- [137] X.J. Liu, I. Ohnuma, R. Kainuma, K. Ishida, *Journal of Alloys and Compounds*, 264 (1998) 201-208.
- [138] X.Y. Yan, Y.A. Chang, F.Y. Xie, S.L. Chen, F. Zhang, S. Daniel, *Journal of Alloys and Compounds*, 320 (2001) 151-160.
- [139] H.E. Kissinger, *Journal of Research of the National Bureau of Standards*, 57 (1956) 217-221.
- [140] H.E. Kissinger, *Analytical Chemistry*, 29 (1957) 1702-1706.
- [141] S.F. Son, M.A. Hiskey, D.L. Naud, J.R. Busse, B.W. Asay, *Proc. Int. Pyrotech. Semin.*, 29th (2002) 871-877.
- [142] J.P. McDonald, M.A. Rodriguez, E.D. Jones, D.P. Adams, *Journal of Materials Research*, 25 (2010) 718-727.
- [143] A.L. Ramaswamy, P. Kaste, *Journal of Energetic Materials*, 23 (2005) 1-25.
- [144] B.R. Strohmeier, *Surface and Interface Analysis*, 15 (1990) 51-56.
- [145] L. Schramm, G. Behr, W. Löser, K. Wetzig, *Journal of Phase Equilibria & Diffusion*, 26 (2005) 605-612.

- [146] K.J. Blobaum, D. Van Heerden, A.J. Wagner, D.H. Fairbrother, T.P. Weihs, *Journal of Materials Research*, 18 (2003) 1535-1542.
- [147] H.S. Craft, R. Collazo, M.D. Losego, S. Mita, Z. Sitar, J.P. Maria, *Journal of Applied Physics*, 102 (2007).
- [148] Z. Sitar, L.L. Smith, R.F. Davis, *J. Cryst. Growth*, 141 (1994) 11-21.
- [149] V. Rosenband, *Combust. Flame*, 137 (2004) 366-375.
- [150] M.A. Trunov, M. Schoenitz, E.L. Dreizin, *Combustion Theory and Modelling*, 10 (2006) 603-623.
- [151] L.P.H. Jeurgens, W.G. Sloof, F.D. Tichelaar, E.J. Mittemeijer, *Journal of Applied Physics*, 92 (2002) 1649-1656.
- [152] O.A. Ruano, J. Wadsworth, O.D. Sherby, *Acta Materialia*, 51 (2003) 3617-3634.
- [153] B. Kingery, Uhlmann, *Introduction to Ceramics*, Second ed., New York, 1976.
- [154] E.G. Colgan, J.W. Mayer, *Nuclear Instruments and Methods in Physics Research Section B: Beam Interactions with Materials and Atoms*, 17 (1986) 242-249.
- [155] G.G.J. Van, d.W.W.F. Van, D. Sigurd, *J. Appl. Phys.*, 49 (1978) 4011-4020.
- [156] A. Habanyama, C.M. Comrie, *Thin Solid Films*, 516 (2008) 5137-5143.
- [157] G.J. Vangurp, D. Sigurd, W.F. Vanderweg, *Appl. Phys. Lett.*, 29 (1976) 159-161.
- [158] A.D. Smigelskas, E.O. Kirkendall, *Transactions of the American Institute of Mining and Metallurgical Engineers*, 171 (1947) 130-142.
- [159] I. Utke, P. Hoffmann, J. Melngailis, *J. Vac. Sci. Technol. B*, 26 (2008) 1197-1276.
- [160] J. Poretz, L.W. Swanson, *Journal of Vacuum Science & Technology B*, 10 (1992) 2695-2698.
- [161] T. Tao, J. Ro, J. Melngailis, Z. Xue, H.D. Kaesz, *Journal of Vacuum Science & Technology B*, 8 (1990) 1826-1829.
- [162] R.M. Langford, T.X. Wang, D. Ozkaya, *Microelectronic Engineering*, 84 (2007) 784-788.

- [163] D.D. Dlott, New Developments in the Physical Chemistry of Shock Compression, in: S.R. Leone, P.S. Cremer, J.T. Groves, M.A. Johnson (Eds.) Annual Review of Physical Chemistry, Vol 62, 2011, pp. 575-597.
- [164] W.J. Nellis, Reports on Progress in Physics, 69 (2006) 1479-1580.
- [165] H.Y. Wei, C.S. Yoo, Journal of Materials Research, 27 (2012) 2705-2717.
- [166] Z.W. Gu, C.W. Sun, J.H. Zhao, N. Zhang, Journal of Applied Physics, 96 (2004) 344-347.
- [167] E. Dunbar, N.N. Thadhani, R.A. Graham, Journal of Materials Science, 28 (1993) 2903-2914.
- [168] H. Fujiwara, K.E. Brown, D.D. Dlott, LASER-DRIVEN FLYER PLATES FOR REACTIVE MATERIALS RESEARCH, in: M.L. Elert, W.T. Buttler, M.D. Furnish, W.W. Anderson, W.G. Proud (Eds.) Shock Compression of Condensed Matter - 2009, Pts 1 and 2, 2009, pp. 1317-1320.
- [169] A.M. Astakhov, R.S. Stepanov, A.Y. Babushkin, Combust Explos Shock Waves, 34 (1998) 85-87.
- [170] N.K. Bourne, J.C.F. Millett, G.T. Gray, Journal of Materials Science, 44 (2009) 3319-3343.
- [171] D.A. Fredenburg, N.N. Thadhani, Journal of Applied Physics, 113 (2013).
- [172] Y. Yang, S. Wang, Z. Sun, D.D. Dlott, Journal of Applied Physics, 95 (2004) 3667-3676.
- [173] T. Bazyn, N. Glumac, H. Krier, T.S. Ward, M. Schoenitz, E.L. Dreizin, Combust. Sci. Technol., 179 (2007) 457-476.
- [174] D.E. Eakins, N.N. Thadhani, Int. Mater. Rev., 54 (2009) 181-213.
- [175] X.X. Zheng, A.D. Curtis, W.L. Shaw, D.D. Dlott, J. Phys. Chem. C, 117 (2013) 4866-4875.
- [176] P.O.K. Krehl, Eur. Phys. J. H, 36 (2011) 85-152.
- [177] Y. Yang, R.D. Gould, Y. Horie, K.R. Iyer, Appl. Phys. Lett., 70 (1997) 3365-3367.
- [178] N.N. Thadhani, Prog. Mater. Sci., 37 (1993) 117-226.
- [179] D. Eakins, N.N. Thadhani, Journal of Applied Physics, 100 (2006).

- [180] K.E. Brown, W.L. Shaw, X. Zheng, D.D. Dlott, *Review of Scientific Instruments*, 83 (2012).
- [181] N.C. Dang, Z.A. Dreger, Y.M. Gupta, D.E. Hooks, *J. Phys. Chem. A*, 114 (2010) 11560-11566.
- [182] S.M. Walley, J.E. Balzer, W.G. Proud, J.E. Field, *Proc. R. Soc. A-Math. Phys. Eng. Sci.*, 456 (2000) 1483-1503.
- [183] F.X. Jette, A.J. Higgins, S. Goroshin, D.L. Frost, Y. Charron-Tousignant, M.I. Radulescu, J.J. Lee, *Journal of Applied Physics*, 109 (2011).
- [184] H.Y. Wei, C.S. Yoo, *Journal of Applied Physics*, 111 (2012).
- [185] K.S. Martirosyan, M. Zyskin, C.M. Jenkins, Y. Horie, *Journal of Applied Physics*, 112 (2012).
- [186] L. Zhou, N. Piekiet, S. Chowdhury, M.R. Zachariah, *J. Phys. Chem. C*, 114 (2010) 14269-14275.
- [187] G. Jian, S. Chowdhury, K. Sullivan, M.R. Zachariah, *Combust. Flame*, 160 (2013) 432-437.
- [188] N.W. Piekiet, R.E. Cavicchi, M.R. Zachariah, *Thermochimica Acta*, 521 (2011) 125-129.
- [189] M. Okeeffe, W.J. Moore, *Journal of Chemical Physics*, 36 (1962) 3009-&.
- [190] A.H. Heuer, *J. Eur. Ceram. Soc.*, 28 (2008) 1495-1507.
- [191] K. Shimizu, R.C. Furneaux, G.E. Thompson, G.C. Wood, A. Gotoh, K. Kobayashi, *Oxidation of Metals*, 35 (1991) 427-439.
- [192] V.I. Levitas, *Philosophical transactions. Series A, Mathematical, physical, and engineering sciences*, 371 (2013) 20120215.
- [193] Y. Aoki, S. Hayashi, H. Komatsu, *J. Cryst. Growth*, 123 (1992) 313-316.
- [194] M. Monagheddu, N. Bertolino, P. Giuliani, C. Zanotti, U.A. Tamburini, *Journal of Applied Physics*, 92 (2002) 594-599.
- [195] M. Hämäläinen, N. Bochvar, L.L. Rokhlin, K. Zeng, *Journal of Alloys and Compounds*, 285 (1999) 162-166.

[196] V.I. Levitas, B.W. Asay, S.F. Son, M. Pantoya, *Journal of Applied Physics*, 101 (2007).

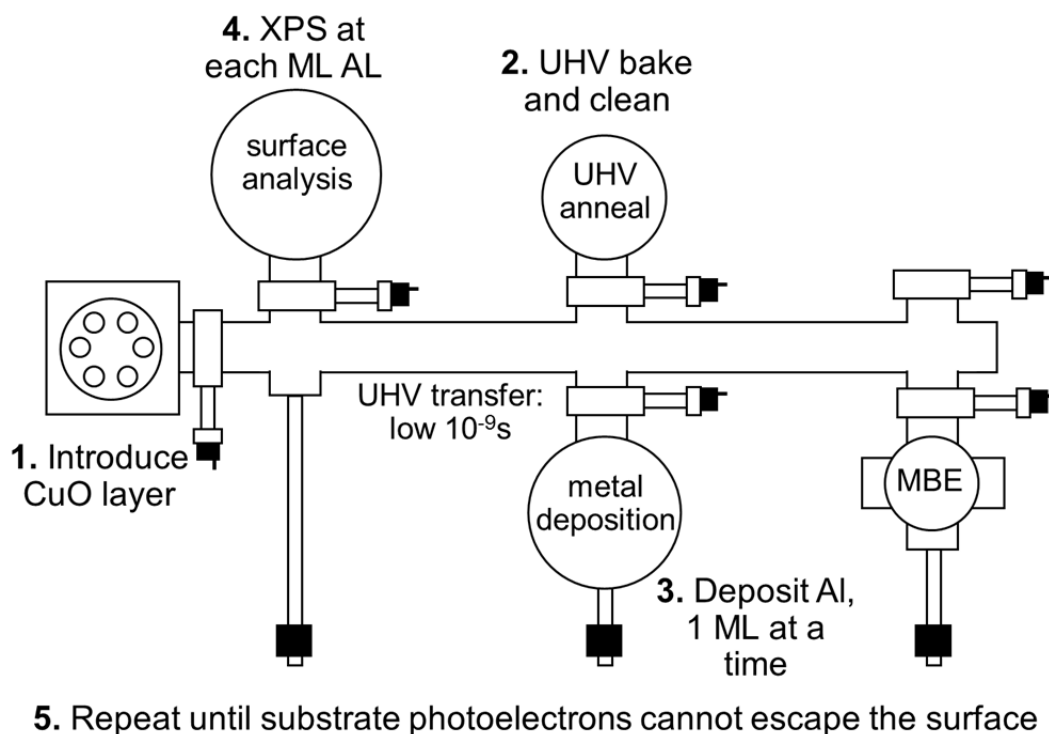
[197] S. Moulder, Sobol, Bomben, in: J. Chastain (Ed.), 1992, pp. 261.

**APPENDICES**

## Appendix A- XPS

### I -Aluminum Aging Study

During the interfacial analysis experiment employing XPS several key issues needed is to be addressed before the experiment could proceed in identifying the thickness of the interfacial reactive layer. While the base pressure of the transfer module between the surface analysis chamber and the deposition chamber was  $1 \times 10^{-9}$  torr the pressure inside the deposition chamber where the metallic species was electron beam evaporated onto the copper oxide surface reached a value of  $1 \times 10^{-7}$  torr. Figure A.1 shows the schematic of the XPS system used.



5. Repeat until substrate photoelectrons cannot escape the surface

**Figure A.1-** Schematic of the XPS chamber used to complete the surface analysis

This rise in pressure is assumed to be due to the vaporization of the metallic species being evaporated, however considering this entire experiment is designed to monitor the oxidation

of evaporated metal it was decided to check the electronic environment of the metal being deposited and confirm that it is not being oxidized by the deposition process or during sample transfer between the analysis chamber and the deposition chamber. In the worst possible case scenario the pressure rise in the deposition chambers due to oxygen outgassing from the metal at a pressure of  $1 \times 10^{-7}$  torr and assuming a sticking coefficient of unity the surface of the aluminum would be completely oxidized and 10 seconds. To monitor the possible oxidation due to the gaseous media in the experimental ultrahigh vacuum chamber a bare silicon substrate was introduced into the vacuum system. It is assumed that surface oxides would reside on the silicon substrate. As a result of the probable oxygen on the surface and not wanting this source of oxygen to skew the oxidation of the deposited aluminum source 10 nm of aluminum were deposited on the surface of the silicon at  $0.8 \text{ \AA}$  a second and then analyzed in the surface analysis compartment of the UHV chamber. After this analysis the sample was immediately transferred back into the deposition system and a monolayer of aluminum was deposited at  $0.4 \text{ \AA}$  a second then analyzed and then another aluminum monolayer was deposited at  $0.2 \text{ \AA}$  a second then analyzed.

**Note:** It was done in this manner because it is assumed that if oxidation is to occur during deposition it will most likely occur at a slower deposition rate. So the successive monitoring of deposition must start at higher deposition rates and incrementally decrease the rate in order to accurately pinpoint the conditions where oxidation is occurring during deposition. If slower deposition rates were to be used first on the same sample and oxidation was seen after a low deposition rate the data collected afterwards on subsequent monolayers deposited at higher deposition rates could falsely indicate oxidation during a higher rate of deposition because photoelectron's from the oxidized layer will still be collected.

XPS spectra was then collected after each deposition and incremental times afterwards up to 15 days afterwards. The results from this experiment are shown in figures A .2 and A.3. In figure A 0.2 the first trace is of a bare silicon substrate scanned around the aluminum 2p binding energy range as a reference. Each subsequent trace after this corresponds to a

different thickness of aluminum and dwell time inside the ultrahigh vacuum chamber. From this graph the only binding energy peak seen is that of Al 2p at 73 eV which corresponds to metallic aluminum. The metallic aluminum peak remains constant even after 126 hours which shows no oxidation is seen during deposition. Allowing the sample to age longer it can be seen in figure A .3 that aluminum bound with oxygen starts to show at the energy 74.7 eV. While this does show that oxidation is possible inside the UHV and the oxygen peak is present after 168 hours, the oxygen peak does not grow appreciably after 15 days of residence time in the analysis chamber. From this analysis it can be then confidently demonstrated that while oxidation is possible, the time needed to oxidize a sample from the vacuum environment is much greater than the length scales at which surface analysis will be conducted.

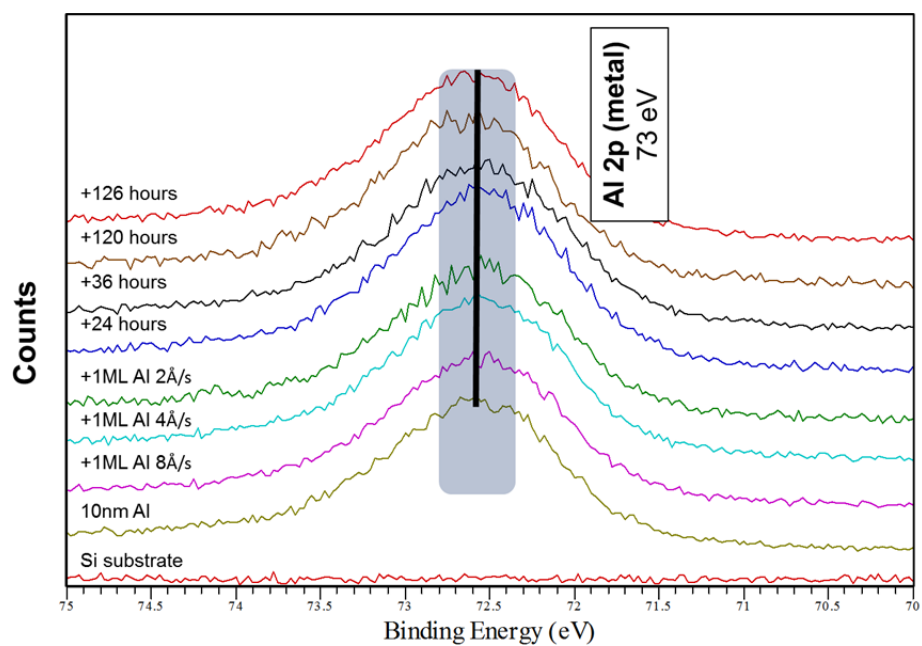


**Figure A.2-** Aluminum 2p photoelectron binding energy spectra taken during the first 126 hours after deposition

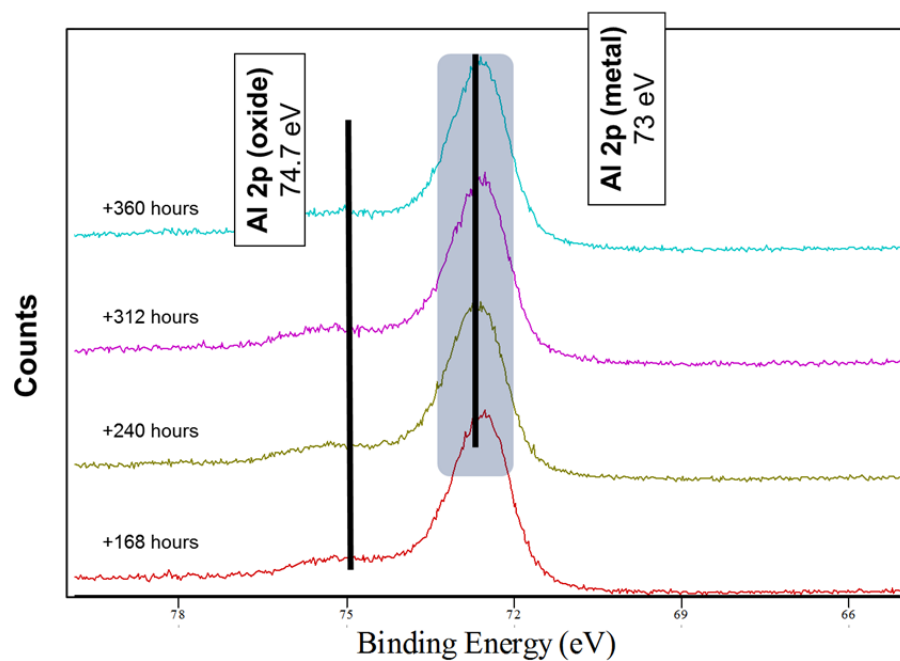


**Figure A.3-** Aluminum 2p photoelectron binding energy spectra taken incrementally up to 15 days after deposition

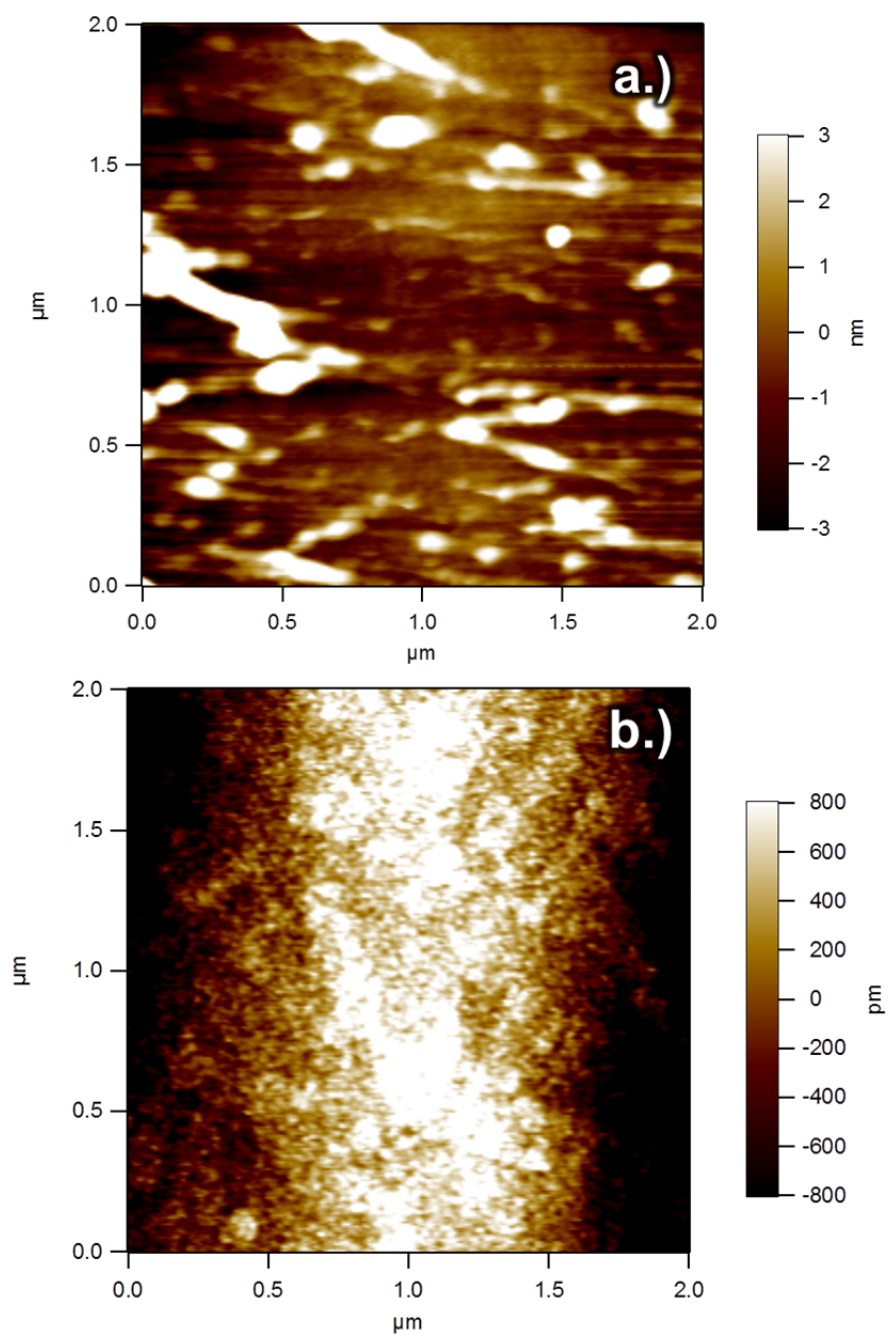
## II. CuO Surface Roughness Study

Preparatory measures to ensure pristine interface quality during the aluminum oxide and zirconium oxide scale thickness experiments in the UHV XPS analysis were undertaken. The sample substrates need to be devoid of any contamination and the deposited copper oxide surface should be as flat as possible. Due to the large time investment that surface analysis requires it was deemed prudent to first characterize and implement a satisfactory cleaning method of silicon substrates as well as determine an optimal copper oxide thickness that provides the smoothest interface possible but is thick enough to act as an oxygen source for the scavenging aluminum metal to be electron beam deposited. AFM analysis of an as received silicon substrate reveal an extremely rough surface that is most likely environmental contamination. Figure A.4 and figure A.5 are AFM micrographs of the as received and cleaned samples respectively. After cleaning the roughness of the silicon substrate is sub nanometer and is clearly the more pristine of the two substrates. The cleaning method that was undertaken first immersed the silicon substrate in an acetone bath and sonicated for 15 minutes. The sample substrate was then removed from acetone then rinsed with water, isopropanol, methanol, purposely in decreasing polarity, rapidly dried with laboratory nitrogen and then introduced into a UVO bath. The purpose of the UVO bath is to clean and remove any organic contaminants that remain on the sample surface. The mechanism of how the organic is removed is not entirely understood however it is believed that the ultraviolet radiation from this technique polymerizes any conjugated organic molecule on the surface that is then easily desorbed from the sample substrate.

After the appropriate cleaning mechanism was demonstrated to sufficiently clear any contaminant off the surface the deposition of copper oxide on the clean silicon was performed to track the roughness of the surface and its morphology. Figures A.5 to figure A.13 show the AFM micrographs of copper oxide films from 10 nm up to 2  $\mu\text{m}$  in thickness. From this simple deposition study the only variable changed was the time

allowed for deposition to occur which is what governs how thick the layer will be. A few features to note during this experiment are the increased roughness from 100 pico meters to 11.5 nm with of the thinnest layers of copper oxide yielding the smallest average roughness values. As surface morphology was tracked an interesting feature of note is observed in figure A.8 which corresponds to 30 nm of copper oxide grown on silicon. What is seen here in this pictograph is the presence of nucleation sites randomly distributed across the surface, which seems to correspond from a transition of planar linear growth to a more Stransky-Krastinov growth of island formation to coalescence classically seen in thin film preparations. From this analysis figure A.8b shows a height re-trace across a 30  $\mu\text{m}$  film of copper oxide on silicon. While the roughness value is not exceedingly elevated, it can be seen that the surface is not homogenous and would not be optimal for an interface oxidation study. Morphology of successively thicker films 50, 100, 200 nm are results of the nucleation and growth of these islands that eventually form a conformal layer and as the thickness increases so too does the roughness. The results from this analysis then suggests that a copper oxide thin film below 30 nm would be optimal for XPS analysis. Typical scale thicknesses of aluminum oxide on aluminum range from 2 nm to 12 nm where 2 nm is usually found to be the case in thin film studies[82]. To supply stoichiometric amounts of oxygen to the incoming depositing aluminum species the copper oxide thickness should be at least 10 nm. However if the scale thickness of alumina should grow larger than 7 nm a thicker copper oxide film would be needed. During the deposition of one of the first trial XPS experiments for aluminum deposition on the sputtered copper oxide on silicon the deposited aluminum yielded spectra that corresponded to only oxidized aluminum after 12 monolayers of aluminum were deposited. This sample as described in chapter 5 was deposited via a ML deposition followed by successive analysis technique that allowed for significant time between each metal ML. Deposition was halted and a new sample was placed in the metallization chamber and 12 monolayers of aluminum were deposited all once and found to have two peaks of one correspondent oxide one corresponding to the metal

meaning that the oxidation was occurring during the transfer of the sample to the analysis chamber and back again. If however this was not the case and a thicker layer of aluminum was needed to be deposited in order to see the metallic species the thickness of the copper oxide would only need to be increased and thickness of 21 monolayers of aluminum were deposited and no oxide was seen. Because of this, copper oxide thicknesses of 10 and 20 nm were used for the XPS experiment allowing for ample amount of oxygen to be supplied to the reactive metal while still maintaining a relatively smooth interface.



**Figures A.4-** AFM map of a.) Uncleaned silicon with a 2.1 nm roughness, b.) a cleaned silicon wafer with a 100pm roughness

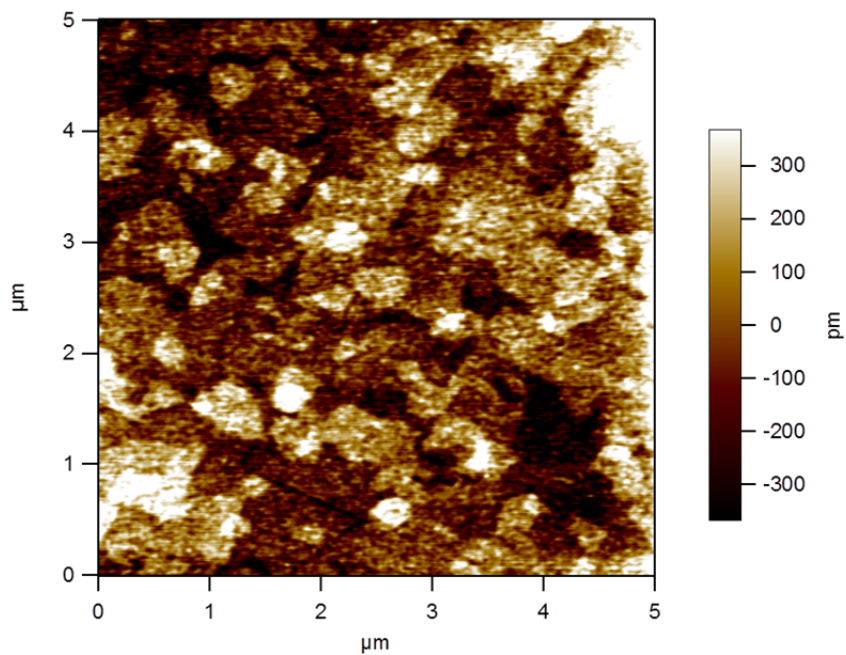


**Figure A.5** – AFM of CuO 10nm on silicon with a roughness of 100pm

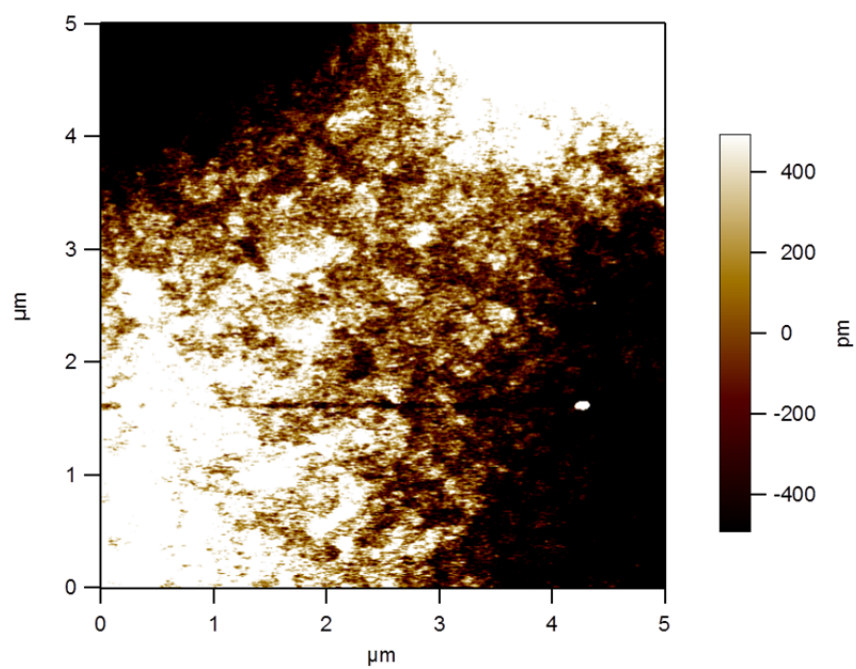


**Figure A.6**- AFM of CuO 20nm on silicon with a roughness of 316pm

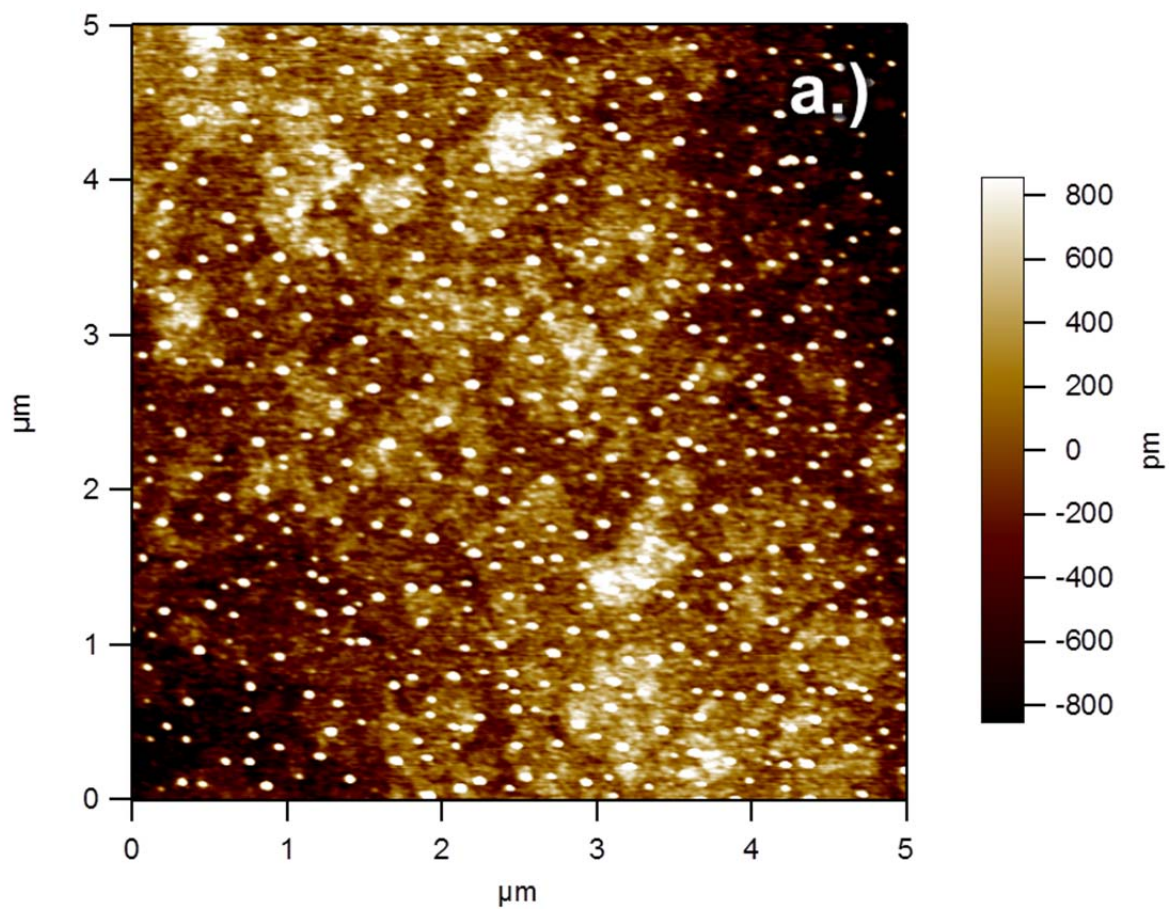


**Figure A.7-** AFM of CuO 30nm on silicon with a roughness of 520pm displaying the transition from layer by layer growth to island growth to coalescence.

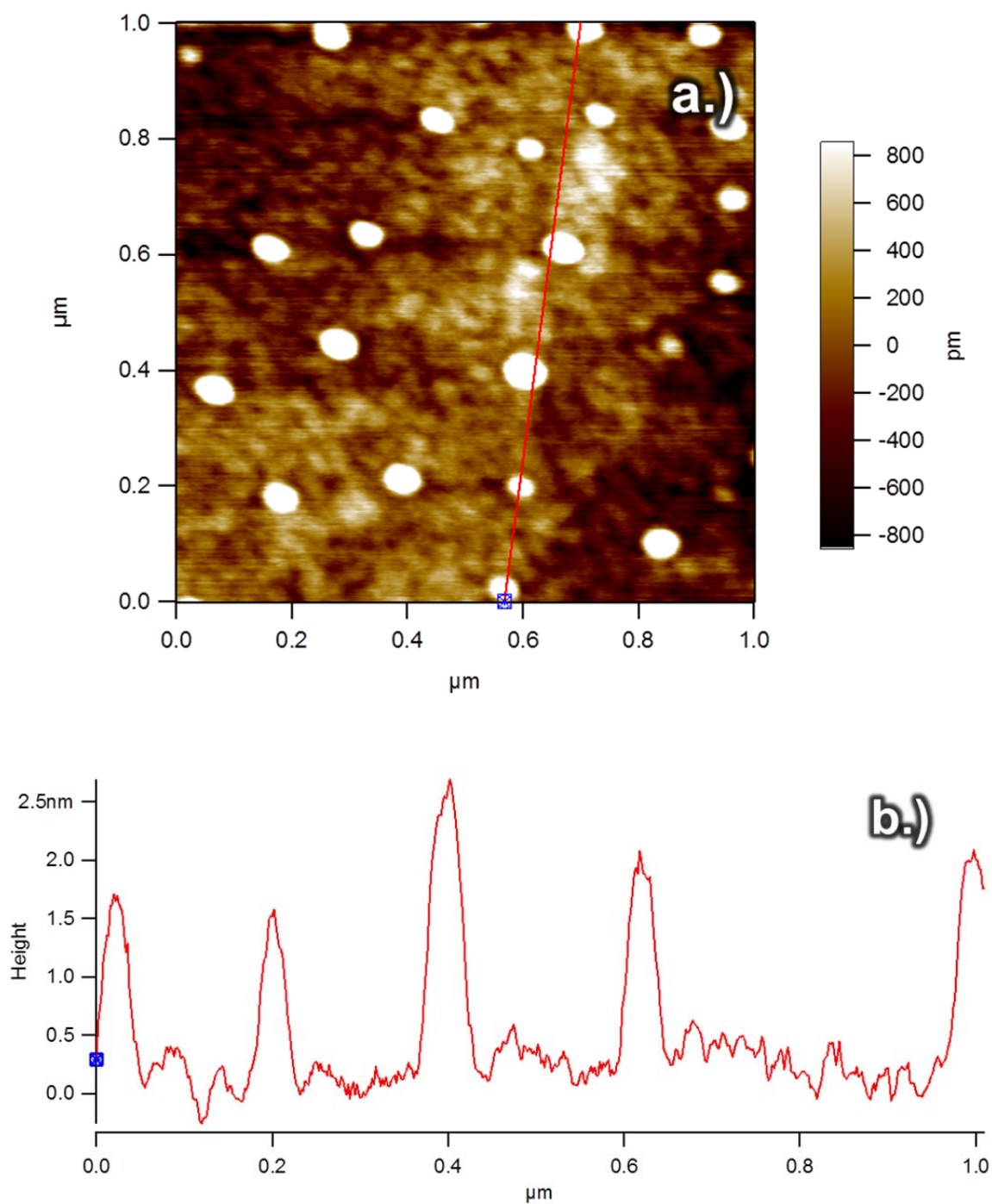


**Figure A.8-** AFM of a.) CuO 30nm on silicon with a b.) line height retrace to display the height of the growing island.

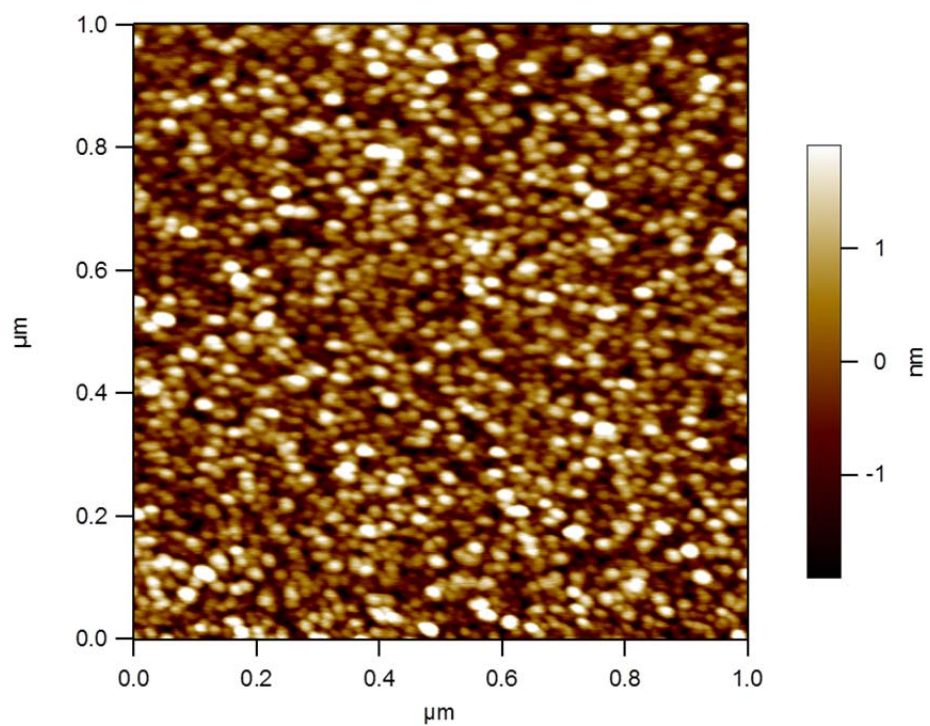


**Figure A.9** – AFM of CuO 50nm with a roughness of 872pm

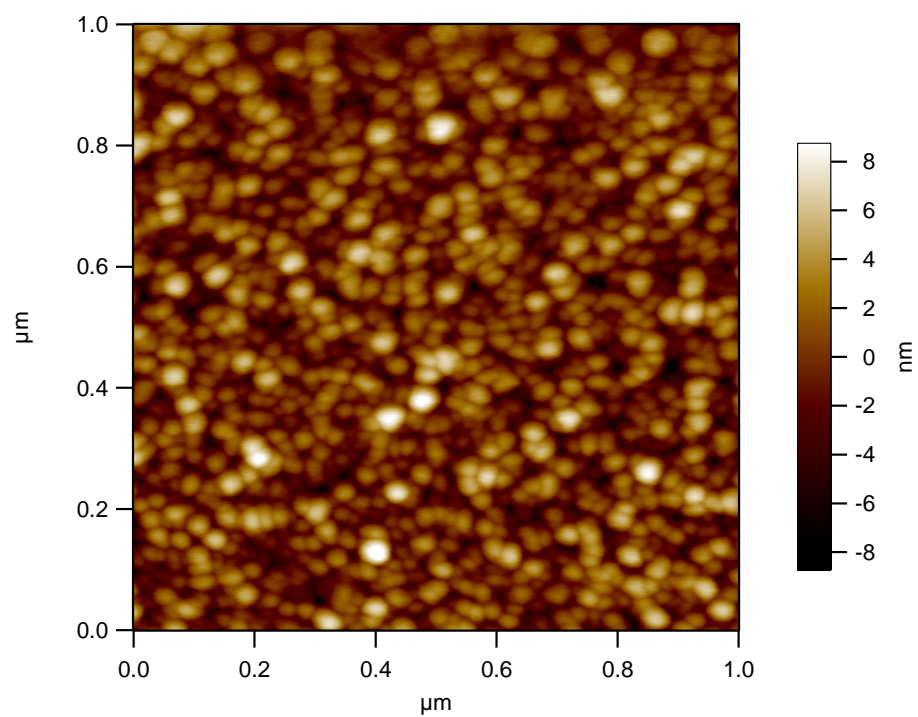


**Figure A.10**- AFM of CuO 100nm with a roughness of 1.5nm

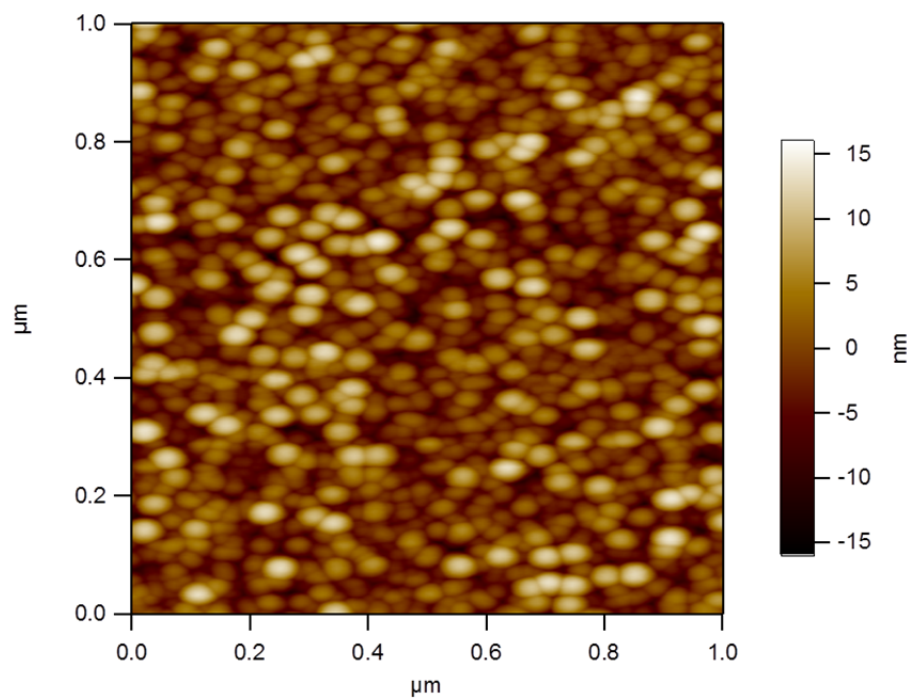


**Figure A.11-** AFM of CuO 200nm with a roughness of 4.5nm

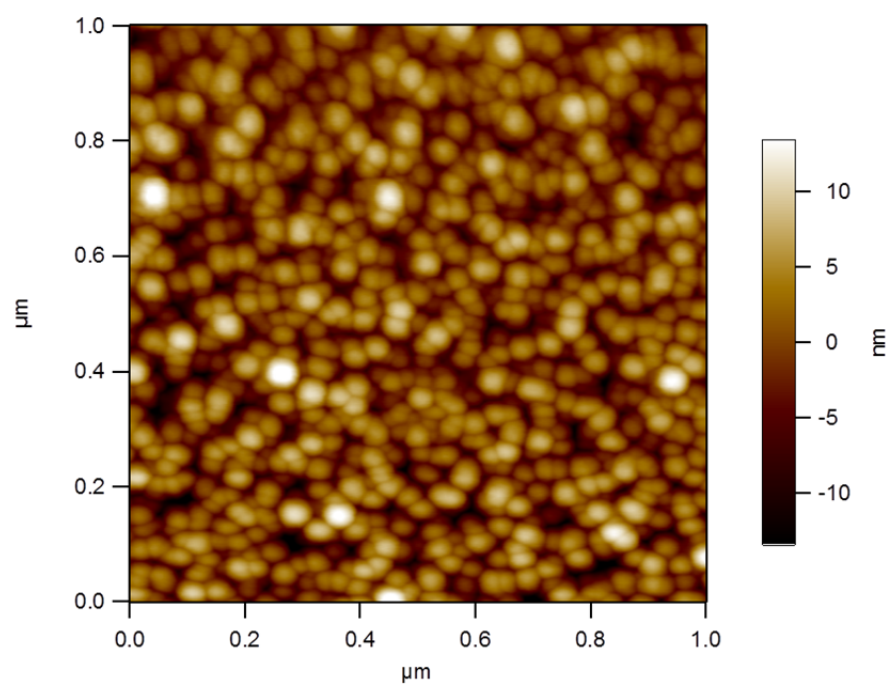


**Figure A.12-** AFM of CuO 300nm with a roughness of 4.8nm

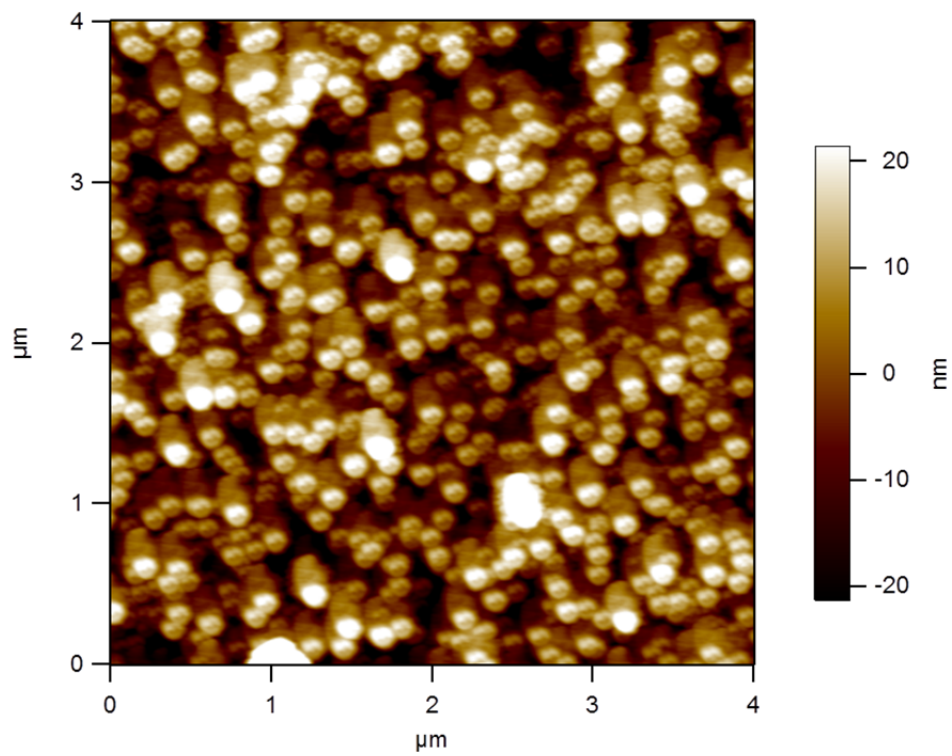


**Figure A.13-** AFM of 2 $\mu\text{m}$  of CuO with a roughness of 11.35nm

### **III. XRR confirmation of thin film thickness at interface for Zr/CUO**

A technique used to determine layer thicknesses of deposited samples on thin films called x-ray reflectivity was described in Chapter 3. This technique takes advantage of the constructive and destructive interference that a beam of light undergoes when interacting with an interface of two materials with varying refractive indices. The equations that describe this phenomena were developed by Fresnel and can be applied to situations that have more than one interface. The nature of the interaction and the shape of the interference pattern is a function of film and interface roughness, the densities of the materials, and the thickness of the films. If a structure of multi-layered thin films is created, modeling software can be employed to test the interference outcome and if the geometry and dimensions of the sample are known good agreement can be found between modeling and experimental data. This technique was then used as a secondary method to test the oxide thickness at the interface of two thermite constituents specifically the zirconium and copper oxide system. Zirconium was laid down on corresponding to a thickness of 50 nm followed by a capping layer of copper oxide with the same thickness. The sample was then analyzed in reflectivity geometry close to the critical angle and reflectivity data was taken to about  $1^\circ$  two Theta. The resulting data from this analysis was then fit to a model that assumed an interface layer of zirconia existed making which created two more interfaces for x-ray radiation to interact with. Figure A.24 results show the empirical data and the fit of a zirconium underlayer with a 3 nm thick zirconia oxide layer followed by the 50 nm copper oxide thin film. This fit allows for a secondary confirmation that while the zirconium and copper oxide system seemingly is more reactive than the aluminum copper oxide system at room temperature the initial oxide thickness that is created is not drastically different.

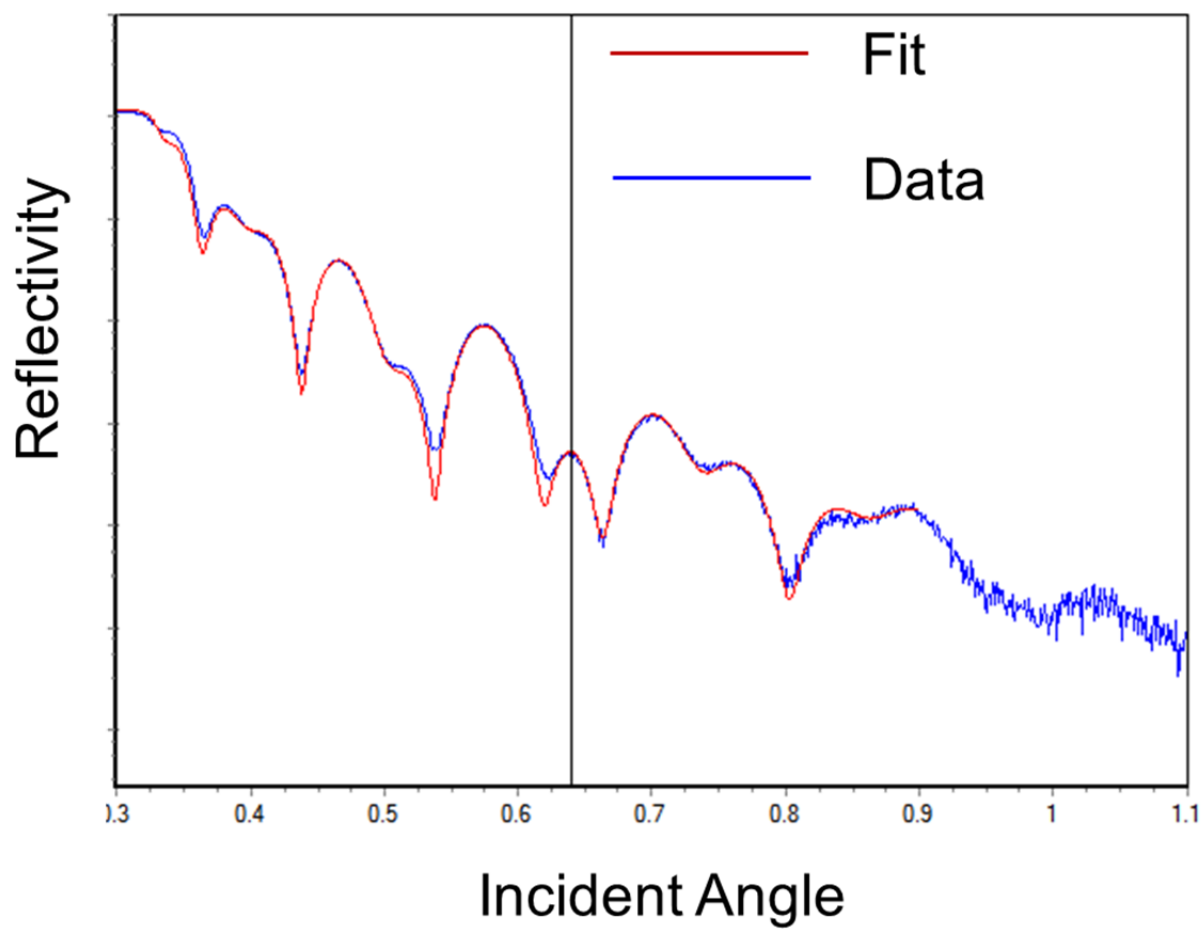


**Figure A.14-** XRR data from the Zr/CuO interface with a modeled fit to account for a 3nm interfacial layer.

#### **IV. XPS cooling System**

The X-ray Photo Electron system used in this work in chapter 5 on the interfacial analysis of thin film thermites, is shown in the schematic in figure A1. During the measurement process of this experiment a cooling error occurred that systematically shut of the analyzer during the measurement. The system shut off due to lack of cooling water flow. The specific electron detection device was significantly aged (20+ years). The age of this device suggested that there could be a significant flow restricting scale inside the water transport cooling system. The entire cooling lines were replaced along with the water filtration and the water pump. During this reconstruction it was noted that previous cooling water used was industrial water as the coolant of choice. From this point it was decided and implemented that only distilled water be used in the x-ray system due to its clean nature and used in place of deionized water because deionized water will etch metal.

## **Appendix B. – TEM Sample Preparation for Kirkendall Analysis**

Electron Beam deposition focused ion beam milling (FIB) was used to create transmission electron microscope samples. The traditional method of creating the TEM samples via fib processing involves a protective deposition of platinum on top of the sample interface of interest. This is followed by the milling out a section in front of and behind the sample interface of interest. A sample transport needle is inserted close to the surface of the sample which is then platinum welded to the thin sample which is then cut out of the surface entirely and lifted out with the needle. The TEM sample is then attached to a TEM grid and detached from the sample transport needle. From this point the sample was then thinned to thicknesses that are transparent to electrons of roughly 100 nm. This thinning process is completed by ion milling at ion energy and currents decreasing in value as the thickness reaches its target value. FIB preparation of the nano Kirkendall sample is no different. The only slight variation to this protocol is that the area of protective platinum laid down on top of the sample was outlined by the flanking platinum bars that were deposited in between the reactive metal and the oxide. Figures B.1 through B.7 show the starting platinum bars next to a milled out location identifier feature followed by the successive

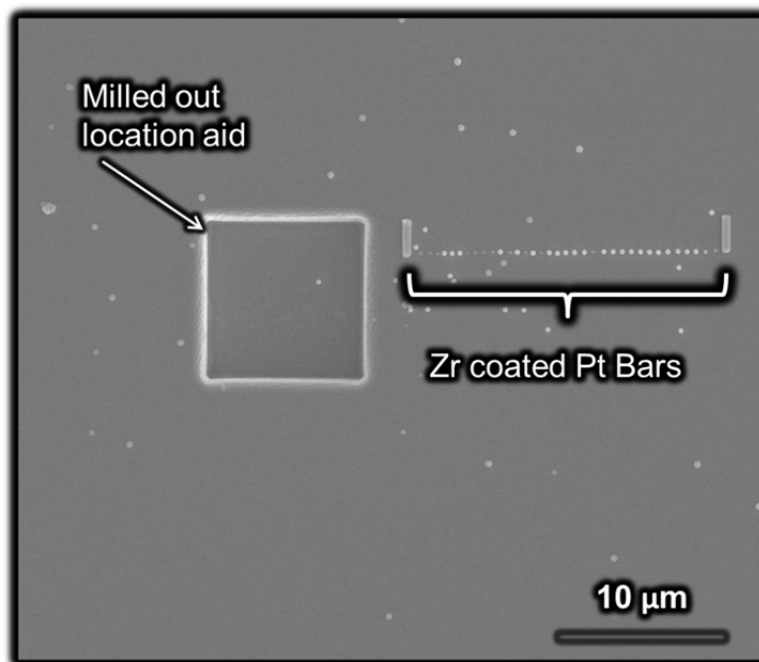


**Figure B.1-** SEM micrograph of a milled location aid next to Pt bars deposited at the interface of

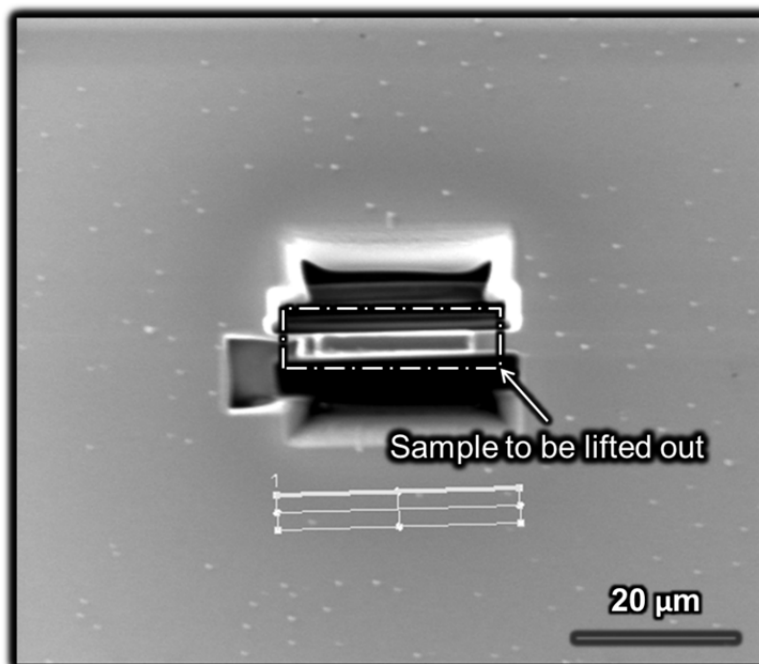


**Figure B.2-** SEM snapshot of milling out a TEM sample

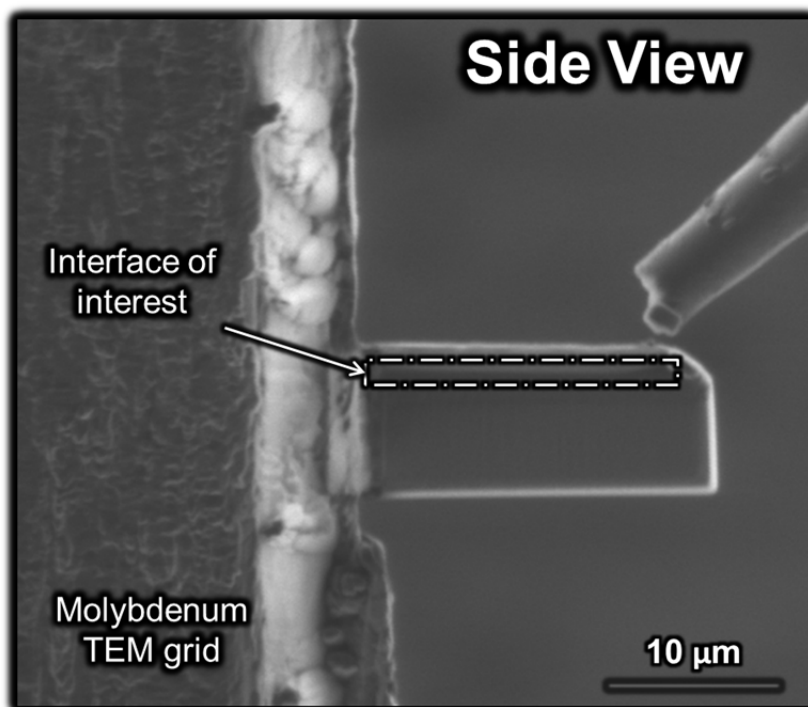


**Figure B.3-** SEM micrograph of the side view of a TEM sample attached to a Molybdenum grid

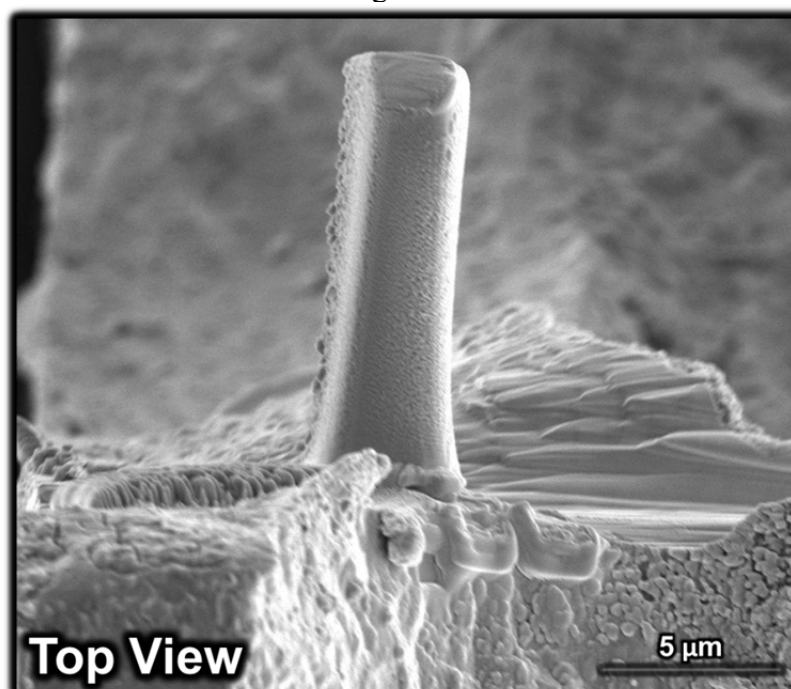


**Figure B.4-** SEM micrograph of the top view of the TEM sample

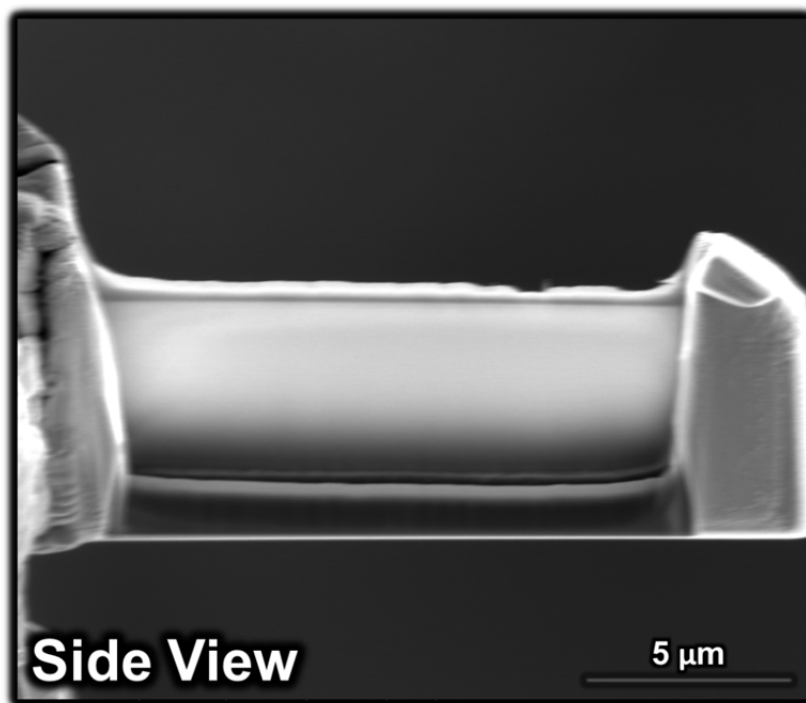


**Figure B.5-** SEM micrograph of the side view of the TEM sample after thinning.

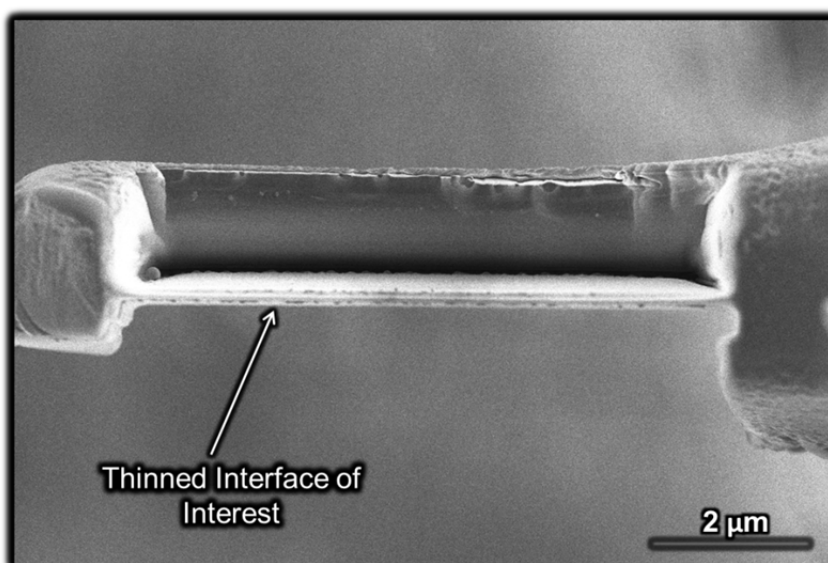


**Figure B.6-** SEM micrograph of the top view of the thinned TEM sample